SUPPORTED OXIDE CATALYSTS:
COBALT OXIDE AND MOLYBDENA ON TITANIA

A Thesis submitted for the degree of Doctor of Philosophy

by

Rashid Jaber Asa'd Shukri

Department of Chemistry, Brunel University

April 1989

To The Memory Of My Late Parents

ABSTRACT

TiO_2 supported MoO_3 catalysts were prepared by aqueous impregnation of low area anatase (10 m^2g^{-1}) with solutions of $(NH_4)_6Mo_7O_{24}.4H_2O$ (MT/C series), and $H_2[MoO_3(C_2O_4)].H_2O$ (MOT/C series). Three series of CoO_x/TiO_2 catalysts were fabricated by aqueous impregnation of the same support with solutions of $Co(NO_3)_2.6H_2O$ (CT/C series), and $Co(CH_3COO)_2.4H_2O$ (CAT/C series), and by homogeneous precipitation using $Co(NO_3)_2.6H_2O$ (CT/HP series). CoO and MoO_3 were deposited on Degussa P-25 (55 m^2g^{-1}) by aqueous impregnation using $(NH_4)_6Mo_7O_{24}.4H_2O$ and $Co(NO_3)_2.6H_2O$ in three ways: (i) CoO impregnated first, MoO_3 second (CMT series); (ii) MoO_3 impregnated first, CoO second (MCT series); and (iii) CoO and MoO_3 together (CMTg series). The catalysts were characterized by laser Raman spectroscopy (LRS), temperature-programmed reduction (TPR), X-ray photoelectron spectroscopy (XPS), and transmission electron microscopy (TEM). Monolayer coverage by XPS was independent of the precursor for the MoO_x/TiO_2 catalysts, but a function of the method of preparation and the precursor for the CoO_x/TiO_2 catalysts. XPS results for the CMTg series differed from those for the CMT and MCT series, suggesting different surface species had been formed by varying the mode of impregnation. Phase diagrams relating semi-quantitatively to the oxide contents are presented. 2-propanol decomposition was studied to probe the acid-base properties of the catalysts. TiO_2 and MoO_3 exhibited dehydration activity, whereas CoO showed dehydrogenation activity. All the supported catalysts gave activation energies for dehydration higher than dehydrogenation. In the sub-monolayer region, the catalytic activity for dehydration was in the order: MCT > CMTg > CMT > MT/C > CT/C, while the selectivity remained almost unchanged. In the monolayer region, the activity was: MT/C > CMT > CMTg > MCT > CT/C and the selectivity increased compared with the sub-monolayer region. In the four-monolayer region, the activity decreased compared with the sub-monolayer and monolayer regions, but the selectivity increased relative to the previous two regimes. "Compensation effect" plots revealed different types of active centres responsible for dehydration and dehydrogenation processes in the MoO_x/TiO_2 and $CoO-MoO_3/TiO_2$ catalysts, while active centres were almost identical with the CoO_x/TiO_2 system.

ACKNOWLEDGEMENTS

My sincere thanks are due to Professor G. C. Bond who gave continuous advice and criticism throughout my research and the preparation of this thesis, Dr. M. R. Gelsthorpe who helped in my experimental work, the Staff of The Experimental Techniques Centre for the use of TEM and XPS facilities, Dr. D. Urwin from Tioxide International Ltd for the chemical analysis of the catalysts, Dr. K. A. K. Lott who kindly proofread the manuscript, and Mrs. E. Tapley who typed this thesis.

Contents

		Page
CHAPTER 1.	INTRODUCTION	
1.1	General Introduction.	1
1.2	The concept of dispersion in supported oxides.	2
1.2.1	The concept of contact angle, interaction energies and wetting.	3
1.2.1.1	The spreading condition.	5
1.3	Methods of preparation of supported oxides.	9
1.4	Characterization of supported oxides.	10
1.4.1	Laser Raman Spectroscopy (LRS).	12
1.4.2	Temperature-programmed reduction (TPR).	13
1.4.2.1	Derivation of kinetic parameters from TPR profiles obtained at different heating rates.	19
1.4.2.2	Effects of variation of experimental parameters.	24
1.4.2.3	Influence of heating rate and initial temperature.	24
1.4.2.4	Influence of reducing gas concentration.	24
1.4.2.5	Influence of gas flow rate.	25
1.4.2.6	Influence of the mass of solid.	26
1.4.2.7	Particle size effects.	26
1.4.2.8	Selection of values for the operating parameters.	28

1.4.3	X-ray photoelectron spectroscopy (XPS).	29
1.4.3.1	Effect of calcination temperature.	32
1.4.4	Transmission electron microscopy (TEM).	33
1.4.5	Catalytic decomposition of 2-propanol	36
1.5	Structure of single supported oxides.	38
1.5.1	Definition of "monolayer".	38
1.5.2	Evidence for "monolayers".	38
1.5.3	Criteria for the presence of a complete monolayer.	41
1.5.4	Comparison of Al_2O_3, SiO_2 and TiO_2 as supports.	42
1.5.5	Surface properties of supports.	43
1.5.5.1	Surface charge in solution.	43
1.5.5.2	Surface functionalities and catalytic properties.	44
1.6	Structure of bicomponent supported oxides.	45
1.6.1	Monolayer model.	45
1.6.2	Pseudo-intercalation model.	47
1.6.3	Defect structure of MoS_2.	48
1.6.4	Mixed sulphide hypothesis.	48
1.6.5	Synergy by contact.	50
1.6.6	Kasztelan, Grimblot and Bonnelle model.	51
1.7	Acidity of supported oxides/monolayers.	54
1.8	Scope of this thesis.	55
1.9	References.	58

CHAPTER 2. PREPARATION OF CATALYSTS

2.1	Introduction.	73
2.2	Factors influencing impregnation profiles.	77
2.2.1	Impregnation step.	77
2.2.2	Drying step.	78
2.3	Preparation of profile-controlled impregnated catalysts.	79
2.3.1	Uniform and pellicular impregnation.	80
2.3.2	Subsurface impregnation.	80
2.3.3	Multicomponent impregnation.	81
2.4	TiO_2 supports.	82
2.4.1	Types of TiO_2 supports.	83
2.5	Pretreatment of TiO_2.	85
2.5.1	Washing of TiO_2 to remove the P and K impurities.	85
2.6	Preparation of MoO_3/TiO_2 catalysts.	85
2.6.1	Preparation of MoO_3/TiO_2 catalysts by impregnation using ammonium hepta-molybdate (AHM) as precursor.	85
2.6.2	Preparation of MoO_3/TiO_2 catalysts by impregnation using molybdenum oxalate as precursor.	86

2.7	Preparation of CoO/TiO_2 catalysts.	87
2.7.1	Preparation of CoO/TiO_2 catalysts by impregnation using cobalt nitrate as precursor.	87
2.7.2	Preparation of CoO/TiO_2 catalysts by homogeneous precipitation using cobalt nitrate as precursor.	87
2.7.3	Preparation of CoO/TiO_2 catalysts by impregnation using cobalt acetate as precursor.	88
2.8	Preparation of $CoO-MoO_3/TiO_2$ catalysts.	89
2.8.1	CoO first.	89
2.8.2	MoO_3 first.	89
2.8.3	CoO and MoO_3 together.	90
2.9	References.	91

CHAPTER 3. EXPERIMENTAL TECHNIQUES

3.1	Introduction.	95
3.2	Characterization methods.	96
3.2.1	Chemical analysis.	96
3.2.2	Laser Raman spectroscopy (LRS).	96
3.2.2.1	Application.	97
3.2.3	Temperature programmed reduction (TPR).	97
3.2.3.1	Apparatus and experimental procedure.	98
3.2.3.2	Application.	100
3.2.4	X-ray photoelectron spectroscopy (XPS).	101
3.2.4.1	Referencing.	101

3.2.4.2 Calculation. 102

3.2.4.3 Application. 104

3.2.5 Transmission electron microscopy (TEM). 105

3.2.5.1 Application. 105

3.3 Catalytic activity measurements. 106

3.3.1 Decomposition of 2-propanol. 106

3.3.2 Apparatus. 106

3.3.3 Experimental procedure. 107

3.3.4 Calculation. 108

3.3.5 Application. 108

3.4 Chemicals used. 109

3.5 References. 110

CHAPTER 4. RESULTS

4.1 Introduction 112

4.1.1 Laser Raman spectroscopy (LRS) 115

4.1.1.1 MoO_3/TiO_2 catalysts 115

4.1.2 Temperature-programmed reduction (TPR) 117

4.1.2.1 MoO_3/TiO_2 catalysts 117

4.1.2.2 CoO/TiO_2 catalysts 127

4.1.2.3 $CoO-MoO_3/TiO_2$ catalysts 141

4.1.3 X-ray photoelectron spectroscopy (XPS) 156

4.1.3.1 MoO_3/TiO_2 catalysts 156

4.1.3.2 CoO/TiO_2 catalysts 162

4.1.3.3 $CoO-MoO_3/TiO_2$ catalysts 170

4.1.4 Transmission electron microscopy (TEM) 178
4.1.4.1 MoO_3/TiO_2 catalysts 178
4.1.4.2 CoO/TiO_2 catalysts 178

4.1.5 Catalytic decomposition of 2-propanol 186
4.1.5.1 MoO_3/TiO_2 catalysts (MT/C series and MOT/C series) 186
4.1.5.2 CoO/TiO_2 catalysts (CT/C series) 198
4.1.5.3 $CoO-MoO_3/TiO_2$ catalysts (CMT series) 209
4.1.5.4 $CoO-MoO_3/TiO_2$ catalysts (MCT series) 212
4.1.5.5 $CoO-MoO_3/TiO_2$ catalysts (CMTg series) 222

4.2 References 229

CHAPTER 5. DISCUSSION

5.1 MoO_3/TiO_2 catalysts 230
5.1.1 Laser Raman spectroscopy (LRS). 230
5.1.2 Temperature-programmed reduction (TPR). 235
5.1.3 X-ray photoelectron spectroscopy (XPS). 240
5.1.4 Transmission electron microscopy (TEM) 249
5.1.5 Catalytic decomposition of 2-propanol. 249

5.2 CoO/TiO_2 catalysts 253
5.2.1 Temperature-programmed reduction (TPR). 253
5.2.2 X-ray photoelectron spectroscopy (XPS). 256
5.2.3 Transmission electron microscopy (TEM) 261
5.2.4 Catalytic decomposition of 2-propanol. 262

5.3 $CoO-MoO_3/TiO_2$ catalysts 263

5.3.1. Temperature-programmed reduction (TPR). 263

5.3.2 X-ray photoelectron spectroscopy (XPS) 265

5.3.3 Catalytic decomposition of 2-propanol. 271

5.4 References 282

CHAPTER 6 CONCLUSIONS 294

6.1 References 299

APPENDICES 300

CHAPTER 1 INTRODUCTION

1.1 General Introduction

In recent years, there has been a growing emphasis on the study of the structure and composition of catalytically active surface phases containing transition metal ions, of their dependence on the method of preparation and on the degree of their coverage of the surface and their relation to catalytic properties.

In the field of heterogeneous catalysis, it is convenient to distinguish, in a perfectly unjustified and oversimplified way, between metal catalysts, and the other catalysts. The first are easy to define: there are those in which a reduced metal is the active phase. It is thus easy to circumscribe. By exclusion, the other class is namely the "non-metals" (1).

Defined in this manner, non-metal catalysts represented, in 1980, 84% of the industrial heterogeneous catalysts(1). To be more specific, this proportion corresponds to catalysts which, under the working conditions in the industrial plant, contain their catalytically active elements in a non-reduced state. It should, however, be recalled that most metal catalysts are supported on oxides, which often represent over 90% (sometimes 99.4% in the case of the Pt reforming catalysts) of the total weight.

A larger number of studies of the preparation, surface characterisation, activation (sulphidation) and catalytic performance with molecules and real feeds of MoO_3/γ-Al_2O_3 catalysts with which a promoter (CoO or NiO) can be associated, have been published in recent years[2]. Those catalysts are generally used in hydrotreatment, namely hydrodesulphurization (HDS), hydrodenitrogenation (HDN), hydrodemetallation (HDM) and hydrodeoxygenation (HDO) of petroleum fractions, heavy residues, or coal liquids. They represent a large proportion of catalysts used in modern petrochemistry, and, according to Jacobsen[3], the hydroprocessing catalyst market is about 25,000-30,000 tons $year^{-1}$ at a value of the order of \$250 million $year^{-1}$.

1.2 The concept of dispersion in supported oxides

In the course of preparation of highly dispersed oxide-on-support systems, a number of different phenomena may take place depending on the chemical nature of the component oxides, temperature and mode of preparation, which may have an important influence on the properties of the final catalyst[4]. All these processes may be summarised in the form of the following scheme:

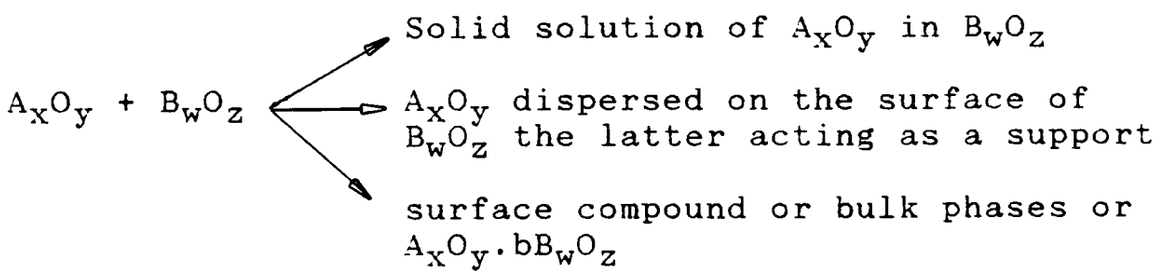

In the first stage of annealing of the mixture of oxides, irrespectively of whether obtained by coprecipitation or impregnation, the oxide to be dispersed may partially dissolve in the support crystallites and accumulate in the surface layers. On further heating, two processes take place simultaneously: the inward diffusion into the bulk of the crystallites of the support, which may result in the modification of its properties, and the evaporation into the gas phase.

Depending on the relative rates of these processes, the surface layers of the resulting solid solution crystallites are either enriched or impoverished in the solute atoms as compared to the deeper layers[4]. Only when the temperature of heating is low enough, or the miscibility of the two oxides is only limited, does the minority oxide accumulate almost entirely at the surface of the host crystallites and the oxide-on-support system is obtained with different degrees of interaction between the supporting and the supported oxide. Thus, when the two oxides are capable of reacting, surface compounds may be formed which determine the adsorptive and catalytic properties of the system.

1.2.1 The concept of contact angle, interaction energies and wetting

The equilibrium shape of supported metal particles is dependent upon the nature of the forces present at the surfaces of the adjoining phases[5]. If one assumes that a

certain degree of atomic mobility exists in the surface layers of the metal particles, then the situation can be described according to Young's equation, which relates the characteristic interfacial energies existing in the system[5]. For a metal-gas-support at equilibrium:

$$\gamma_{sg} = \gamma_{ms} + \gamma_{mg} \cos\theta \qquad (1)$$

where θ is the contact angle between the metal particle and the support, γ is the surface energy, and the subscripts s, m and g refer to the support, metal and gas, respectively.

Two cases can be considered, as illustrated schematically in Fig. 1.1.

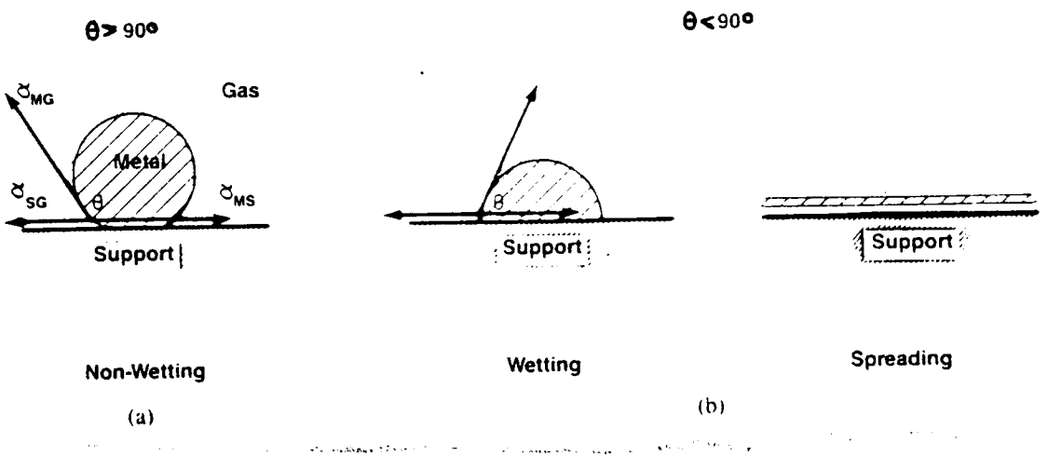

Fig. 1.1 Particle morphologies as predicted from Young's equation. (a) Wetting condition ($\gamma_{sg} > \gamma_{ms}$) b) Non-wetting condition ($\gamma_{sg} < \gamma_{ms}$) (ref. 5)

(a) If $\gamma_{sg} > \gamma_{ms}$, then $\cos\theta > 0$ and $\theta < 90^{o}$. Under these conditions the metal particles will spread over the support in order to minimize the surface energy. In this case the particles would be expected to be cap-shaped, possibly faceted, and in the extreme might spread to form thin flat structures due to the metal-support interactions.

(b) If $\gamma_{sg} < \gamma_{ms}$, then Cos $\theta < 0$ and $\theta > 90°$. Under these circumstances, the particles will be in a non-wetting condition and will tend to assume the energetically favoured form of a sphere or polyhedron due to the weaker interaction between the metal and support.

Examples of these situations are confirmed for Pt/TiO_2[7], and observed for Ni/TiO_2[8-12] and Fe/TiO_2[13,14].

1.2.1.1. The spreading condition

The ability of a crystallite to wet a substrate is determined by the following interfacial free energies[6]: substrate-gas (σ_{sg}), crystallite-gas (σ_{cg}) and crystallite-substrate (σ_{cs}). Let us consider a thick film of material on a substrate. The specific free energy of formation σ_∞ of such a film on a uniform substrate is given by:

$$\sigma_\infty = \sigma_{cg} + \sigma_{cs} - \sigma_{gs} \qquad (2)$$

where the subscript ∞ emphasises the film is thick. The first two terms on the right-hand side are due to the two new interfaces, namely crystallite-gas and crystallite-substrate which form, and the last is due to the interface substrate-gas, which disappears. When $\sigma_\infty < 0$, the film spreads over the surface of the substrate because this causes a decrease of the free energy of the system [6]. In the opposite case, when $\sigma_\infty > 0$, the material does not wet the substrate, and therefore islands with a distribution of sizes form. In order to decrease the free

energy of the system, particles will tend to coalesce into a single island, forming an angle Θ with the substrate given by the following equation:

$$\sigma_{cg} \cos\Theta = \sigma_{gs} - \sigma_{cs} \qquad (3)$$

The kinetic process can, however, be so slow that thermodynamic equilibrium is not achieved during the life span of the specimen [6]. Each crystallite can, however, achieve the equilibrium wetting angle in a time which is short compared to the lifetime of the specimen[6].

Under vacuum and in an inert atmosphere, the metals used as catalysts have high values of the interfacial free energy σ_{cg}, as well as high interfacial free energies σ_{cs} with the commonly used substrates [6]. This leads to values of Θ greater than 90°, i.e. the metal does not wet the substrate well. In a H_2 atmosphere, the chemisorption of the gas on the surface of metal decreases the value of σ_{cg} and the metal wets the substrate somewhat better [6]. However, in an oxidizing atmosphere, because of the formation of oxide, σ_{cg} and σ_{cs} can become much smaller than in the above-mentioned cases, and the contact angle can decrease substantially. The interaction energy between the solid phases in contact plays a major role in this decrease, and in what follows σ_{cs} will be related to this interaction energy [6].

When two phases are brought into contact to form an interface and the molecular interactions between them are ignored, then the interfacial free energy between the two is given by the sum:

$$\sigma_{cs} = \sigma_c + \sigma_s \qquad (4)$$

where σ_c and σ_s are the surface free energies of the two phases. However, in reality, there are attractive molecular interactions between the two phases brought into contact, and as a result there is a corresponding decrease in the interfacial free energy. These interactions are particularly strong when chemical compounds are formed, or when some degree of electron exchange occurs between the two phases. Interactions are weak when they are of a physical nature, such as dispersion or polar interactions. The interfacial tension is therefore given by the expression:

$$\sigma_{cs} = \sigma_c + \sigma_s - U_{int}, \qquad (5)$$

where U_{int} is the interaction energy per unit area of crystallite-substrate interface, between the atoms (molecules) of the two phases. In addition, the mismatch of the two lattices generates a strain energy per unit area, U_{str}, which increases the interfacial free energy. Consequently, one can write:

$$\sigma_{cs} = \sigma_c + \sigma_s - U_{int} + U_{str} \equiv \sigma_c + \sigma_s - U_{cs}, \qquad (6)$$

Approximately, $\sigma_c \approx \sigma_{cg}$; therefore, combining Equations (2) and (6), yields:

$$\sigma_\infty = 2\sigma_{cg} - U_{cs}, \qquad (7)$$

Equation (7) shows that if the interaction energy U_{cs} between the two materials is greater than twice the surface free energy σ_{cg} of the crystallite, then the crystallite will spread over the surface of the substrate [6]. Since σ_{cg} is large for metals, and the interactions between metal and substrate are relatively weak, metal crystallites will

not spread over the surface of an oxide substrate [6]. In an O_2 atmosphere, the metal is oxidized and, as a result, the surface free energy σ_{cg} becomes much smaller than that of the metal. The interactions between the oxidised metal and the oxide substrate are also stronger than those between metal and substrate. However, only if they are sufficiently strong can the oxidized metal spread over the substrate. This is more likely to happen when chemical compounds form, because then U_{cs} becomes very large[6].

It may be noted that an oxide crystallite wets a metal substrate better than the metal crystallite wets the oxide substrate. This happens because σ_{cg} is much smaller in the former case. For spreading to occur, U_{cs} must be greater than $2\sigma_{cg}$[6].

1.3 Methods of preparation of supported oxides

See Table 1.1.

Table 1.1. Methods of preparation

Method	Mo Compound	V Compound	W Compound
1. Aqueous impregnation	$(NH_4)_6Mo_7O_{24}.4H_2O$[15] $H_2[MoO_3(C_2O_4).H_2O]$(*)	NH_4VO_3[19] $VOCl_3$[20]	$(NH_4)_6H_{12}W_{12}O_{40}$[24]
2. Nonaqueous impregnation	$Mo(\pi\text{-}C_3H_5)_4$[16] $MoO(AcAc)_2$[17]	$VO(AcAc)_2$[16] $VOCl_3$ in $C_6H_5\text{-}CH_3$[17]	WCl_6 in CH_3OH[24]
3. Alkoxide		$VO(i\text{-}C_4H_9O)$[21]	
4. Grafting	$MoO_2(OH)_2$[18]	$V_2O_3(OH)_4$[19] $VOCl_3$ vapour[22] VCl_4 vapour[23]	WCl_6 vapour[25]
5. Ion-exchange	$C(M_xO_yH_2)_n$, where C is an exchangeable cation and M is Ti, Zr, Nb, or Ta[26]		
6. Homogeneous precipitation	$Co(NO_3)_2.6H_2O$ in excess of $(NH_2)_2CO$ (ref. 27 and this work)		
7. Solid-Solid wetting	Physical mixtures of active oxides MoO_3, V_2O_5 and WO_3 on the surface of $\gamma\text{-}Al_2O_3$, TiO_2 (anatase) and SiO_2[28,29].		

(*) this work

1.4 Characterization of supported oxides

In the real world of the industrial scientist there is generally much respect, even admiration, for the significant advances that have recently been made by academically oriented investigators in the study of solid surfaces[30]. During the past decade several ingenious ways of establishing the composition, crystallographic structures and electronic properties of the last few layers of adsorbents and catalysts - or - sub-monolayer amounts of adsorbed species - have been devised, thanks largely to the arrival of new techniques such as photoelectron spectroscopy, Auger and electron-energy-loss spectroscopy, ion scattering procedures, low energy electron diffraction (LEED), and the extension of more traditional ones such as infrared and Raman spectroscopy.

It is, however, undeniable that a certain sense of disappointment - if not frustration, which, at times, borders on cynicism - pervades the catalyst community when it reflects on the paucity of techniques that are capable of being utilized to study "live" catalysts, under actual operating conditions. Some individuals, whose task it is to design new catalysts or to improve existing ones, have become inured to the waves of enthusiasm that frequently overtake (or overwhelm) the purist surface chemist or chemical physicist when the discovery of another potent, all-conquering technique is announced. They greet with scepticism descriptions of identification of a new state of a surface-bound molecule or a new "electronic surface

state", that exist under conditions (typically 10^{-10} to 10^{-4} torr) widely removed from those relevant to commercial catalytic reactors (e.g. a few hundred atmospheres pressure and temperatures of several hundred Kelvin).

No one denies the great importance of an academic concern for fundamentals [30]: indeed the dictum that 'the more closely we enquire into the nature of things the greater is our reward' is universally valid[30]. Without paying due attention to fundamentals it ceases to become possible to confirm or reject plausible models of adsorption and catalysis, irrespective of whether or not the conditions under which the model applies may be far removed from a given, desired set. It often follows that, with due allowance for error, an effect or feature identified under one set of well-defined conditions may indeed be equally valid under another. Thus, if it is incontrovertibly established (by EXAFS for example) that rafts of metal atoms, rather than three-dimensional arrays (clusters) of active metal catalysts are distributed in a given manner or an appropriate oxide support, it is not improbable that those rafts also exist under the actual real-life conditions of the "live" catalyst. Clearly the principal point here is to know whether the facts pertaining to the existence of the rafts have been incontrovertibly established.

1.4.1. Laser Raman spectroscopy (LRS)

The principle of the technique is schematized in Fig. 1.2.

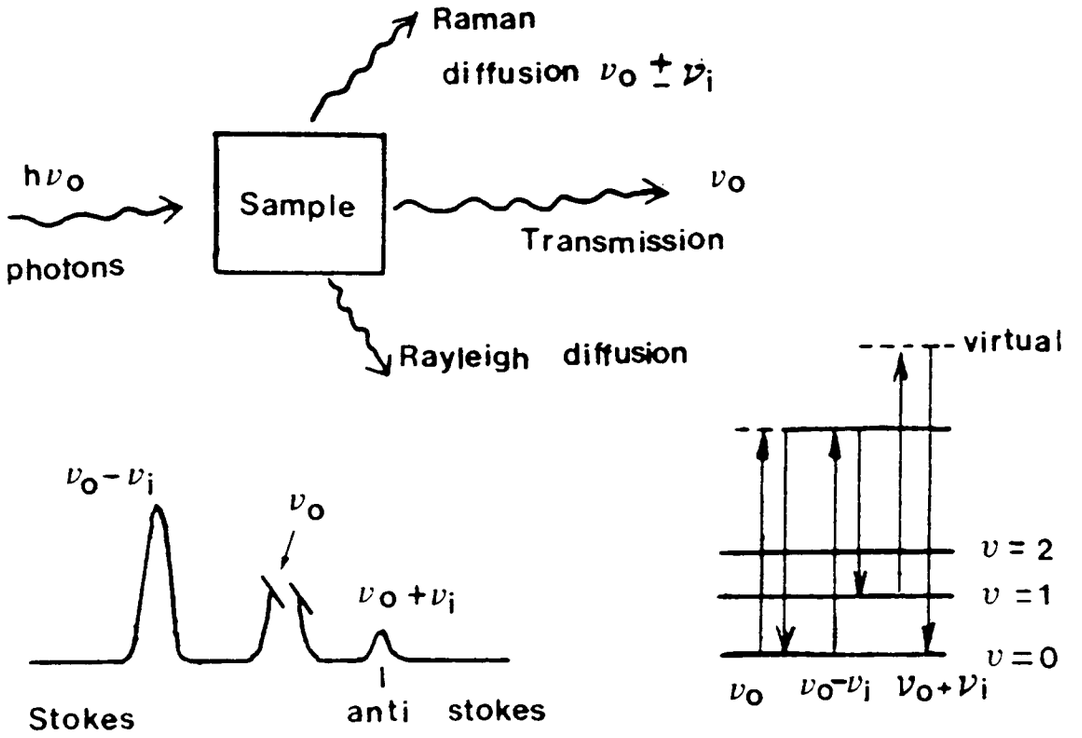

Fig. 1.2. Principle of Raman spectroscopy involving vibrational level transitions (bottom right side) (31)

The so-called Stokes and anti-Stokes transitions have a very low probability. A highly intense incident beam was therefore necessary to obtain detectable signals. Laser sources were recently used but the beam has to be chopped to avoid a too intense heating of the sample. The technique involves a vibrational transition (Fig. 1.2.) and is therefore used for characterizing lattice vibration modes of solid catalyst. The allowed transition involves changes in the bond polarizability whereas infrared involves changes in dipole moment. It follows that many more transitions are

allowed in Raman spectroscopy, which then turns out to be complementary to infrared. The technique has an increasing field of applications, for instance, for CoMo or NiMo catalysts[32].

1.4.2. Temperature-programmed reduction (TPR)

Temperature-programmed reduction (commonly abbreviated to TPR) is a technique used for the chemical characterization of solids. The essence of the technique is the reduction of a solid by a gas at the same time that the temperature of the system is changed in a predetermined way[33]. The method is based on measuring H_2 removal, but chemical information can also be derived from analysis of the gaseous products.

In the most commonly encountered apparatus, the solid is reduced by flowing H_2, the concentration of which is monitored downstream of the reactor. Provided that reduction has taken place over the temperature excursion of the reactor, the record is simply that of H_2 consumption and is usually displayed as a function of the temperature of the reactor.

A typical reduction profile, as shown in Fig. 1.3, consists of a series of peaks. Each peak represents a distinct reduction process involving a particular chemical component of the solid. The position of a peak in the profile is determined by the chemical nature and environment of the chemical component, and the area of the peak reflects the concentration of that component present in the solid.

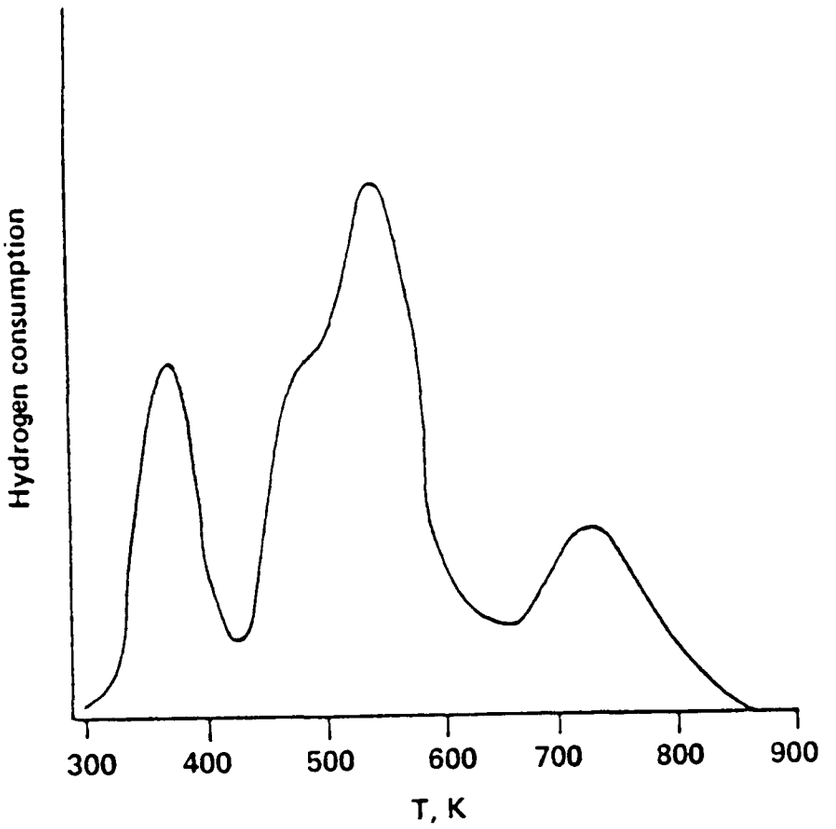

Fig. 1.3 A typical reduction profile (ref. 33)

TPR is a relatively new technique for characterizing solids. It is highly sensitive and does not depend on any specific property of the solid under investigation other than its reducibility. The technique was first investigated about 13 years ago by Jenkins [34] during a study of catalysts using the temperature-programmed desorption technique pioneered by Cvetanovic and Amenomiya[35]. Jenkins realized that valuable information could be obtained from the reduction pretreatment stage of this technique if the reduction were also performed in the temperature-programmed mode. A series of experiments provided data which, together with information from other techniques, enabled the catalysts to be fully characterized.

The technique was soon exploited by others, and a notable early study[36] was made using the technique to characterize a series of solid catalysts of noble metals supported on refractory oxides. Over the last decade the technique has been exploited and developed considerably by workers around the world, to the extent that TPR now has a place alongside other techniques for the characterization of solids, and in 1982 the first review article on the subject was published[37].

The technique can be regarded as the principal member of a family of temperature-programmed reaction techniques. Its status as principal member is due only to the fact that reduction has attracted the most attention from researchers. In principle, valuable information can be obtained by investigating many different types of chemical reactions in a temperature-programmed mode. Using the same or similar apparatus, temperature-programmed oxidations, methanations, sulphidations, and carbonizations have been reported[33].

On the basis of the type of information it can provide, the TPR technique can be classified with the spectroscopic and X-ray techniques that have been traditionally and indeed are currently used to characterize solids. Almost all of those techniques impose severe requirements on the solid or on the conditions under which it can be investigated. These requirements necessarily limit the information that can be obtained and the range of solids that can be investigated. The TPR technique, while capable of providing chemical information similar to that from the other techniques, has,

in general, a much wider range of application. Even the condition that the solid must be reducible is not mandatory, since valuable information has been obtained on reduced solids using TPR by first mildly oxidizing the solids and then subjecting them to the TPR experiment.

In another sense, and certainly on the grounds of similarity of experimental procedures, TPR can be classified with a broad range of techniques, known as thermoanalytical techniques, that are used to generate physical and chemical information on solids[38]. In general, these techniques depend on the measurement of a parameter of a physical or chemical property of a solid as the temperature of the solid is varied, as for TPR, in a predetermined manner. Fig. 1.4. presents a classification of the principal techniques. These techniques provide information on a wide range of phenomena from the purely physical to the totally chemical[38]. Temperature-programmed desorption (TPD) is included in Fig. 1.4 under techniques dependent on the evolution of "volatiles" since there are broad experimental similarities with evolved gas analysis (EGA) and both techniques can give information on the physical desorption of gases as well as on gases evolved by chemical mechanisms. Temperature-programmed reduction, along with the other temperature-programmed reaction techniques, is thus identified as a more chemically based technique concerned with analysis of gases from purely chemical processes.

Temperature-programmed reduction profiles of complex solids can show a great deal of detail, reflecting complex

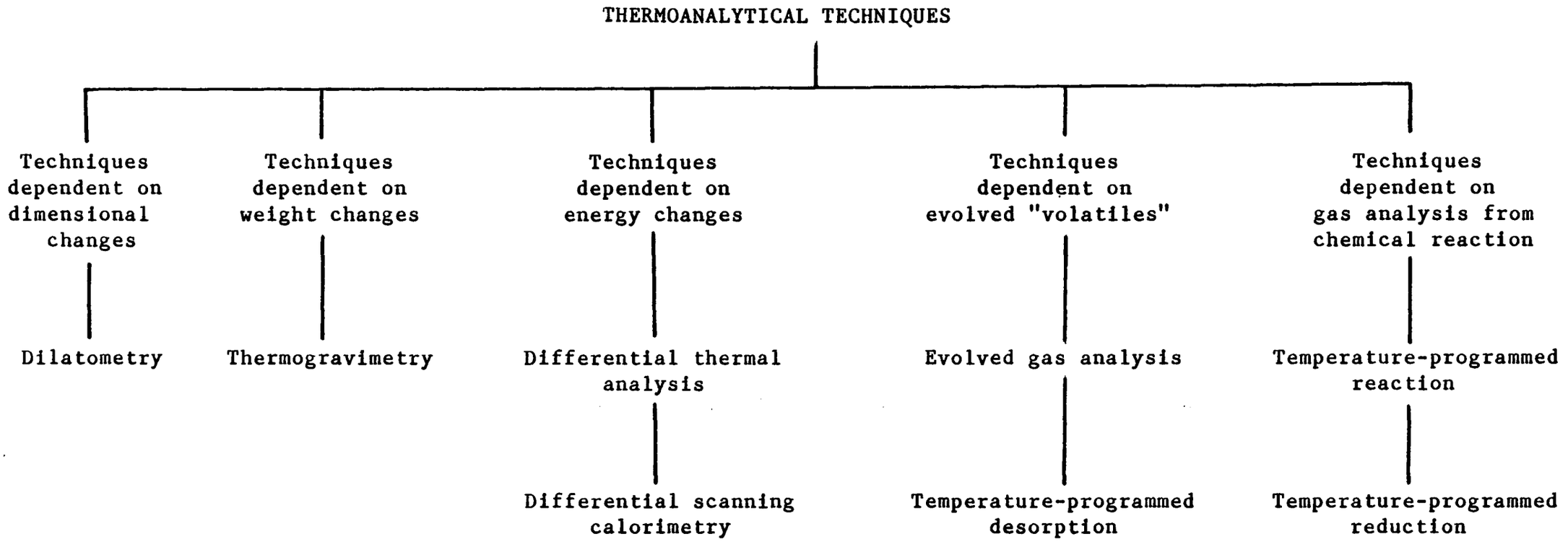

Fig. 1.4 A classification of thermoanalytical techniques (ref. 33)

reduction processes. The use of such profiles as "fingerprints" to provide a rapid assessment of the correctness of the composition of a solid has proved useful in many applications. In particular, the fingerprint temperature reduction profile has found application as a tool for quality control in the preparation of industrial catalysts.

Although many analytical techniques are also capable of providing similar fingerprint analysis, for solid catalysts temperature-programmed reaction techniques have the advantage that the fingerprint can more truly reflect the chemical and structural features essential for its use because the analytical reaction and reaction conditions can be made closely similar to the conditions experienced by the catalyst in its industrial use. Thus, a temperature-programmed reduction profile can provide a fingerprint reflecting the essential features of a reduction catalyst, just as a temperature-programmed methanation profile can for a methanation catalyst.

In this role in particular, three other factors have contributed to the success of the TPR techniques. First, the sensitivity is such that a reduction profile can be obtained from the consumption of as little as 1 μmol of H_2 requiring only milligrams of sample. Second, the apparatus, consisting of simple temperature programmers and thermal conductivity detectors, is inexpensive when compared with that required for the X-ray and spectroscopic techniques. Third, the relative robustness of the apparatus and its

minimal maintenance requirements make it an ideal tool for industrial application.

The problems facing the science of the characterization of solids include the identification of low concentrations of impurities, or dopant; alloy formation between metals; other interactions between solids (e.g. between a metal and an oxide); particle sizes of compounds; and the influence of thermal treatments. Experience in the catalyst characterization area has shown that TPR is well suited to the study of such phenomena. Particular advantages have been the few, if any, limitations imposed on materials, the sensitivity of the technique and the ability, for a number of catalysts, to study phenomena in realistic conditions hitherto not possible with other techniques.

1.4.2.1. Derivation of kinetic parameters from TPR profiles obtained at different heating rates

Banerjee et al. [39,40] have used the method of Coats and Redfern [41] originally developed for thermogravimetric data to derive kinetic parameters from a study of the changes in the solid phase in excess reducing gas.

For the reaction

$$\text{Gas} + \text{solid} \longrightarrow \text{products} \qquad (1)$$

The rate of reaction of the gas [G] or solid [S] at constant temperature may be expressed as:

$$\text{Rate} = \frac{-d[G]}{dt} \text{ or } \frac{-d[S]}{dt} = k[G]^P[S]^q \qquad (2)$$

where the rate constant k is given by the Arrhenius equation

$$k = Ae^{-E/RT} \tag{3}$$

In TPR, temperature is also a function of time. Thus

$$\beta = \frac{dT}{dt} \tag{4}$$

where β is the linear heating rate, so that

$$\frac{-d[G]}{dt} = \frac{-\beta d[G]}{dT} \tag{5}$$

or

$$\frac{-d[S]}{dt} = \frac{-\beta\, d[S]}{dT} \tag{5a}$$

In excess reducing gas the reaction is independent of gas concentration, and Eq. (2) is rewritten

$$\frac{d\alpha}{dt} = k(1-\alpha)^q \tag{6}$$

where α is the fraction reduced at time t. Combining Eqs. (3), (4) and (6), rearranging, and integrating gives

$$\int_0^{\alpha} \frac{d\alpha}{(1-\alpha)^q} = \frac{A}{B} \int_0^{T} e^{-E/RT}\, dT \tag{7}$$

Using an approximation[42] for the right-hand integral gives, for all values of q except q = 1,

$$\frac{1-(1-\alpha)^{1-q}}{1-q} = \frac{ART^2}{\beta E}\left[1-\frac{2RT}{E}\right] e^{-E/RT} \tag{8}$$

Taking logs gives

$$\log\left[\frac{1-(1-\alpha)^{1-q}}{T^2(1-q)}\right] = \log\frac{AR}{\beta E}\left[1-\frac{2RT}{E}\right] - \frac{E}{2.3RT} \tag{9}$$

When q = 1, Eq. (7) after taking logs becomes

$$\log\left[-\log\frac{(1-\alpha)}{T^2}\right] = \log\frac{AR}{\beta E}\left[1-\frac{2RT}{E}\right] - \frac{E}{2.3RT} \tag{10}$$

It can be shown that for most values of E over the temperature range of these experiments the expression $\log(AR/E) \cdot \left[1-2RT/E\right]$ is essentially constant. Thus plotting the left-hand side of Eq. (9) or (10) against 1/T for the correct value of q yields a straight line of slope -E/2.3R. This method of analysis is not, however, generally useful as an aid to the interpretation of TPR data since most experimental TPR systems monitor the rate of change of gas concentration as a function of temperature, producing reduction profiles with peaks corresponding to maxima for the rate processes.

Thus, a more generally useful analysis by Gentry et al.[43] started with a statement of the reaction rate in terms of the rate of consumption of a gas for a reaction taking place between a solid held in a tubular reactor, at constant temperature, and a gas flowing through it. Provided that the flow can be described as plug flow (i.e. radial and longitudinal mixing are absent) the rate of consumption of a gas, at low conversions, is given[44] by

Rate = fx

where f is the feed rate of the gas and x is the fractional conversion of the gas.

Now

$f = F[G]_i$

where F is the flow rate and $[G]_i$ is the concentration of gas G at the reactor inlet and

$$x = \frac{[G]_i - [G]}{[G]_i} = \frac{\Delta[G]}{[G]_i}$$

where [G] is the concentration of gas at the reactor outlet. Thus, the rate can be measured as

$$\text{Rate} = F\Delta[G] \tag{11}$$

By using a recirculation reactor, Jacobs and colleagues[45] obtained reaction rates directly by monitoring the reaction pressure as a function of time.

Differentiating Eq.(2) with respect to temperature gives

$$\frac{d(\text{rate})}{dT} = A \exp(-E/RT) \left[[G]^p[S]^q \frac{E}{RT^2} + q[G]^p[S]^{q-1} \frac{d[S]}{dT} + p[G]^{p-1}[S]^q \frac{d[G]}{dT} \right] \tag{12}$$

at the maximum rate

$$\frac{d(\text{rate})}{dT} = 0 \tag{13}$$

and from Eq. (11)

$$\frac{d[G]}{dT} = 0 \tag{14}$$

Denoting parameters relating to the maximum rate by the subscript m and simplifying, Eq. (12) becomes

$$\frac{E}{RT_m^2} + \frac{q}{[S]_m} \frac{d[S]_m}{dT} = 0 \tag{15}$$

Combining Eqs. (2), (3), (5a) and (15) gives

$$\frac{E}{RT_m^2} = \frac{A[G]_m^p \, q[S]_m^{q-1}}{\beta} \exp(-E/RT_m)$$

Taking logs and rearranging gives

$$\ln \frac{T_m^2[G]_m^p}{\beta} + \ln q[S]_m^{(q-1)} = \frac{E}{RT_m} + \ln \frac{E}{RA} \tag{16}$$

Thus, if the values of p and q are known, a plot of the left-hand side of Eq. (17) against $1/T_m$ yields a straight line of slope E/R and intercept lnE/RA. Both E and A can be obtained in this way.

The reaction order with respect to reducing gas and solid may, in theory, be derived by substitution of values of p and q into Eq.(16). However, orders with respect to the solid phase are frequently fractional and expressions such as Eq.(16) may be insensitive to the value of q. Consequently, exact derivation of a value of q is not possible. If it is assumed that q = 1, then

$$\ln \frac{T_m^2[G]_m^p}{\beta} = \frac{E}{RT_m} + \ln \frac{E}{RA} \qquad (17)$$

The value of E derived from this expression is dependent on the chosen value of p. Thus, for the reduction of CuO[46] it was found for a zero order reaction in H_2, E was a function of H_2 concentration, whereas for p = 1 a unique value of E was obtained for all concentrations used.

In a similar analysis, Monti and Baiker[47] considered that the use of a mean H_2 concentration was more appropriate to a reaction occurring in a differential reactor. For the case of first order kinetics (i.e. p = q = 1 these authors derived an expression:

$$\ln \frac{T_m^2 \bar{C}_m}{\beta} = \frac{E}{RT_m} + \ln \frac{E}{RA} \qquad (18)$$

where $\bar{C}_m$ is the mean H_2 concentration at the temperature of the maximum reduction rate. At low conversions where $[G]_i \approx [G]$ the two equations are identical.

1.4.2.2. Effects of variation of experimental parameters

TPR measurements reported in the literature have been taken over a wide range of experimental conditions. It is vital if a meaningful comparison is to be made between different studies to be clear on the sensitivity of the results to the experimental conditions used.

1.4.2.3. Influence of heating rate and initial temperature

The variation of T_m with heating rate β is most commonly used to obtain activation energies for the reduction process. When the change in T_m is due to kinetic parameters as described in Eq. (17) above, other parameters remaining constant, the sensitivity of T_m to changes in heating rate is established.

Thus, in a systematic study of the H_2 reduction of NiO (a simple, one-step reduction, first order in H_2 and NiO), Monti and Baiker[47] found that an increase in heating rate from 0.09 to 0.31 Ks^{-1} produced an increase in T_m of 33K.

1.4.2.4 Influence of reducing gas concentration

Fig. 1.5 shows the results obtained by Monti and Baiker[44] for the H_2 reduction of NiO. An increase in H_2 concentration from 3%v (1.23 μmol cm^{-3}) to 15%v (6.15 μmol cm^{-3}) produced a decrease in T_m from 604 to 563K in line

with expectations from the kinetic analysis given above for this simple one-step reduction. The same authors used the variation of T_m with H_2 concentration to derive values for the activation energy of the reduction using Eq. (18).

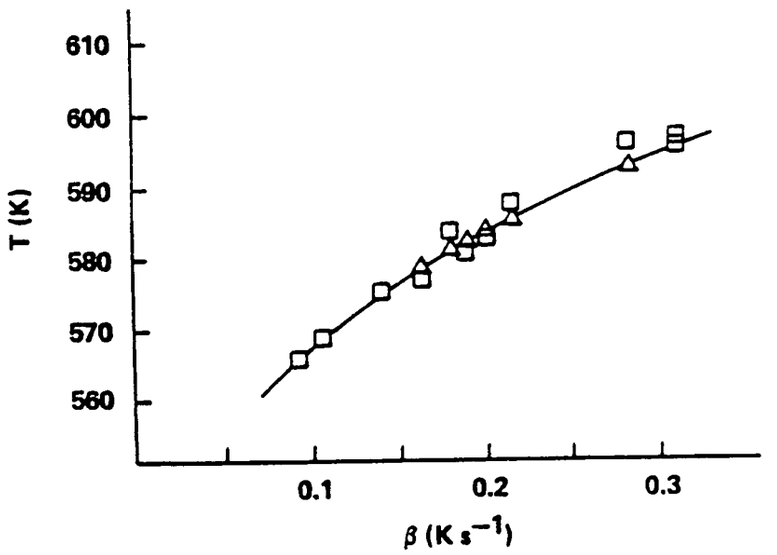

Fig. 1.5 Parametric sensitivity of the temperature of the maximum reduction rate for the hydrogen reduction of nickel oxide. Influence of heating rate, β. Standard conditions: hydrogen concentration, 2.46 μmol cm^{-3}; mass of sample, 504 μmol; flow rate, 1.25 cm^3 (NTP) s^{-1}. The NiO mean particle size was 13.5 um. Only particles of less than 100 um were used. □ Experimental values; △ Values calculated from the integration of Eq. (17). (From Ref. 47).

1.4.2.5 Influence of gas flow rate

The influence of gas flow rate has been investigated by Gentry et al.[43] for the H_2 reduction of Cu-exchanged zeolite. They found that an increase in flow rate of 4%v H_2 from 10 to 20mL min^{-1} at constant total pressure lowered the value of T_m by 15-30K.

Flow reactor theory[44] shows that an increase in flow rate for a reactant consumed by a first-order process results in a lowering of the degree of conversion and hence an increase of reactant concentration in the reactor.

Experimental results showed that the above increase in flow rate increased $[H_2]_m$ by $\approx$ 1%, where $[H_2]_m$ is H_2 concentration at the temperature of the maximum reduction rate. Eq. (17) predicts that such a change in $[H_2]_m$ will produce a decrease in T_m of $\approx$ 15K, in broad agreement with the observed result.

1.4.2.6 Influence of the mass of solid

Theory predicts that T_m should be independent of the mass of the solid and indeed in their study of the H_2 reduction of NiO Monti and Baiker[47] found only a minimal change in T_m for an increase in sample mass from 200 to 500 μmol.

In a systematic study of the effects of sample mass, Gentry et al.[43] obtained TPR profiles at β = 9.1 $Kmin^{-1}$ using 4%v H_2 for masses of (Cu, Na)-X-50 between 50 and 400mg. The main effect of changing the mass was that the resolution of two separate reduction processes obtained with a 50-mg sample was completely lost when the mass of zeolite was increased to 400 mg. In addition, the value of T_m for the composite reduction peak was higher than those of the two separate reduction peaks.

1.4.2.7 Particle size effects

It is one of the strengths of TPR as a "fingerprint" method that in many cases it can differentiate between materials that have been prepared in nearly identical ways.

Some work recently published by Tonge[48] suggests that such differences may be explained in terms of particle size effects. Tonge's analysis was based on a reduction that accords with the contracting sphere model, i.e. a reduction that obeys the relationship

$$1 - (1-\alpha)^{1/3} = Kt$$

where α is the fraction reduced and t is time.

Considering a contracting cube model, the rate of reaction is expressed as the rate of decrease in volume V of the solid;

$$\frac{dV}{dt} = \frac{d}{dt}(X_o - 2Kt)^3$$

where K is the linear rate of movement of the reaction interface and X_o is the initial side length.

Incorporating the simple Arrhenius equation and the linear heating rate equation [Eqs.(3) and (4)] gives

$$\frac{dV}{dt} = 6X_o^2 A\exp[-E/R(T_o + \beta t)] - 24X_o tA^2\exp[-2E/R(T_o+\beta t)]$$

$$+ 24t^2A^3\exp[-3E/R(T_o+\beta t)] \qquad (19)$$

Tonge used interactive computer programs using Eq.(19) to investigate the effects on dV/dt (proportional to peak height) versus temperature curves of varying X_o and other parameters. The program used a Newton-Raphson iterative method to calculate the time taken for a particle of a given size to disappear so that calculation on that particle could be stopped at that point. The program was adapted to deal with mixtures of different sized particles. Calculations using monodisperse systems showed that the peak widths and

the temperatures of the peak maximum increase by increasing the values of X_o.

1.4.2.8 Selection of values for the operating parameters

Certain restrictions on the choice of combinations of operating parameters are self-evident if meaningful TPR profiles are to be obtained. Of particular importance, in the case of H_2 reduction of an oxide, is that the H_2 feed rate should be equal to the maximum possible reduction rate; otherwise drastic distortion of the reduction profile will occur. There are thus only certain combinations of flow rate, H_2 concentration, sample mass, and heating rate that are allowable.

Bosch et al.[49] have derived a relation to describe this constraint. Thus,

$$f_{H_2} > r_{red}\, S_{MO_n}$$

where f is the feed rate of H_2, r is the specific reduction rate, and SMO_n is the sample weight.

If it is assumed that all the oxygen removed in the particular reduction step at a constant rate during the interval of the peak, $t = \triangle T_{1/2}/\beta$, then

$$S_{MO_n} < f_{H_2} \frac{\Delta T_{1/2}}{\beta} \frac{M_{MO_n}}{O/M}$$

where

$\triangle T_{1/2}$ is the peak width at half height

O/M is the molar ratio of oxygen removed and metal present and

MMO_n is the molar weight of MO_n.

In order to obtain TPR profiles that can be analyzed using simple kinetic models there are, in fact, two opposing experimental requirements: (1) the H_2 depletion must be kept as low as possible and (2) enough depletion must occur to ensure reasonable precision of the measurements.

Monti and Baiker[47] propose two criteria to meet these requirements: (1) the amount of H_2 consumed at the peak maximum should not exceed two-thirds of the H_2 feed to the reactor and (2) the minimum conversion at the peak maximum should be 10%. Using these criteria for given values of heating rates, Monti and Baiker[47] computed a set of operating variables (sample mass, flow rate, H_2 concentration, and heating rate) that meet the two criteria.

1.4.3 X-ray photoelectron spectroscopy (XPS)

Photoelectron spectroscopy has undergone a large development in the last decade relating to its applications in catalysis, particularly in heterogeneous catalysis[50]. The general principle is the ejection of electrons by impact of photons (X-ray or UV light) of appropriate energy, schematically shown in Figures 1.6 and 1.7.

The techniques are then called X-ray or UV-photoelectron spectroscopies (X-PS and U-PS) respectively. The ejected electrons are readily absorbed by matter and subsequently stem from the first surface layers of the material. The energy of the electrons is given by the relation:

$$h\nu = E_k + E_b + \phi \qquad (1$$

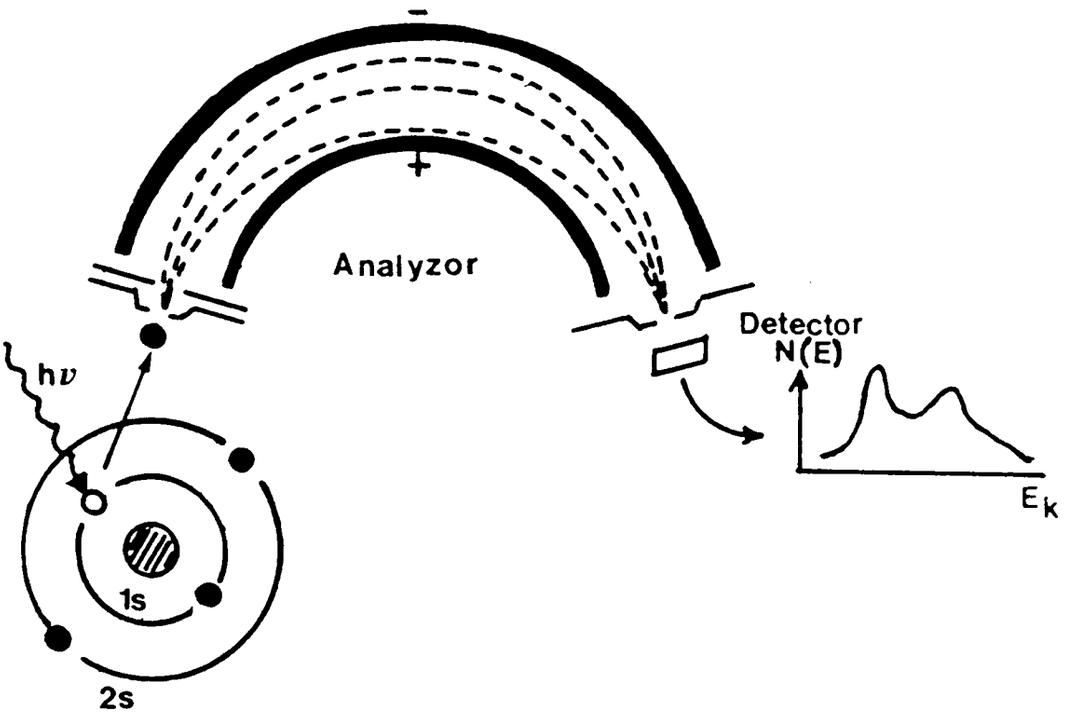

Figure 1.6 Principle of the photoemission techniques (XPS and UPS) (ref. 28)

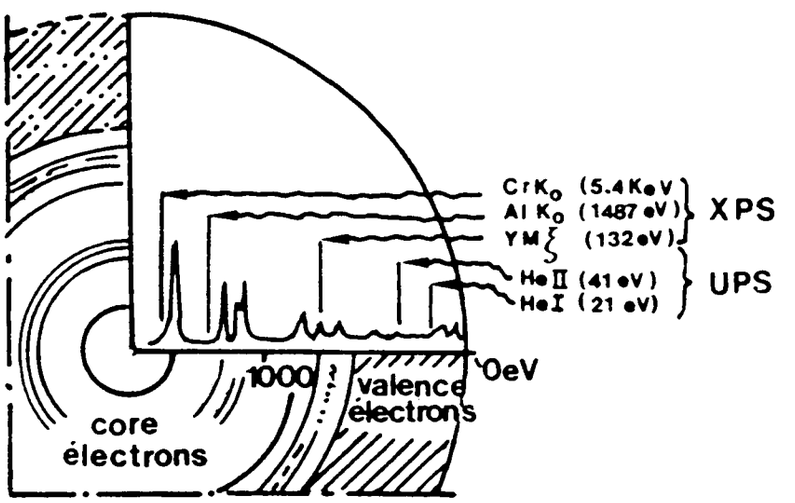

Figure 1.7 Ejection of photoelectrons from core or valence level as a function of the energy of the incident beam photons (ref. 28)

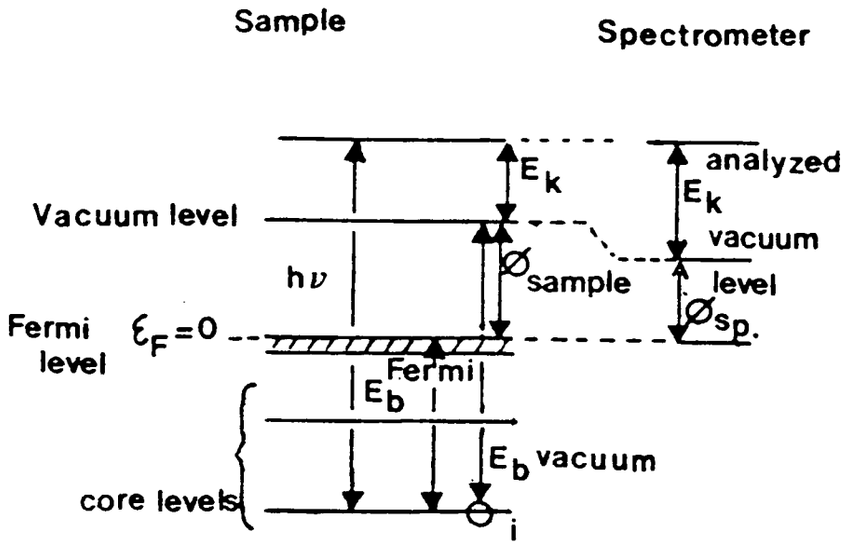

Figure 1.8 Principle of the energetic transitions in XPS as a function of the reference level from the sample or from the spectrometer (ref. 28).

where $h\nu$ is the photon energy (1486.6eV for K_α of Al, 1253.6 for K_α of Mg or 21.2 and 40.8eV for HeI and HeII UV radiations), E_k is the kinetic energy of the electrons, E_b their binding energy and ϕ is the work function of the spectrometer (Fig. 1.8). From experimentally determined values of E_k one gets E_b values which characterize the element. Tables of E_b values for s, p, d, f ..... orbitals exist in the literature and one has then an elemental analysis of all components of a catalyst. The XPS technique was initially designated for this reason as "Electron Spectroscopy for Chemical Analysis" (ESCA).

One of the most important features of XPS applied to catalysis is the ability to quantitatively analyze surfaces[51]. The number of emitted electrons is a function of the number of atoms on the surface. However, the measured signal depends on many factors. Equation (2) describes the intensity of the XPS signal originating from the surface layers[51]:

$$I_i = FSN_i \cdot \bar{\sigma}_i \lambda_i \cdot T_i (1 - e^{-d/\lambda_i}) \quad (2)$$

where I_i = intensity of i^{th} photoelectron of a given energy
F = X-ray photon flux
S = fraction of electrons detected by spectrometer
N_i = number of atoms per cubic centimeter emitting i photoelectrons
$\bar{\sigma}_i$ = atomic cross sections of i-level ionization
λ_i = mean free path of ith electron
T_i = transmission factors of i photoelectrons through a surface layer of contaminants
d = sample thickness.

In order to obtain absolute quantitation, all the parameters must be known accurately. This has not been accomplished because of difficulties involved in evaluating the parameters. In the past, workers have either used calibration standards or have measured empirical sensitivity factors to obtain relative concentrations of the surface species[52, 53].

In order to obtain quantitative information, a number of models have been proposed to predict XPS intensities for solid catalysts[54 - 56]. Kerkhof and Moulijn[57] showed that for high surface area supports, covered with a monolayer of metal or metal oxide, the XPS intensity ratio can be predicted from the bulk ratio of the metal and support and from the relative photoelectron cross sections.

1.4.3.1 Effect of calcination temperature

Chin and Hercules[58] have observed that the loading of Co affects the surface species of Co/Al_2O_3 catalysts. The calcination temperature also affects the surface concentration and the degree of metal-support interaction. By

examining the $Co2p_{3/2}/Al2p_{3/2}$ XPS signal ratios for the same loading but different calcination temperatures, it was determined that, as the calcination temperature increased, the $Co2p_{3/2}/Al2p_{3/2}$ ratio were found to decrease (Fig.1.9). Also, at a high calcination temperature, Co was found to be less reducible than in catalysts calcined at a lower temperature (Fig. 1.9).

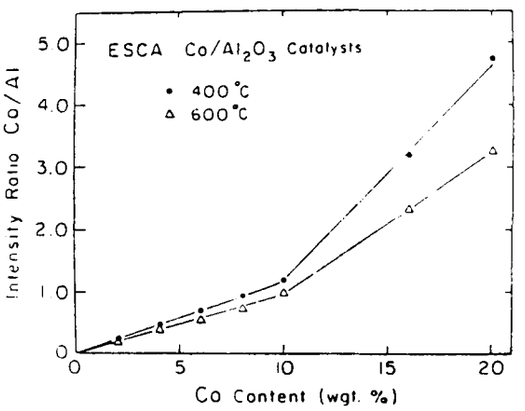

Fig.1.9 ESCA peak area intensity ratios (Co/Al) versus metal content for catalysts calcined at 400°C and 600°C. (After Chin.) (ref. 58).

1.4.4 Transmission electron microscopy (TEM)

Over the last 30 years, one of the major advances in instrumental methods that have become available to materials scientists has undoubtedly been the development of electron microscopy and related microanalytical techniques[59].

The interaction of a high-energy electron beam with a solid specimen generates a variety of "signals" all of which yield information on the nature of the solid (Fig. 1.10). It would be impossible to present in a single chapter all the techniques that have been developed to exploit these "signals". Two classes of instruments may be distinguished according to the type of specimen studied: bulk samples or electron-transparent films.

The scanning electron microscope (SEM) is especially designed for the study of bulk samples. This instrument makes use essentially of the electrons emitted from the surface of a specimen exposed to the impinging electron beam. The low-energy electrons (secondary electrons)

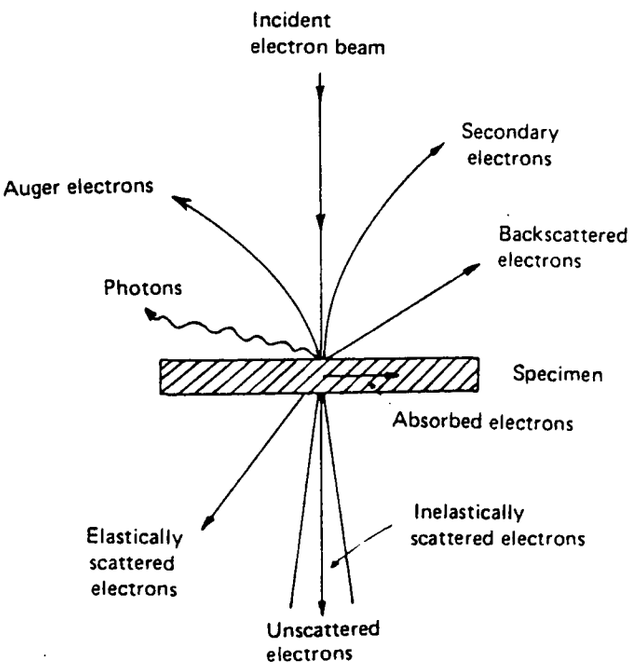

Fig. 1.10 Possible "signals" generated by the interaction of a high-energy electron beam with a thin solid specimen. (ref. 59)

provide topographical contrast, allowing study of the relief of the surface, whereas the high-energy (back-scattered) electrons give indications about variation in mean atomic weight across the specimen surface. A resolution down to less than 10nm is now currently available with this technique. The capabilities of the SEM may be easily extended by the addition of attachments which allow the formation of images by collecting various other signals: absorbed electron current, emitted optical photons (cathodoluminescence), Auger electrons (although this technique usually requires specially designed high-vacuum instruments)

or emitted X-rays. The use of the electron-beam-induced characteristic X-ray emission for the analysis of bulk samples is often designated as electron probe microanalysis (EPMA). This technique was pioneered in the early 1950s[60] and is currently often combined with SEM. Understanding of the physical phenomena governing X-ray emission is by now so well established that EPMA has become one of the most precise tools we have for the measurement of the atomic composition of solids.

The transmission electron microscope (TEM) makes use of the information carried by transmitted electrons (either unscattered or elastically or inelastically scattered) in order to form high-resolution images of the specimen. Various technical improvements have progressively transformed the TEM into the "analytical electron microscope" (AEM), an instrument allowing comprehensive analysis of the structure and chemical composition of the specimen with a resolution on the order of 10nm[61]. These developments undoubtedly deserve an updated discussion stressing the new prospects that are offered for the characterization of practical catalysts.

When interacting with the atoms of a solid, impinging electrons may suffer two types of scattering processes: elastic scattering, which does not involve transfer of energy to the atom, and inelastic scattering, which does involve such a transfer. Both elastically and inelastically scattered electrons carry useful information about the nature of the solid. Although transmission electron

microscopy will make use of both of them, the major imaging techniques are based on the elastic processes, which deserve, consequently, a somewhat more detailed presentation[62, 63].

Interpretation of the images is still not straightforward even when there seems to be a simple one-to-one correspondence between black (or white) dots in the image and atom positions. Especially when quantitative data on interatomic distances is to be derived, detailed calculations based on many-beam dynamical theory[64] must be applied to derive calculated images for comparison with experiment. For this purpose the experimental parameters describing the imaging conditions and the specimen thickness and orientation must be known with high accuracy.

1.4.5 Catalytic decomposition of 2-propanol

Decomposition of 2-propanol has gained a prominent place as a model reaction for studying the principles of catalyst selection[65]. The two main paths of this decomposition are:

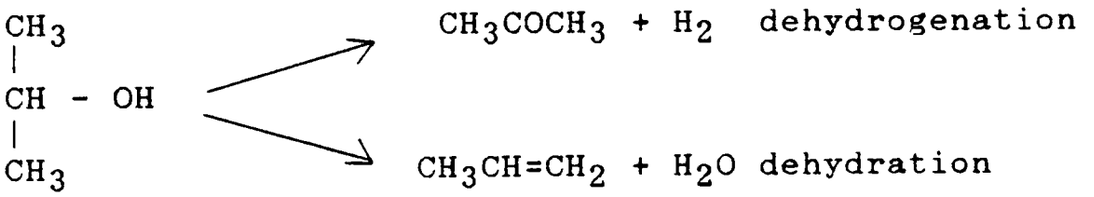

both of which are free of side reactions.

According to Mamoru Ai[66], it has been found that TiO_2 much like UO_3, SnO_2, and Fe_2O_3, is a metal oxide inter-

mediate between such acidic metal oxides as V_2O_5, MoO_3, and WO_3,. and such basic metal oxides with a high oxidation power as NiO, Co_2O_3, MnO_2, CuO and Cr_2O_3.

In the dehydrogenation of 2-propanol over ZnO/TiO_2, the addition of ZnO to TiO_2 increased the basicity and catalytic activity[67]. The formation of $ZnTiO_3$ was observed with X-ray diffraction analysis. A linear relation between the dehydrogenation activity and the number of basic sites at $H_o \geq +9.5$ was obtained, however, acidic sites also take part in the dehydrogenation of 2-propanol.

Recently, Bond and Flamerz published[68] a paper on 2-propanol decomposition over V_2O_5/TiO_2 catalysts. At about 473K both TiO_2 and V_2O_5 act principally as dehydration catalysts, the latter being much more active than the former. However, VO_x/TiO_2 catalysts prepared either by impregnation with NH_4VO_3-oxalic acid solutions or by grafting methods employing either $VOCl_3$, or $VO(O\text{-}iBu)_3$ exhibit faster rates for acetone formation than for propene formation. Rates are almost independent of V_2O_5 content in the one to ten equivalent monolayer range, and at the monolayer point are some 50 times faster on a weight basis than for unsupported V_2O_5. Activation energies for both are markedly lower for the monolayer catalysts than for the TiO_2 supports, and selectivity to acetone increases with decreasing temperature. Activity is chiefly due to vanadate groups in the monolayer, and a mechanism for the dehydrogenation involving V=O and V-OH groups was proposed.

1.5 Structure of single supported oxides

Monolayer materials have the advantage that the active metal oxide is more effectively used than if it is present as crystallites on the support. Moreover, the mechanical and thermal stabilities are also increased, large surface areas (depending on the support used) can be obtained and the influence of the support is at its maximum.

Vejux and Courtine[69] suggested that both the reduction of V_2O_5 and the transformation of anatase into rutile are topotactic reactions activated by a remarkable fit of the crystallographic patterns in contact at the V_2O_5/TiO_2 (anatase) interface. These structural properties, allowing changes ordered in space and time, are thought to be responsible, during the reactions, for atomic movements, which cannot occur otherwise.

1.5.1 Definition of "monolayer"

The question arises as to what the term "monolayer" exactly means. It could be thought that an epitaxial layer of Mo(VI) oxide units is formed on a support or that in the top layer already supported ions are present, i.e. that a two dimensional layer looking like a three dimensional one is formed.

1.5.2 Evidence for "monolayers"

The presence of TiO_2 bands in the Raman spectra of V_2O_5 supported catalysts makes it possible to estimate the

penetration depth of the incident laser light[70]. Fig. 1.11 shows the resulting titania bands when the recorded spectra are corrected for V_2O_5 bands and standardized for sensitivity. It is seen that the intensities of the TiO_2 bands are reduced by a factor of 6 when the support is covered with 6.3 wt % V.

From the TPR profile in Fig. 1.12 it follows that at 6.3 wt % V about 50% of the V_2O_5 is present as V_2O_5 crystallites, and 50% (i.e. 3.15 wt %) as a surface species. The latter phase will be present as a two-dimensional monolayer,

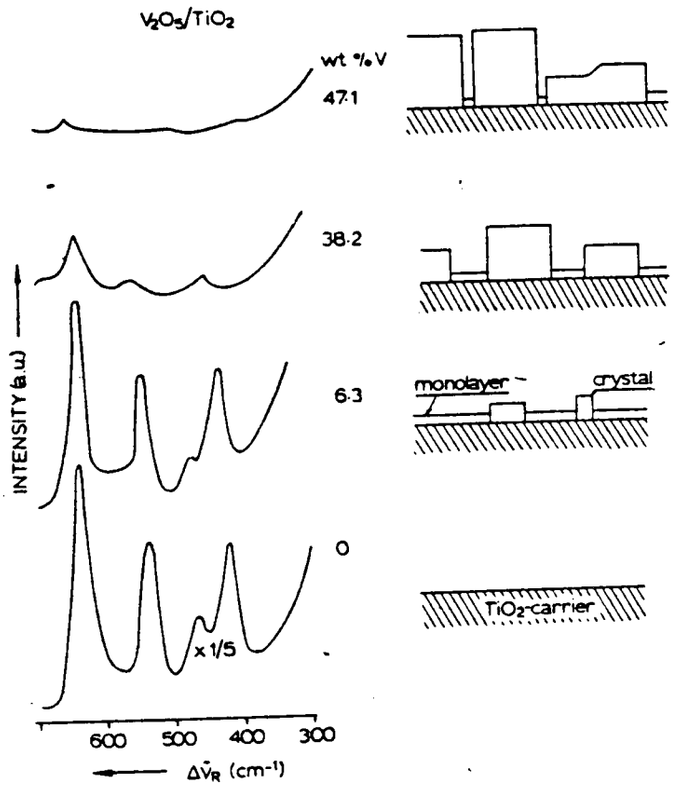

Fig. 1.11 Raman spectra of the TiO_2 carrier in a series of impregnated vanadium (V) oxide/TiO_2. Spectra are corrected for vanadium oxide and standardized for sensitivity. The spectrum of pure TiO_2 has been scaled down by a factor of 5. (ref. 70).

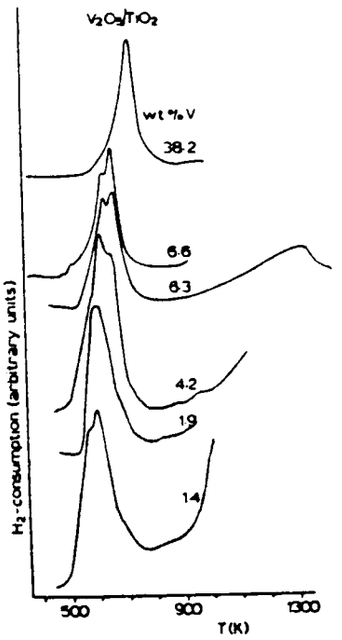

Fig. 1.12 TPR profiles of impregnated V_2O_5/TiO_2 catalysts (57)

as can be calculated from the amount of vanadia involved ($\sim$3.15 wt % V) and the BET surface area of 40 m^2g^{-1}, yielding 10.3$\mathring{A}^2$ per V oxide unit. In crystallized V_2O_5, which has a lamellar structure, the calculated surface area per $VO_{2.5}$ unit in the (010) plane is exactly 10.3$\mathring{A}$. Thus, as a model, the 6.3 wt % V consists of 3.15 wt % V as a monolayer array together with an equal amount of vanadia as very small crystallites. This is illustrated schematically in Fig. 1.11.

Monolayer contents for MoO_x/TiO_2 catalysts have been estimated by other workers, employing various preparation methods [71]. For low area anatase, a value of 0.9 wt % MoO_3 has been reported[72], while for P-25 TiO_2 values of between 3.9 and $\sim$ 6.3 wt % MoO_3 have been given [59-62]. For WO_x/TiO_2, a value of 9.3 wt % WO_3 has been quoted[60].

Two types of species may be postulated to account for an $M:Ti_s$ ratio of 0.5 (M = Mo or W): either MO_3 groups co-

ordinated to alternate pairs of oxygen atoms or MO groups co-ordinated to four oxygen atoms, as depicted below (71).

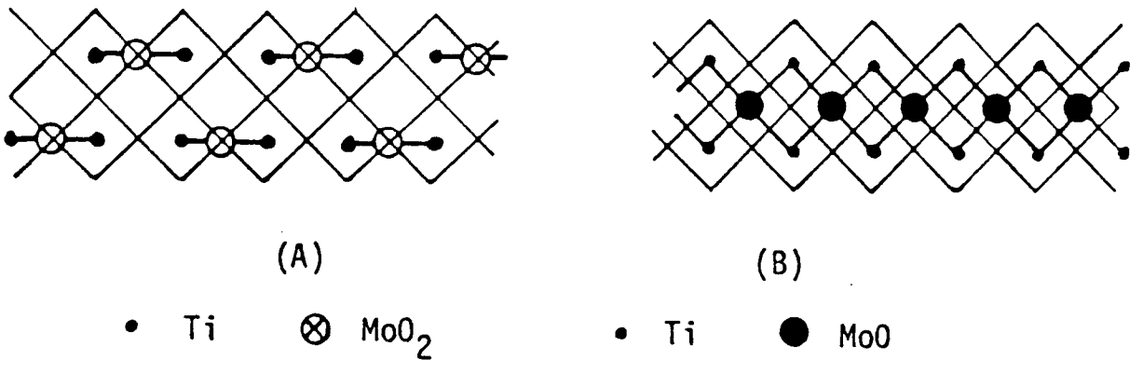

The fact that the $M:Ti_s$ ratio is apparently slightly greater than 0.5 may imply that on some part of the surface MO_2 groups are co-ordinated to adjacent pairs of oxygen atoms(71).

1.5.3 Criteria for the presence of a complete monolayer(73):

If a full monolayer of MoO_3 is formed, several physical and chemical criteria should be obeyed:

1. After preparation, via the adsorption methods, the amount of Mo present per unit of surface area must be independent of the place in the adsorbent bed and of the adsorption time,

2. The calculated mean surface area available per Mo-oxide unit (Φ_{Mo-ox}) must have the same order of magnitude as the units in the oxide supports and those in pure MoO_3.

3. Infrared transmission spectroscopy should show the absence of the surface (i.e. OH groups) of the support.

4. The monolayer, being chemically influenced by the support, should show different catalytic behaviour than that of pure MoO_3 at least for some reactions,

5. The X-ray diffraction pattern of MoO_3 must be absent.

1.5.4 Comparison of Al_2O_3, SiO_2, and TiO_2 as supports[74]

The selection of supports is the first important step in designing supported metal catalysts and is determined by parameters like surface area, porosity, thermal stability, and mechanical strength. Support materials can be classified as follows:

(a) Inert Supports e.g. SiO_2, supplying high surface area for dispersion of the active component,

(b) Catalytically Active Supports e.g. aluminas, silica-aluminas, zeolites, etc. Those materials make up about 80% of all industrial supports (see U.S. Sales 1971. Chem. Tech. (April) 1979),

(c) Supports Influencing Active Component by Strong Interaction; e.g. partially reducible oxides, TiO_2, Nb_2O_5, V_2O_5, etc.,

(d) Structural Supports - which are of increased importance for exhaust gas purification (monoliths).

1.5.5 Surface properties of supports

1.5.5.1 Surface charge in solution

When oxide particles are suspended in aqueous solutions, a surface polarization results in a net electrical surface charge, which has been associated with two processes[75], (i) dissociation of surface hydroxyl groups, or (ii) re-adsorption of hydroxo-complexes formed by partial dissolution of the oxide particle. Both processes involve H^+ and OH^- ions and thus are controlled by the pH value of the solution. In acid media the surface is most likely positively charged ($\delta-OH_2^{\oplus}$) and will preferentially adsorb anions, while in alkaline solutions the particles carry a negative surface charge ($\delta-O^-$) and adsorb cations. At some intermediate pH, a zero net charge will result. That value is called zero point of charge (ZPC) or isoelectric point (IEP) and is generally determined by electrophoretic velocity measurements. Colloid chemists have acquired detailed knowledge of the oxide-solution interface and a very comprehensive collection of isoelectric points, of oxides and hydroxides was published by Parks[76]. Isoelectric points on different samples of the same oxide may vary markedly. This has been attributed to factors like impurity levels, surface crystallinity, dehydration and ageing.

According to their surface charge in solution, support materials can be classified within the pH range 1-14 as:

(i) cation adsorbers - silicas, silica-aluminas and zeolites.

(ii) anion adsorbers - magnesia,

(iii) amphoteric supports - alumina, chromia, titania and zirconia.

1.5.5.2 Surface functionalities and catalytic properties

The surfaces of inorganic oxides will expose oxygen ions, hydroxyl groups and incompletely co-ordinated cations in various configurations in close relation to the chemical and thermal treatment of the oxides, while on carbon surfaces the main functionalities originate from carboxyl groups, phenolic hydroxyls and carbonyl groups. Those functionalities are of twofold interest in supported metal catalysis:

a) to supply anchoring sites for metal precursor compounds during catalyst preparations - ligand displacement reactions between functional groups on the support surface and metal compounds (metal carbonyls, organometallic compounds, alkoxides, halides, etc.); and

b) to supply active sites in multifunctional catalysis.

Most support materials exhibit acid-base catalytic properties[77-82] and/or oxidation-reduction functions [83-87].

The importance of those materials as catalysts in their own right, as supports for active phases (e.g. metals, oxides, halides, carbonyl compounds) as adsorbents, etc., ensured continuous interest in their surface properties.

Comprehensive reviews on the characterisation, identification, estimation and reactivity of surface functional groups[88], the determination of surface acidity[81], and the catalytic properties have been published[65, 80, 82, 83, 86, 89].

1.6 Structure of bicomponent supported oxides

The combination of two or more metallic elements into a single catalyst frequently results in a composite catalyst with properties which are superior to those of the individual metals. The demand for low-sulphur fuels has placed renewed emphasis on the development of efficient hydrodesulphurization (HDS) catalysts for industrial applications. Of special importance are the catalysts containing Mo or W compounds in admixture with Co and Ni, dispersed on an γ-Al_2O_3 support. In the interpretation of the role played by the additives, different models are discussed below.

1.6.1 Monolayer model

The first model was the so-called monolayer model, which was developed by G. C. A. Schuit and several scientists working with him or in proximity to him[90-94]. Originally, it applied to the oxide form (MoO_3 + CoO on Al_2O_3) of the catalyst, before its transformation to the active sulphided form. The model rested on the well-established fact that MoO_3 can easily form a monolayer in "registry" (avoiding the probably too precise word

"epitaxy") with the γ-Al_2O_3 lattice. The activation by Co was thought to be caused by Co^{2+} ions coming into combination with the γ-Al_2O_3/MoO_3 monolayer system, near the interface. Although it is clear now that the original monolayer model deals with the precursor form of the catalyst and not with the active catalyst itself[91], its contribution to the understanding of the genesis of supported hydrodesulphurization catalysts cannot be underestimated.

Concerning the active, sulphided form of hydrodesulphurization catalysts, a very detailed modified monolayer model, including atomic models, was proposed by the same group of investigators[91, 95-97]. Essentially it was supposed that, going upwards from the bulk of the support to the surface, the following succession of species was found: (a) γ-Al_2O_3, (b) Co-containing γ-Al_2O_3, (c) a layer containing Mo and Co bound, below, to oxygen ions, and above, to sulphur ions, and finally, (d) an incomplete layer of sulphur ions.

As recognized by the authors, this model is unsatisfactory on many grounds[91]. A major objection against it is that unsupported sulphides also exhibit synergy[98-100]. Its value is to give a picture of the interface between γ-Al_2O_3 and the supported sulphides, namely of the "glue" between those radically different phases.

1.6.2 Pseudo-intercalation model

The model was initially proposed by R. J. H. Voorhoeve and J. C. M. Stuiver[101-103] and developed by A. L. Farragher and P. Cossee[104, 105], mainly on the basis of observations on the Ni-WS_2 system. According to this model, the atoms of the Group VIII metal intercalate, between the edges of the sulphide crystals of the Group VIA elements, as suggested in Fig. 1.13; a precise atomic model was given by the authors[91, 95, 104].

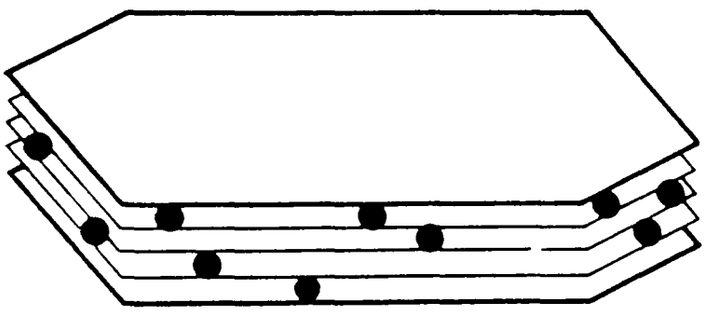

Fig. 1.13 Schematic representation of pseudo-intercalated MoS, or WS_2, crystals. (ref. 91)

What can be considered as the first physico-chemical evidence of intercalation or pseudo-intercalation has been presented only recently[106]. It rests on Mössbauer spectroscopy of CoMo catalysts. The results, however, are far from self-consistent. The spectrum attributed to intercalated Co is visible when 1 ppm Co is incorporated into unsupported MoS_2, a value which is indeed believed to fall within the range where incorporation of Co is possible. But the corresponding lines constitute the whole spectrum in carbon-supported catalysts containing 1% Co and 6% Mo (about

10^5 more Co with respect to Mo than in the unsupported catalysts), and contribute to an appreciable extent ($\simeq$ 5%) to the spectrum of SiO_2-supported catalysts and nearly to the whole spectrum (the remainder being Co in Al_2O_3) in Al_2O_3 supported catalysts of the same composition. In addition, the line attributed by the authors to Co_9S_8 is completely absent in these spectra, a result which contradicts many observations.

1.6.3 Defect structure of MoS_2

P. R. Wentrcek and H. Wise tried to explain the synergy by a change of the defect structure of MoS_2 upon doping by Co^{2+} ions[107-109].

Some doping seems to take place and to bring about changes in the semiconducting properties of MoS_2; but the effect on catalytic activity is less clear. The objection to this explanation is of the same kind as against the pseudo-intercalation models, and even stronger: the number of Co atoms which can enter the MoS_2 lattice is extremely low, at any rate lower than 1 Co for 1,000 Mo[109]. This composition is quite far from that at which the maximum synergetic effect is observed.

1.6.4 Mixed sulphide hypothesis

Quite recently, Y. Jacquin has proposed that a $(Co_rMo_{1-r})S_{2\pm x}$ compound sulphide can form in a given composition range[110]. The hypothesis would be presented in the phase diagram of Fig. 1.14. A one-phase region would

exist on the Mo side for a given range of S content. The hypothesis is inspired by our own physico-chemical and catalytic results on unsupported catalysts(99, 100, 111, 112).

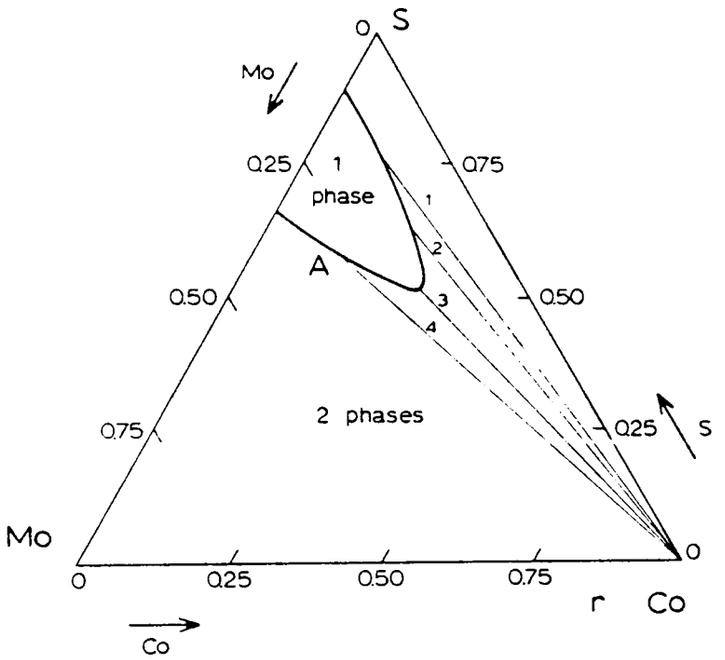

Fig. 1.14 Supposed phase diagram of the mixed sulphide hypothesis. (re. 112)

The author had not yet completely worked out his hypothesis, but proposed that the hypothetical compound sulphide, the maximum Co content of which is suggested by curve A, might play an essential role in the catalysis of at least one kind of reaction (hydrogenation). Catalysts with r = Co/(Co + Mo) outside the A curve would behave as mixtures of Co_9S_8 and compound sulphide (in properties corresponding to the usual rules, using the conoidal lines 1, 2, 3, 4,etc.).

At present, the major objection to this hypothesis is that no compound sulphide has ever been detected in cobalt sulphide-molybdenum sulphide catalytically active mixtures(100, 113) even when it has been looked for specif-

ically, and even when considering the possibility of a partly crystallized compound[114, 115]. One might argue that such compounds form under the condition of catalysis, at high reactant pressure, and immediately decompose upon cooling and withdrawing from the reactor. In view of the sluggishness of solid-solid reactions in general, it is difficult to believe that the formation and decomposition of such a solid could occur so quickly, and especially with special catalysts composed of well crystallized mixed sulphides[100] or with mechanical mixtures of sulphides[116, 117], which clearly exhibit the synergetic effect.

1.6.5 Synergy by contact

B. Delmon proposed another hypothesis[100, 113, 118], namely that the system is essentially bi-phasic (this part of the hypothesis corresponds to all observations), and that synergy is a consequence of the mere contact, or vicinity of Group VIII sulphide particles to Group VIA sulphide crystallites (Fig. 1.15) and of some interaction which takes place between these particles or crystallites.

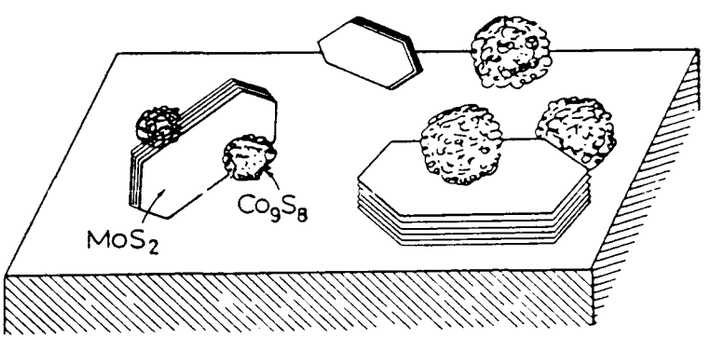

Fig. 1.15 Schematic representation of a biphasic MoS_2-Co_9S_8 system, and of the possible contacts between phases. The system may be supported (as represented here) or unsupported. (ref. 119).

The problem is to identify the kind of interaction which takes place between the crystallites[113]. Delmon had proposed[113] that some promotion of one phase could take place by electron transfer at the MoS_2/Co_9S_8 junction, this favourably modifying the electronic density of the active sites (presumably on MoS_2)[100]. Another explanation would be that some transfer (spill-over) of H atoms from one phase to the other (probably from Co_9S_8 to MoS_2) takes place. Hydrogen would be activated to atomic H on Co_9S_8, transferred to MoS_2, and would then react, on MoS_2 active sites, with sulphur containing molecules or with unsaturated hydrocarbons; the rate determining step would be this transfer[95]. In this picture, the catalyst functions essentially as a bi-functional catalyst, with two different kinds of sites.

The results of B. Delmon's group on the "anatomy" of the catalysts support, as did the former ones, their biphasic nature, and thus favour the contact synergy hypothesis. Although the "physiology" of the catalysts is still far from elucidated, several of Delmon's ideas on the way the catalysts work seem to be almost incompatible with the other models or hypotheses.

1.6.6 Kasztelan, Grimblot, and Bonnelle Model

The evolution of the surface structure of a MoO_3/Al_2O_3 sample during the preparation and after the addition of the promoter (Co or Ni), as well as the effect of the calcination temperature, have been studied[120]. The results,

when compared with previous studies by X-ray photoelectron and laser Raman spectroscopy, confirm the description of the supported species as small oxomolybdenum entities, well dispersed and occupying only a small fraction of the support surface. A strong shielding effect of the Mo element by the promoter Co or Ni has been detected; this gives direct evidence of a chemical interaction between the promoter and the oxomolybdenum species. A description of this association as an isopolymolybdate salt of Co or Ni is proposed.

In Scheme I, the excess Ni is located differently and probably interacts with the oxomolybdenum species. Interestingly, such a scheme can be viewed as a bilayer system, since the Ni ions in the surface aluminate are less accessible than the molybdenum species.

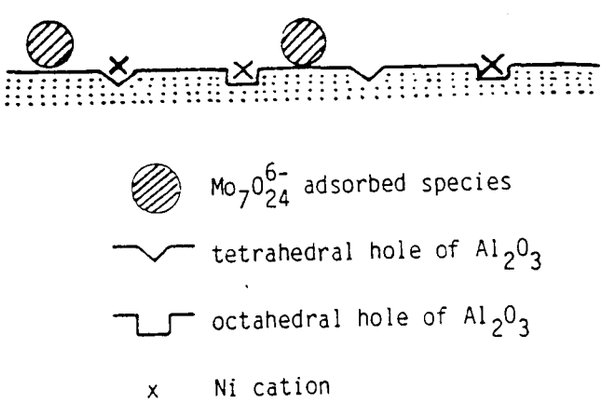

Scheme I (ref. 120)

After the addition of the Co or Ni nitrate solution to the calcined Mo samples and drying, a net decrease of the $(I_{Mo}/I_{Al})_{ISS}$ ratio is observed whereas the XPS variation is far less important. This effect can be due to a large shadowing effect on Mo by the promoter ions (Ni^{2+} or Co^{2+})

rather than the modification of the Mo distribution on the support. After the final calcination at 500°C, the Mo intensity (ISS) increases again but does not reach the value obtained before the promoter impregnation. During the transformation (dried or calcined) the Co or Ni intensity ratios slightly decrease. These later observations can be rationalized by three simultaneous events: (1) a dehydroxylation of the oxomolybdenum species; (2) the presence of the promoter in close contact with the Mo adsorbed species, which provokes a real shadowing effect of Mo by Co or Ni, and; (3) a migration, at that calcination temperature, of a fraction of the promoter ions from the oxomolybdenum species to the free surface of the support (decrease of I_{Co} and I_{Ni}).

Of particular importance is the strong evidence of an interaction between the promoter and the molybdate species (event 2) which can be depicted with Scheme II (same symbols as Scheme I).

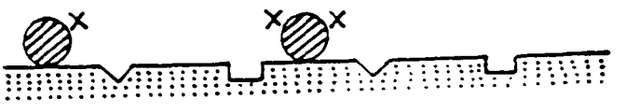

Scheme II (ref. 119)

Evidently this scheme describes a limiting case and a distribution of Ni ions between those interacting with the molybdate species and those interacting with the support surface's octahedral and tetrahedral sites is more reasonable.

The reasons the two schemes have different distributions of Ni ions are not obvious at the moment. However, both the support and the preparation methods used were not exactly the same and the preparation parameters may influence the final architecture of these catalysts.

1.7 Acidity of supported oxides/monolayers

Bernholc et al.[121] have developed the first technique for calculation of Brønsted acid strengths of transition metal compounds. It is based on first-principles local density pseudo-potential calculations for a cluster model of an acidic site and it includes a polarization contribution of the surrounding medium to the proton removal energies directly in the cluster calculations.

The method has been applied to free and alumina-supported transition metal oxide clusters of Ti, Nb and W. For free clusters, Bernholc et al. found that the number of terminal oxygen atoms forming double bonds to the transition metal atom has a strong effect on Brønsted acidity. This is due to charge delocalization of the electron left behind after removal onto the terminal oxygen atoms. A similar effect has been observed experimentally in the chemistry of main-group elements and Mn, although the microscopic original of this effect has been confirmed by calculations for the first time in works by Bernholc et al. It has been found that the transition metal atom acts as a charge acceptor.

For the supported clusters, Bernholc et al. found an additional, strong increase in Brønsted acidity due to delocalization of the extra charge onto the support. The stabilization of the acidic state for supported catalysts occurs via charge delocalization to the terminal oxygen atoms, the transition metal atom and the support.

The strong support effect on Brønsted acidity discovered in the work of Bernholc et al. may have important practical implications. It suggests optimization of transition metal oxide catalysts not only by changing the transition metal oxide but also by optimization of the support. One possible avenue would be an addition of strong electron-withdrawing groups to the support. However, the extent of changes in Brønsted acidity induced by such promoters needs to be investigated either experimentally or theoretically.

1.8 Scope of this thesis

TiO_2 generally has fairly low catalytic activity[122]. It possesses some activity for alcohol dehydration and dehydrogenation although, of the two, the former function is the more important. It also has some activity as an oxidation catalyst for substances such as hydrocarbons and hydrogen, but again the activity is relatively very low. However, its oxidation activity is augmented by u.v. irradiation and the photocatalytic activity of TiO_2 has been the subject of a good deal of study[123]; it is associated with centres which are deficient in oxygen.

Reviewing the introductory considerations presented above several questions arise:

1. Is it possible to prepare monolayers of MoO_3, CoO, CoO-MoO_3, and if so, which preparation methods are to be preferred and what are the limitations of the existence of monolayers?

2. Which techniques are appropriate for the elucidation of monolayer structures, what is the precise structure of the monolayers on the support and how stable are these structures towards treatment and/or reduction?

3. Which mechanisms are operative in 2-propanol decomposition; what are the active sites?

4. Does a relation exist between the structure and the activity or selectivity of a monolayer catalyst?

5. Which factors influence or determine the chemical behaviour (stability, catalytic activity and selectivity)? Is it possible to define an overall catalyst parameter accounting for these properties?

The research described in this thesis was carried out in order to answer some of these questions.

Chapter 2 deals with the preparation of supported oxide catalysts by different methods. The monolayer catalysts prepared by reaction from solutions of ammonium heptamolybdate (AHM) and molybdenum oxalate and cobalt nitrate, and cobalt acetate with surface hydroxyl groups of the support, and the aqueous impregnation method which was used to produce catalysts having more than one monolayer of oxide.

Chapter 3 presents an overview of the experimental techniques which were employed to characterize the catalysts and to measure the catalytic activities.

Chapter 4 gives the results for characterizing MoO_3, CoO, and CoO-MoO_3 catalysts supported on TiO_2, by means of the following techniques: LRS, TPR, XPS and TEM.

Chapter 5 consists of the discussion and comparison of the results of several active phases supported on TiO_2 with those of the corresponding bulk oxides. Furthermore, an attempt is made to correlate these results with the catalytic properties in 2-propanol decomposition.

Chapter 6 comprises the main conclusions, and some problems which are still unresolved are discussed.

1.9 References

1. J. Haber, in "Surface properties and Catalysis by Non-Metals" edited by J. P. Bonnelle, B. Delmon and E. Derouane, Nato ASI No 105, D. Reidel Publishing Co. Paper 1 (1983).

2. S. Kasztelan, E. Payen, H. Toulhoat, J. Grimblot and J. P. Bonnelle, Polyhedron, Vol. 5, No. 1/2 pp. 157-167 (1986).

3. A. C. Jacobsen, in "Surface Properties and Catalysis by Non-Metals" edited by J. P. Bonnelle, B. Delmon and E. Derouane, D. Reidel, Dordrecht p. 305 (1983).

4. J. Haber, Proc. 8th Intern. Symp. Reactivity of Solids, ed. J. Haber and J. Nowotny, Elsevier (1982).

5. R. T. K. Baker, Scott A. Stevenson, J. A. Dumesic, Gregory B. Raupp and S. J. Tauster in "Metal-Support Interactions in Catalysis, Sintering and Redispersion" (edited by Scott A. Stevenson, J. A. Dumesic, R. T. K. Baker and Eli Ruckenstein) Van Nostrand Reinhold Co. New York Ch. 5 (1987).

6. Eli Ruckenstein, in "Metal-Support Interactions in Catalysis, Sintering and Redispersion" (edited by

Scott A. Stevenson, J. A. Dumesic, R. T. K. Baker and Eli Ruckenstein) Van Nostrand Reinhold New York Ch. 13 (1987).

7. T. Huizinga, J. van Grondelle, and R. Prins, Appl. Catal., 10, 199 (1984).

8. J. S. Smith, P. A. Thrower, and M. A. Vannice, J. Catal., 68, 270 (1981).

9. D. G. Mustard and C. H. Bartholomew, J. Catal., 67, 186 (1981).

10. C. H. Bartholomew, R. B. Pannell, J. L. Butler, and D. G. Mustard, Ind. Eng. Chem. Prod. Res. Dev. 20, 296 (1981).

11. T. Huizinga and R. Prins, J. Phys. Chem., 85, 2156 (1981).

12. A. J. Simoens, R. T. K. Baker, D. J. Dwyer, C. R. F. Lund, and R. J. Madon, J. Catal., 86, 359 (1984).

13. B. J. Tatarchuk and J. A. Dumesic, J. Catal., 70, 308 (1981).

14. B. J.Tatarchuk, J. J. Chludzinski, R. D. Sherwood, J. A. Dumesic and R. T. K. Baker, J. Catal., 70, 433 (1981).

15. R. Thomas, PhD Thesis, Twente University of Technology, The Netherlands (1979).

16. A. J. Van Hengstum, J. G. Van Ommen, H. Bosch, and P. J. Gellings, Appl. Catal., 1983, 5, 207.

17. Yu. I. Yerma kov, Catal. Rev. Sci. Eng. 13 (1976) 77.

18. T. Fransen, P. C. Van Berge and P. Mars, in "Preparation of Catalysts I" (B. Delmon, P. A. Jacobs and G. C. Poncelet, eds.) P. 405, Elsevier, Amsterdam (1976).

19. F. Roozeboom, T. Fransen, P. Mars, and P. J. Gellings, Z. Anorg. Allg. Chem., 449, 25 (1979).

20. W. Hanke, R. Bienert and H. G. Jerschkewitz, Z. Anorg. Allg. Chem., 414, 109 (1975).

21. M. Gliński and J. Kijeński, in "Preparation of Catalysts III (G. Poncelet, P. Grange, and P. A. Jacobs eds.) p. 553, Elsevier, Amsterdam (1983).

22. G. C. Bond and P. Konig, J. Catal, 77, 309, (1982).

23. J. C. W. Chien, J. Am. Chem. Soc. 93, 4675 (1971).

24. F. P. J. M. Kerkhof, J. A. Moulijn, R. Thomas and J. C. Oudejans in "Preparation of Catalysts II" (B. Delmon, P. Grange. P. Jacobs and G. Poncelet eds;) Elsevier, Amsterdam, p. 77 (1979).

25. J. B. Peri, J. Phys. Chem., 70, 2937 (1966).

26. H. P. Stephens and R. G. Bosch in "Preparation of Catalysts IV" (B. Delmon, P. Grange, P. A. Jacobs and G. Poncelet, eds.) Elsevier, Amsterdam p. 271 (1987).

27. J. W. Geus, in "Preparation of Catalysts III" (G. Poncelet, P. Grange and P. A. Jacobs, eds.) Elsevier, Amsterdam, p. 1 (1983).

28. Xie Youchang, Gui Linlin, Lui Yingjuu, Zhang Yufen, Zha Biying, Yang Naifang, Guo Qinlin, Duan Lianyun, Huang Huizhong, Cai Xiaohai and Tang Youchi, in: Adsorption and Catalysis on Oxides Surfaces, (Eds. M. Che and G. C. Bond) Elsevier, Amsterdam p. 139 (1985).

29. J. Leyrer, R. Margraf, E. Taglauer and H. Knözinger, Surf. Sci. 201, 603-623 (1988).

30. J. M. Thomas and R. M. Lambert, in "Characterization of Catalysts" J. Wiley and Sons, Ch. 1 (1980).

31. J. C. Vedrine, in "Surface Properties and Catalysis by Non-Metals" (Edited by J. P. Bonnelle et al.) D. Reidel, Dordrecht, p. 123 (1983).

32. P. Dufresne, E. Payen, J. Grimblot, and J. P. Bonnelle, J Phys. Chem., 85, 2344 (1981).

33. A. Jones and B. D. McNicol, in "Temperature-programmed reduction for solid materials characterization" (Chemical Industries Vol. 24, Marcel Dekker, Inc. New York, Basel) (1986).

34. J. W. Jenkins, Gordon Research Conference on Catalysis, Colby-Sawyer College, New London, New Hampshire (1975).

35. R. J. Cvetanovic and Y. Amenomiya, Catal. Rev., 6(1), 21 (1972).

36. S. D. Robertson, B. D. McNicol, J. H. DeBass, S. C. Kloet, and J. W. Jenkins, J. Catal., 37, 424 (1975).

37. N. W. Hurst, S. J. Gentry, A. Jones, and B. D. McNicol, Catal. Rev. Sci. Eng. 24(2), 233 (1982).

38. R. C. Mackenzie (ed.) "Differential Thermal Analysis" Academic Press, London and New York (1970).

39. A. K Banarjee, S. R. Naidu, N. C. Ganguli, and S. P. Sen, Technology, 11, 249 (1974).

40. A. K. Banarjee, Technology, 11, 162 (1974).

41. N.W. Coats and J. P. Redfern, Nature, 201, 68 (1964).

42. E. D. Rainville, "Special Functions", Macmillan, New York p.44, (1960).

43. S. J Gentry, N. W. Hurst, and A. Jones, J. Chem. Soc., Faraday I, 75, 1688 (1979).

44. J. M Thomas and W. J. Thomas "Introduction to the Principles of Heterogeneous Catalysis" Academic, London (1968).

45. P. A. Jacobs, J.-P. Linart, H. Nijs, and J. B. Uytterhoeven, J. Chem. Soc., Faraday I, 73. 1745 (1977).

46. S. J. Gentry, N. W. Hurst and A. Jones, J. Chem. Soc., Faraday I, 77, 603 (1981).

47. D. A. M. Monti and A. Baiker, J. Catal., 83, 323 (1983).

48. K.H. Tonge, Thermochimica Acta, 74, 151 (1984).

49. H. Bosch, B. J. Kip, J. C. Van Ommen, and P. J. Gellings, J. Chem. Soc. Faraday I, 80, 2479 (1984).

50. C. R. Brundle and A. D. Baker, "Electron Spectroscopy theory, techniques and applications" Academic Press, Lond., Vol. 1, 1977 —>Vol. 5, 1984.

51. D. M Hercules and J. C Klein, in "Applied Electron Spectroscopy for Chemical Analysis" (edited by H. Windawi and Floyd F.-L. Ho) Vol. 63 in Chemical Analysis. J. Wiley and Sons, Ch. 8 (1982).

52. W. E. Schwartz and D. M Hercules, Anal. Chem., 43, 1774 (1971).

53. C. D. Wagner, Anal. Chem., 44, 1050-1053 (1972).

54. C. Defossé, P. Canesson, P. G. Rouxhet, and B. Delmon, J. Catal., 51, 269 (1978).

55. R. B. Shalvoy and P. J. Reucroft, J. Electron Spectrosc. Relat. Phenom., 12, 35, (1987).

56. P J. Angevine, J. C. Vartuli, and W. N. Delgass, Proc. Int. Congr. Catal., 6th, 1976, 2, (1987).

57. F. P. J. M. Kerkhof and J. A Moulijn, J. Phys. Chem., 83(12), 1612, (1979).

58. R. L. Chin and D. M. Hercules, J. Phys. Chem., 86, 360 (1982).

59. F. Delanney, in "Characterization of Heterogeneous Catalysts" (Chemical Industries Vol. 15, Marcel Dekker, Inc. Basel and New York Ch. 3, (1984).

60. R. Casting, PhD Thesis, University of Paris, ONERA Publ., 55, (1951).

61. J. J. Hren, J. I. Goldstein, and D. C. Joy, eds., "Introduction to Analytical Electron Microscopy" Plenum Press, New York, (1979).

62. P. B. Hirsch, A. Howie, R. B. Nicholson, D. W. Pashley, and M. J. Whelan, "Electron Microscopy of Thin Crystals", R. E. Krieger, New York (1977).

63. C. J. Humphreys, Rep. Prog. Phys. 42, 1825, (1979).

64. J. M. Cowley, "Diffraction Physics", 2nd Ed. North Holland Publ. Co. (1981).

65. O. V. Krylov "Catalysis by Non-Metals" Academic Press, London and New York (1970).

66. M. Ai, Bull. Chem. Soc. Jpn., 49(5), 1328-1334 (1976).

67. K. Akito and O. Susumn, Nippon Kagaka Kaishi, 12, 1794-8 (1977).

68. G. C. Bond and S. Flamerz, Appl. Catal., 33, 219-230, (1987).

69. A. Vejux and P. Courtine, J. Solid State Chem. 23, 93-103 (1978).

70. F. Roozeboom, M. C. Mitteimeijer-Hazeleger, J. A. Moulijn, J. Medema, V. H. J. de Beer, and P. J. Gellings, J. Phys. Chem. 84, 2783-2791, (1980).

71. G. C. Bond, S. Flamerz and LK. Van Wijk, Catal. today, 1, 229 (1987).

72. A J. Van Hengstum, J. G. Van Ommen, H. Bosch, and P. J. Gellings, Appl. Catal., 5, 207 (1983).

73. T. Fransen, PhD Thesis, Twente University of Technology, Enschede, The Netherlands (1977).

74. K. Foger, in "Catalysis, Science and Technology" (J. R. Anderson and M. Boudart, Eds.) Vol. 6, Ch. 4, (1984).

75. G. A. Parks, P. L. De Bruyn; J. Phys. Chem. 66, 967 (1962).

76. G. A. Parks, Chem. Rev. 65, 177 (1965).

77. K. Tanabe, in "Metal Oxides and Complex Oxides" K. Tanabe, T. Seiyama and K. Heucki (eds.) Tokyo: Kodansha Scientific p. 407 (1978).

78. K. Tanabe, "Solid Acid and Bases" Academic Press, London and New York (1970).

79. K. Tanabe, in "Catalysis, Science and Technology" (J. R. Anderson and M. Boudart, Eds.) Vol. 2, p. 231 (1981).

80. J. Happel, M. Hnatow, and L Bajars in "Base Metal Oxide Catalysts" New York, Basel, Marcel Dekker (1977).

81. H. A. Benesi and B. H. C. Winquist, Adv. Catal. 27, 97 (1977).

81. H. A. Benesi and B. H. C. Winquist, Adv. Catal. 27, 97 (1977).

82. H. Knozinger, Adv. Catal. 25, 184 (1969).

83. R. L. Burwell, G. L. Haller, K.C. Taylor and J. F. Read, Adv. Catal. 20, 1 (1969).

84. M. P. Rosynek; Catal. Rev. Sci. Eng. 16, 111 (1977).

85. F. S. Stone; Adv. Catal. 13, 1 (1962).

86. I. E. Maxwell; Adv. Catal. 31, 2 (1982).

87. M. Che and A. J. Tench; Adv. Catal. 31, 77 (1982).

88. H. P. Boehm and H. Knozinger, in "Catalysis, Science and Technology" (J. R. Anderson and M. Boudart eds.) Berlin, Springer Vol. 4, p. 40 (1983).

89. P. A. Jacobs "Carboniogenic Activity of Zeolites" Amsterdam, Oxford, New York, Elsevier (1977).

90. G. C. A. Schuit and B.C. Gates, A.I.Ch.E.J. 19, 417 (1973).

91. B. C. Gates, J. R. Katzar, and G. C. A. Schuit "Chemistry of Catalytic Processes" McGraw Hill, New York, Ch. 5, (1979).

92. J. M. J. C. Lipsch and G. C. A. Schuit, J. Catal., 15, 163 and 179 (1974).

93. V. H. J. de Beer, T. H. M. van Sint Fict, J. F. Engelen, A. C. van Haandel, M. V. J. Wolfs, C. H. Amberg and G. C. A. Schuit, J. Catal. 27, 327 (1972).

94. J. Sonnemans and P. Mars, J. Catal., 31, 209 (1973).

95. V. H. J. de Beer and G. C. A. Schuit, in "Preparation of Catalysts I" B. Delmon, P. A. Jacobs, and G. Poncelet, Eds. Elsevier, Amsterdam, P. 343 (1976).

96. J. Medema, C. Van Stam, V. H. J. de Beer, A. J. A. Konnings, and D. C. Knoingsberger, J. Catal., 53, 386 (1978).

97. H. Knözinger and H. Jeziorowski, J. Phys. Chem. 82, 2002 (1978).

98. G. Hagerbach, Ph. Courty, and B. Delmon, C. R. Acad. Sci. Ser. C. 271, 783 (1970).

99. G. Hagerbach, Ph. Courty and B. Delmon, J. Catal. 23, 295 (1971).

100. G. Hagerbach, Ph. Courty and B .Delmon, J. Catal. 31, 264 (1973).

101. R. J. H. Voorhoeve and J. C. M. Stuiver, J. Catal. 23, 228 (1971).

102. R.J. H. Voorhoeve, J. Catal. 23, 236 (1971).

103. R. H. J. Voorhoeve and J. C. M. Stuiver, J. Catal. 23, 243 (1971).

104. A. L. Farragher and P. Cossee in "Catalysis" Proc. 5th Int. Congr. on Catal., J. W. Hightower, ed. North Holland, Amsterdam. p.1301 (1973).

105. A. L. Farragher, Symposium on the Role of Solid State Chemistry in Catalysis, ACS meeting, New Orleans, March 20-25 (1977).

106. H. Topsøe, B.S. Clansen, N. Burriesci, R. Candia, and S. Mørup, in "Proceedings, 2nd. Int. Symp. on the Scientific Bases for the Preparation of Heterogeneous Catalysts II" B. Delmon, P.Grange and P. A. Jacobs and G. Poncelet eds. Elsevier, Amsterdam. Communication E3 (1979).

107. P. R. Wentrcek and H. Wise, J. Catal. 45, 349 (1976).

108. P. R. Wentrcek and H. Wise, Preprint, Div. Petrol. Chem. ACS. 22, 525 (1977).

109. P. R. Wentrcek and H. Wise, J. Catal. 51, 80 (1978).

110. Y. Jacquin in "Catalyse de Contact" J. F. Le Page et al. Technip Publ. Paris p. 495-500 (1978).

111. G. Hagenbach, P. Menguy and B. Delmon, C. R. Acad. Sci. Ser. C. 273, 1220 (1971).

112. G. Hagenbach, P. Menguy and B. Delmon, Bull. Soc. Chim. Belges. 83, 1 (1974).

113. B. Delmon, Preprints, Div. Petrol. Chem. ACS. 22, 503 (1977).

114. G. Delvaux, A. Leonard, P. Grange, B. Delmon and M. Genet, 5th Iberoamerican Symposium on Catalysis, Lisbon, July 25-30, 1976, Abstract pp. 276-277.

115. G. Delvaux, P. Grange and B. Delmon, Bull. Soc. Chim. Fr. (1), 24 (1979).

116. J. M. Zabala, M. Mainil, P. Grange and B.Delmon, React. Kinet. Catal. Lett. 3, 285 (1975).

117. P. Canesson, B. Delmon, G. Delvaux, P. Grange, and J. M. Zabala, Proc. 6th Int. Congr. On Catal., (G. C. Bond, P. B. Wells, and F. C. Tompkins Eds.) The Chemical Society, London, p. 927 (1977).

118. P. Grange and B. Delmon, J. Less-Common Met. 36, 353 (1974).

119. B. Delmon in "Third Int. Conf. on Chem. and Uses of Molybdenum". ed. by H. F. Barry and P. C. H. Mitchell, Ann Arbor, Michigan, U.S.A., 73 (1979).

120. S. Kasztelan, J. Grimblot, and J. P. Bonnelle, J. Phys. Chem., 91, 1503-1508, (1987).

121. J. Bernholc, J. A. Horsley, L. L. Murrell, L. G. Sherman, and S. Soled, J. Phys. Chem. 91, 1526-30 (1987).

122. M. E. Winfield "Catalysis" (P. H. Emmett, ed.) Vol. 7, Reinhold, New York P. 63 (1960).

123. G. K. Boreskov, Disc. Faraday Soc. 41, 263 (1966).

CHAPTER 2. PREPARATION OF CATALYSTS

2.1 Introduction

Solid catalysts in common use are typically in the form of small metal crystallites dispersed on the internal surface of the porous support. Advantages of these supported-metal catalysts lie in their high surface-to-volume ratio and the high thermal stability endowed by the dispersion[1]. Such catalysts are commonly produced by liquid-phase impregnation in which a dry pellet of the porous support is impregnated with a solution of a compound of the desired catalytic constituent. During impregnation and subsequent drying, small crystallites of the catalyst precursors are deposited on the internal surface of the support material. The impregnation and drying steps involve mass and/or heat transfer processes which often do not reach equilibrium, resulting in non-uniform concentration profiles of impregnant, or "impregnation profiles" along the radius of the support pellet.

It is of considerable industrial as well as academic interest to predict and control these impregnation profiles. If, for example, the reaction for which the catalyst is to be used may become mass-transport limited, it would be desirable to have the catalytic constituent deposited as close as possible to the external surface of the catalyst pellet, whereas a uniformly distributed profile would be desired if the reaction is kinetically limited. If the

reaction may be poisoned by an impurity which is strongly adsorbed on the pore mouth, it would be beneficial to produce a subsurface impregnation in which a band of catalyst-free support is established on the exterior of the pellet to keep the poison spatially separated from the active component.

Attempts to control impregnation profiles, in order "to make more effective catalysts", as Maatman[2] referred to it, were first reported by Maatman and Prater[3]. Since then, theoretical and experimental work on the prediction and/or control of impregnation profiles has been published, particularly in recent years, with the efforts to transform the art of catalyst preparation into a science[4-6]. Most of the theoretical work up to 1979 on the preparation of impregnated catalysts has been excellently reviewed by Neimark, Kheifets, and Fenelonov[7].

Before proceeding to the main subject, it is worthwhile to mention the problems that exist in the design and the preparation of impregnated catalysts. The design of impregnation profiles is in many cases made to optimize the catalytic activity for main or side reactions and deactivation. From this point of view the meaningful quantity is the intrapellet "activity profiles", as commonly referred to in the field of reaction engineering. On the other hand, for catalyst preparation and characterization, the intrapellet "concentration profiles" of the catalytically active components are often controlled and/or measured. The correspondence between the activity profiles and these concen-

tration profiles is not straightforward due to the complexity of heterogeneous catalysis. At the least, one must know the local surface area of the active material that, in the simplest case, would be in close proximity to the local activity, or one may wish to know the local metal particle size distribution when the reaction is structure sensitive. In general, local catalytic activity may be taken to be proportional to the local density of active sites, assuming that the turnover frequencies over these sites are constant. The difficulty lies in the fact that not only may the turnover frequencies be inconsistent from site to site due, for instance, to the difference in the extent of catalyst-support interaction, but also it would be difficult at the present time to determine the local concentration of active sites as a function of pellet radius. This difference between the activity and concentration profiles is also encountered when one attempts to compare experimentally the reaction characteristics of different impregnation profiles.

With the above-mentioned complexity in mind, the present introduction will use the term "impregnation profiles" to mean the intrapellet concentration profiles of the catalytically active material, and intrapellet activity profiles will be referred to as "activity profiles". Where less precise definitions suffice, also employed for the ease of discussion are the limiting types[7, 8] of impregnation and/or activity profiles shown in Fig. 2.1. Cross-hatching of slabs and spherical pellets of catalyst supports in Fig. 2.1 indicates the regions where catalytically active

components are deposited. The schematic impregnation or the activity profile for each type is also depicted in Fig. 2.1. The Type I profile is sometimes referred to as "uniform", although the local activity or local metal concentration may not be constant with respect to pellet radius, as exemplified by the schematic profile. Type II is often referred to as "pellicular" or "egg-shell", Type III as "egg-yolk", and Type IV as "egg-white". Types III and IV, in which bands devoid of active material are established on the exterior of the support pellet, are also termed "subsurface impregnation".

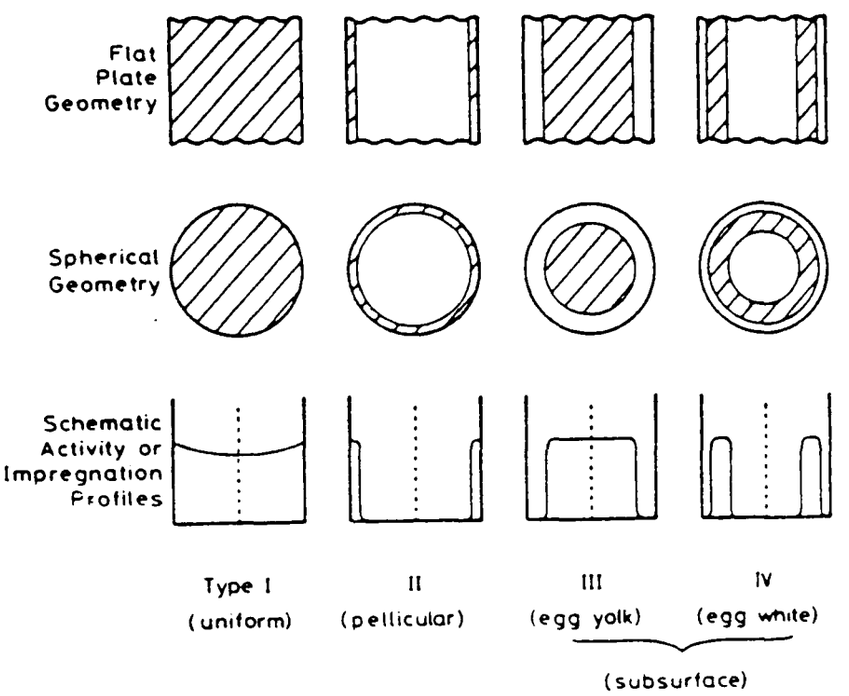

Fig.2.1 Four limiting types of impregnation or activity profiles. Hatched areas in the cross sections of slabs and pellets (top and middle rows) indicate the regions where active components are deposited. The bottom row shows schematic examples of impregnation or activity profiles. (ref. 1).

2.2 Factors influencing impregnation profiles

The preparation of impregnated catalysts commonly involves (i) contacting a dry support with an impregnating solution which consists of a compound of the desired catalytic constituent dissolved in a liquid (impregnation step), (ii) drying the product (drying step), and (iii) calcining and/or reducing if necessary (activation step). In order to establish the methods of controlling impregnation profiles so as to embody their blueprints for particular applications, understanding the physical chemistry of the above steps and a proper modelling of each step based on it are indispensable. An excellent review on "theory of preparation of supported catalysts" covering the above three steps has been given[7], and therefore discussions in this chapter will be limited to covering the basic aspects of catalyst preparation by impregnation. Examined here are the factors controlling the impregnation profiles in the first and second steps, both of which strongly affect the profiles in the finished catalysts. Discussion of the third step is not included because it appears to have a relatively small influence in determining impregnation profiles, although it may play a significant role in determining activity profiles.

2.2.1 Impregnation step

When a dry support pellet is immersed in an impregnating solution, the solution is imbibed into pores due to capillary pressure, and at the same time impregnant

diffusion and adsorption start. This time-dependent flow of the impregnating solution inside the pellet ceases when the impregnation solution reaches the centre of the pellet (at time t_L), and after that only diffusion and adsorption continue. These processes may be represented by the following equation[9]:

$$\frac{\partial C}{\partial t} + v\nabla C = D\nabla^2 C + R_A \qquad (1)$$

where C is the concentration of the impregnant in the liquid phase, t is the time, v is the flow velocity of the penetrating solution, D is the diffusion coefficient of the impregnant in the liquid phase, and R_A is some function describing the rate of impregnant removal from the system.

It is apparent that there are two limiting regimes in the impregnation step[2]: one with non-zero velocity of impregnating solution ($v \neq 0$) and the other with no flow of solution ($v = 0$) inside the pellet. The former may be called[7] "capillary impregnation" because in this regime the impregnant is mainly carried into a pellet from the exterior by convection caused by capillary suction, and the latter "diffusional impregnation" because the transfer of impregnant from the exterior to the interior is carried out by diffusional relaxation.

2.2.2 Drying step

At the end of the impregnation step, viz., when the impregnated pellets are withdrawn from the impregnating solution, the pore volume of the pellet is filled with

solution, and the impregnant in it is distributed between the adsorbed phase on the pore wall and the liquid phase in the pore volume. The drying step that follows the impregnation phase causes the transfer and evaporation of this liquid, and in the process redistributes the impregnant remaining in the pore volume. The extent of the effect of this redistribution on the impregnation profile of a finished catalyst depends on the adsorptivity of the impregnant[3, 10, 11]. It may be estimated by a parameter[11],

$$P = C_a S/\varepsilon C \quad \text{(quasi-homogeneous porous body)}$$
$$= 2C_a/rC \quad \text{(single pore)} \qquad (2)$$

which is the ratio between the amount of impregnant adsorbed and the amount remaining in the pore at the end of the impregnation step. A system with $P << 1$ retains much of the impregnant in the pore volume at the end of the impregnation step, and the way it is deposited during drying practically determines the final impregnation profile. In a system with $P >> 1$, the adsorbed phase contains most of the impregnant, and the impregnation profile established during the impregnation step is little affected by drying.

2.3 Preparation of profile-controlled impregnated catalysts

In the previous section the factors that strongly influence impregnation profiles of finished catalysts were enumerated. Reviewed in this section are examples of

impregnated catalyst preparations in which these factors are utilized as means of controlling the impregnation profiles.

2.3.1 Uniform and pellicular impregnation

Let us first examine the preparation of Type I (uniform) and Type II (pellicular) profiles (cf. Fig.2.1). These profiles may be considered as limiting cases of a spectrum of impregnation profiles. For example, if a family of impregnation profiles is represented by $a(x) = x^n$, where x is the fractional distance from the pellet centre, profiles with $n \simeq 0$ are classified as Type I and those with $n >> 1$ as Type II. The relevant characteristics of these two limiting profiles are the level of local impregnant loading and, in case of Type II profiles, the thickness of the impregnated layer as well.

2.3.2 Subsurface impregnation

Preparation of subsurface impregnation profiles (Types III and IV in Fig. 2.1) is commonly achieved by co-impregnation in which a support pellet is impregnated with a solution containing a catalyst precursor and an inorganic or organic acid. For example, a Type III (egg-yolk) Ni profile was obtained by capillary impregnating a γ-alumina pellet with a solution of nickel chloride and nitric acid[12]. In this case the initial acid concentration in the impregnating solution determined the thickness of the unimpregnated external surface band, and the initial nickel chloride concentration determined the Ni loading at the impregnated

core. Citric acid in place of nitric acid was equally effective in producing a subsurface Ni profile on the same alumina, although a higher acid concentration was needed to obtain the same thickness of the catalyst-free layer compared to the nitric acid impregnation[13]. A Type IV (egg-white) Pt profile was obtained by capillary impregnating an alumina pellet with a solution of platinum chloride and citric acid[14] in which the concentration of the acid determined the thickness of the catalyst-free band on the external surface. A number of other acids may also be employed for the production of a subsurface Pt profile on alumina pellets[15].

2.3.3 Multicomponent impregnation

When several catalytic components are needed in one pellet, such as in a case of a three-way automotive emission control catalyst, multi-component impregnation is performed. Two methods may be employed: sequential impregnation or simultaneous impregnation. The sequential method involves single-component impregnation followed by drying and calcining or some other immobilization step, then the second single-component impregnation, drying, and immobilization, and so on. The simultaneous method employs single impregnation using a solution of two or more catalytic ingredients.

Several reports[16-18] compare the impregnation profiles produced by these two methods. Summers and Hegedus[16] prepared Pt-Pd/alumina; Melo, Cervello, and

Hermana[17] Ni-Ba/γ-alumina; and Chen, Gillies, and Anderson[18] Cu-Cr/γ-Al_2O_3. In all these cases the simultaneous impregnation gave overlapped profiles of both components. In contrast, sequential impregnation gives more freedom in controlling profiles of each component, since impregnation conditions such as time or pH can be varied for each impregnation. Thus simultaneous impregnation of hexachloroplatinic acid and palladium chloride onto alumina gives a Type II profile in which Pt and Pd are deposited in one pellicular band[16]. By employing the sequential method with appropriate conditions for each impregnation, however, it was possible to produce a pellicular (Type II) Pt band with an egg-white(Type IV) Pd band inside, or a pellicular band with an inner egg-yolk (Type III) Pt deposition[16].

Theoretical calculations have been performed for both multicomponent impregnation methods, simultaneous[19, 20, 21] and sequential[22]. Note that, in the sequential impregnation, it must be taken into account that the adsorption parameters for the second impregnation may be affected by the presence of the first component on the pore wall[22].

2.4 TiO_2 supports

Turning to TiO_2, the mechanism of ammonium heptamolybdate (AHM) adsorption is similar to that on γ-Al_2O_3[23]. Only basic hydroxyl groups and coordinatively unsaturated (cus) Ti^{4+} sites are involved in the adsorption process. This follows, for instance, from the fact that the

difference in the amount of Mo adsorbed between an untreated TiO_2 sample and one whose hydroxyl groups have been reacted away with $Fe(acac)_3$[24] is exactly equal to the amount calculated from the number of basic hydroxyl groups present in the following equation:

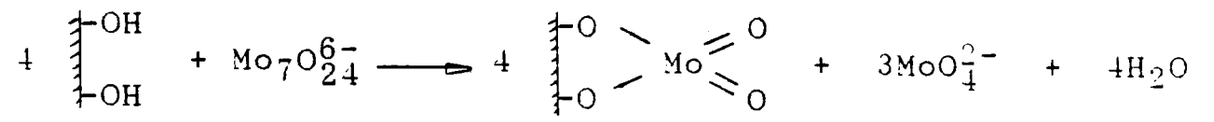

For example, P-25 TiO_2 contains 0.14 mmol basic OH groups[24] and this accounts for 0.7 wt % Mo adsorbed, the cus Ti^{4+} sites accounting for the remaining 3.3 wt %.

Since TiO_2 contains quite a few fairly acidic surface OH groups as well (in the present case, 0.33 mmol g^{-1}, determined by NaOH adsorption)[25], and since insoluble species tend to form in AHM solution when it is acidified[26], van Veen and Hendricks suggest that TiO_2 does not really adsorb a Mo species, but that it catalyses the formation of a surface precipitate.

2.4.1 Types of TiO_2 supports

The supports used in this work were supplied by Tioxide International Ltd., and Degussa, and their characteristic properties are shown in Table 2.1. In order to remove the impurities listed in Table 2.1, the support (CLD 867) was washed with water as described below.

Table 2.1

Characteristic properties of the TiO_2 samples used as support

TiO_2	support washing	surface area m^2g^{-1}	phase	impurities (wt.%)				
				Al_2O_3	SiO_2	P_2O_5	K_2O	SO_3
CLD 867	unwashed	9.6	anatase	<0.01	<0.01	0.41	0.29	76ppm
CLD 867-W	washed	9.6	anatase	n.d.	n.d.	0.15	0.05	n.d.
Degussa P-25	unwashed	55.0	anatase (76%)	<0.03	<0.02	<0.02	<0.02	- -

n.d. = not determined

2.5 Pretreatment of TiO_2

2.5.1 Washing of TiO_2 to remove the P and K impurities

Before using the TiO_2 as a support in some preparations of the catalysts, a preliminary washing was carried out to remove impurities such as P and K. 25g of TiO_2 (CLD 867 9.6 m^2g^{-1}, anatase) was washed with deionized water by refluxing for $\sim$ 72h in a Soxhlet apparatus. After washing, the material was then dried in an air oven at 120°C and designated as TiO_2 (washed).

Using this treatment, it was found that P and K were partially removed from the TiO_2 (Table 2.1).

2.6 Preparation of MoO_3/TiO_2 catalysts

2.6.1 Preparation of MoO_3/TiO_2 catalysts by impregnation using ammonium hepta-molybdate (AHM) as precursor

Ammonium hepta-molybdate $[(NH_4)_6Mo_7O_{24}.4H_2O]$ was supplied by Hopkin & Williams Ltd. A series of catalysts was prepared (from 0.5 to 4 weight percent MoO_3). The appropriate amount of AHM was dissolved in 10 ml of saturated oxalic acid solution and then added to the previously weighed titanium dioxide. The mixture was evaporated gently on a hotplate with continuous stirring until it became a thick paste. In the solution an equilibrium exists between molybdate and hepta-molybdate ions. The equilibrium is influenced by pH, for instance, in acidic solutions more hepta-molybdate ions adsorb. The two major

equilibria which may occur in the solution may be written as:

$$7MoO_4^{2-} + 8H^+ \rightleftharpoons Mo_7O_{24}^{6-} + 4H_2O$$

$$8MoO_4^{2-} + 12H^+ \rightleftharpoons Mo_8O_{26}^{4-} + 6H_2O$$

The relaxation spectra reported by Honig and Kustin[27] also suggested the presence of these molybdates. The major molybdate species at concentrations above 1×10^{-3} M that are present at various pH ranges can be roughly illustrated by the scheme below:

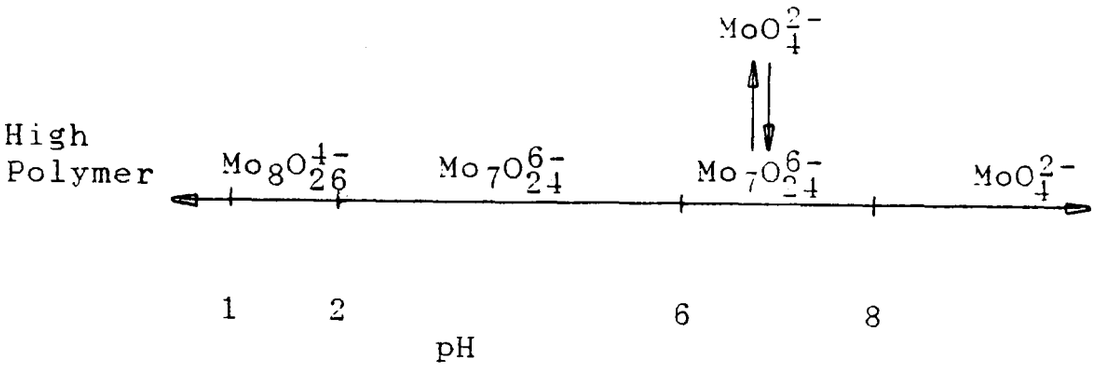

The drying was then completed by placing the sample in an oven at 120°C overnight. After removing from the oven, the sample was calcined in a furnace at 450°C for 5 hours.

2.6.2 Preparation of MoO_3/TiO_2 catalysts by impregnation using molybdenum oxalate as precursor

Molybdenum oxalate was supplied by The Climax Molybdenum Company. The same procedure was used as in the prev-

ious preparation, except that the precursor was dissolved in distilled water. (The estimation of monolayer capacity is described in Appendix I).

2.7 Preparation of CoO/TiO_2 catalysts

2.7.1 Preparation of CoO/TiO_2 catalysts by impregnation method using cobalt nitrate as precursor

AnalaR cobalt (II) nitrate, $Co(NO_3)_2.6H_2O$ was supplied by BDH. A series of catalysts was prepared (from 0.6 to 9.6% wt. % loading CoO). The appropriate amount of cobalt nitrate was dissolved in 10ml distilled water and then added to a previously weighed sample of TiO_2. The mixture was evaporated gently on a hotplate with continuous stirring until it became a thick paste. The drying was then completed by placing the sample in an oven at 120°C overnight. After removing from the oven, the sample was calcined in a furnace at 450°C for 5 hours.

2.7.2 Preparation of CoO/TiO_2 catalysts by homogeneous precipitation using cobalt nitrate as precursor

The reaction vessel was charged with the appropriate amount of TiO_2 in 400 cm^3 of $Co(NO_3)_2.6H_2O$ solution, and heated to 353K. Excess of urea was added, and the mixture heated for about 5 hours. The change in pH (5.9 - 6.1) with time was recorded automatically. Precipitation from homogeneous solution has been described by Geus[28], for the

purpose of producing small metal particles. The method requires a medium strength interaction between the precipitated metal hydroxide and the support. Hydroxyl ions, formed by the slow decomposition of urea in water at 70-90°C, are used as a precipitating agent as shown below:

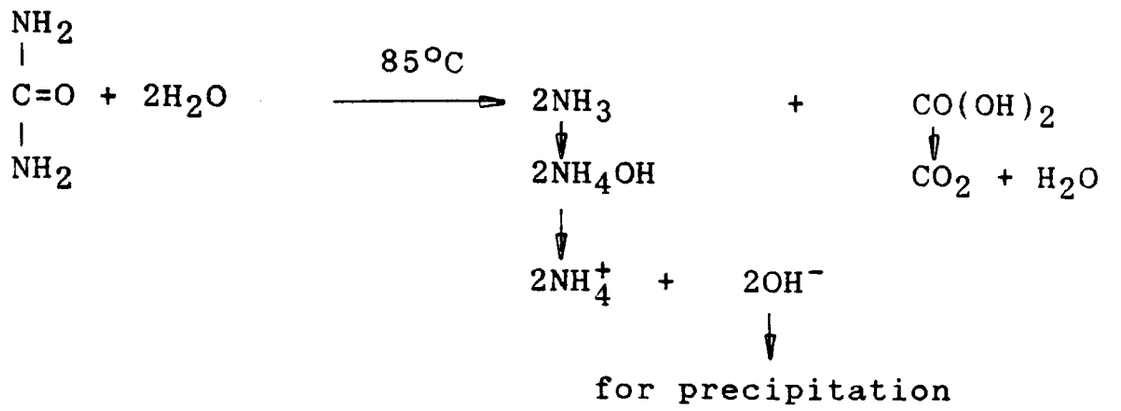

2.7.3 Preparation of CoO/TiO_2 catalysts by impregnation using cobalt acetate as precursor

Cobalt acetate, $Co(CH_3COO)_2.4H_2O$, was supplied by BDH Chemicals Ltd. A series of catalysts was prepared (from 0.19 to 3 wt % CoO loading). The appropriate amount of $Co(CH_3COO)_2.4H_2O$ was dissolved in 10ml distilled water and then added to the previously weighed TiO_2. The mixture was evaporated gently on a hotplate with continuous stirring until it became a thick paste. The drying was then completed by placing the sample in an oven at 120°C overnight. After removing from the oven, the sample was calcined in a furnace for 5 hours. (For estimation of monolayer capacity, see Appendix II).

2.8 Preparation of $CoO-MoO_3/TiO_2$ catalysts

$CoO-MoO_3/TiO_2$ catalysts were prepared by impregnation in three different ways, CoO deposited first, MoO_3 deposited first, and CoO and MoO_3 together.

2.8.1 CoO first

Cobalt nitrate $Co(NO_3)_2.6H_2O$ (0.42% - 6.68% CoO wt%) was dissolved in 10ml distilled water and then added to the previously weighed TiO_2. The mixture was evaporated gently on a hotplate with continuous stirring until it became a thick paste. The drying was then completed by placing the sample in an oven at 120°C overnight. Ammonium heptamolybdate $(NH_4)_6Mo_7O_{24}.4H_2O$ (0.8%-12.8% MoO_3 wt.%) was dissolved in 10ml of saturated oxalic acid solution and then added to the previously dried sample (CoO + TiO_2 P-25, anatase). The mixture was evaporated gently on a hotplate with continuous stirring until it became a thick paste. The mixture was dried overnight in an oven with temperature at 120°C. After removing from the oven, the sample was calcined in a furnace at 450°C for 5 hours.

2.8.2 MoO_3 first

Ammonium heptamolybdate $(NH_4)_6Mo_7O_{24}.4H_2O$ (0.80%-12.8% MoO_3 wt.%) was dissolved in 10ml of saturated oxalic acid solution and added to the previously weighed TiO_2. The mixture was evaporated gently on a hotplate with continuous stirring until it became a thick paste. The drying was then completed by placing the sample in an oven at 120°C over-

night. Cobalt nitrate $Co(NO_3)_2.6H_2O$ (0.42%-6.68% CoO wt.%) was dissolved in 10ml distilled water and then added to the previously dried sample (MoO_3 + TiO_2 P-25, anatase). The mixture was evaporated gently on a hotplate with continuous stirring until it became a thick paste. The mixture was dried overnight in an oven with temperature at 120°C. After drying, the sample was calcined in a furnace at 450°C for 5 hours.

2.8.3 CoO and MoO_3 together

Appropriate amounts of ammonium heptamolybdate $(NH_4)_6Mo_7O_{24}.4H_2O$ and cobalt nitrate $Co(NO_3)_2.6H_2O$ were dissolved in saturated oxalic acid solution and distilled water, respectively, and added simultaneously to the previously weighed TiO_2. The mixture was evaporated gently on a hotplate with continuous stirring until it became a thick paste. The drying was then completed by placing the sample in an oven at 120°C overnight, after which the sample was calcined in a furnace at 450°C for 5 hours. (For estimation of monolayer capacity, see Appendix III).

2.9 References

1. M. Komiyama, Catal. Rev. - Sci. Eng., 27(2), 341-372 (1985).

2. R. W. Maatman, Ind. Eng. Chem. 51, 913 (1959).

3. R. W. Maatman and C. D. Prater, ibid., 49, 253 (1957).

4. B. Delmon, P. A. Jacobs, and G. Poncelet (eds.) in "Preparation of Catalysts I", Elsevier, Amsterdam, 1976.

5. B. Delmon, P. Grange, P. Jacobs and G. Poncelet (eds.), in "Preparation of Catalysts II", Elsevier, Amsterdam, 1979.

6. G. Poncelet, P. Grange, and P. A. Jacobs (eds.), in "Preparation of Catalysts III", Elsevier, Amsterdam, 1983.

7. A. V. Neimark, L. I. Kheifets, and V. B. Fenelonov, Ind. Eng. Chem. Prod. Res. Dev., 20, 439 (1981).

8. E. R. Becker and J. Wei, J. Catal, 46, 365 (1977).

9. R. C. Vincent and R. P. Merrill, J. Catal., 35. 296 (1974).

10. G. K. Boreskov, in Ref. 4, p.223.

11. V. B. Fenelonov, A. V. Neimark, L.I. Kheifets, and A. A. Samakhov, in Ref. 5, p.223.

12. M. Komiyama, R. P. Merrill, and H. F. Harnsberger, J. Catal., 63, 35 (1980).

13. M. Komiyama and R. P. Merrill, Bull. Chem. Soc. Jpn., 57, 1169 (1984).

14. H. C. Chen and R. B. Anderson, J. Catal., 43, 200 (1976).

15. Y. S. Shyr and W. R. Ernst, ibid., 63, 425 (1980).

16. J. C. Summers and L. L. Hegedus, ibid., 51, 185 (1978).

17. F. Melo, J. Cervello, and E. Hermana, Chem. Eng. Sci., 35, 2175 (1980).

18. H. C. Chen, G. C. Gillies, and R. B. Anderson, J. Catal., 62, 367 (1980).

19. S. S. Kulkarni, G. R. Mauze and J. A. Schwarz, J. Catal., 69, 445 (1981).

20. S. Y. Lee and R. Aris, in Ref. 6, p.35.

21. L. L. Hegedus, T. S. Chou, J. C. Summers, and N. M. Potter, in Ref. 5, p. 171.

22. F. Melo, J. Cervello and E. Hermana, Chem. Eng. Sci., 35, 2165 (1980).

23. J. A. R. van Veen, H. de Wit, C. A. Emeis and P. A. J. M. Hendricks, J. Catal., 107, 579-582 (1987).

24. J. A. R. van Veen, F. T. G. Veltmaat, and G. Jonkers, J. Chem. Soc. Chem. Commun., 1656 (1985).

25. J. A. R. van Veen and P. A. J. M. Hendricks, Polyhedron vol. 5, No. 1/2, pp. 75-78, (1986).

26. K.-H. Tytko and O. Glemser, Adv. Inorg. Chem. Radiochem., 19, 239 (1976).

27. D. S. Honig and K. Kustin, Inorg. Chem., 11, 65 (1972).

28. J. W. Geus, in "Preparation of Catalysts III" (G. Poncelet, P. Grange, and P. A. Jacobs, eds.), Elsevier, Amsterdam, p.1 (1983).

CHAPTER 3. EXPERIMENTAL TECHNIQUES

3.1 Introduction

In this century catalysis has advanced from a laboratory curiosity to a major component of the chemical and petroleum industries. Catalysis will play an equally important role in new processes for producing alternative fluid fuels. The development of catalysis was initially a mysterious art requiring laborious empirical testing. These tests will probably always be a part of catalyst development, but the process can be performed expeditiously by utilizing the vast store of scientific and practical information currently available and by employing modern research tools. Concurrent with practical developments, new research tools were applied to the investigation of catalysts and catalytic reactions. Some of these new experimental procedures were developed especially for catalysis, and others were adapted from chemistry and physics. The improved research tools and the concepts resulting from their use have dispelled many of the mysterious aspects of catalysis: however, they have disclosed a host of new and challenging problems. Since the mid-1930s the experimental methods used in catalytic research have increased in number and complexity, so that mastery of all the techniques available is difficult.

3.2 Characterization methods

3.2.1 Chemical analysis

The Co and Mo contents of the catalysts are expressed as wt.% CoO and MoO_3 respectively. These were measured in our Department by Atomic Absorption Spectroscopy. Samples were dissolved in concentrated HCl and extracted in a solvent extraction apparatus for about 48 hours. The samples were analysed to an accuracy of $\pm$ 0.1%. The CoO - MoO_3 / TiO_2 samples were analysed by X-ray Fluorescence Spectroscopy at Tioxide International Ltd.

3.2.2 Laser Raman spectroscopy (LRS)

Laser Raman spectroscopy is a vibration-analysis technique, which gives information on the nature of the compounds present in a sample. The use of laser Raman spectroscopy in chemical applications has been reviewed (1-3). In the interpretation of the spectra, it should be kept in mind that not all vibrations of a molecule are Raman active: only when the polarizability of the molecule changes during a vibration is it Raman active, as mentioned in the previous chapter (Section 1.4.1).

The laser Raman spectra of the samples were recorded on a SPEX RAMALAB spectrometer using am EMI 9862B photomultiplier. The green (514.5nm) emission line from a Coherent Radiation model 52 M. G. Ar^+ laser was used for excitation. The output power of the laser was always about 100 mW and 60 mW at the sample. The spectral slit width was

6 cm^{-1} and the scanning speed was 50 cm^{-1} min^{-1}. A cylindrical lens was used just before the sample to image the laser beam as a line rather than a point and thus minimise any decomposition of the sample. Catalysts were ground into a very fine powder, pelletized and placed in the sample holder for analysis. The spectrometer was calibrated by reference to the known lines of CCl_4. The wave numbers obtained from the spectra are accurate to within about 2cm^{-1}.

3.2.2.1 Applications

In the present work, the laser Raman spectroscopy technique has been applied to the structure of the following catalysts and pure compounds.

(i) MoO_3/TiO_2 catalysts prepared by an impregnation method using ammonium heptamolybdate (AHM) as a precursor,

(ii) MoO_3/TiO_2 catalysts prepared by an impregnation method using molybdenum oxalate $H_2[MoO_3(C_2O_4.H_2O]$ as a precursor, and

(iii) unsupported MoO_3, and TiO_2 anatase (CLD 867) samples.

3.2.3 Temperature programmed reduction (TPR)

TPR measurements reported in the literature have been taken over a wide range of experimental conditions. It is vital if a meaningful comparison is to be made between different studies to be clear on the sensitivity of the results to the experimental conditions used.

In the case of heterogeneous catalysts, the compounds to be reduced are present on the surface or are potentially available to the surface. This method is a convenient tool to obtain "fingerprint" characterizations of the reducibility of catalysts, as mentioned in the previous chapter (Section 1.4.2).

3.2.3.1 Apparatus and experimental procedure

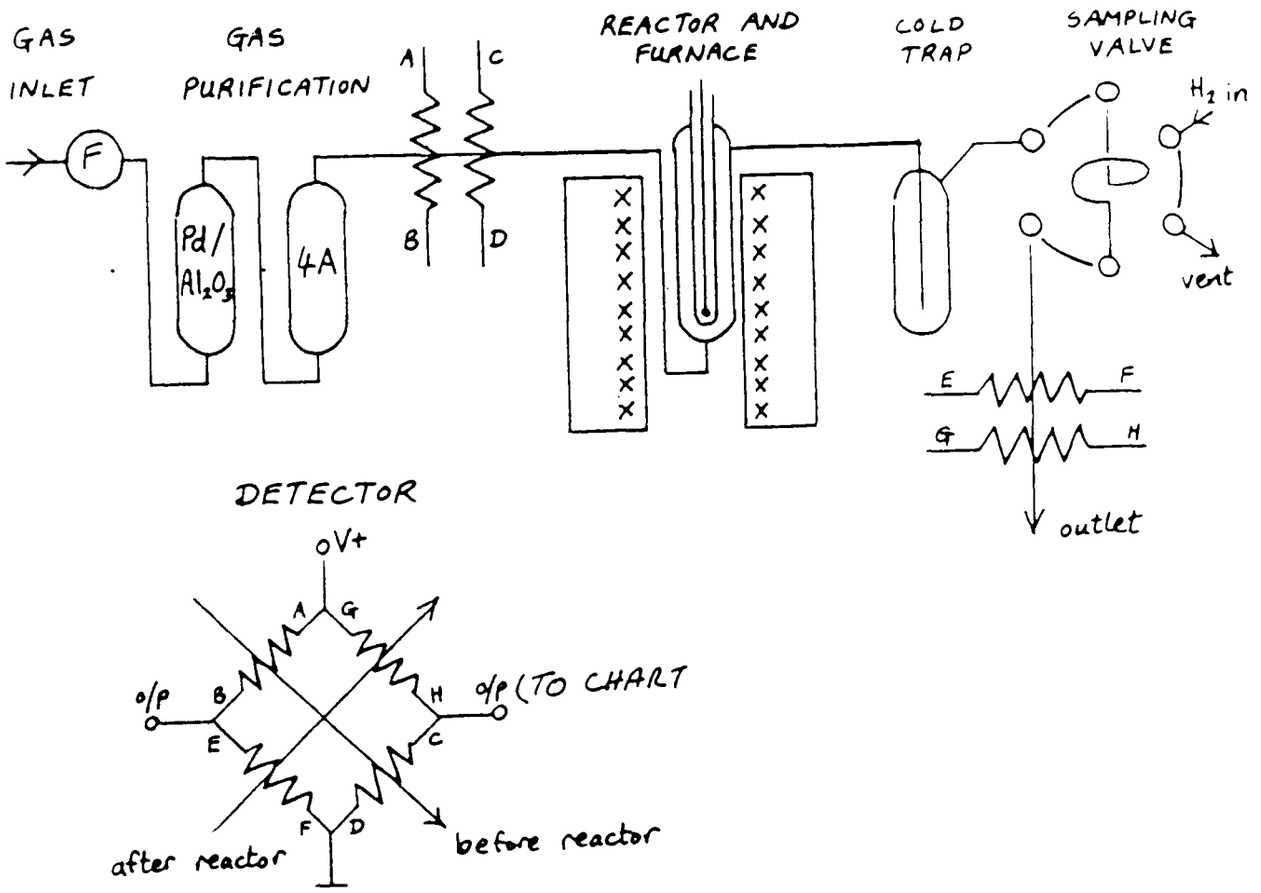

Fig 3.1 TPR Equipment

The TPR apparatus used in the present work is shown in Fig. 3.1. The catalyst samples contained in a quartz reactor (inner diameter 10 mm) was surrounded by a tubular electric furnace whose temperature was controlled by a linear temperature programmer (Stanton Redcroft model LVP).

The reducing gas, which is a mixture of 6% H_2/Ar, was passed over 0.5% Pd/Al_2O_3 catalyst (for deoxygenation) and also through a trap of molecular sieve type 4A for drying. The gas then flowed through the reference side of the thermal conductivity cell and then through the reactor to the cold trap kept at -78°C (to remove water and other reduction products that otherwise would interfere with the H_2 analysis). The gas then flowed to the sample side of the thermal conductivity cell.

The change in the concentration before and after the reactor was monitored by the thermal conductivity cell. When the concentration of H_2 in the gas stream remained constant, the response displayed on the recorder was the base line. Any change in H_2 concentration will cause the base line to shift, indicating the start of reduction, until a peak is reached and the base line returns to its normal position, showing that reduction is complete. The area under the peak represents the amount of H_2 needed for the reduction of the sample. The detector response is calibrated by injecting a known volume of pure H_2 into the system at the end of the experiment, using a gas sampling valve.

The amount of H_2 in cm^3 consumed for the reduction per gram of sample is calculated by the following equation:

$$cm^3\ H_2\ \text{consumed/g} = \frac{WPS \times L \times SS \times CC \times F}{WPC \times SC \times CS \times WS}$$

where: WPS = weight of area under sample peak;

WPC = weight of area under calibration peak;

SS = sensitivity used for the sample;

SC = sensitivity used for the calibration;

CS = chart speed used for the sample;

CC = chart speed used for calibration;

WS = weight of sample;

L = volume of H_2 injected (0.125 cm^3);

F = temperature correction factor converting volumes of gas from room temperature (298K) to STP (0.9381).

Small samples (5-990 mg) of catalysts were reduced in a 6% H_2/Ar mixture (flow rate 40 cm^3 min^{-1}). The temperature was raised from room temperature (298K) to 1273K at a constant heating rate of 5K min^{-1}.

3.2.3.2 Application

In the present work, the TPR technique was used to study oxidation state changes and to detect and identify different Co and Mo species for the following catalysts and pure compounds:

(i) MoO_3/TiO_2 catalysts prepared by an impregnation method using different precursors,

(ii) CoO/TiO_2 catalysts prepared by different methods and precursors,

(iii) $CoO-MoO_3/TiO_2$ catalysts prepared by an impregnation method,

(iv) unsupported MoO_3, CoO, Co_3O_4, $CoTiO_3$, $CoMoO_4$, TiO_2 anatase (CLD 867), and TiO_2 (P - 25).

3.2.4 X-ray photoelectron spectroscopy (XPS)

XPS studies have shown that TiO_2 can be clearly distinguished from TiO in the $Ti2p_{3/2}$ spectrum (4-6). TiN, a compound potentially formed within some high durability surfaces, can also be distinguished from TiO and TiO_2 on the basis of the $Ti2p_{3/2}$ chemical shift (5).

The Auger $L_3M_{23}V$ spectra of TiO and TiO_2 are shifted by 2eV, thus allowing their chemical identification by AES(7). Lineshape changes in this transition have been used to differentiate metallic titanium and TiH_2(8).

3.2.4.1 Referencing

A number of methods exist for referencing the binding energies of a photoemission spectrum. The first type of reference is an external standard. The most common external standard used is adventitious carbon; but, because the composition and electrical continuity between the carbon and the sample are not well known, this method of referencing can be somewhat unreliable. For example, the C1s line is very reliable on pure metals foils; however, when used on Al_2O_3 (as insulator) the C1s line has been observed to shift by 1eV to higher binding energies(9). Therefore, when this method is employed on catalysts, the measured binding energies that result may be lower than their true values. Therefore, some workers have tried using graphite mixed with their sample as a reference(10). Graphite is used because it is electrically conductive and the chemical structure is well known. However, mixing does not ensure sample reprodu-

cibility and electrical continuity. Other materials have also been used as mixing standards such as metal oxides and inorganic salts[11].

The second type of referencing is an internal standard method. An internal standard is a component of a sample that is chemically stable during experimentation and is chemically known. For example, the photoemission lines of supports in supported catalysts can sometimes be used as a reference, such as Al_2O_3, SiO_2, or TiO_2. In this case, the support and the promoter are in direct contact with each other. In our work the $Ti2p_{3/2}$ photoelectron line of the support (458.5 eV) served as the reference for catalyst samples on the grounds that most of this signal will originate from the Ti^{4+} ions within the bulk, and that many shifts due to modification of the surface layer will be minimal[12].

3.2.4.2 Calculation

In this work, the variation in the intensity of the Co or Mo signals relative to the Ti signal was determined as a function of Co or Mo content. The areas of the peaks of interest ($Co2p_{1/2}$, $Co2p_{3/2}$, $Mo3d_{3/2}$, $Mo3d_{5/2}$, $Ti2p_{1/2}$ and $Ti2p_{3/2}$) were measured. These areas were adjusted by photoelectron sensitivity factors (Co, 3.31; Mo, 3.73; Ti, 2.39)[13]. An example of this calculation can be seen in Fig. 3.2, for the MoO_3/TiO_2 catalysts.

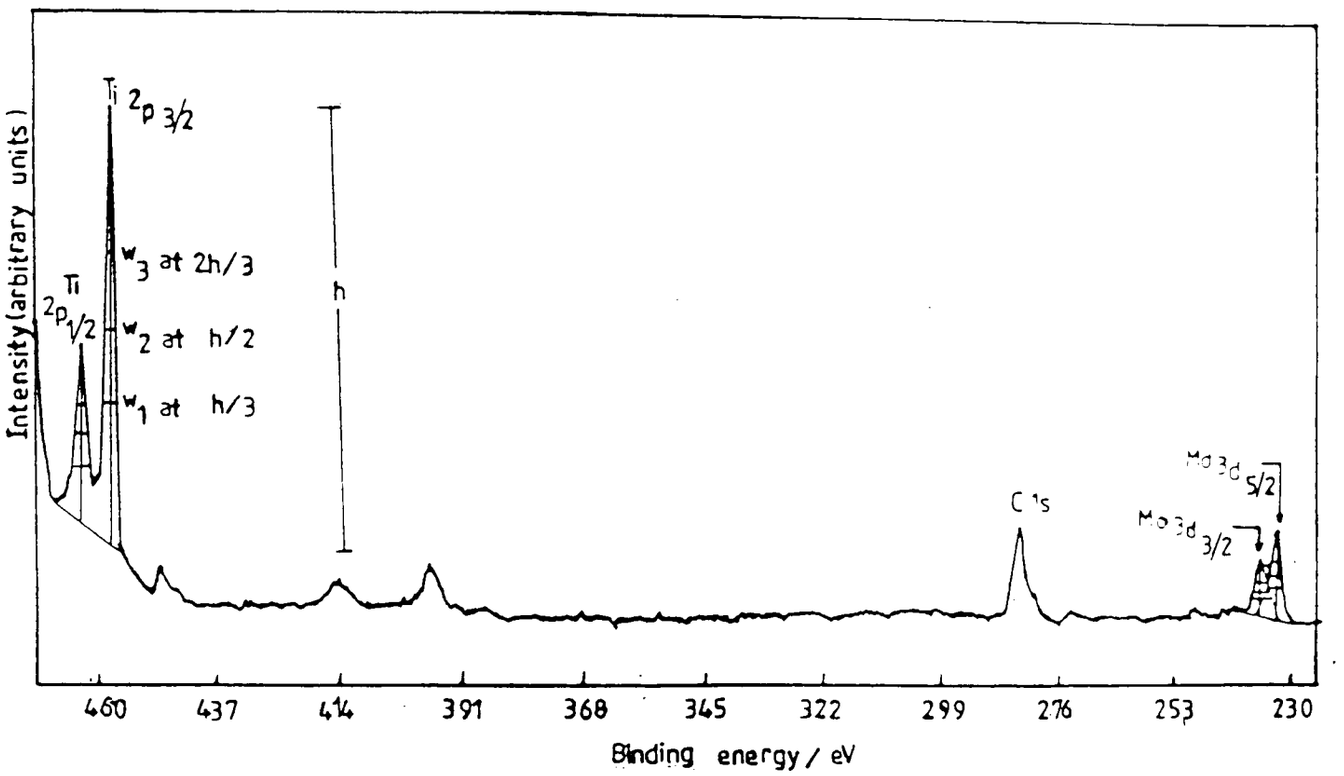

Fig.3.2 A typical XPS spectrum indicating the base lines used in estimating peak heights (1% MoO_3 on washed TiO_2 anatase CLD 867 prepared by an impregnation method).

The areas of the four peaks of interest ($Mo3d_{3/2}$, $Mo3d_{5/2}$, $Ti2p_{1/2}$ and $Ti2p_{3/2}$) were measured by triangulation, using the average of the widths at 1/3, 1/2 and 2/3 of full peak height. These areas were divided by sensitivity factors and the four intensity ratios calculated:

$R_1 = Mo3d_{3/2}/Ti2p_{1/2}$; $R_2 = Mo3d_{3/2}/Ti2p_{3/2}$;

$R_3 = Mo3d_{5/2}/Ti2p_{1/2}$; $R_4 = Mo3d_{5/2}/Ti2p_{3/2}$.

The ratios R_1 and R_2 are therefore generally less accurate than R_3 and R_4, and for this reason R_3 and R_4 only are used in this work. The value of R_4 has been scaled to that of R_3 at the highest Mo content measured, the adjusted R_4 values and the R_3 values were then averaged, it being assumed that R_3 and R_4 values are comparably accurate. In most cases the values of this mean ($R_{3,4}$) are reliable to

about ± 5%. Although the intensities of the two Mo peaks increase, and those of the two Ti peaks decrease, with increasing Mo content, it was impossible to obtain satisfactory reproducibility of absolute intensities from sample to sample, because the amount of sample exposed to the X-ray beam could not be controlled.

In the case of CoO/TiO_2 catalysts, four peaks are observed ($Co2p_{1/2}$, $Co2p_{3/2}$, $Ti2p_{1/2}$ and $Ti2p_{3/2}$). The peak intensity ratio of $Co2p_{3/2}/Ti2p_{3/2}$ was measured by triangulation. The ratios of the other peaks were less accurate.

In the case of $CoO\text{-}MoO_3/TiO_2$ catalysts, the same procedure for MoO_3/TiO_2 and CoO/TiO_2 systems was employed. The relative peak intensity ratio of $Mo3d_{5/2}/Ti2p_{3/2}$, and $Co2p_{3/2}/Ti2p_{3/2}$ was calculated by the triangulation method. The free mean path, i.e. escape depth, was calculated by using the following equation[14]:

$$(E_k) = 0.2\ E_k^{1/2}.tp$$

giving values of Co; 2.15nm, Mo; 2.63nm, and Ti; 2.10nm.

3.2.4.3 Application

In the present work, the XPS technique has been applied to the following catalysts and pure compounds, using a Kratos ES300 spectrometer and radiation source Al.K (1486.6eV):

(i) MoO_3/TiO_2 catalysts prepared by an impregnation method using different precursors,

(ii) CoO/TiO_2 catalysts prepared by different methods and different precursors,

(iii) $CoO-MoO_3/TiO_2$ catalysts prepared by an impregnation method,

(iv) unsupported MoO_3, CoO, Co_3O_4, $CoTiO_3$, $CoMoO_4$, and TiO_2 samples.

3.2.5 Transmission electron microscopy (TEM)

TEM studies of catalysts were carried out using a JEOL TEM 100C transmission electron microscope with a resolution better than 2.5Å.

The catalyst samples for the microscopic studies were ground using a mullite mortar and pestle and were ultrasonically dispersed in methanol. A drop of the suspension was then air dried on a carbon-coated copper grid. Electron micrographs were made to determine the particle size of Co and Mo in CoO/TiO_2 and MoO_3/TiO_2 systems, respectively. The magnification was calibrated using:
(1 cm → 10K → 1um).

3.2.5.1 Application

In the present study, the TEM technique has been applied to the following catalysts:

(i) MoO_3/TiO_2 catalysts prepared by an impregnation method using different precursors,

(ii) CoO/TiO_2 catalysts prepared by different methods and different precursors.

3.3 Catalytic activity measurements

3.3.1 Decomposition of 2-propanol

The catalytic decomposition of 2-propanol was used as a model reaction for the determination of activity and selectivity of MoO_3/TiO_2, CoO/TiO_2, and $CoO-MoO_3/TiO_2$ systems. The 2-propanol dehydrogenation product (acetone) was also analyzed. Acetone and propene were the only products, no side reactions were observed. The same reaction was run over unsupported MoO_3, CoO, $CoTiO_3$, $CoMoO_4$, TiO_2 anatase (CLD 867) and TiO_2 (P-25).

3.3.2 Apparatus

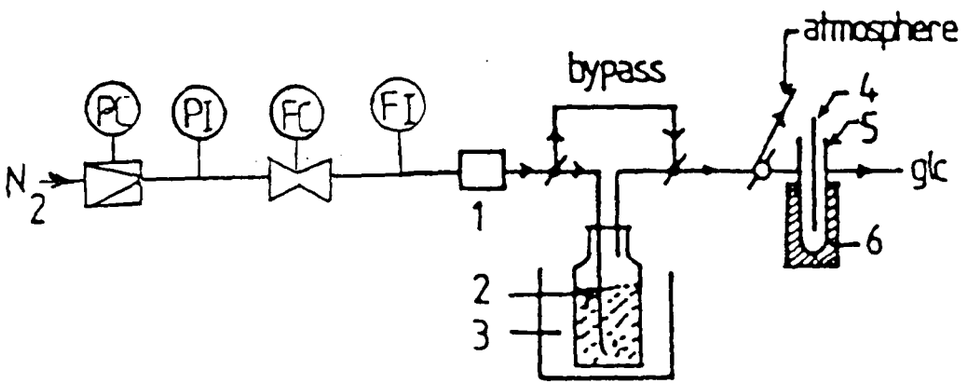

Fig.3.3 Flow diagram of apparatus for 2-propanol decomposition. 1. tube with molecular sieve; 2. saturator filled with 2-propanol; 3. thermostat; 4. thermocouple; 5. reactor; 6. furnace.

The apparatus is outlined in Fig. 3.3. The reaction was carried out in a conventional flow apparatus at atmospheric pressure. The experiments were performed with a mixture containing about 1.08 mol% 2-propanol in N_2 made by passing N_2 through the saturator filled with 2-propanol at

273K. The N_2 gas was dried with molecular sieve (type 4A). The dried gas was then passed through a pressure controller (PC), then a pressure indicator (PI), followed by a flow controller (FC) and flow indicator (FI) before entering the saturator. The reactor was a glass U-tube (1 cm inner diameter and about 16.5 cm long) and in one arm was a quartz sintered disc supporting the catalyst bed. The reactor temperature was controlled by a Chromel-Alumel thermocouple (located with its tip in the catalyst bed) connected to a temperature controller. The analysis of all the products was performed by a Perkin-Elmer 8410 model with a chart recorder connected (model Nippon R50). The gas chromatograph has a flame ionization detector and the carrier gas was N_2 with flow rate 25 ml/min. Propene, acetone, and unreacted 2-propanol were separated on a stainless steel column packed with Porapak T (6ft x 2mm, mesh size 80/100), pretreated at 175°C.

3.3.3 Experimental procedure

0.1g of catalyst was placed on the quartz sinter in the U-tube. The temperature was raised to 373K. With the gaseous mixture flowing over the catalyst, the sample was stabilized for 2h before measurements were started. The activity of the catalyst was measured and the temperature was then changed and the above procedure repeated.

3.3.4 Calculation

$$\% \text{ conversion} = \frac{100A}{A + N_2\text{-propanol}}$$

where A = No. of moles of 2-propanol transformed to produce propene + acetone

$$= N_{prop.} + N_{acet.}$$

$$\text{Selectivity } (S_i) = \frac{N_i}{A}$$

where N_i = No. of moles of component i

A = as above

$$\text{Rate} = \frac{\%C}{100} \times F \times \frac{60}{22414} \times \frac{1}{wt.}$$

F = Flow rate of 2-propanol (100 ml/min)

wt. = weight of catalyst

where rate (r) is expressed in $mmol.h^{-1}.g_{cat}^{-1}$.

% conversion for 2-propanol and % selectivities for propene and acetone formation were calculated. The apparent activation energies of the catalysts for 2-propanol removal, and for propene and acetone formation, were also calculated for the temperature range (373-473K) and (473-573K).

3.3.5 Application

In the present work, the 2-propanol decomposition has been used for the following catalysts and pure compounds:

(i) MoO_3/TiO_2 catalysts, prepared by an impregnation method using different precursors,

(ii) CoO/TiO_2 catalysts prepared by different methods and precursors,

(iii) $CoO-MoO_3/TiO_2$ catalysts prepared by an impregnation method, and

(iv) unsupported MoO_3, CoO, $CoTiO_3$, $CoMoO_4$, TiO_2 anatase (CLD 867) and TiO_2 (P-25).

3.4 Chemicals used

For operating the TPR apparatus and the G.C., cylinders of $6\%H_2/Ar$ mixture, air, H_2 and N_2 were supplied by the British Oxygen Company.

Propene was supplied by Cambrian Gases Ltd. 2-propanol and acetone were obtained from Fisons Products (Laboratory reagent grade).

3.5 References

1. J. Loader, "Basic laser Raman spectroscopy", Heyden-Sadtler (1970).

2. T. T. Nguyen, J. Singapore National Acad. Sci., 10-12, 84 (1983).

3. P. P. Shorygin, Russ. Chem. Rev., 47, 907 (1978).

4. C. D. Wagner, W. M. Riggs, L. E. Davis, J. F. Moulder and G. E. Muilenberg, "Handbook of X-ray Photoelectron Spectroscopy", Physical Electronics Division, Perkin-Elmer Corporation, Eden Prairie, Minnesota (1979).

5. L. Ramqvist, K. Hamrin, G. Johansson, A. Fahlmann and C. Nordling, J. Phys. Chem. Solids, 30, 1935 (1969).

6. J. F. Fransen, M. X. Umana, J. R. McCreary and R. J. Thorn, J. Solid State Chem., 18, 363 (1976).

7. J. S. Solomon and W. L. Baun, Surf. Sci., 51, 228 (1985).

8. M. L. Knotek and J. Houston, Phys. Rev., R15, 4580 (1977).

9. G. Johansson, J. Hedman, A. Berndtsson, M. Klasson and R. Nilsson, J. Electron Spectr., 2, 295-317 (1973).

10. K. S. Kim, N. Winograd, and R. E. Davis, J. Amer. Chem. Soc., 93, 6296 (1971).

11. W. Bremser and F. Linneman, Chem. Ztg., 95, 1011 (1971).

12. J. Mendialdua, PhD Thesis, University of Science and Technology of Lille, France (1983).

13. Theoretical photoionization cross sections from 1 to 1500 eV. J. H. Scofield (Lawrence Livermore Lab., Univ. of California), 376 (1973).

14. C. C. Chang, Surf. Sci., 48, 9 (1975).

Chapter 4 RESULTS

4.1 Introduction

There are many reasons for catalyst characterization. Two illustrations will suffice. At one extreme, characterization can be a matter of commercial necessity: a catalyst manufacturer needs to demonstrate that his product meets a given set of specifications. At another extreme, characterization is an integral part of any worth-while catalytic research and development programme.

The characterization of a catalyst provides information on three distinct but related areas. These are: chemical composition and chemical structure, texture and mechanical properties, and catalytic activity.

By chemical composition and chemical structure, we refer to matters such as: elemental composition; the composition, structure, and proportions of individual phases which may be present: surface composition; the nature and proportions of functional groups which may be present on the surface[1].

The texture of a catalyst refers to its geometric structure and morphology, ranging from the grossest macroscale down to the finest microscale. This deals with, for instance, size and shape of individual catalyst units (for example, individual particles, pellets); pore structure; total surface area; the way in which individual phases are

arranged relative to one another. The mechanical properties refer to those which are important to the integrity of the catalyst in an industrial application. This refers to matters such as abrasion or attrition resistance, strength, and thermal shock resistance.

The characterization of a catalyst in terms of its activity is obviously a quantitative measure of the ability of a catalyst to carry out a particular chemical transformation under specified conditions. Basically this will specify a quantity such as speed of reaction, or some quantity related to speed of reaction, per unit quantity of catalyst. Bearing in mind that many catalytic reactions are not specific for the formation of a particular product, the specification of activity must also include product selectivity.

Ideally a catalyst would be characterized in terms of activity under exactly the same conditions as those under which it will be used in practice. This will often not be possible because the ultimate use may be in a very large-scale reactor, whereas for reasons of economy and convenience it is highly desirable, indeed often mandatory, that activity assessment be made on a small scale under reaction conditions that differ from those used on the large scale. It will often not be possible to estimate accurately large-scale behaviour from activity assessments made on a small scale, unless recourse is made to empirical correlations between results obtained in the two regimes. In any case, in assessing catalytic activity it is essential that the

catalytic reactor be understood, so that the significance of the results obtained with it can be properly gauged.

Under reaction conditions all catalysts suffer from progressive deactivation to some extent at least. In practice, deactivation limits the lifetime of the catalyst, and the effective lifetime is a parameter of considerable economic significance. In general, deactivation results either from a change in the chemical composition of the catalyst resulting from the addition or removal of matter, from a change in the texture and structure of the catalyst, or from a combination of these factors. If the reasons for deactivation are understood it may be possible to devise regeneration procedures, although in many cases this may not be possible, or be possible to only a limited extent. It will be clear that any study of deactivation and regeneration necessarily involves a study of the same characterization parameters as are used with a pristine catalyst.

In principle, an account of methods for catalyst characterization has a vast range of scientific and technical techniques to draw upon. It is possible to make the case that virtually every technique known to materials science is of some potential value, and in addition there are many types of measurement which are peculiar to catalytic science. Nevertheless, experience has shown that out of this vast range, a relatively restricted number of techniques and types of measurement are of dominant importance.

4.1.1 Laser Raman spectroscopy

4.1.1.1 MoO_3/TiO_2 catalysts

Structural characterization of the supported molybdate species was carried out by Raman spectroscopy. For comparison, Fig. 4.1 shows Raman spectra for the MT/C series prepared by impregnation using ammonium heptamolybdate (AHM) as a precursor, whereas Fig. 4.2 shows Raman spectra for the MOT/C series prepared by impregnation using molybdenum oxalate as precursor. The TiO_2 anatase gives a number of relatively intense bands (640, 558 and 399 cm^{-1}), Bands at 995, 821 and 668 cm^{-1} in pure MoO_3 were readily detectable (2).

With the supported MoO_3 catalysts, however, no significant bands were observed due to MoO_x species at MoO_3 contents of 1% or below in both series. The anatase phase of the TiO_2 support has a weak second-order feature at 795 cm^{-1}(2).

At 2wt.% MoO_3 catalyst, there is a small band at 980 cm^{-1} and a shoulder on the low-frequency side at 970 cm^{-1}. At 3wt.% MoO_3, the intensity of the band at 980 cm^{-1} has increased, and the shoulder at 970 cm^{-1} remains constant, while a band at 820 cm^{-1} and a shoulder at 995 cm^{-1} appear (due to crystalline MoO_3). Above 2wt.% MoO_3, the intensity of the bands at 820,980 and 995 cm^{-1} increase in both series, while at 4wt.% MoO_3 the band at 995 cm^{-1} has increased at the expense of the band at 980cm^{-1} (Figs. 4.1 and 4.2).

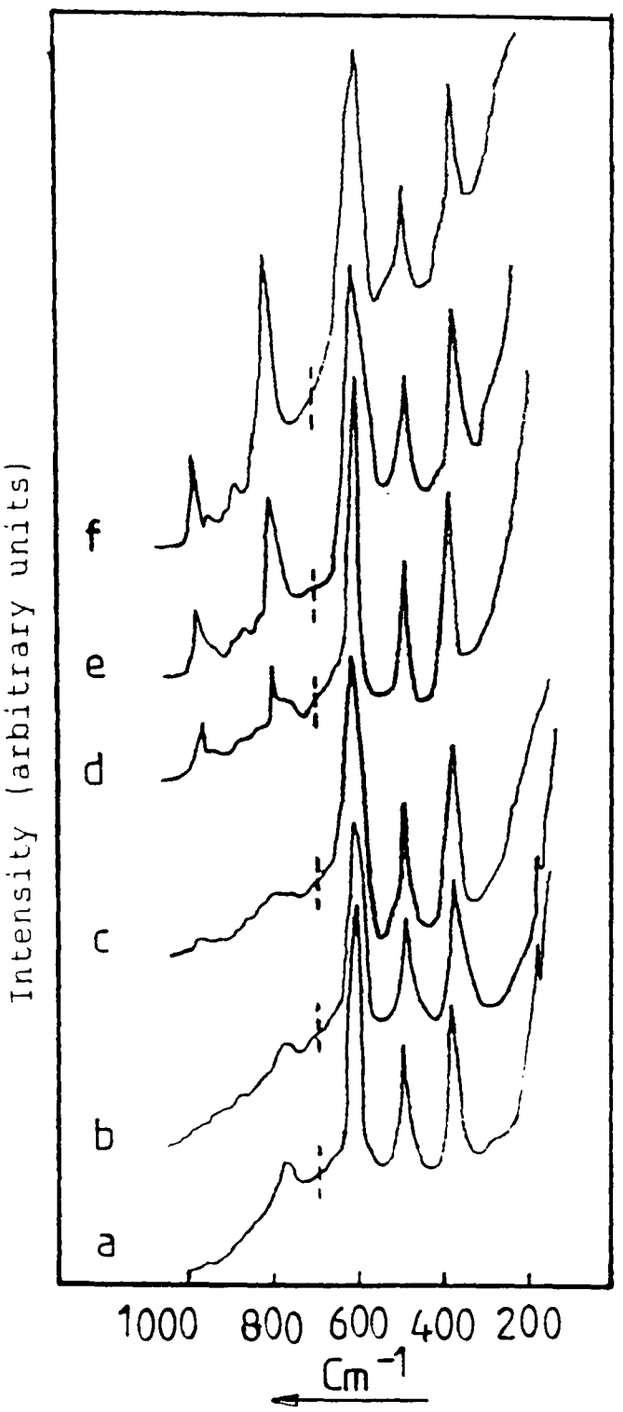

Fig. 4.1 Raman spectra of pure TiO_2 and MoO_3/TiO_2 series prepared from AHM precursor as a function of Mo content, whereas a, for pure TiO_2, b, c, d, e, and f for .5%, 1%, 2%, 3% and 4%, respectively.

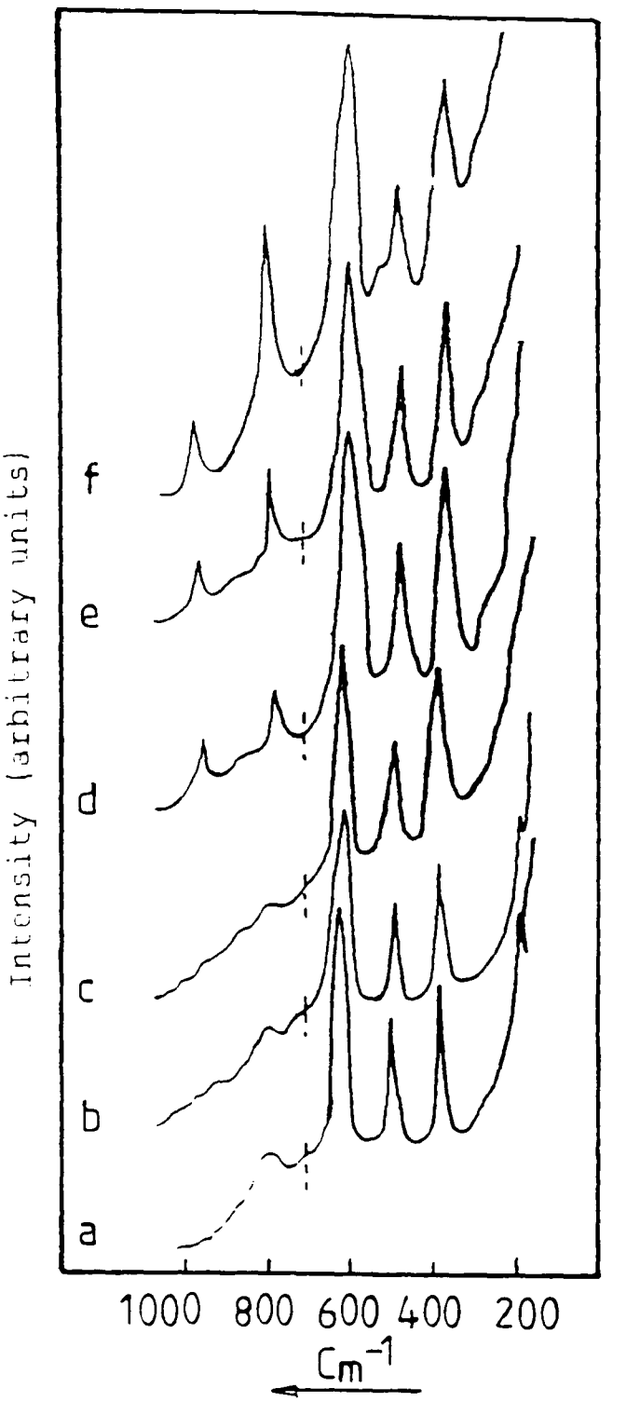

Fig. 4.2 Raman spectra of pure TiO_2 and MoO_2/TiO_2 catalysts prepared from molybdenum oxalate precursor as a function of Mo content, whereas a for pure TiO_2, b, c, d, e, and f are .5%, 1%, 2%, 3% and 4% loadings, respectively.

The intensity of the band of the support at 640 cm^{-1} decreases with increasing Mo content due to the change in the colour of the catalyst from white to creamish in both series, as shown in Figs. 4.3 and 4.4. Below the 1 wt. % MoO_3, no bands of 820 and 995 cm^{-1} were observed in both MT/C and MOT/C series. At 2 wt. % MoO_3, the 820 and 995 cm^{-1} increases in both series. In 3-4 wt. % MoO_3, the 820 cm^{-1} band intensity remains constant, while the 995 cm^{-1} intensity keeps increasing in both MT/C and MOT/C series. This implies that bands due to particulate MoO_3 are about twice as intense with MT/C series as with MOT/C series. This indicates that the former has more crystalline MoO_3 than the latter.

4.1.2 Temperature-programmed reduction (TPR)

4.1.2.1 MoO_3/TiO_2 catalysts

TPR profiles for the MoO_3/TiO_2 series prepared by impregnation using ammonium heptamolybdate (AHM) as precursor, i.e. MT/C, and for the MoO_3/TiO_2 series prepared by impregnation using molybdenum oxalate, i.e. MOT/C, which indicate the H_2 consumption, are shown in Figs. 4.5 and 4.6, respectively. They include samples of pure MoO_3 and TiO_2 anatase (CLD 867).

Generally all the samples in both series start to reduce at a temperature below that at which the reduction of pure MoO_3 starts. In Fig. 4.5 four peaks are observed with 0.5 wt % and 1 wt. % MoO_3, with T_{max} values of 390°C, 580°C, 740°C and a peak or shoulder at 840°C. At 2 wt. %

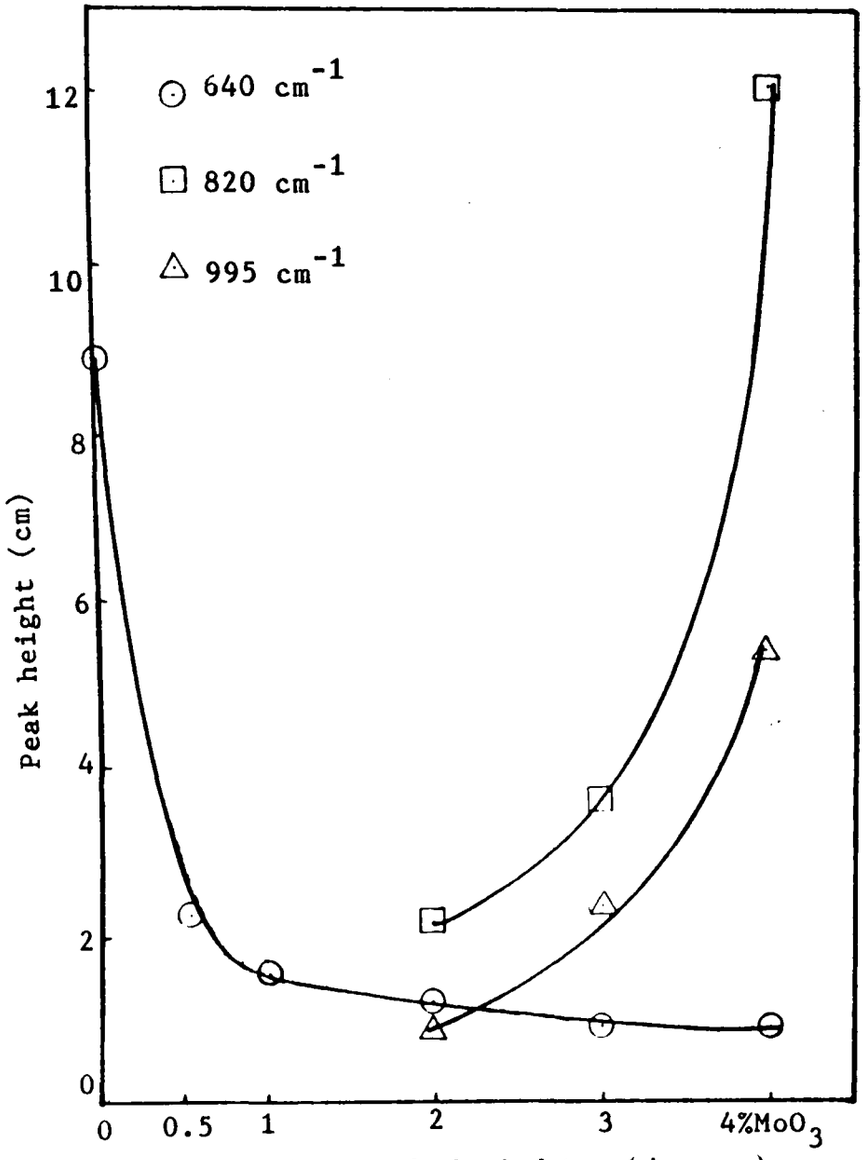

Fig. 4.3 Variation in peak heights (in cm) of 820, 995 cm^{-1} bands (O-Mo-O, M=O), and 640 cm^{-1} (anatase) band with Mo content for the MT/C series.

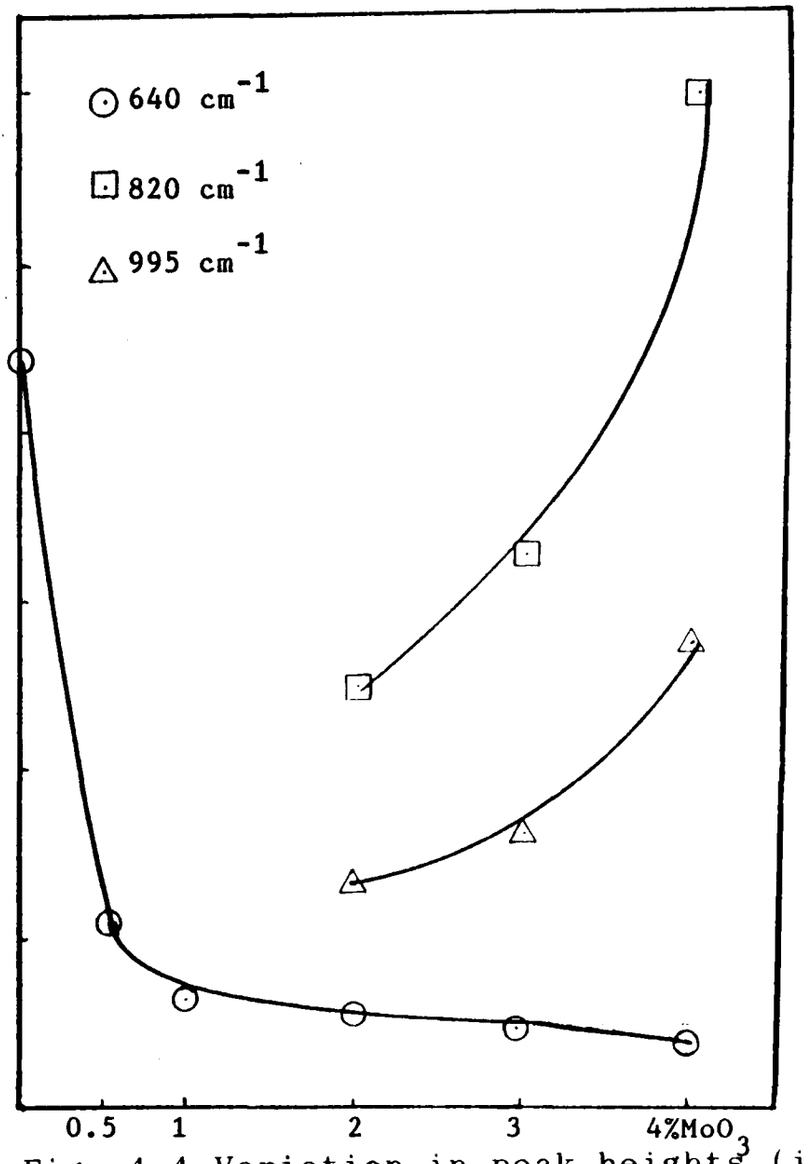

Fig. 4.4 Variation in peak heights (in cm) of 820, 995 cm^{-1} bands, (O-Mo-O, M=O) and 640 cm^{-1} (anatase) band with Mo content for the MOT/C series.

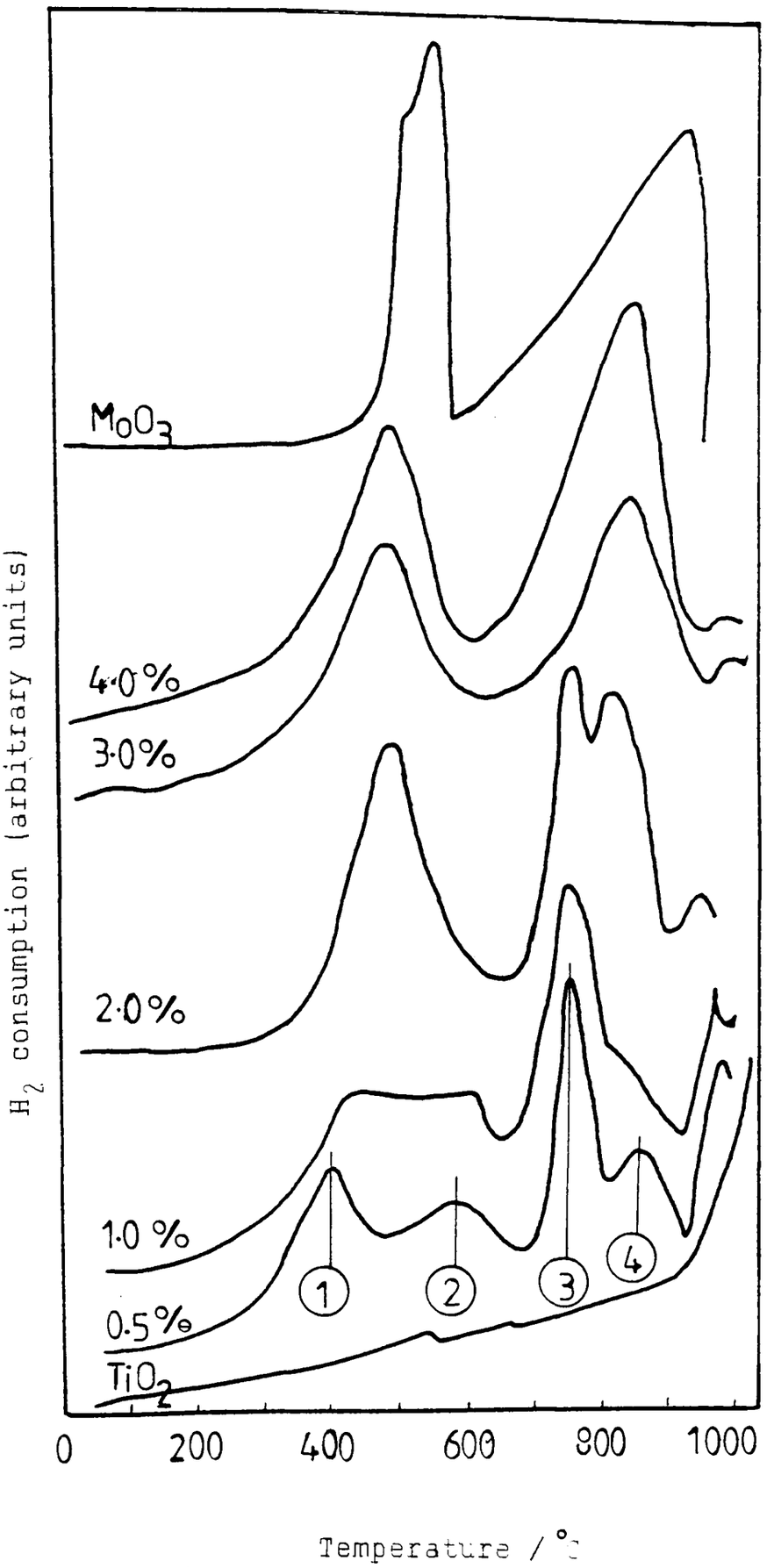

Fig. 4.5 TPR patterns of pure MoO_3, the support (anatase) TiO_2 CLD 867, and MoO_x/TiO_2 catalysts prepared by impregnation using ammonium heptamolybdate as precursor. (MT/C series).

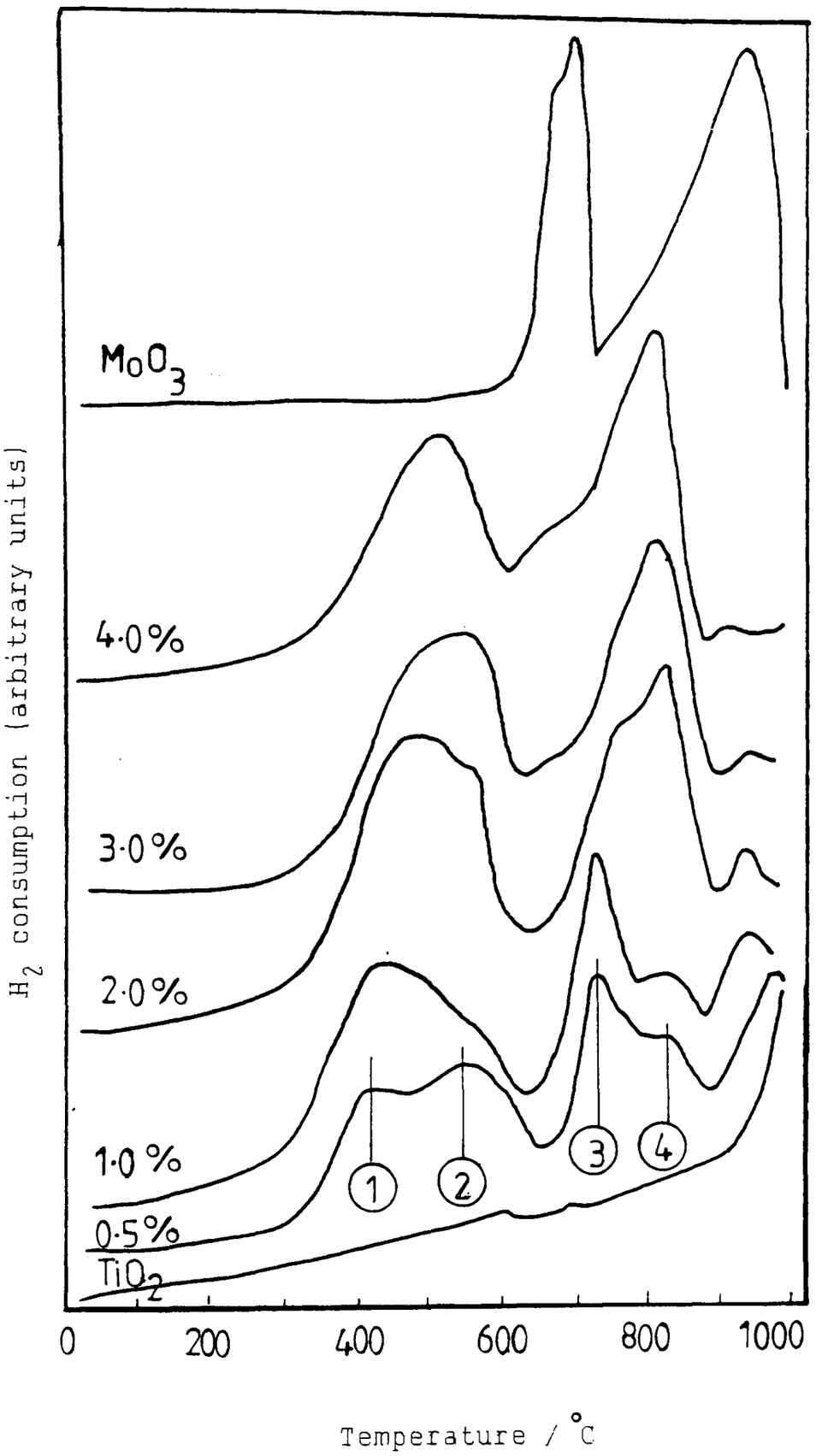

Fig. 4.6 TPR patterns of pure MoO_3, the support (anatase), TiO_2 CLD 867, and the MoO_x/TiO_2 catalysts prepared by impregnation using molybdenum oxalate as precursor. (MOT/C series).

MoO_3 peaks are observed with T_{max} values of 490°C, 760°C and 825°C. Above 2 wt. % MoO_3, there are only two main peaks with T_{max} values of 500°C and 840°C, close to the T_{max} of pure MoO_3 which has peaks at 580°C and 920°C. In Fig. 4.6 similar TPR profiles are found with approximately the same kind of T_{max} variations (see Fig. 4.8). Tables 4.1 and 4.2 give the values of T_{max} for the MT/C and MOT/C series, respectively.

Table 4.1 T_{max} in °C for MT/C series

Sample	1st peak	2nd peak	3rd peak	4th peak
0.5%MT/C	390	580	740	840
1%MT/C	410	580	740	840
2%MT/C	490	-	760	825
3%MT/C	500	-	-	800
4%MT/C	485	-	-	780

Table 4.2 T_{max} in °C for MOT/C series

Sample	1st peak	2nd peak	3rd peak	4th peak
0.5%MOT/C	420	540	740	840
1%MOT/C	440	560	710	810
2%MOT/C	480	540	750	820
3%MOT/C	480	540	-	830
4%MOT/C	510	-	-	810

Figs. 4.7 and 4.8 show T_{max} values as a function of MoO_3 content. In each series there are clearly two species, each being reduced in two steps: species I is responsible for the peaks at $\sim$ 400-480 and $\sim$ 700-750°C, and species II for the peaks at $\sim$ 500-580 and 800-850°C. The differences between the median temperatures (i.e. 440 to 725, 540 to 825°C) is the same for both series, suggesting that peaks 1 and 3 are due to the first stages of reduction and peaks 2 and 4 to the second stages. By reference to unsupported MoO_3, it would be logical to associate the two stages with Mo^{VI} to Mo^{IV}, and Mo^{IV} to Mo^{O}, but, while accurate deconvolution is impossible, the areas under the relevant pairs of peaks do not appear to conform to this suggestion, as they seem to be almost equal in size. However, quite clearly it is species II that grows at the expense of I, so that at high MoO_3 contents only the latter is detectable. Species I is therefore likely to be the MoO_x monolayer species, and II the particulate MoO_3. The lack of substantial variation of T_{max} for peaks 2 and 4, especially clear in Fig. 4.8, supports this assignment.

Tables 4.3 and 4.4 give the total H_2 uptakes for the MT/C and MOT/C, respectively; whereas Fig. 4.9 and 4.10 show the variation in the H_2 consumptions as a function of MoO_3 content for the previous series. The observed curves approach the theoretical H_2 uptakes at high Mo contents because MoO_3 particulates can be reduced to Mo^{o} but monolayer species apparently cannot.

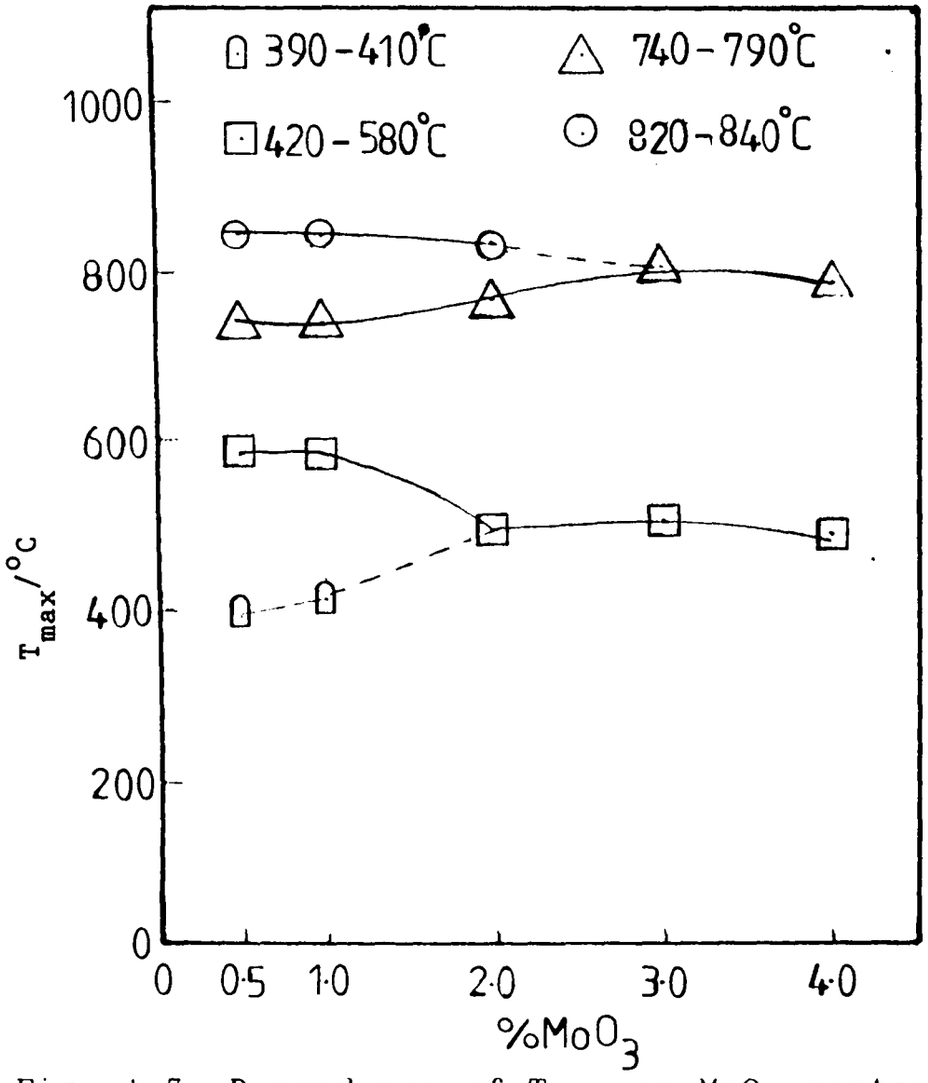

Fig. 4.7 Dependence of T_{max} on MoO_3 content for the MT/C series.

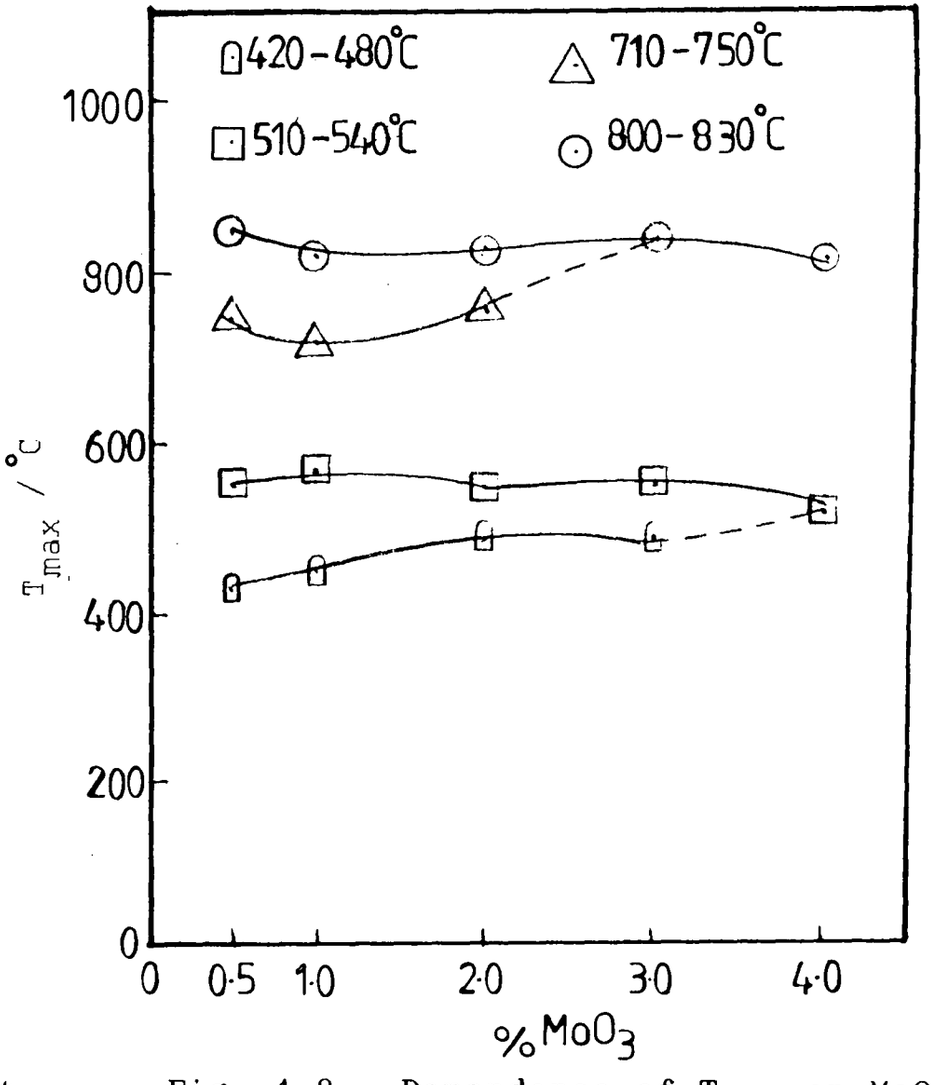

Fig. 4.8 Dependence of T_{max} on MoO_3 content for the MOT/C series.

Table 4.3 H_2 uptakes in mol/g for the MoO_x/TiO_2 catalysts prepared by impregnation using (AHM) as precursor (MT/C series).

sample	Chemical analysis(a)	theoretical H_2 uptake mol/g	by computer mol/g	cutting & weighing mol/g	% reduction based on computer values
0.5%MT/C	0.4%	1.04×10^{-4}	1.18×10^{-4}	0.85×10^{-4}	113%
1%MT/C	0.9%	2.10×10^{-4}	1.62×10^{-4}	1.70×10^{-4}	77.1%
2%MT/C	1.7%	4.20×10^{-4}	3.87×10^{-4}	3.14×10^{-4}	92.1%
3%MT/C	2.6%	6.30×10^{-4}	4.27×10^{-4}	4.55×10^{-4}	68.3%
4%MT/C	3.5%	8.40×10^{-4}	8.24×10^{-4}	7.56×10^{-4}	98.1%

(a) by atomic absorption spectroscopy

Table 4.4 H_2 uptakes in mol/g for the MOT/C series

sample	Chemical analysis(a)	theoretical H_2 uptake mol/g	by computer mol/g	cutting & weighing mol/g	%reduction based on computer values
0.5%MOT/C	0.41%	1.04×10^{-4}	7.37×10^{-5}	8.89×10^{-5}	70.8%
1%MOT/C	0.95%	2.10×10^{-4}	1.50×10^{-4}	2.10×10^{-4}	71.4%
2%MOT/C	1.85%	4.20×10^{-4}	3.92×10^{-4}	3.15×10^{-4}	93.3%
3%MOT/C	2.79%	6.30×10^{-4}	5.0×10^{-4}	5.63×10^{-4}	79.4%
4%MOT/C	3.63%	8.40×10^{-4}	7.10×10^{-4}	7.22×10^{-4}	84.5%

(a) by atomic absorption spectroscopy

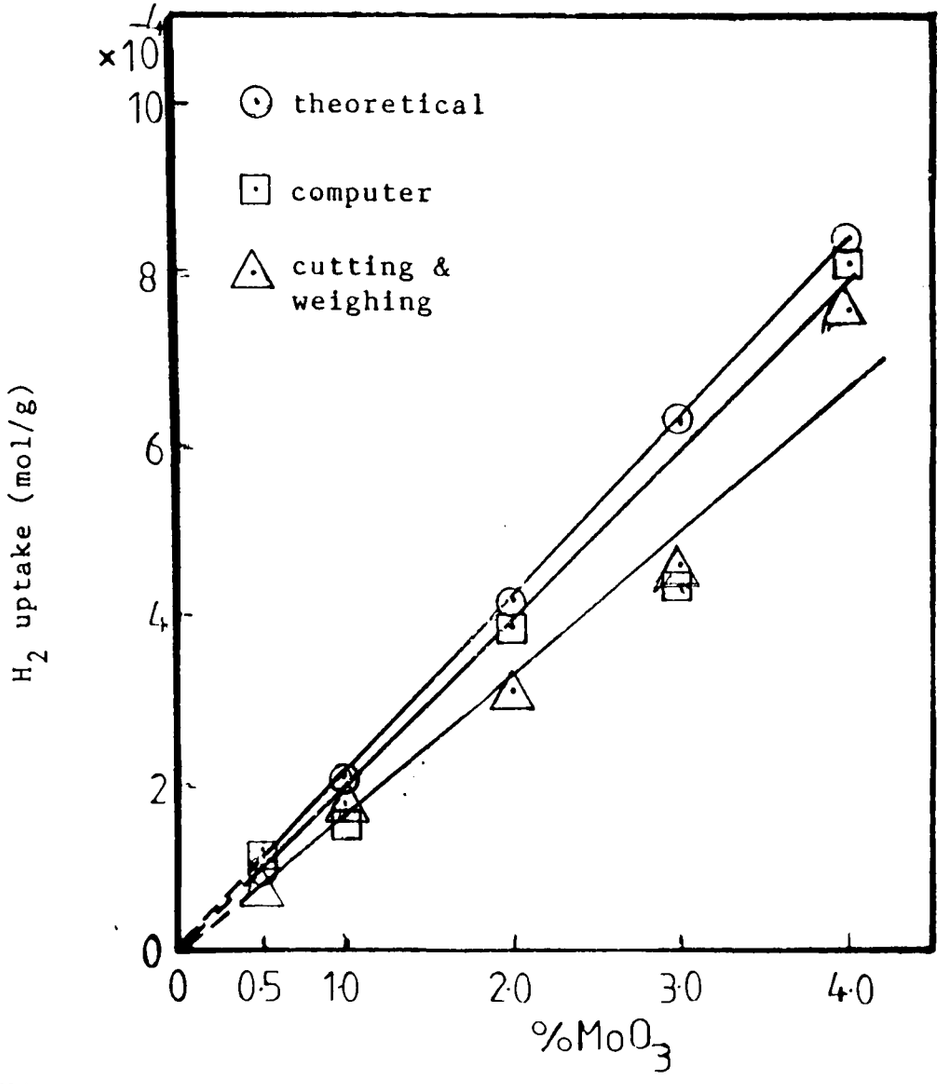

Fig. 4.9 Variation of total H_2 uptake with MoO_3 content for the MT/C series.

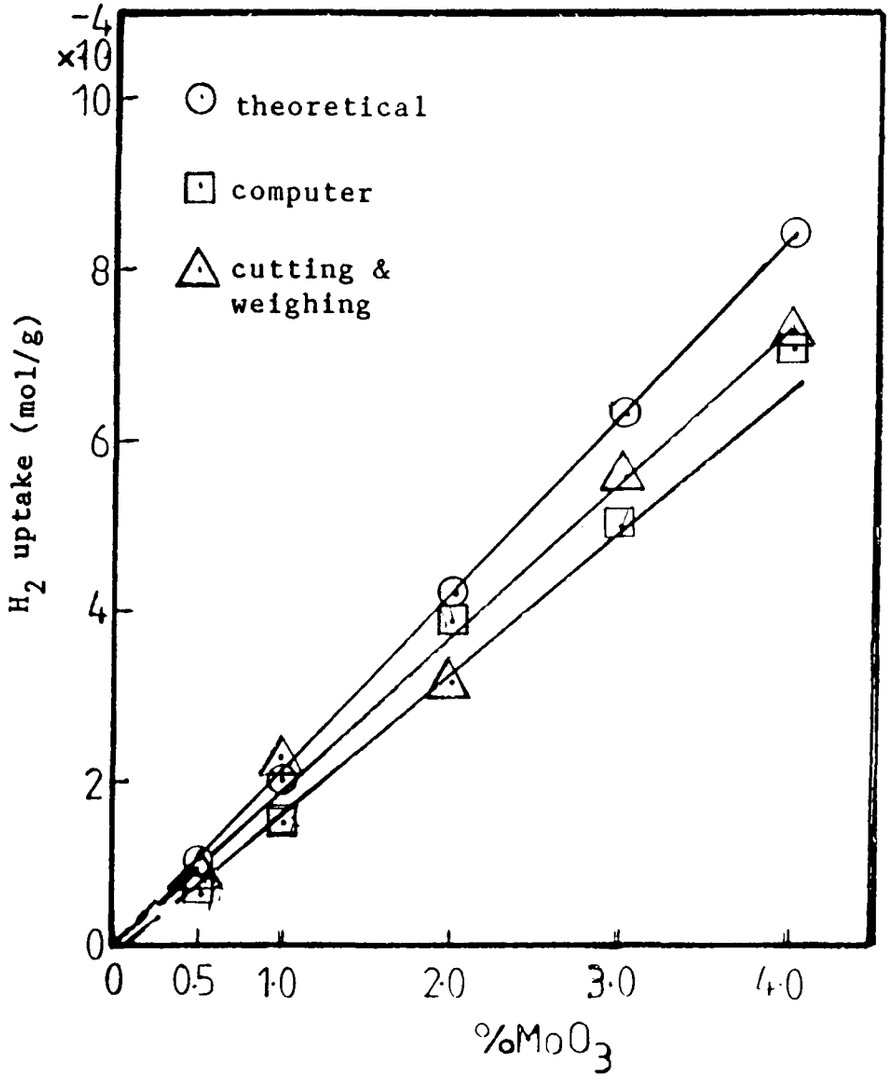

Fig. 4.10 Variation of total H_2 uptake with MoO_3 content for the MOT/C series.

4.1.2.2 CoO_x/TiO_2 catalysts

Three series of the CoO_x/TiO_2 catalysts were prepared by impregnation using cobalt nitrate as precursor, i.e. CT/C and cobalt acetate, i.e. CAT/C and by homogeneous precipitation, i.e. CT/HP. (see Sections 2.7.1 - 2.7.3).

Fig. 4.11 shows the TPR profiles for the CoO_x/TiO_2, i.e. CT/T series and Table 4.5 contains the T_{max} values. These are plotted against Co content in Fig. 4.12. Unsupported CoO reduces in one single step from Co^{2+} to Co^{o}. Co_3O_4 starts to reduce before CoO in two steps; Co^{3+} to Co^{2+} and then Co^{2+} to Co^{o} with a peak area ratio of 1:3. Two peaks, or more generally a peak and a shoulder are observed at all Co concentrations, their T_{max} values being almost constant for Co contents above 2.4 wt.%. However, although that having the higher T_{max} is usually the smaller, so it is more likely we are seeing two different CoO_x species that exist in roughly comparable concentrations than a two-stage reduction of a single species. For the supported samples, the two peaks are of similar size, suggesting that Co^{2+} and Co^{3+} are present in comparable amounts. This justifies the basis of theoretical calculation of total H_2 consumption.

Table 4.6 gives the values of total H_2 uptake theoretically, by computer, and by cutting and weighing. Fig. 4.13 shows the variation in total H_2 consumption as a function of Co concentration for the CT/C series.

The extent of reduction in Table 4.6 tells us that the reduction of Co^{3+} and Co^{2+} to Co^{o} is complete and independent of Co concentration.

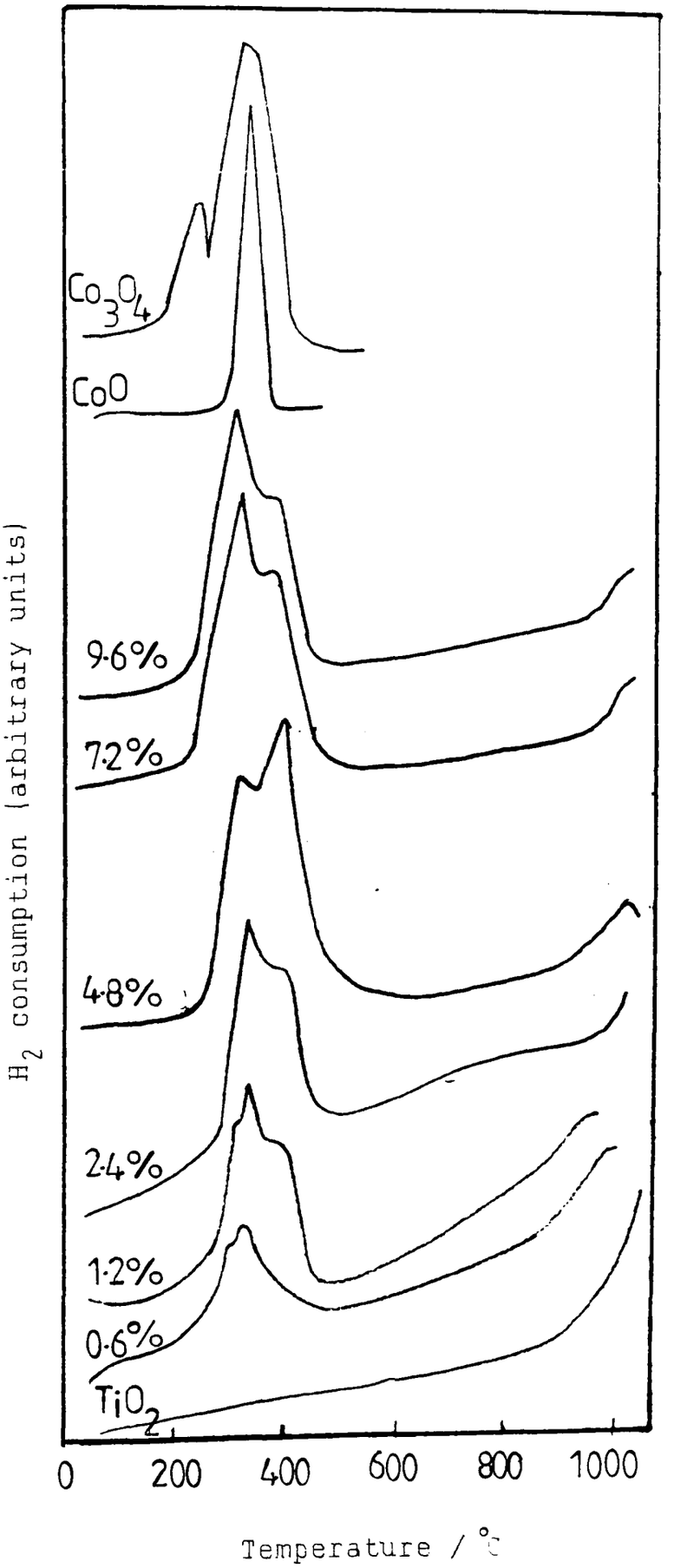

Fig. 4.11 TPR profiles of the CoO/TiO_2 catalysts prepared by impregnation using cobalt nitrate as precursor (CT/C series).

Table 4.5 T_{max} values for the CoO_x/TiO_2 series prepared by impregnation using $Co(NO_3)_2.6H_2O$ (CT/C series).

Sample	$T_{max}/^oC$	
	1st peak	2nd peak
CoO	370	-
Co_3O_4	250	340
0.6%CT/C	340	-
1.2%CT/C	340	405
2.4%CT/C	370	410
4.8%CT/C	370	415
7.2%CT/C	370	420
9.6%CT/C	370	420

Fig. 4.14 shows TPR profiles for the CoO_x/TiO_2 catalysts (CT/HP series). Two main peaks are formed up to 4.8 wt.% CoO_x with T_{max} values $\sim$ 510-550°C for the first peak and $\sim$ 680-760°C for the second peak. Above 4.8 wt.% CoO_x catalyst, two more peaks are found at lower temperatures with T_{max} occurring at 340°C and 360°C for both 7.2 wt.% and 9.6 wt.% Co concentrations. Table 4.7 gives the T_{max} values as a function of Co concentration, while the variation in T_{max} with Co content is shown in Fig. 4.15. By comparing T_{max} values of the unsupported CoO, Co_3O_4 and $CoTiO_3$ with all the T_{max} of all the catalysts, the attribution of the peaks remains very ambiguous. It could be that because these

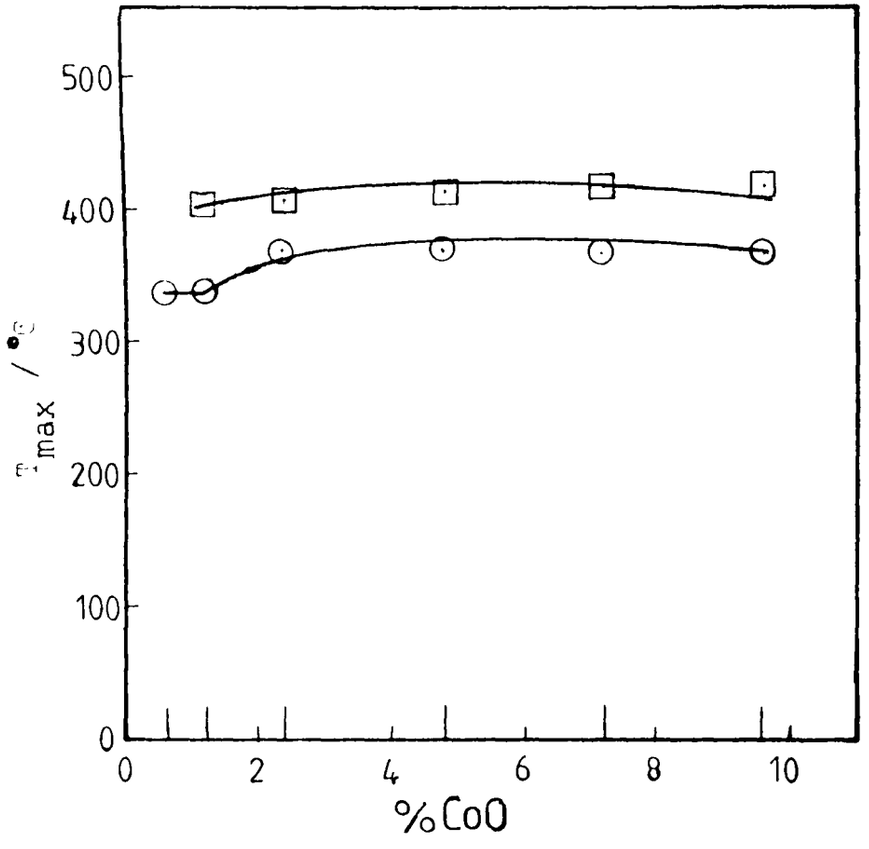

Fig. 4.12 Dependence of T_{max} on CoO content for the CT/C series.

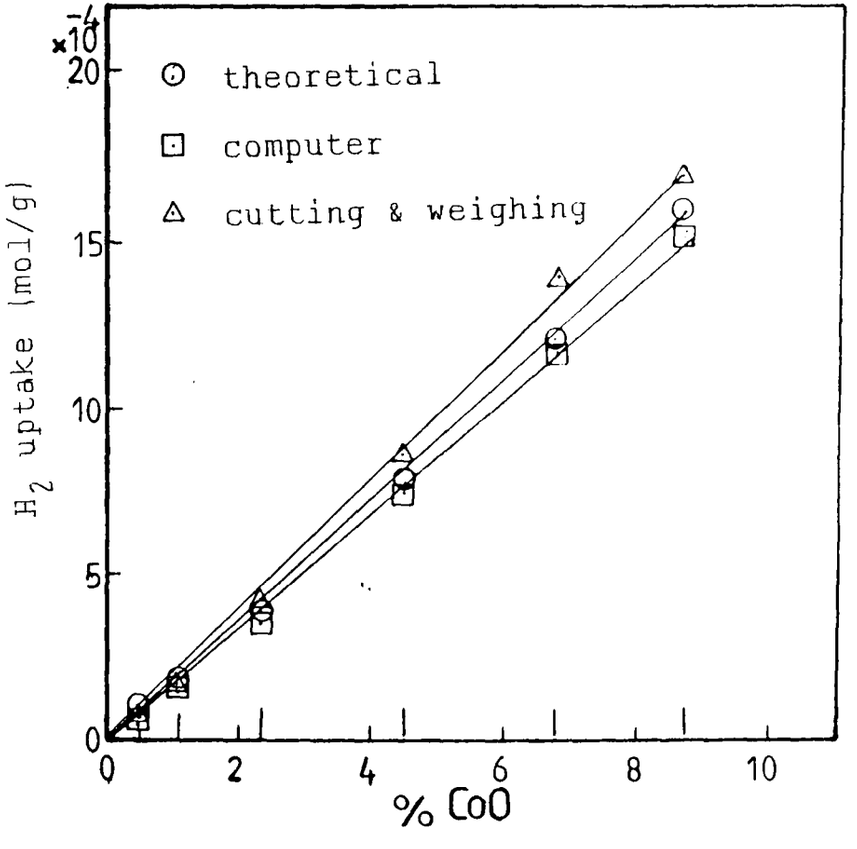

Fig. 4.13 Variation of total H_2 uptake with CoO content for the CT/C series.

Table 4.6 H_2 uptakes in $mol.g^{-1}$ for the CoO_x/TiO_2 series prepared by impregnation using $Co(NO_3)_2.6H_2O$ as precursor (CT/C) series.

Sample	Chemical analysis(a)	theoretical H_2 uptake	Computer	cutting & weighing	%reduction (b)
0.6%CT/C	0.55	$8.71x10^{-5}$	$8.73x10^{-5}$	$9.81x10^{-5}$	100.2%
1.2%CT/C	1.11	$1.92x10^{-4}$	$1.91x10^{-4}$	$1.76x10^{-4}$	99.5%
2.4%CT/C	2.35	$3.98x10^{-4}$	$3.96x10^{-4}$	$3.96x10^{-4}$	99.4%
4.8%CT/C	4.63	$7.97x10^{-4}$	$7.96x10^{-4}$	$8.66x10^{-4}$	99.8%
7.2%CT/C	6.80	$1.21x10^{-3}$	$1.18x10^{-3}$	$1.39x10^{-3}$	97.5%
9.6%CT/C	8.70	$1.60x10^{-3}$	$1.57x10^{-3}$	$1.73x10^{-3}$	98.1%

(a) by atomic absorption spectroscopy.

(b) based on computer values.

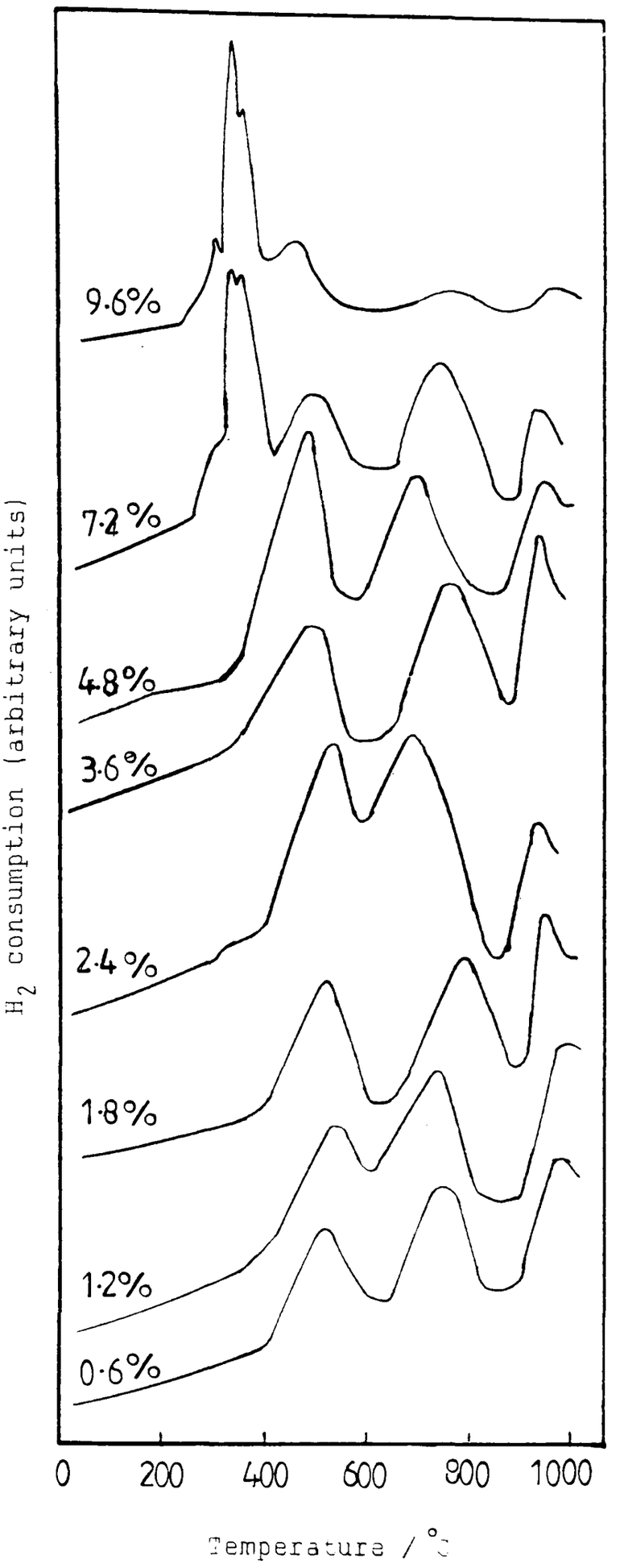

Fig. 4.14 TPR profiles of the CoO/TiO_2 catalysts prepared by homogeneous precipitation using cobalt nitrate as precursor (CT/HP series).

Table 4.7 T_{max} values for the CoO_x/TiO_2 series prepared by homogeneous precipitation using $Co(NO_3)_2.6H_2O$. (CT/HP series).

Sample	$T_{max}/^oC$				
	1st peak	2nd peak	3rd peak	4th peak	5th peak
0.6%CT/HP	-	-	-	510	750
1.2%CT/HP	-	-	-	520	750
1.8%CT/HP	-	-	-	510	780
2.4%CT/HP	-	-	-	540	680
3.6%CT/HP	-	-	-	490	780
4.8%CT/HP	-	-	-	470	680
7.2%CT/HP	320	340	360	490	750
9.6%CT/HP	320	340	360	550	760

catalysts, i.e. CT/HP, were prepared by homogeneous precipitation rather than impregnation as in the previous series (CT/C), the Co is more uniformly dispersed on the support, and that this has led to a shift in T_{max} values to higher temperatures.

Table 4.8 gives the total uptakes for the CT/HP series, whereas the variation in total H_2 consumption as a function of Co content is shown in Fig. 4.16. The extent of reduction in Table 4.8 suggests that the reduction of CoO_x to Co^o is complete at high temperature reduction region (850-900°C).

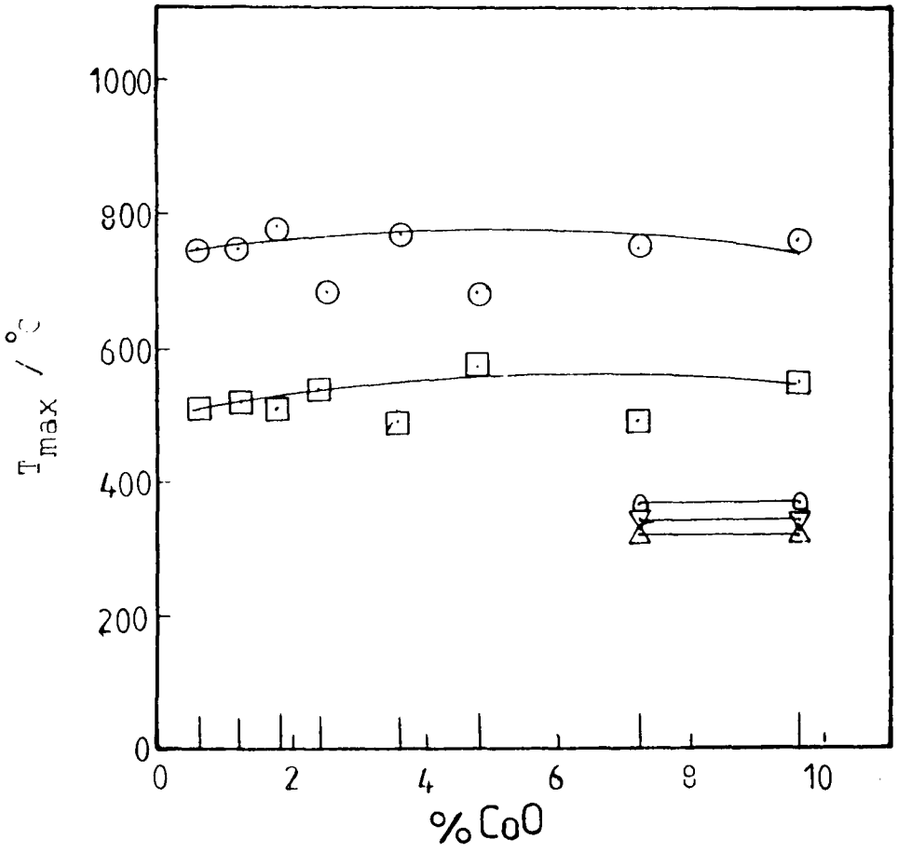

Fig. 4.15 Dependence of T_{max} on CoO content for the CT/HP series.

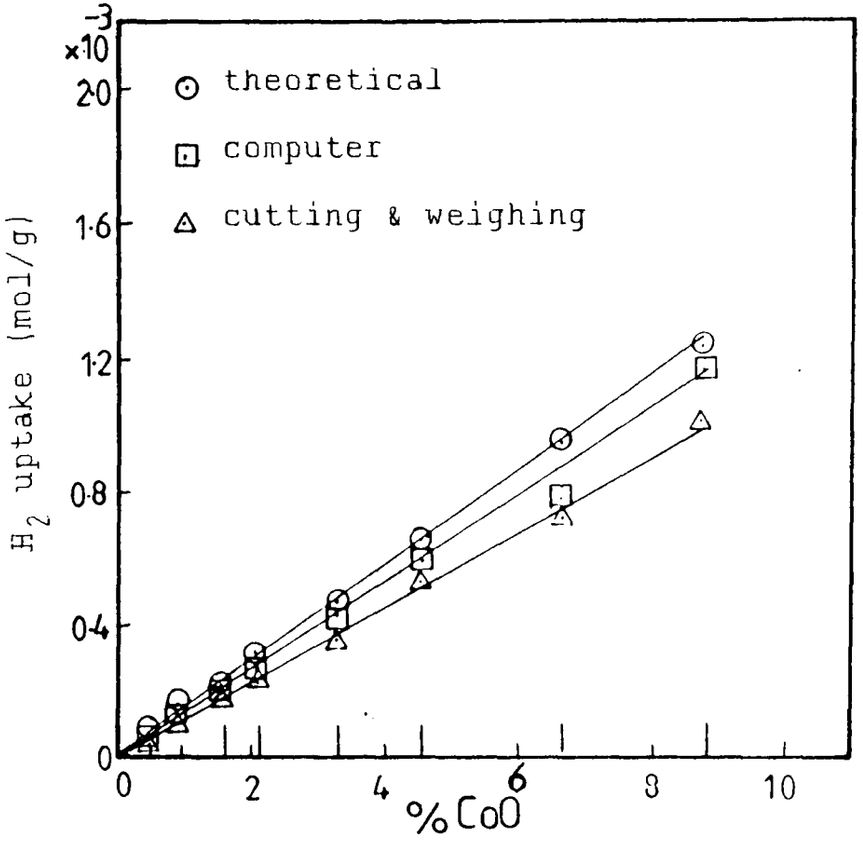

Fig. 4.16 Variation of total H_2 uptake with CoO content for the CT/HP series.

Table 4.8 H_2 uptakes in mol/g for the CoO_x/TiO_2 catalysts prepared by homogeneous precipitation using $Co(NO_3)_2.6H_2O$ as precursor (CT/HP series).

Sample	Chemical analysis[a]	theoretical H_2 uptake	Computer	Cutting & weighing	%reduction (b)
0.6CT-HP	0.50	8.0×10^{-5}	8.5×10^{-5}	9.5×10^{-5}	106.2
1.2CT-HP	0.95	1.50×10^{-4}	1.58×10^{-4}	1.52×10^{-5}	105.3
1.8CT-HP	1.65	2.10×10^{-4}	2.13×10^{-4}	1.81×10^{-4}	101.4
2.4CT-HP	2.14	3.20×10^{-4}	2.81×10^{-4}	2.40X1-$^{-4}$	87.9
3.6CT-HP	3.35	4.50×10^{-4}	4.37×10^{-4}	3.51×10^{-4}	97.1
4.8CT-HP	4.55	6.50×10^{-4}	6.08×10^{-4}	5.40×10^{-4}	93.5
7.2CT-HP	6.69	9.50×10^{-4}	7.97×10^{-4}	7.20×10^{-4}	84.9
9.6CT-HP	8.83	1.23×10^{-3}	1.18×10^{-3}	1.05×10^{-3}	95.9

(a) by atomic absorption spectroscopy.

(b) based on computer values.

Fig. 4.17 shows TPR profiles for the CoO_x/TiO_2 series prepared by impregnation using cobalt acetate as precursor. Four groups of peaks are formed: the first peak, with T_{max} values of $\sim$ 310-350°C is present in all the catalysts; the second peak, with T_{max} of 370-450°C is found only with 0.38 wt%, 2.25 wt.% and 3.00 wt% CoO contents; the third peak, with T_{max} of $\sim$ 430-580°C, and, finally, the fourth peak at $\sim$ 780-810°C are seen in all the catalysts. The reduction process of the supported CoO_x catalysts starts at a temperature lower than that at which unsupported CoO and Co_3O_4 start to reduce.

Table 4.9 gives T_{max} values for the CAT/C series, while the variation in T_{max} with Co content is shown in Fig. 4.18. Above 0.75 wt.%, T_{max} remains constant for three of the previous groups, i.e. at $\sim$ 300-400°C, 430-580°C, and 780-810°C.

Table 4.10 gives total H_2 uptakes for the CoO_x/TiO_2 series (CAT/C), while the total H_2 consumption against the Co concentration is plotted in Fig. 4.19. At low loadings, such as 0.15 wt.% to 0.49 wt.% the degree of reduction is slightly higher than 100% which can be attributed to the partial surface reduction of the support. For the rest of the samples in the series, the extent of reduction is almost 100%, which indicates that the reduction of CoO_x in this series to Co^o is complete.

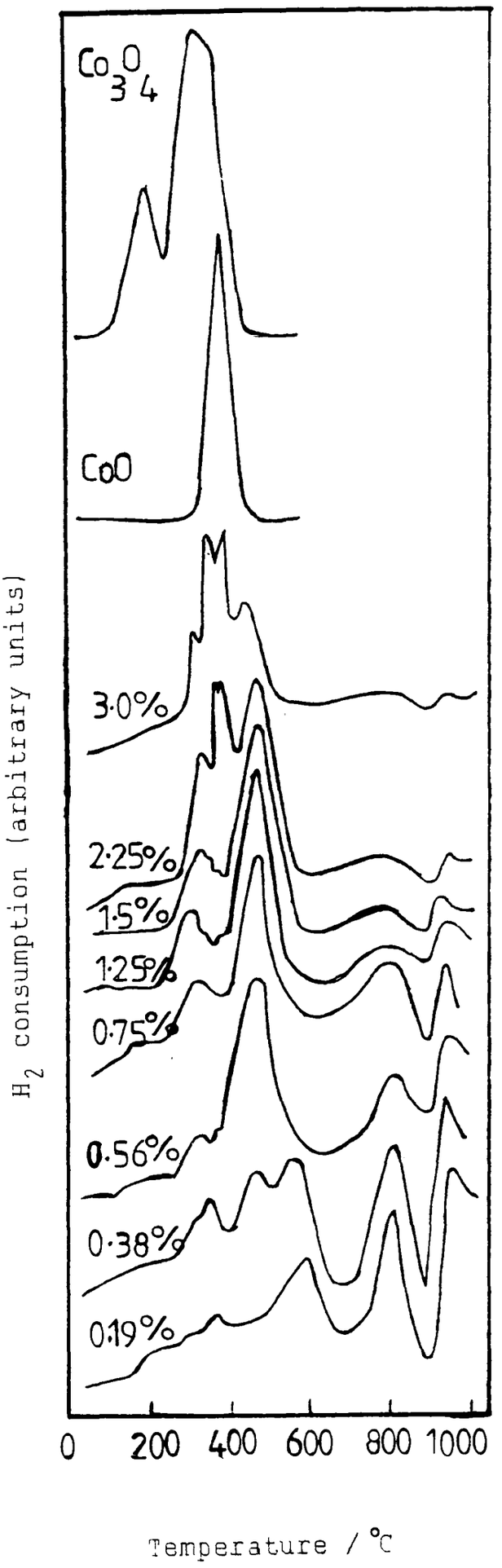

Fig. 4.17 TPR profiles of the CoO/TiO_2 catalysts prepared by impregnation using cobalt acetate as precursor (CAT/C series).

Table 4.9 T_m values for the CoO/TiO_2 series prepared by impregnation using $Co(CH_3COO)_2.4H_2O$ (CAT/C series).

Sample	$T_m/^oC$			
	1st peak	2nd peak	3rd peak	4th peak
0.19%CAT/C	350	-	580	810
0.38%CAT/C	340	450	560	820
0.56%CAT/C	310	-	550	820
0.75%CAT/C	320	-	470	790
1.25%CAT/C	300	-	470	810
1.50%CAT/C	315	-	470	780
2.25%CAT/C	320	370	470	790
3.00%CAT/C	310	370	430	780
CoO	370	-	-	-
Co_3O_4	250	340	-	-
$CoTiO_3$	810	-	-	-

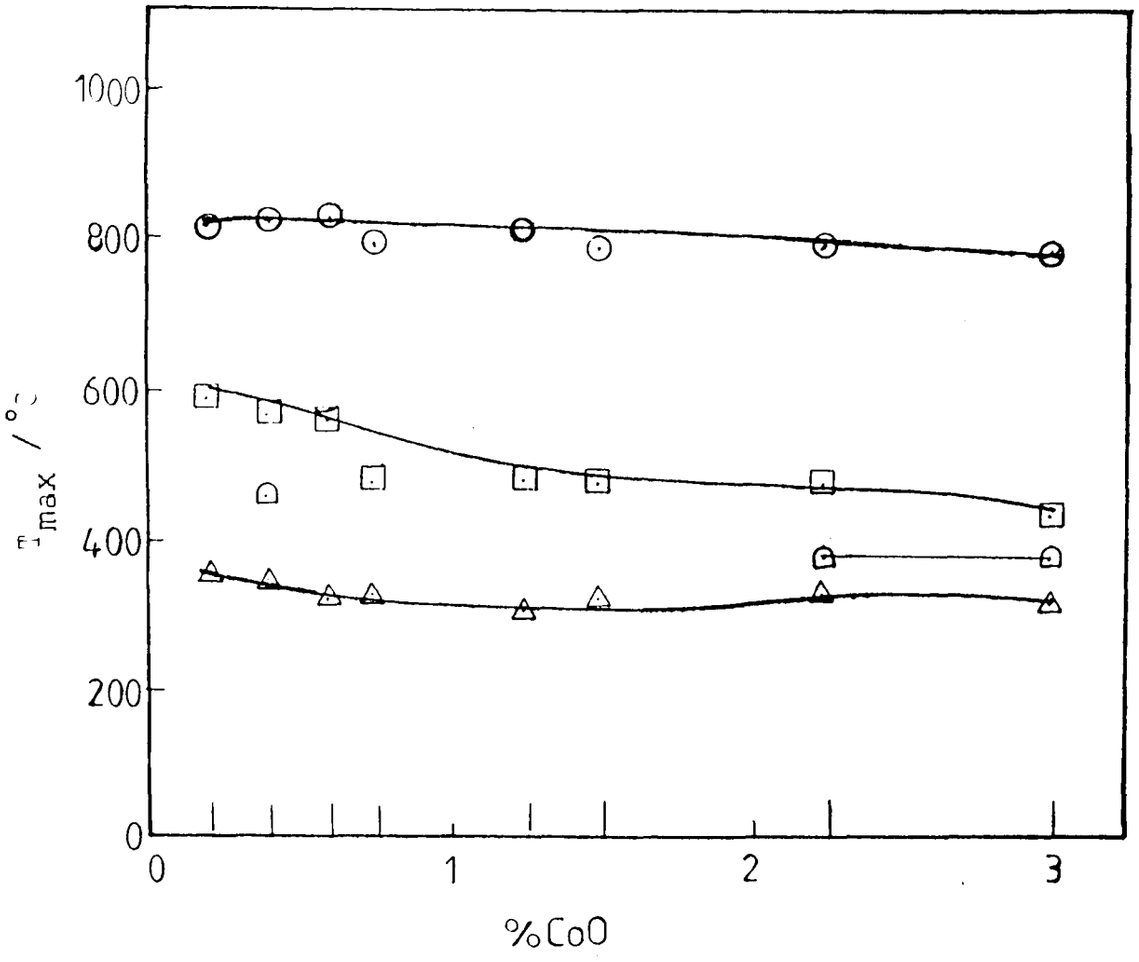

Fig. 4.18 Dependence of T_{max} on CoO content for the CAT/C series.

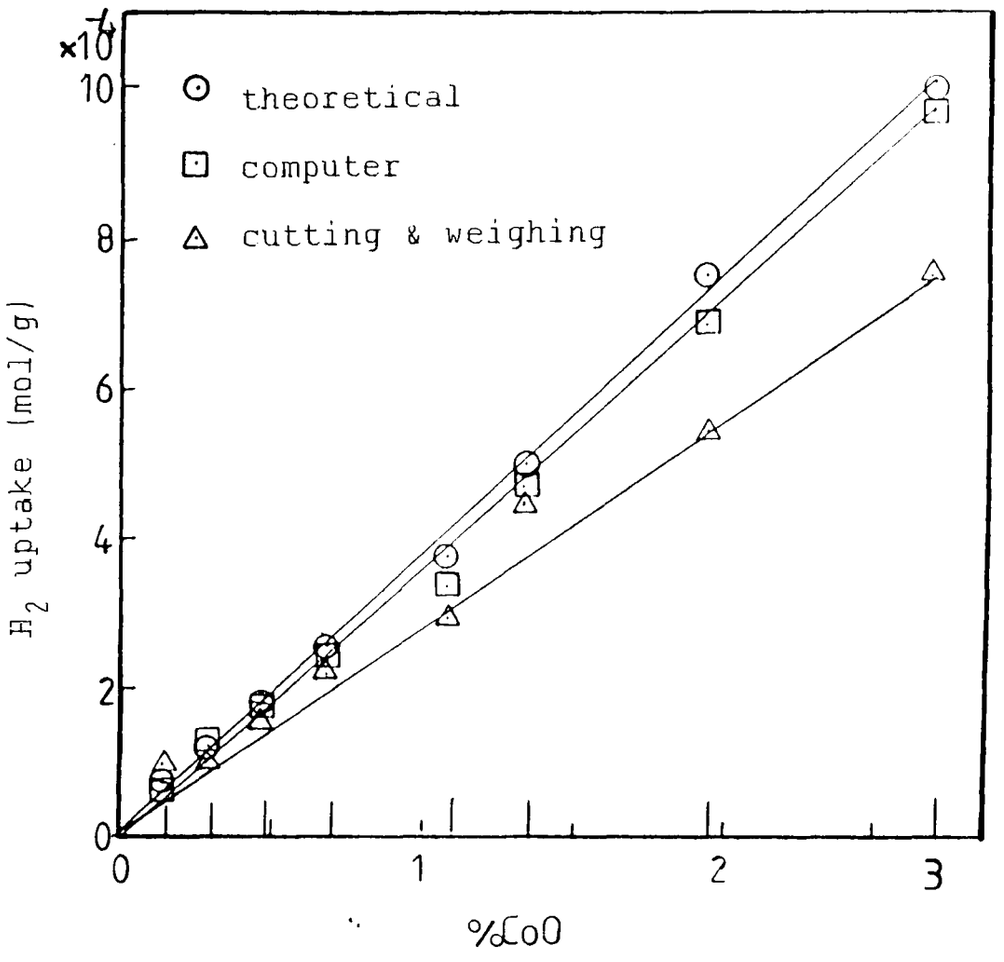

Fig. 4.19 Variation of total H_2 uptake with CoO content for the CAT/C series.

Table 4.10 H_2 uptakes in mol/g for the CoO_x/TiO_2 catalysts prepared by impregnation using $Co(CH_3COO)_2.4H_2O$ as precursor (CAT/C series).

sample	Chemical analysis(a)	theoretical H_2 uptake	Computer	Cutting & weighing	%reduction (b)
0.19CAT/C	0.15	6.25×10^{-5}	6.93×10^{-5}	9.05×10^{-5}	110.9%
0.38CAT/C	0.31	1.25×10^{-4}	1.34×10^{-4}	1.08×10^{-4}	107.3%
0.56CAT/C	0.49	1.87×10^{-4}	1.92×10^{-4}	1.68×10^{-4}	102.6%
0.75CAT/C	0.69	2.50×10^{-4}	2.41×10^{-4}	2.28×10^{-4}	96.4%
1.25CAT/C	1.10	3.75×10^{-4}	3.36×10^{-4}	2.93×10^{-4}	89.6%
1.50CAT/C	1.35	5.00×10^{-4}	4.67×10^{-4}	4.58×10^{-4}	93.4%
2.25CAT/C	1.95	7.50×10^{-4}	6.88×10^{-4}	5.44×10^{-4}	91.8%
3.00CAT/C	2.69	10.0×10^{-4}	9.79×10^{-4}	7.50×10^{-4}	97.9%

(a) by atomic absorption spectroscopy
(b) based on computer values.

4.1.2.3 $CoO-MoO_3/TiO_2$ catalysts

Three series of $CoO-MoO_3/TiO_2$ catalysts were prepared by aqueous impregnation using cobalt nitrate and ammonium heptamolybdate (AHM) as precursors, by varying the sequence of impregnation, i.e. CoO first, CMT series; MoO_3 first, MCT series; and CoO and MoO_3 together, CMT_g series (see Sections 2.8.1 - 2.8.3).

Firstly, TPR profiles of the CMT catalysts are shown in Fig. 4.20. Four phases can be seen up to one and half monolayer, i.e. 2.50%CoO-4.8%MoO_3 catalyst as follows: phase I with T_{max} occurring between 330-425°C, phase II T_{max} of 370-470°C, phase III T_{max} at 500-600°C, and phase IV T_{max} within 700-730°C. Above one and a half monolayer catalyst, only three phases are formed. Compared with the unsupported CoO, Co_3O_4, MoO_3, and $CoMoO_4$, these TPR profile groups may be attributed to the formation of surface species of a type of unsupported oxides. For CoO and Co_3O_4, there is a shift in T_{max} to high temperatures, while for MoO_3 and $CoMoO_4$, T_{max} shifts to lower temperatures, which may be due to the phenomenon of the so-called "strong metal-support interaction", i.e. SMSI. Fig. 4.21 shows the variation in T_{max} values as a function of total CoO and MoO_3 content for all four groups. Table 4.11 gives the chemical analysis by atomic absorption spectroscopy (AAS) for CoO and MoO_3 contents, and the total H_2 consumption per g catalyst as a function of CoO and MoO_3 content.

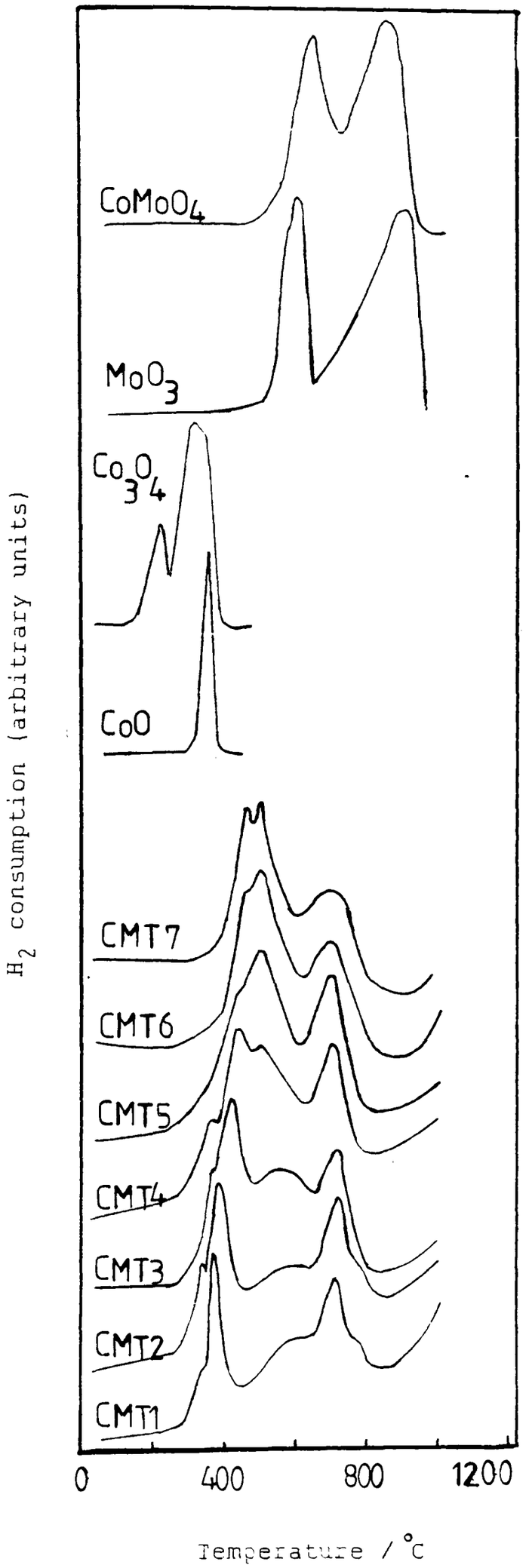

Fig. 4.20 TPR patterns for CoO-MoO/TiO_2 catalysts (CMT series)

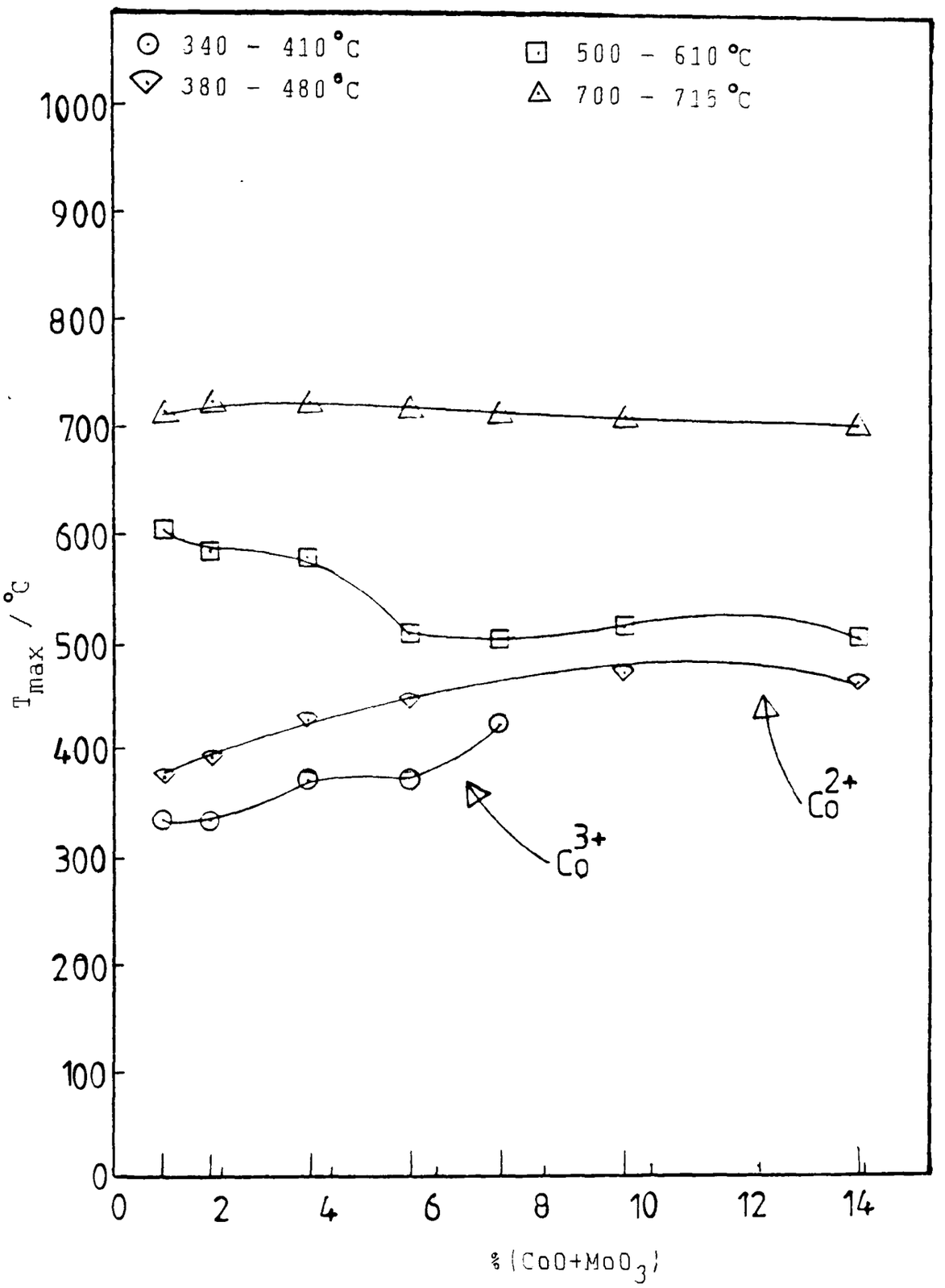

Fig. 4.21 Dependence of T_{max} on CoO and MoO_3 contents for the CMT series.

Table 4.11 Chemical analysis and total H_2 uptake in $mol.g^{-1}$ for CMT series.

Sample	Nominal loading		Actual loading(a)		total actual ($CoO+MoO_3$)	theoretical H_2 uptake (c)	Computer	Cutting & weighing	% reduction (b)
	CoO	MoO_3	CoO	MoO_3					
CMT1	0.42	0.80	0.30	0.60	0.90	2.16×10^{-4}	2.07×10^{-4}	1.82×10^{-4}	95.8
CMT2	0.82	1.60	0.60	1.20	1.80	4.32×10^{-4}	4.54×10^{-4}	4.53×10^{-4}	105.8
CMT3	1.67	3.20	1.20	2.40	3.60	8.63×10^{-4}	8.22×10^{-4}	8.04×10^{-4}	95.2
CMT4	2.51	4.80	1.80	3.70	5.50	12.9×10^{-4}	13.7×10^{-4}	13.1×10^{-4}	105.8
CMT5	3.34	6.42	2.30	4.90	7.20	17.3×10^{-4}	17.7×10^{-4}	17.9×10^{-4}	102.5
CMT6	5.01	9.63	3.10	6.40	9.50	25.9×10^{-4}	25.8×10^{-4}	25.2×10^{-4}	99.6
CMT7	6.68	12.8	4.70	9.20	13.9	34.5×10^{-4}	36.5×10^{-4}	38.2×10^{-4}	105.8

(a) by atomic absorption spectroscopy

(b) based on computer values

(c) see Appendix IV

The extent of reduction in table 4.11 is within 90-100%. Although there is a shift in T_{max} values in this series to lower or higher temperatures, compared with the unsupported oxides, the degree of reduction is not higher or lower than 100%, which may suggest that "SMSI" is independent on the extent of reduction compared with single supported oxide. This observation remains a matter of great controversy. Fig. 4.22 shows the total H_2 uptake as a function of total CoO and MoO_3 contents.

Secondly, TPR profiles of the MCT catalysts are shown in Fig. 4.23. Three main groups of peaks are formed up to 3.21%MoO_3 - 1.67%CoO catalyst, then two of the peaks coalesce and another main peak is seen up to 6.42%MoO_3 - 3.34%CoO catalyst and above this catalyst composition, two main peaks only are formed as shown in Fig. 4.23.

The variation in T_{max} values with CoO and MoO_3 contents is shown in Fig. 4.24. In Fig. 4.23, TPR profiles of all the samples are lower in their reduction behaviour than $CoMoO_4$ and MoO_3 and higher than CoO and Co_3O_4. Table 4.12 gives the chemical analysis and total H_2 uptakes per g catalyst as a function of CoO and MoO_3 loadings.

Fig. 4.25 shows the plots of total H_2 uptakes against CoO and MoO_3 concentrations, theoretically, by computer, and by cutting and weighing. It appears that the estimation of H_2 consumption calculated by computer and cutting and weighing methods is in good agreement with the theoretical estimation.

Finally, TPR profiles of CoO-MoO_3-TiO_2 catalysts are shown in Fig. 4.26 (CMTg series).

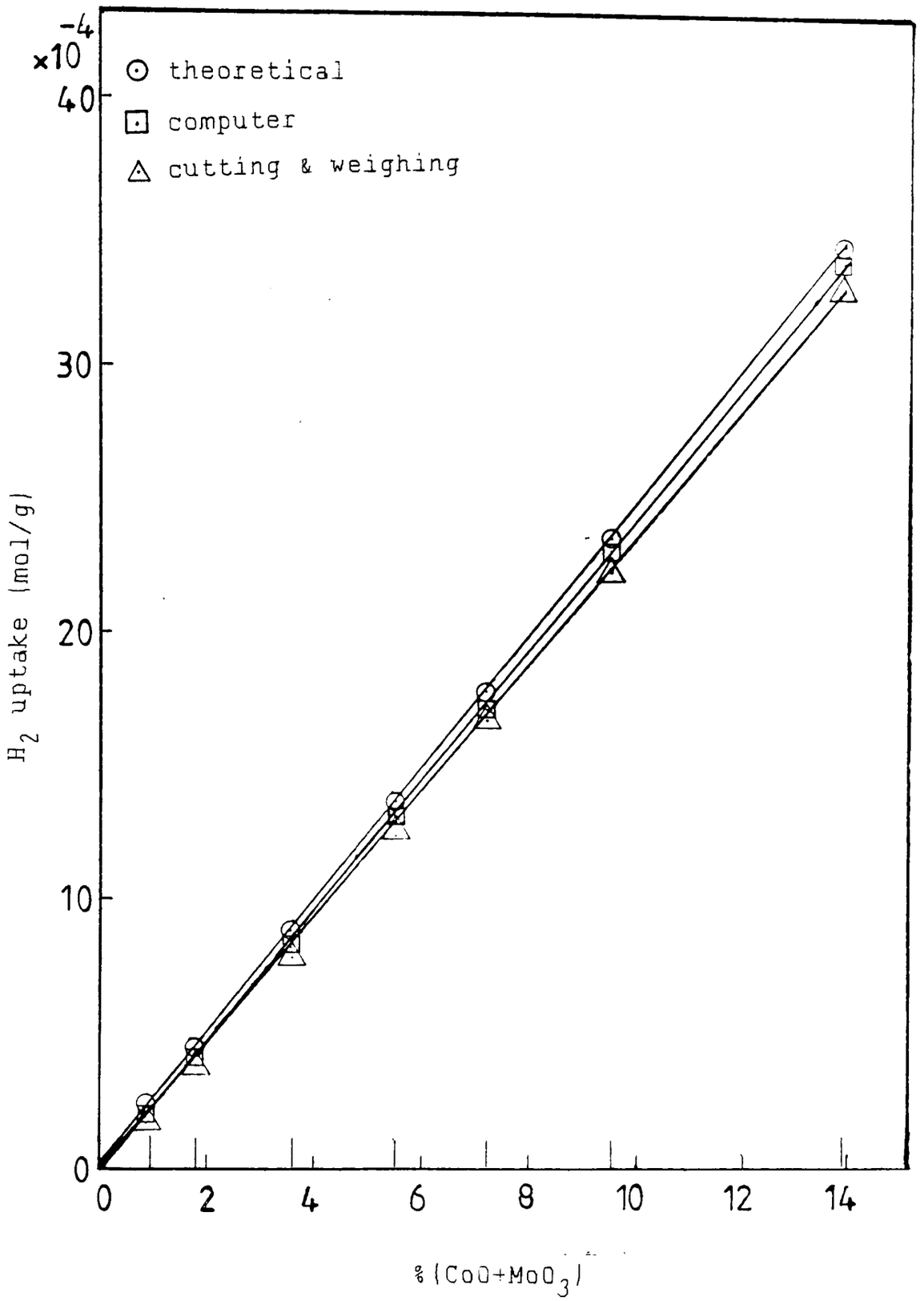

Fig. 4.22 Variation of total H_2 uptake with CoO and MoO_3 contents for the CMT series.

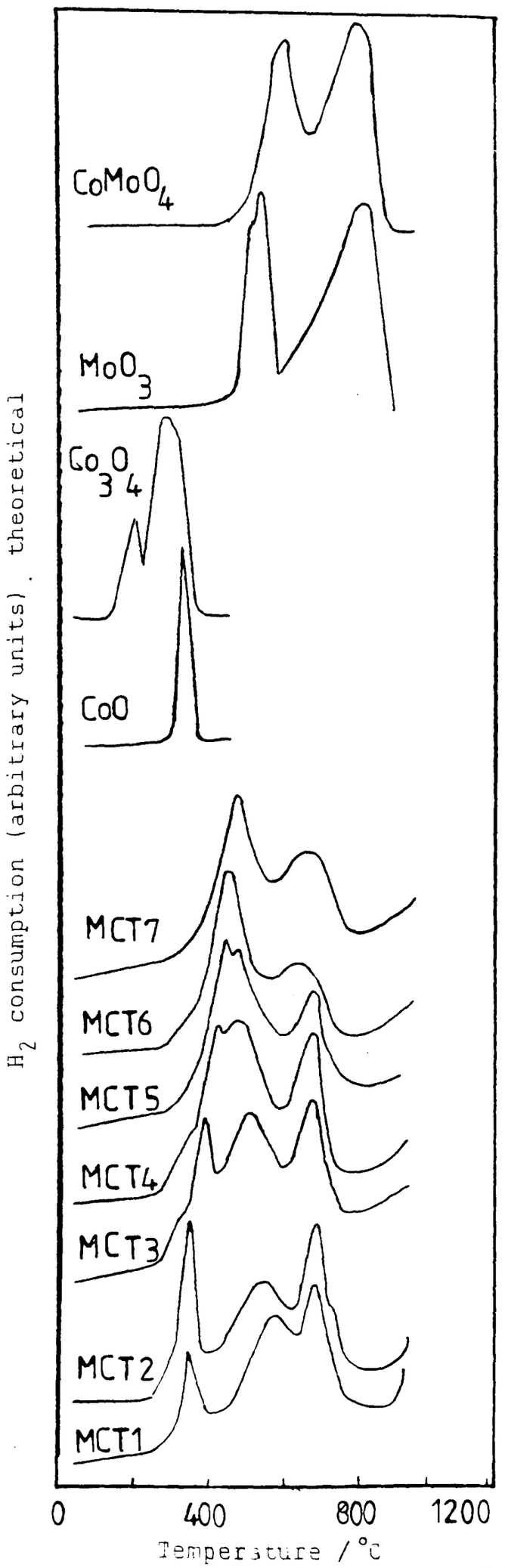

Fig. 4.23 TPR profiles for $CoO-MoO_3/TiO_2$ catalysts (MCT series)

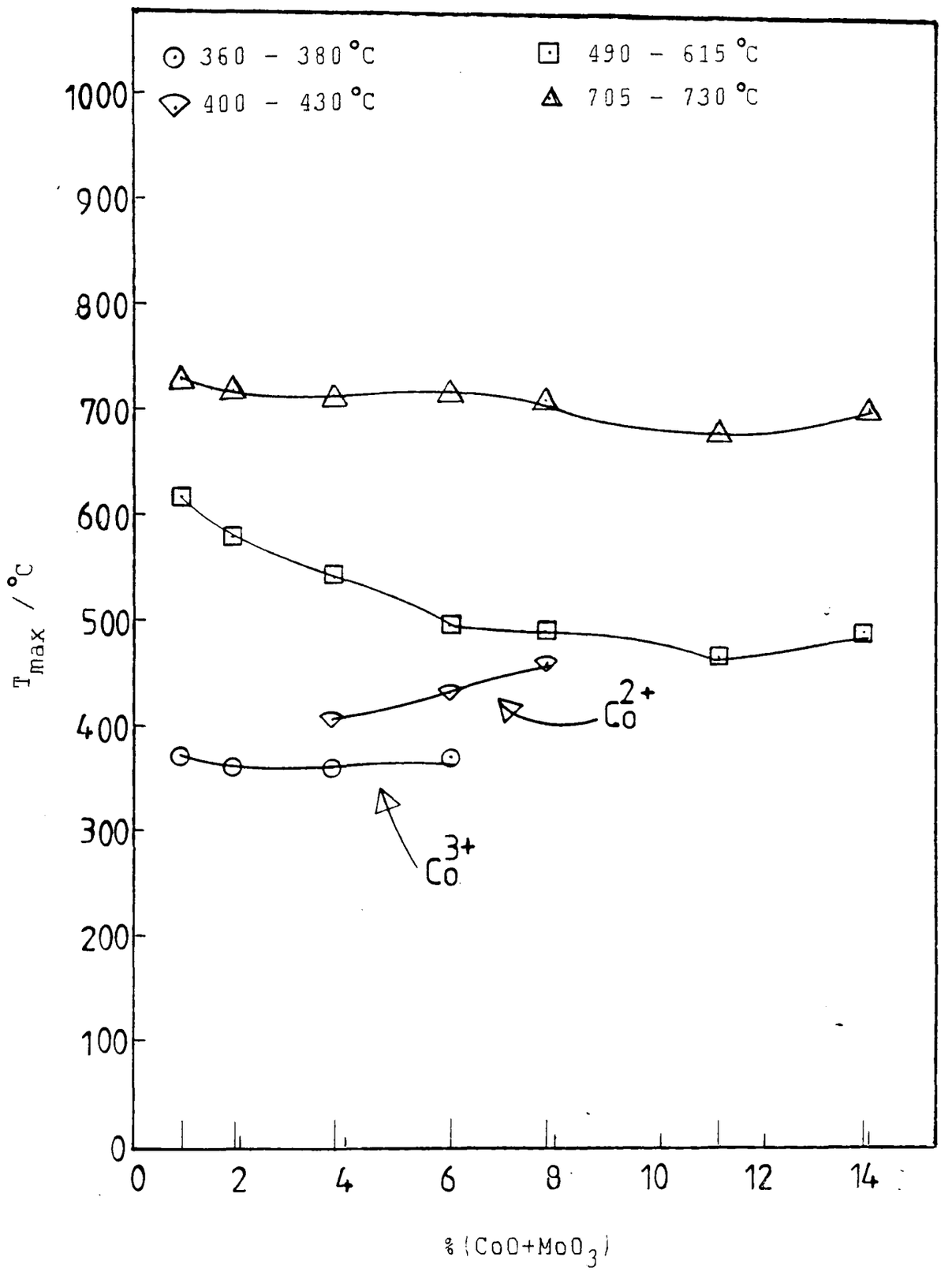

Fig. 4.24 Dependence of T_{max} on CoO and MoO_3 contents for the MCT series.

Table 4.12 Chemical analysis and total H_2 uptake in $mol.g^{-1}$ for MCT series,

Sample	Nominal loading		Actual loading(a)		total actual ($CoO+MoO_3$)	theoretical H_2 uptake(c)	Computer	Cutting & weighing	% reduction (b)
	CoO	MoO_3	CoO	MoO_3					
MCT1	0.42	0.80	0.30	0.60	0.90	2.16×10^{-4}	2.30×10^{-4}	2.27×10^{-4}	106.5
MCT2	0.84	1.60	0.70	1.20	1.90	4.32×10^{-4}	4.22×10^{-4}	3.57×10^{-4}	97.7
MCT3	1.67	3.20	1.40	2.40	3.80	8.64×10^{-4}	7.91×10^{-4}	6.80×10^{-4}	91.6
MCT4	2.51	4.81	2.30	3.70	6.00	12.9×10^{-4}	13.3×10^{-4}	12.6×10^{-4}	103.1
MCT5	3.34	6.42	2.80	5.00	7.80	17.3×10^{-4}	16.6×10^{-4}	16.1×10^{-4}	96.2
MCT6	5.01	9.63	4.10	7.00	11.1	25.9×10^{-4}	24.5×10^{-4}	23.2×10^{-4}	94.6
MCT7	6.68	12.8	5.00	8.90	13.9	34.6×10^{-4}	32.4×10^{-4}	30.5×10^{-4}	93.9

(a) by atomic absorption spectroscopy

(b) based on computer values.

(c) see Appendix IV

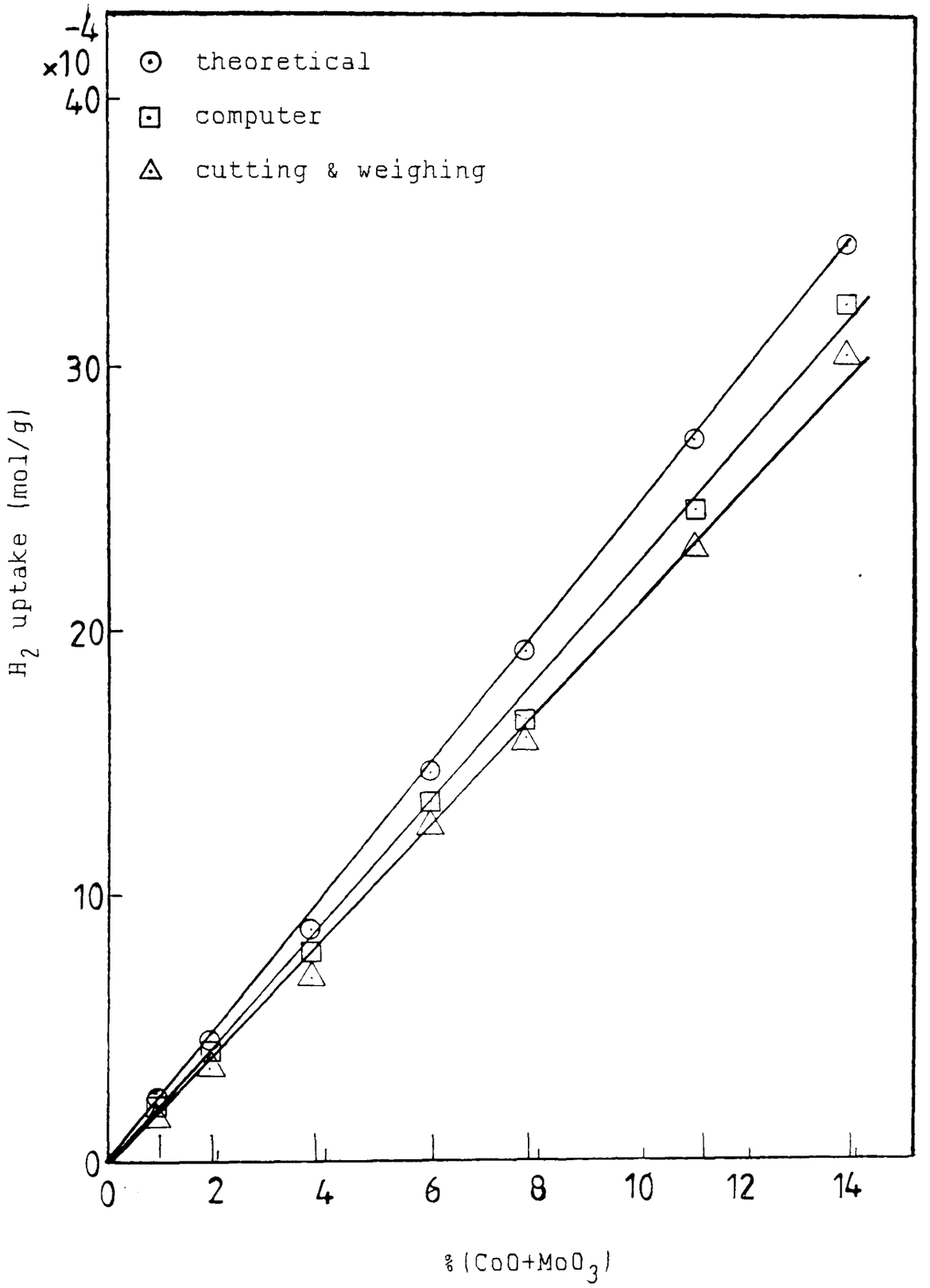

Fig. 4.25 Variation of total H_2 uptake with CoO and MoO_3 contents for the MCT series.

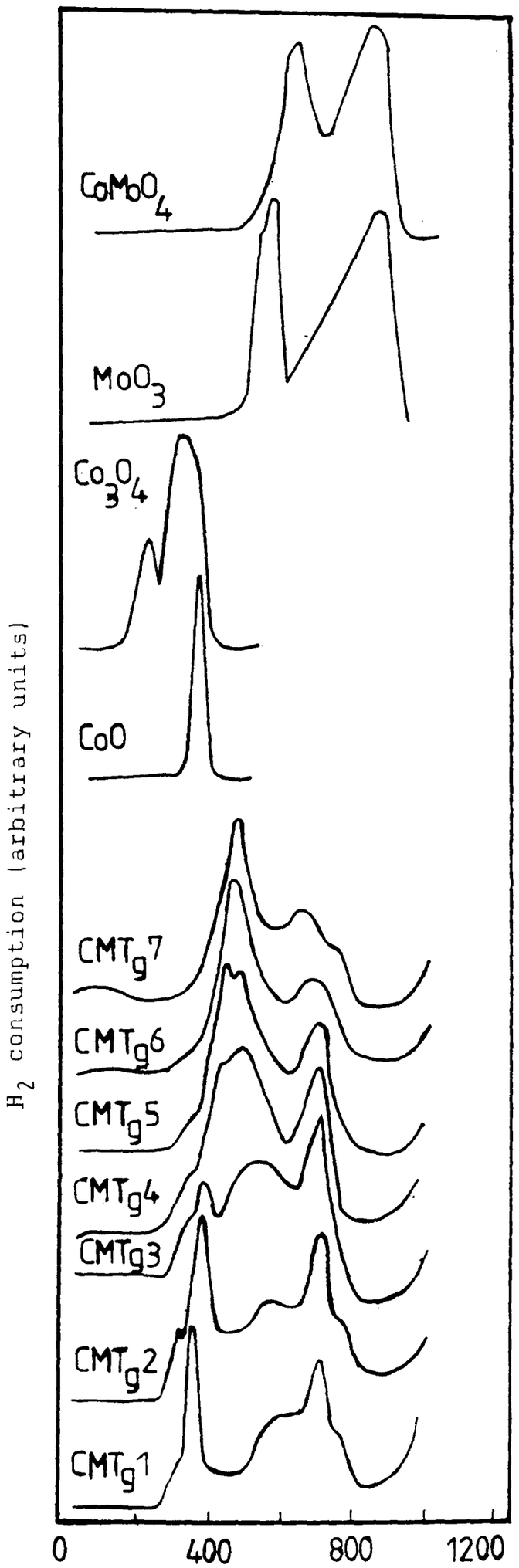

Fig. 4.26 TPR profiles for $CoO-MoO_3/TiO_2$ catalysts (CMTg series)

Up to 1.10%CoO + 2.30%MoO_3 catalyst, i.e. a monolayer region, four peaks are formed, with T_{max} values of ~ 325-370°C in all the catalysts, 360-460°C up to 4.8%CoO + 7.80%MoO_3 catalyst, i.e. 3 monolayers, 475-580°C in all the samples and finally 670-720°C in all of the catalysts, as shown in Fig. 4.27. A shift to lower temperatures in T_{max} values can be noticed for $CoMoO_4$ and MoO_3 and to higher temperatures for unsupported CoO and Co_3O_4. As this shift has occurred in the previous two series, i.e. CMT and MCT, it is difficult to distinguish between them just by varying the sequence of impregnation.

Table 4.13 gives the chemical analysis of CoO and MoO_3 contents and total H_2 uptake per g of catalyst as a function of CoO and MoO_3 loadings. The extent of reduction is ~ 90-100% which indicates that the reduction process is complete.

A plot of the variation in total H_2 uptake against the CoO and MoO_3 loadings is shown in Fig. 4.28. All the three series; CMT, MCT and CMTg, showed similarity in their TPR profiles, which leaves us with the dilemma of how the structure of a bicomponent supported oxide varies with the mode of impregnation? It cannot be a straightforward answer from only one characteristic technique.

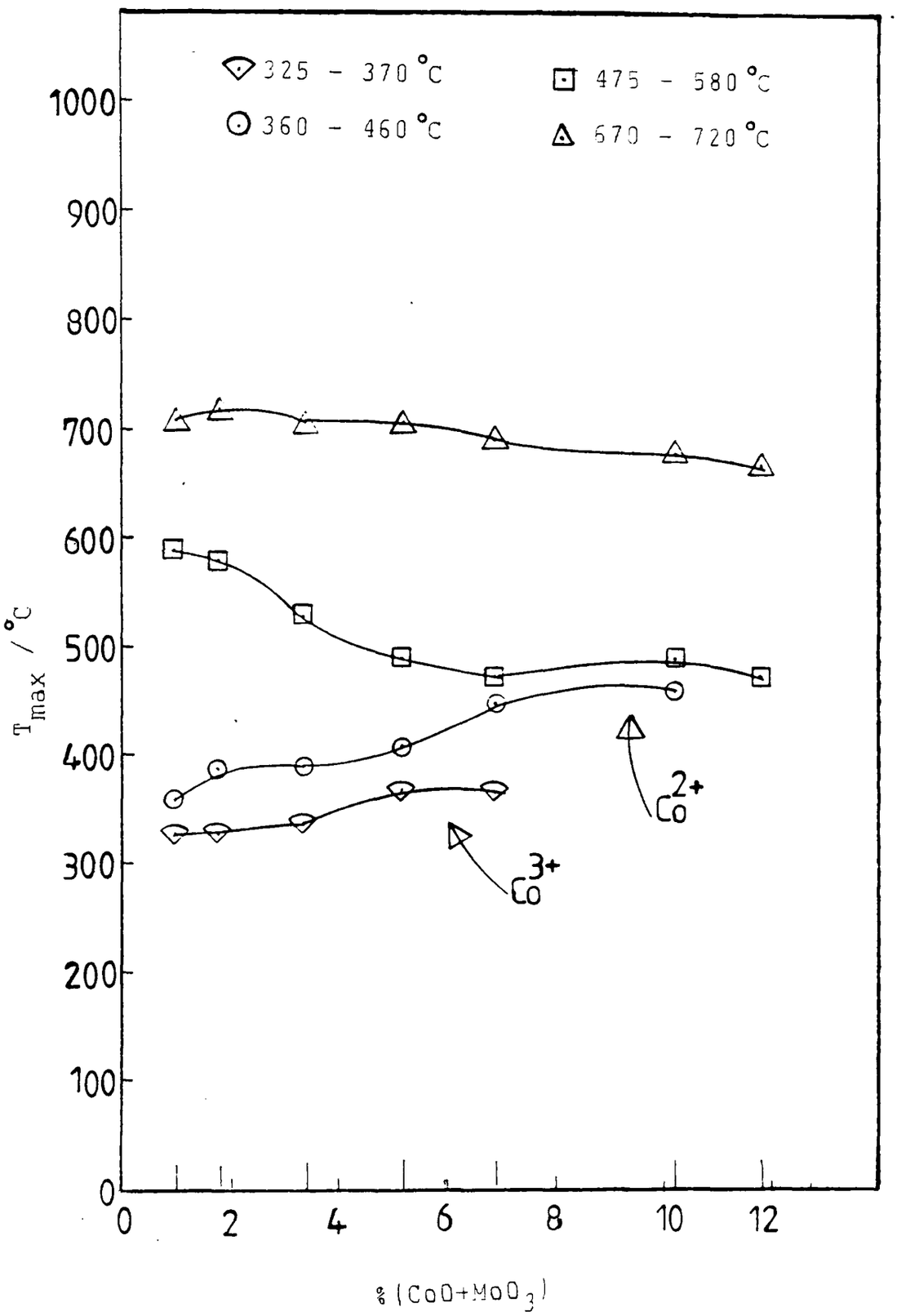

Fig. 4.27 Dependence of T_{max} on CoO and MoO_3 contents for the CMTg series.

Table 4.13 Chemical analysis and total H_2 uptake in $mol.g^{-1}$ for CMTg series.

Sample	Nominal loading		Actual loading(a)		total actual ($CoO+MoO_3$)	theoretical H_2 uptake(c)	Computer	Cutting & weighing	% reduction (b)
	CoO	MoO_3	CoO	MoO_3					
CMTg1	0.42	0.80	0.30	0.70	1.00	2.16×10^{-4}	2.01×10^{-4}	2.02×10^{-4}	93.1
CMTg2	0.84	1.60	0.60	1.20	1.80	4.32×10^{-4}	4.30×10^{-4}	4.16×10^{-4}	99.5
CMTg3	1.67	3.21	1.10	2.30	3.40	8.63×10^{-4}	7.18×10^{-4}	7.35×10^{-4}	88.2
CMTg4	2.51	4.81	1.70	3.50	5.20	12.9×10^{-4}	16.2×10^{-4}	12.1×10^{-4}	125.1
CMTg5	3.34	6.42	2.10	4.80	6.90	17.3×10^{-4}	15.6×10^{-4}	15.6×10^{-4}	90.4
CMTg6	5.01	9.63	4.80	7.80	12.6	25.9×10^{-4}	24.2×10^{-4}	23.5×10^{-4}	93.4
CMTg7	6.68	12.8	6.00	10.2	16.2	34.5×10^{-4}	30.5×10^{-4}	30.3×10^{-4}	88.4

(a) by atomic absorption spectroscopy

(b) based on computer values

(c) see Appendix IV

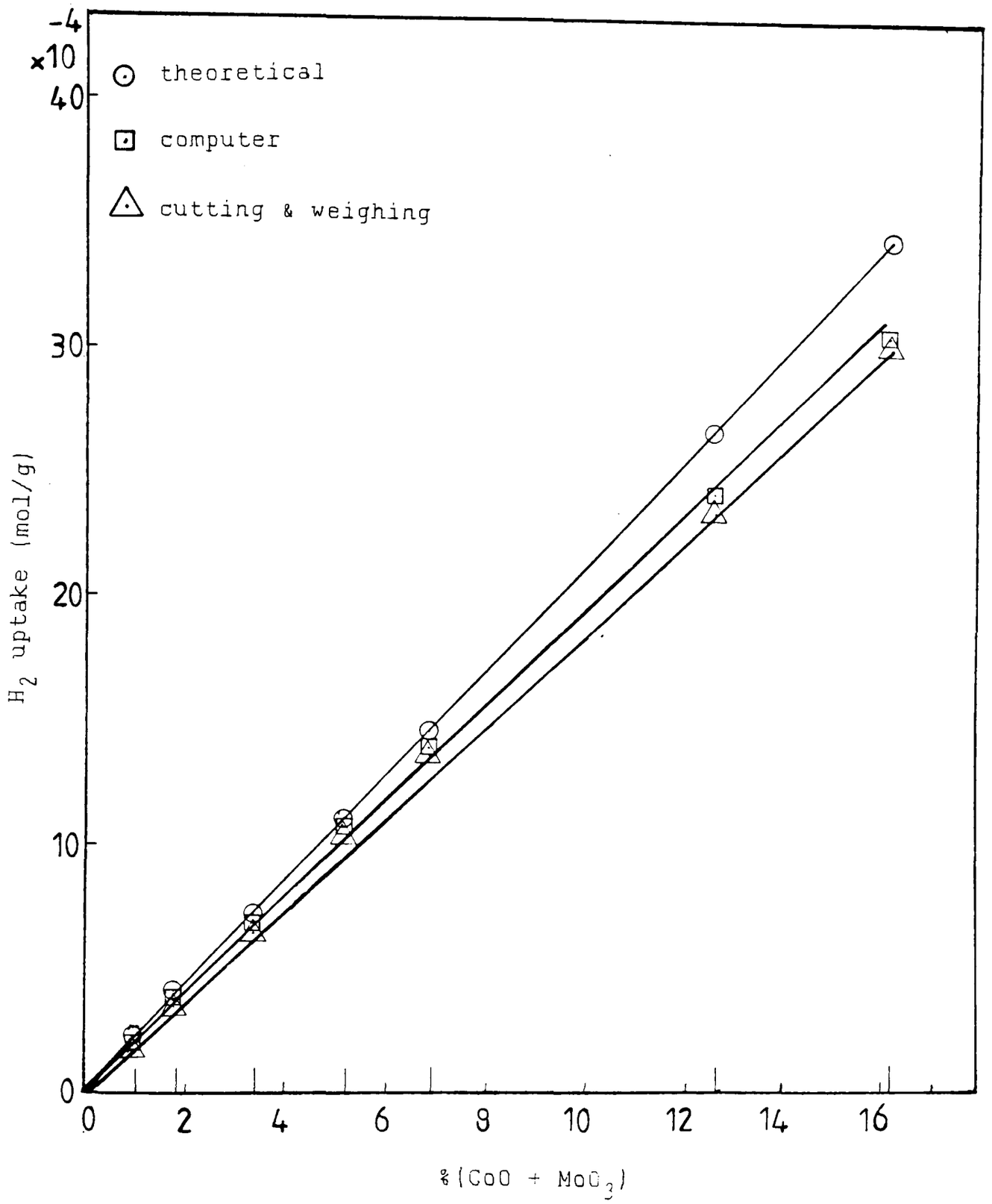

Fig. 4.28 Variation of total H_2 uptake with CoO and MoO_3 contents for the CMTg series.

4.1.3 X-ray photoelectron spectroscopy (XPS)

4.1.3.1 MoO_3/TiO_2 catalysts

The XPS spectra of the MT/C and MOT/C series (prepared from AHM and molybdenum oxalate precursors) are illustrated in Fig. 4.29 and 4.30, respectively. The resolution and an attendant sharpness of the doublet, i.e. $Mo3d_{3/2}$ and $Mo3d_{5/2}$, is observed to be as well resolved as the Mo3d doublet of pure MoO_3. This trend, as indicated by the shape of the spectra, is confirmed by the full width at half maximum (fwhm) data displayed in Tables 4.14 and 4.15 for both series. It is important to note that Mo/TiO_2 catalysts have fwhm values very close to that of pure MoO_3, whereas Mo/Al_2O_3 and Mo/SiO_2 have slightly higher values[3-5].

In both series, no change in binding energy (BE) as a function of Mo content is noticed. However, the magnitudes of the average BE of these catalysts, for the most intense peak, i.e. $Mo3d_{5/2}$, 232.9 $\pm$ 0.07eV, show appreciable shift from that of pure MoO_3 (232.2eV).

The XPS peak intensity ratio for both series, i.e. MT/C and MOT/C series, is shown in Figs. 4.31 and 4.32, respectively. The ratio increases linearly up to the monolayer capacity of 1 wt.% MoO_3 and then deviates above the monolayer coverage, with increasing Mo loadings. These results are similar to other workers' results on different supports such as Al_2O_3, SiO_2, etc.[3-5].

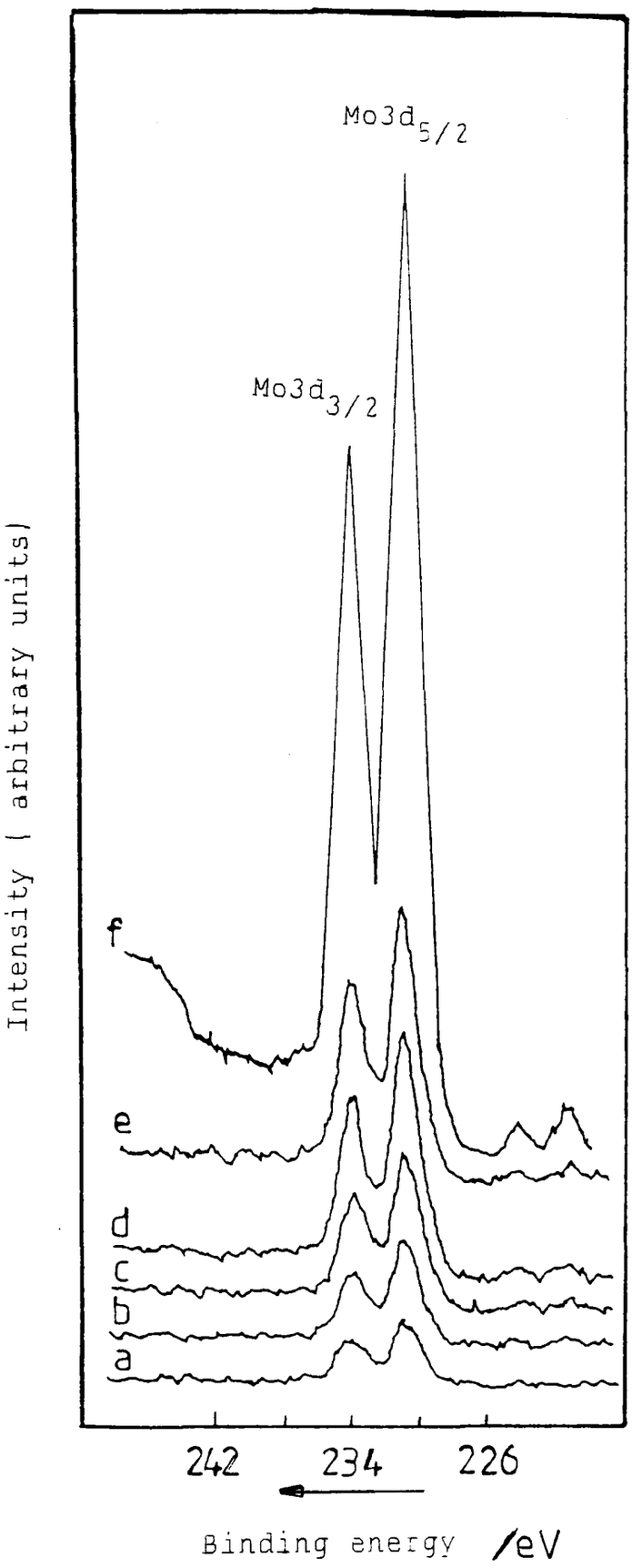

Fig. 4.29 XPS spectra for the MT/C catalysts, where (a) 0.5% MoO_3, (b) 1%MoO_3, (c) 2% MoO_3, (d) 3% MoO_3, (e) 4% MoO_3, and (f) MoO_3.

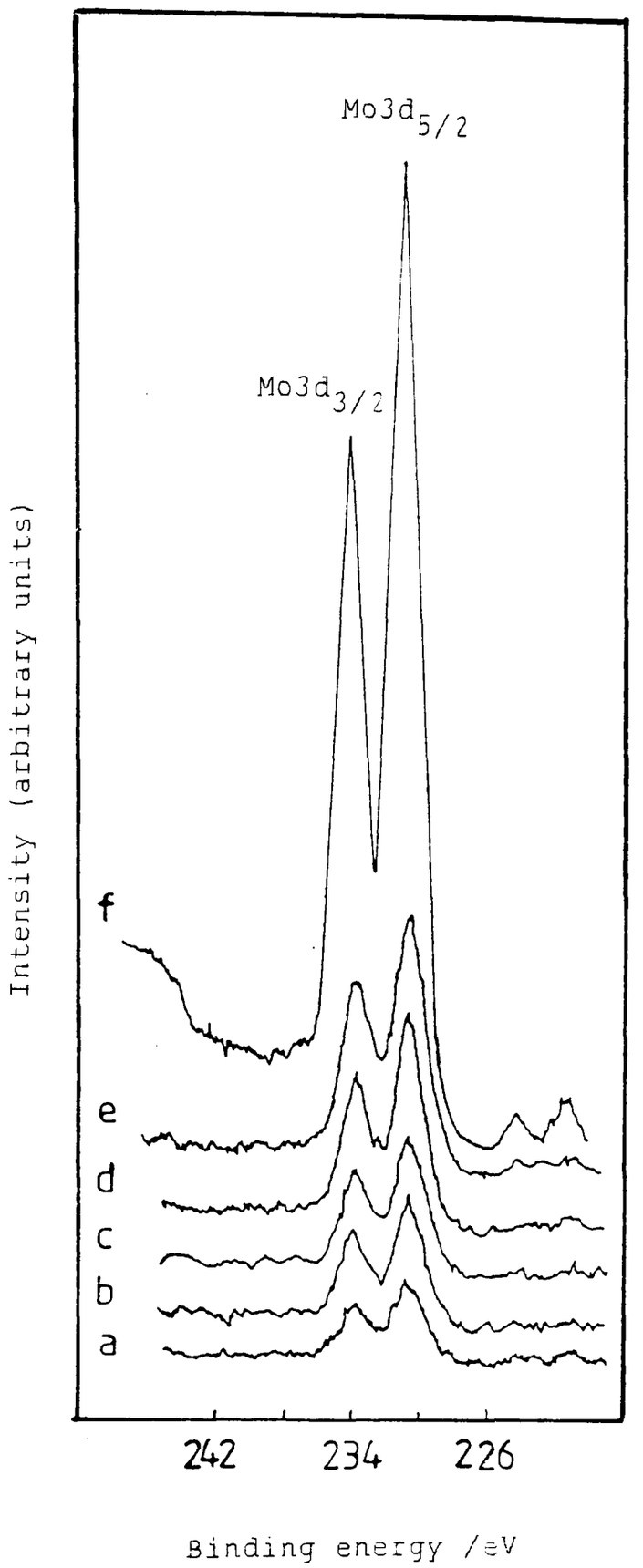

Fig. 4.30 XPS spectra for the MOT/C catalysts where (a) 0.5 wt.% MoO_3, (b) 1 wt.%MoO_3, (c) 2 wt.% MoO_3, (d) 3 wt.% MoO_3, (e) 4 wt.% MoO_3, and (f) MoO_3.

Table 4.14

Binding energy values in eV of MoO/TiO_2 prepared by impregnation using (AHM), and pure MoO_3 and TiO_2.

wt.% MoO_3	sample state	Binding energy (FWHM) $Mo3d_{3/2}$	$Mo3d_{5/2}$	C1s	$Ti2p_{1/2}$	FWHM(eV)[a] $Ti2p_{3/2}$
0.5	powd. calc.	235.4(2.3)	232.2(2.4)	284.1(--)	464.1(2.3)	1.5
1.0	"	235.8(2.2)	232.6(2.3)	284.3(--)	464.1(2.3)	1.5
2.0	"	236.2(2.1)	232.9(2.2)	284.6(--)	464.2(2.4)	1.5
3.0	"	235.8(2.0)	232.6(2.1)	284.2(--)	464.3(2.5)	1.5
4.0	"	236.2(1.9)	232.9(2.0)	284.6(--)	464.1(2.3)	1.5
MoO_3	powd.	235.1(1.9)	232.2(1.9)			
TiO_2	"				464.1(2.5)	458.2(1.5)

FWHM = full width at half of the maximum height;

a = Binding energies of the catalysts were determined by referring to the $Ti2p_{3/2}$ line at 458.5 eV;

b = Binding energies of the standard compounds were determined by referring to the C1s line at 284.6 eV.

Table 4.15

Binding energy values in eV of MoO/TiO_2 catalysts prepared by impregnation using molybdenum oxalate,[2] and pure MoO_3 and TiO_2

wt.% MoO_3	sample state	Binding energy (FWHM) $Mo3d_{3/2}$	$Mo3d_{5/2}$	C1s	$Ti2p_{1/2}$	FWHM(eV)[a] $Ti2p_{3/2}$
0.5	powd. calc.	235.4(2.2)	232.2(2.3)	284.1(--)	464.3(2.5)	1.5
1.0	"	235.4(2.1)	232.6(2.1)	284.4(--)	464.1(2.4)	1.5
2.0	"	236.7(2.1)	233.4(2.1)	284.7(--)	464.4(2.4)	1.5
3.0	"	235.8(2.0)	232.9(3.0)	284.5(--)	464.3(2.3)	1.5
4.0	"	235.2(1.9)	232.1(1.9)	284.3(--)	464.2(2.3)	1.5
MoO_3[b]	powd.	235.1(1.8)	232.2(1.8)			
TiO_2	"				464.1(2.5)	458.2(1.5)

FWHM = full width at half of the maximum height;

a = Binding energies of the catalysts were determined by referring to the $Ti2p_{3/2}$ line at 458.5 eV;

b = Binding energies of the standard compounds were determined by referring to the C1s line at 284.6 eV.

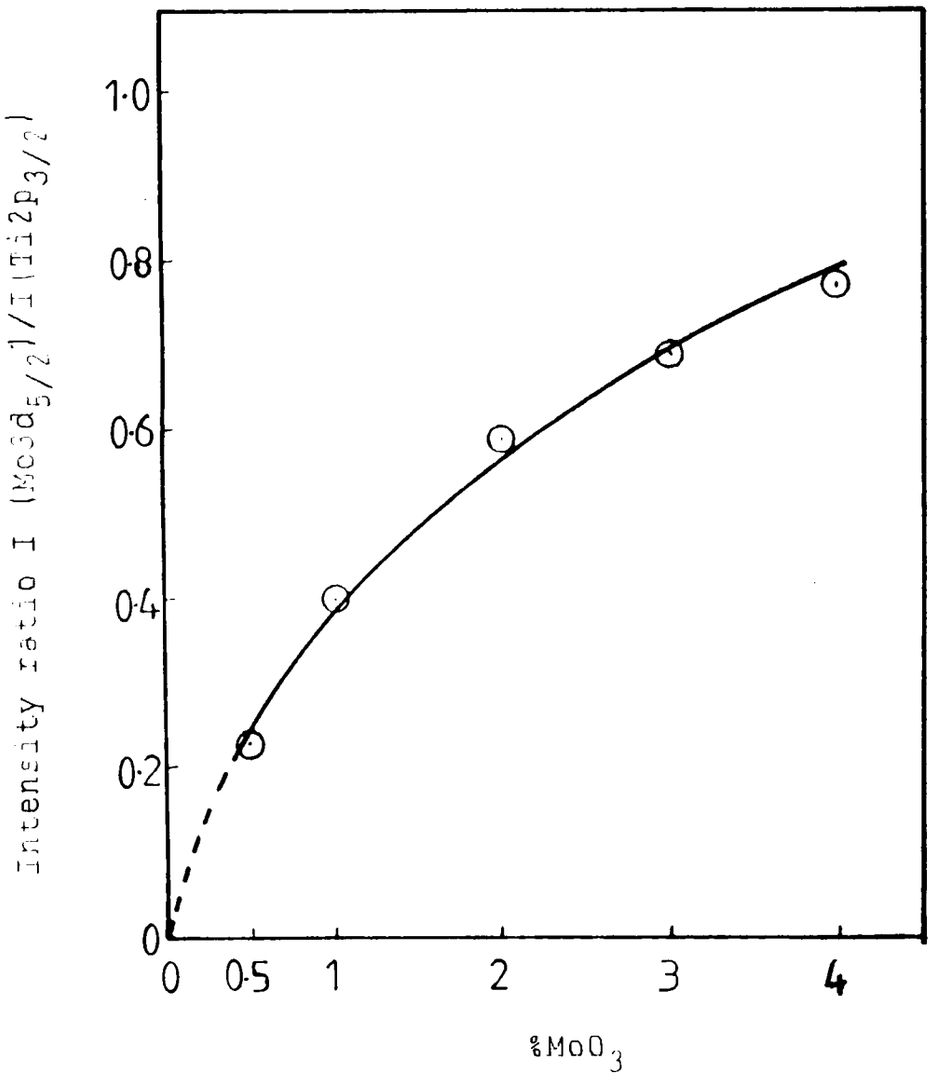

Fig. 4.31 Variation of XPS intensity ratios with MoO_3 content for the MT/C catalysts.

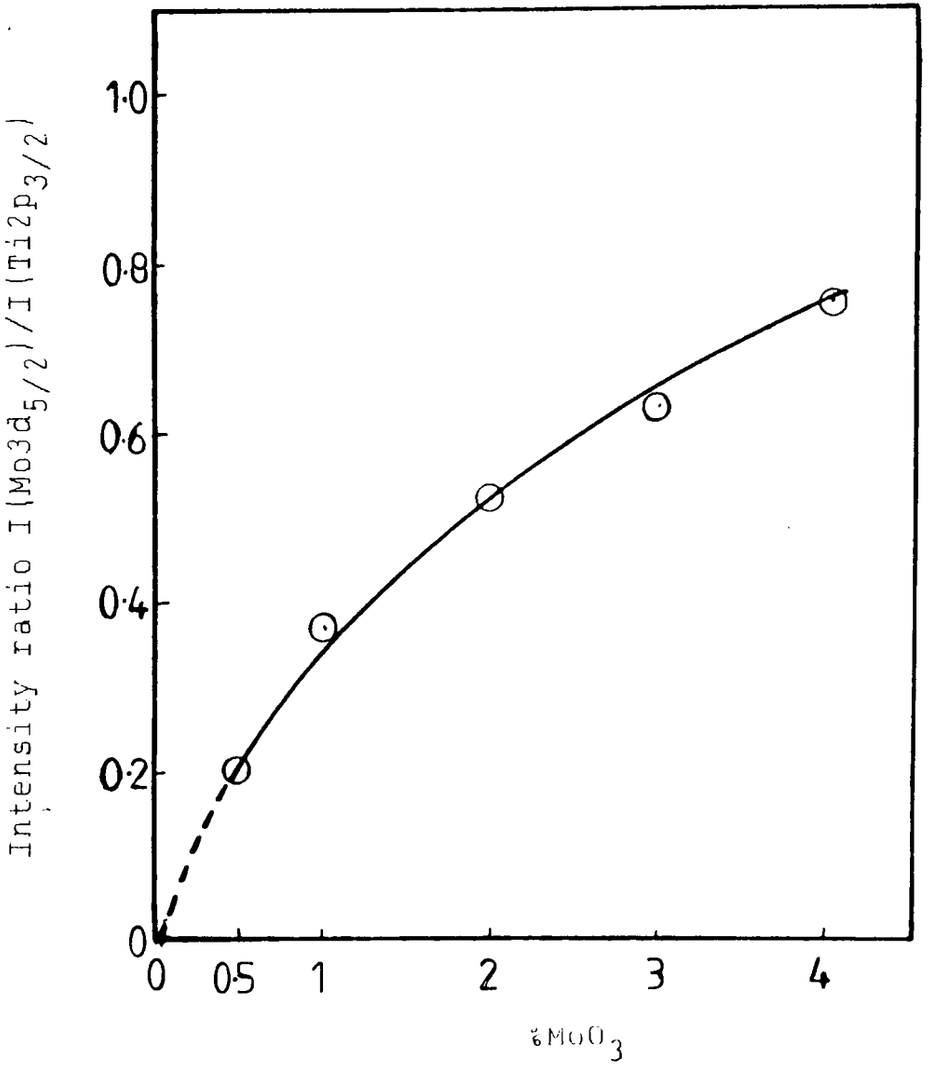

Fig. 4.32 Variation of XPS intensity ratios with MoO_3 content for the MOT/C catalysts.

4.1.3.2 CoO_x/TiO_2 catalysts

Three series of CoO_x/TiO_2 catalysts were prepared, (i) by impregnation using cobalt nitrate as precursor (CT/C), (ii) by homogeneous precipitation using the same precursor (CT/HP), and (iii) by impregnation using cobalt acetate as precursor (CAT/C).

The XPS spectra for the calcined samples from the CT/C series are shown in Fig. 4.33, while Figs. 4.34 and 4.35 illustrate the XPS spectra for the calcined samples in CT/HP and CAT/C series, respectively. The binding energy values (BE) for CT/C, CT/HP, and CAT/C series are given in Tables 4.16, 4.17 and 4.18, respectively. When the assignment of the peak is dubious, only BE for $Co2p_{1/2}$ is given. The XPS spectra in CoO, CoO_3O_4, and $CoTiO_3$ are shown in Fig. 4.36. In all the three series, it is clear that the binding energies and the peak shapes change as the metal loading is altered. As the Co concentration is increased there is a consistent decrease in binding energy. Moreover, the peak shape becomes less symmetrical, which is particularly evident when the slopes of the loading (i.e., low binding energy) edges are examined.

Comparison of peak shapes and binding energies reveals that at low concentrations, the catalysts (0.6 wt.% and 1.2 wt.% CoO) closely resemble $CoTiO_3$, whereas the peak shape and binding energy of the high concentration catalyst (7.2 wt.% and 9.6 wt.% CoO) and Co_3O_4 are nearly identical. The binding energy and peak shape of the CoO 2.4 wt.% and 4.8 wt.% samples are intermediate between the two. These

Fig. 4.33 XPS spectra for the CoO_x/TiO_2 catalysts (CT/C series)

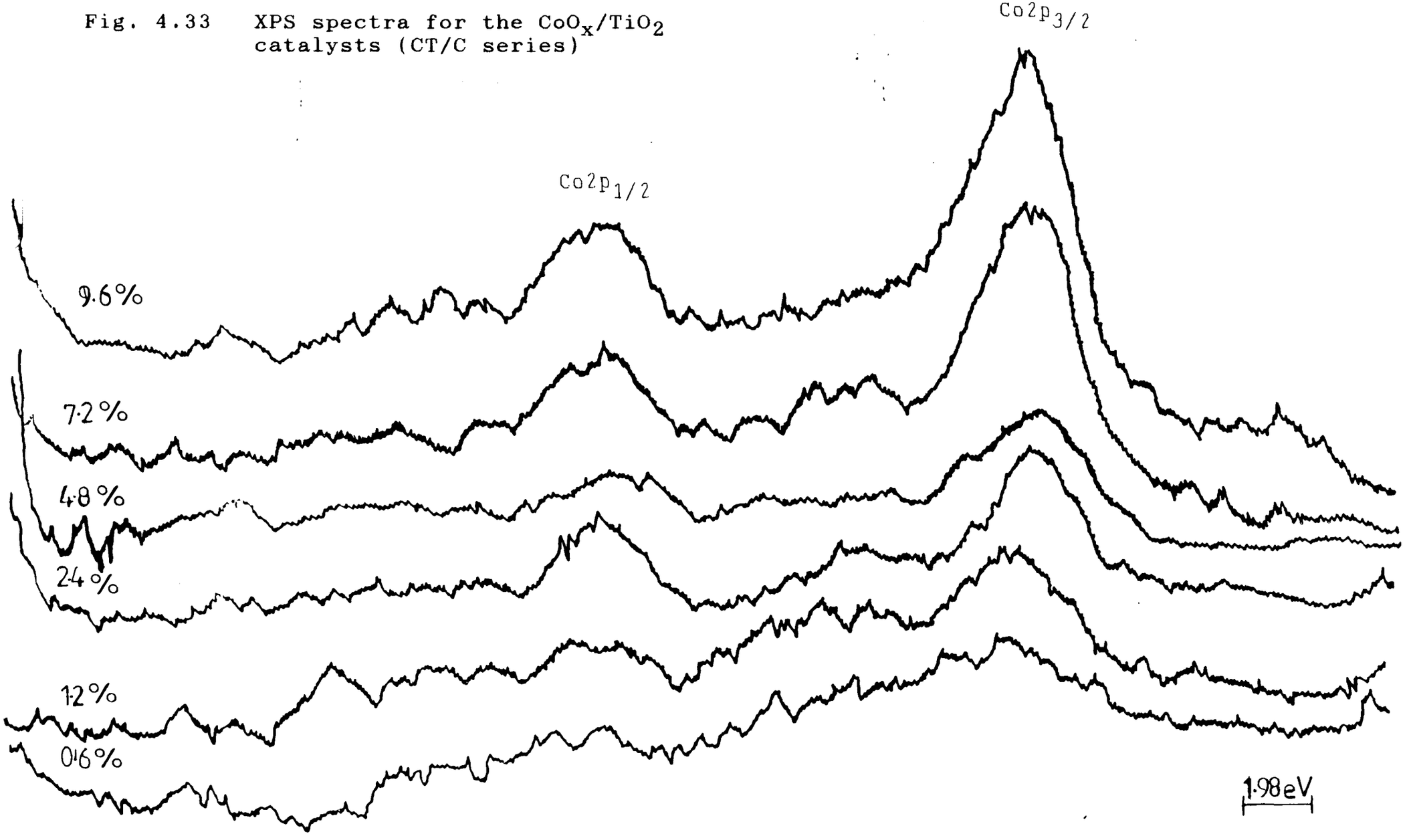

Fig. 4.34 XPS spectra for the CoO_x/TiO_2 catalysts (CT/HP series).

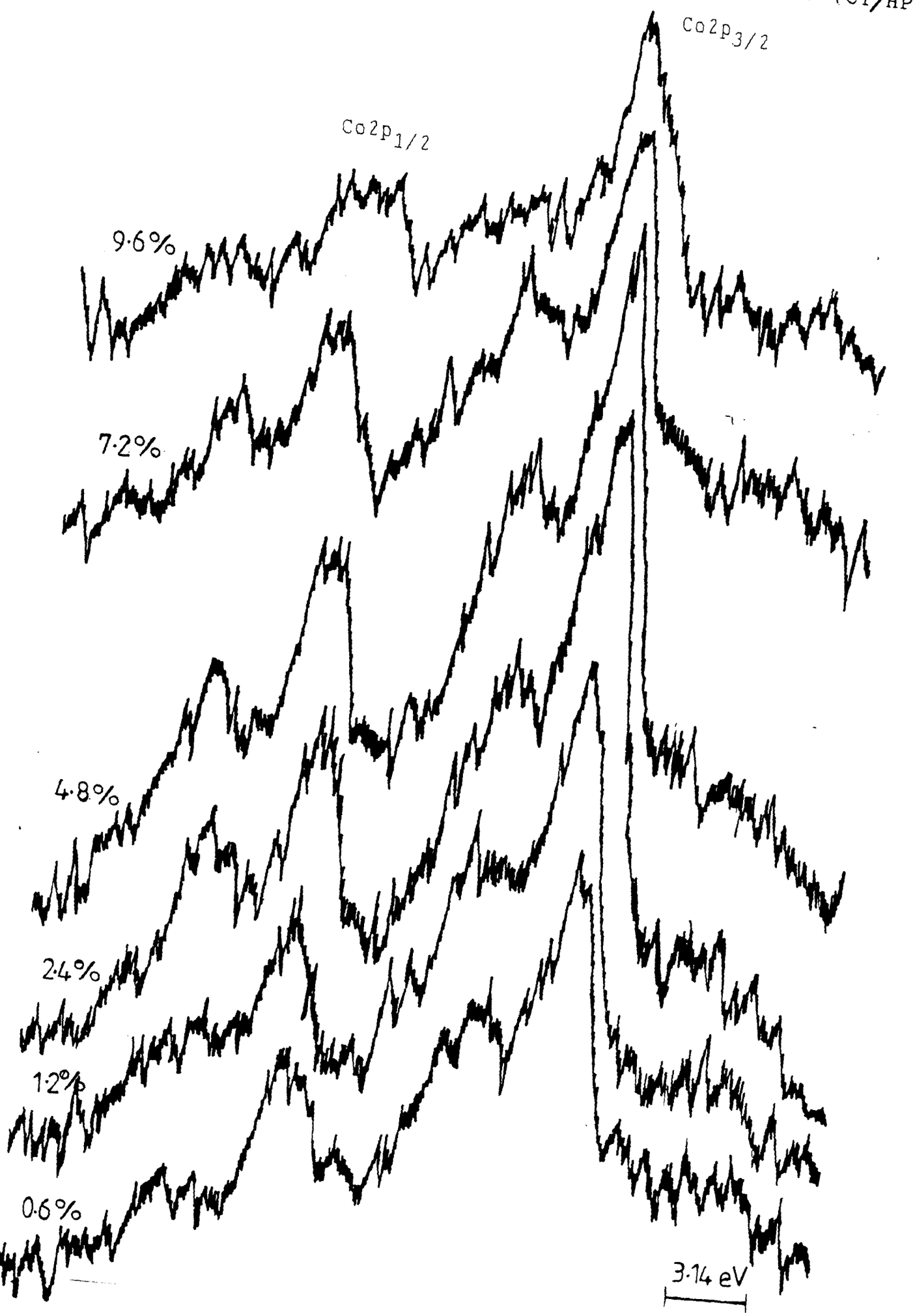

ig. 4.35 XPS spectra of the CoO_x/TiO_2 catalysts (CAT/C series).
(a) 0.19 wt.% CoO
(b) 0.38 wt.% CoO
(c) 0.75 wt.% CoO
(d) 1.5 wt.% CoO
(e) 2.25 wt.% CoO
(f) 3.00 wt.% CoO

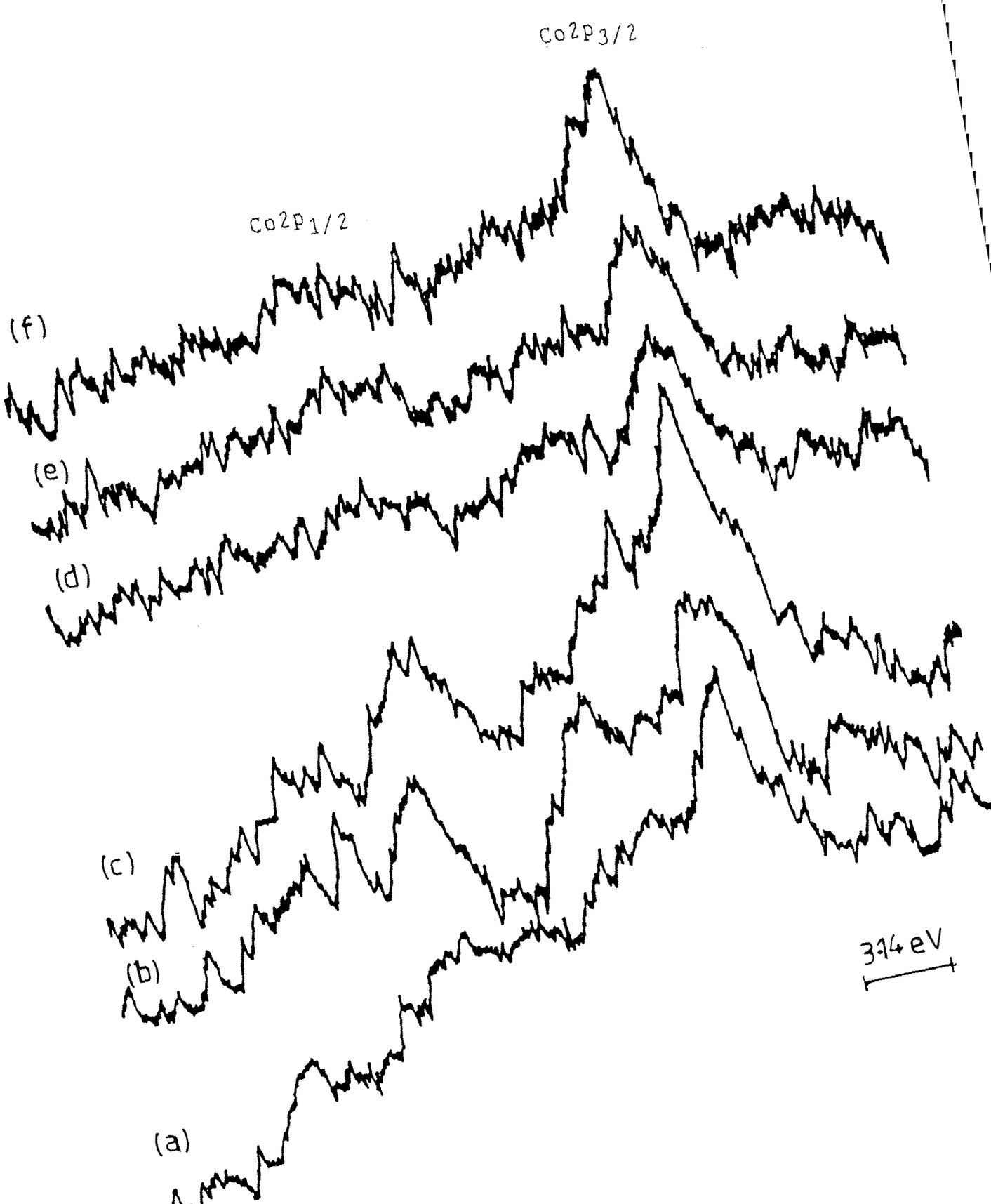

Table 4.16 Binding energy values in eV for the CoO/TiO_2 catalysts prepared by impregnation using cobalt nitrate, and for unsupported CoO, Co_3O_4, and $CoTiO_3$ (CT/C series).

CoO%	sample condition	Ti $2p_{1/2}$	Co $2p_{1/2}$	$Co^{+2}2p_{3/2}$	$Co^{+3}2p_{3/2}$
0.6	calcined	463.8	796.4	782.4	780.9
1.2	"	463.9	797.1	782.7	780.7
2.4	"	463.8	796.7	782.5	780.4
4.8	"	464.1	796.6	782.4	780.2
7.2	"	464.1	796.4	782.2	780.3
9.6	"	464.2	795.1	782.0	780.2
^{x}CoO	-		796.7[c] 796.2[l]	780.3[c] 780.3[l]	
$^{\lozenge}Co_3O_4$	-		795.9[c] 795.4[l]		781.1[c] 781.1[l]
$CoTiO_3$	-		796.8[c]	780.6[c]	

c = calculated

l = literature

x (ref. 6)

◊ (ref. 7)

Table 4.17 Binding energy values in eV for the CoO/TiO_2 catalysts prepared by homogeneous precipitation using cobalt nitrate, and for unsupported CoO, Co_3O_4, and $CoTiO_3$. (CT/HP series).

CoO%	sample condition	Ti $2p_{1/2}$	Co $2p_{1/2}$	$Co^{2+}2p_{3/2}$	$Co^{+3}2p_{3/2}$
0.60	calcined	464.7	796.7	782.3	781.7
1.20	"	464.6	796.6	782.2	781.6
1.80	"	464.6	796.5	782.1	781.4
2.40	"	464.5	796.3	782.0	781.2
3.60	"	464.5	796.4	781.9	780.8
4.80	"	464.5	796.2	781.3	780.6
7.20	"	464.4	796.1	781.2	779.5
9.60	"	464.2	796.0	781.1	779.3
^{x}CoO	-	-	796.7[c]	780.3[c]	
	-	-	796.2[l]	781.1[l]	
$^{\Diamond}Co_3O_4$			795.9[c]		780.3[c]
			795.4[l]		780.3[l]
$CoTiO_3$			796.8[c]	780.6[c]	

x see ref. (6)

◊ see ref. (7)

Table 4.18 Binding energy values in eV for the CoO/TiO_2 catalysts prepared by impregnation using cobalt acetate, and for unsupported CoO, Co_3O_4, and $CoTiO_3$. (CAT/C series).

CoO%	sample condition	Ti $2p_{1/2}$	Co $2p_{1/2}$	$Co^{2+}2p_{3/2}$	$Co^{+3}2p_{3/2}$
0.19	calcined	464.3	796.7	782.1	780.5
0.38	"	464.2	796.5	781.5	780.4
0.56	"	464.1	796.3	781.4	780.3
0.75	"	464.1	795.9	781.2	780.1
1.25	"	463.9	795.7	780.9	779.8
1.50	"	463.7	795.6	780.7	779.7
2.25	"	463,6	795.4	780.3	779.4
3.00	"	463.5	795.4	780.1	779.2
^{x}CoO			796.7[c] 796.2[l]	781.1[c] 781.1[l]	
$\Diamond Co_3O_4$			795.9[c] 795.4[l]		780.3[c] 780.3[l]
$CoTiO_3$			796.8[c]	780.6[c]	

x ref. (6)

◊ ref. (7)

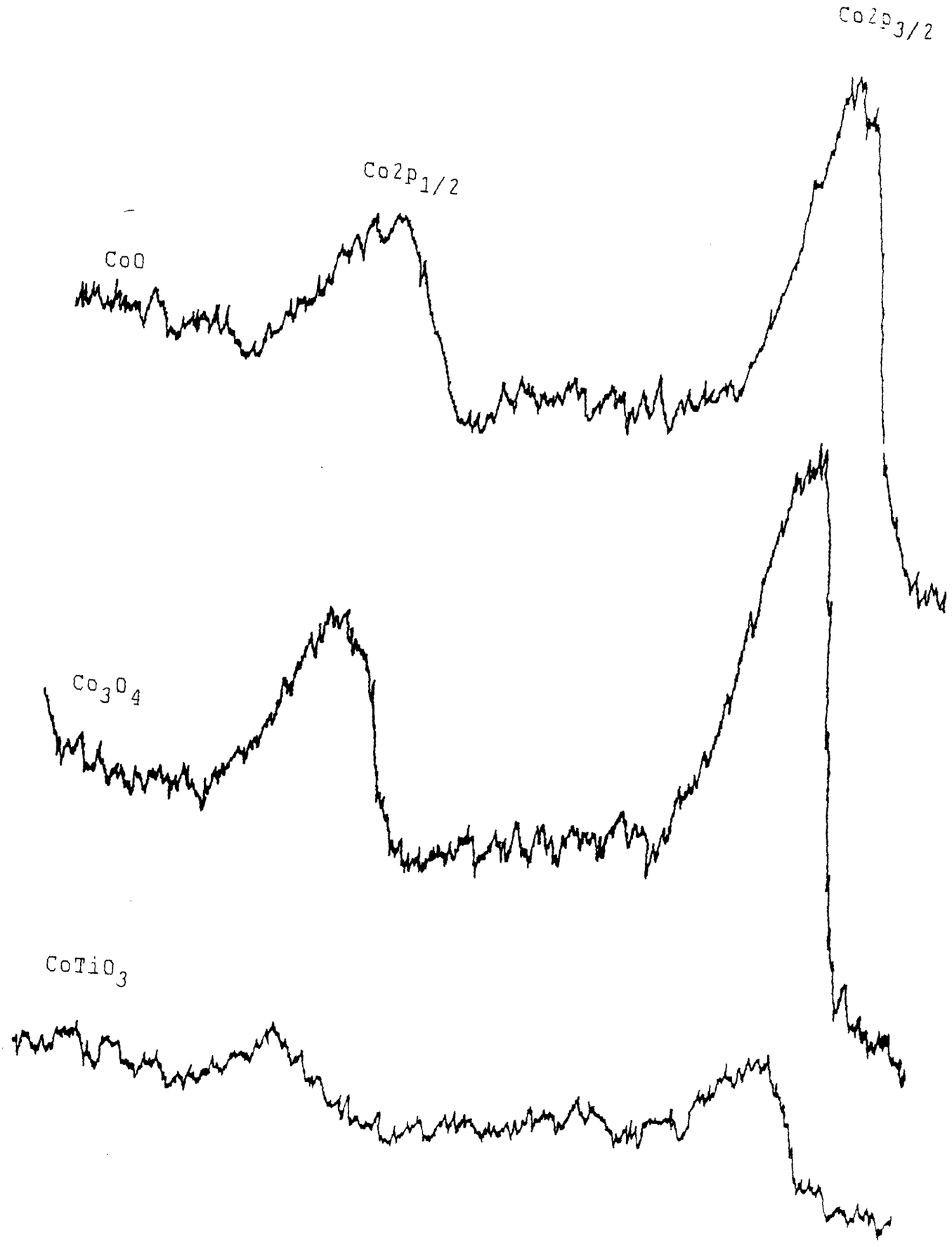

Fig. 4.36 XPS spectra of CoO, Co_3O_4 and $CoTiO_3$.

results indicate that the surface characterization of the three series of catalysts depends on the metal loadings. At low CoO loadings the CoO species on the surface closely resembles CoO and $CoTiO_3$; however, exact matching of XPS binding energies is not a sufficient criterion to confirm an exact species. Increasing the metal concentration results in a shift in the relative distribution of Co species which favours segregation of Co_3O_4. These results are consistent with results of other workers[3-5] who have performed XPS measurements on a set of Co/Al_2O_3 catalysts.

The $Co2p_{3/2}/Ti2p_{3/2}$ peak intensity ratio as a function of Co content for all three series is shown in Fig. 4.37. For the CT/C series (Curve I), the intensity ratio generally increases with increasing the CoO content, while for the CT/HP series (Curve II), the ratio increases linearly with CoO loadings up to 2.1 wt.% CoO, then rapidly up to 3.35 wt.% CoO and levels off until 8.7%CoO. With the CAT/C series, the rapid increase that is observed in the CT/HP series starts at lower loadings (0.15 - 0.31 wt.% CoO) and then a plateau is formed up to 1.9 wt.%CoO, and the intensity ratio increases again at 2.70 wt.% CoO (Curve III). The differences in the shape of the three curves is obviously due to different methods of preparation.

4.1.3.3 $CoO-MoO_3/TiO_2$

Three series of the $CoO-MoO_3/TiO_2$ system were prepared; (i) CoO impregnated first, then the MoO_3 (CMT series), (ii) MoO_3 impregnated first, then the CoO (MCT series) and (iii) the CoO and MoO_3 impregnated simultaneously (CMTg

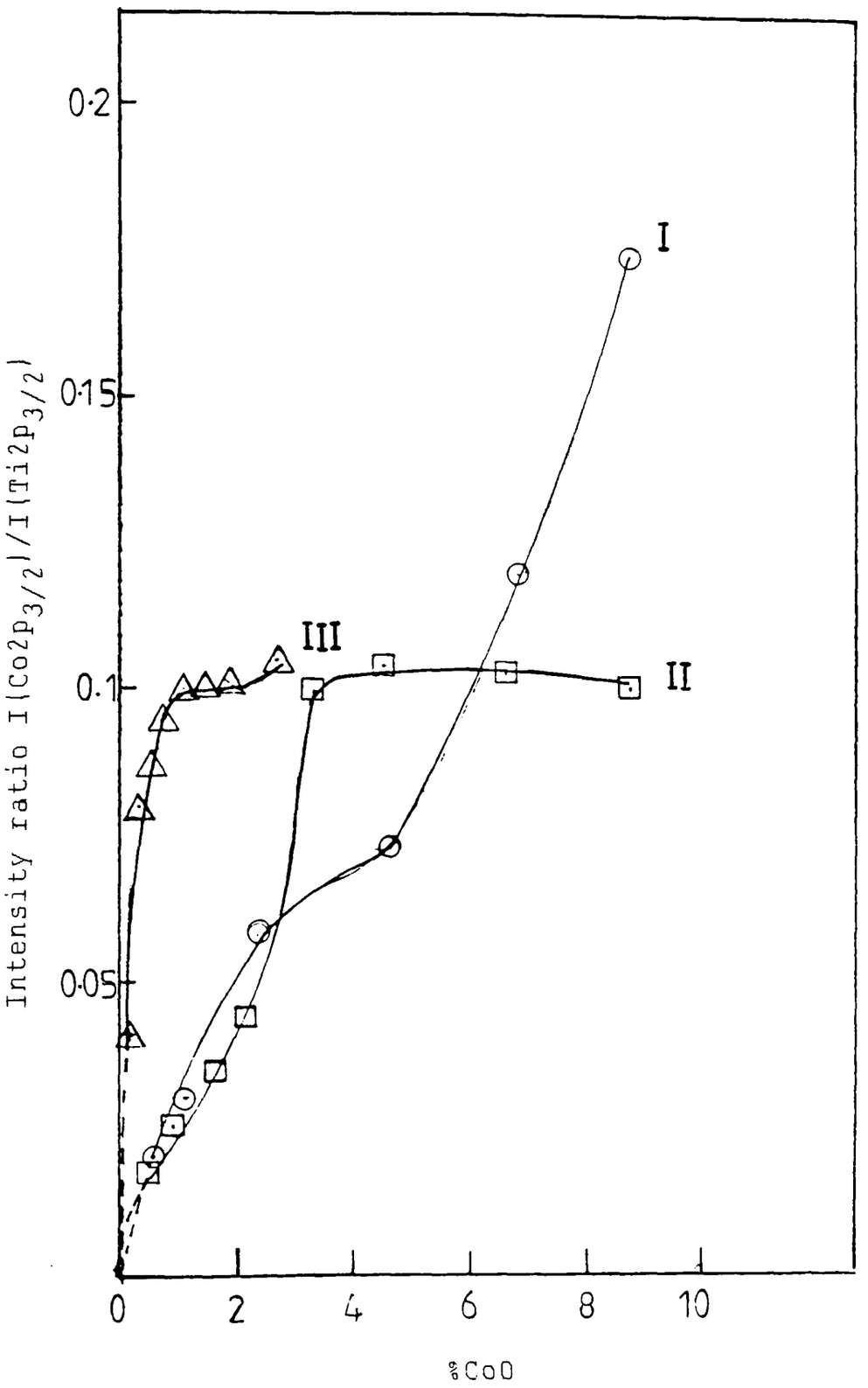

Fig. 4.37 Variation of intensity ratios of $Co2p_{3/2}/Ti2p_{3/2}$ with CoO content for,(I) CT/C series, (II) CT/HP series and, (III) CAT/C series.

series). The XPS spectra of Co in CMT7, MCT7 and CMTg7 catalysts are shown in Fig. 4.38. The peak shape does not vary much, but the peak intensity is slightly higher in (b) and (c) than in (a), which is due to variations in the quantity of sample exposed to the X-ray radiation. Fig. 4.39 shows the XPS spectra of Mo in the same previous three catalysts compared with pure $CoMoO_4$. The split of Mo3d levels, i.e. $Mo3d_{3/2}$ and $Mo3d_{5/2}$ is almost identical, in other words, it is independent on the sequence of impregnation.

Binding energy values of CMT, MCT, and CMTg series are given in Tables 4.19, 4.20 and 4.21, respectively. By comparing the BE's in all the three series, one observes the trend of a decrease in BE values with increasing metal loadings; also a shift in BE compared with pure compounds such as CoO, MoO_3, $CoTiO_3$, and $CoMoO_4$ can be seen.

A decrease of the XPS signal of one of the metal ions (Co or Mo) can arise from one of the following: (i) a reduction of the total amount of the referred metal ion, i.e. changes in the ratio r = Co/(Co + Mo); (ii) a decrease of its dispersion on the surface; (iii) an overlaying of it by layers of the second metal ion (or a dissolution in this layer); (iv) a migration of the referred metal ion into the support. On the other hand, a decrease of the $Ti2p_{3/2}$ signal indicates that the support is covered by Co and/or Mo ions.

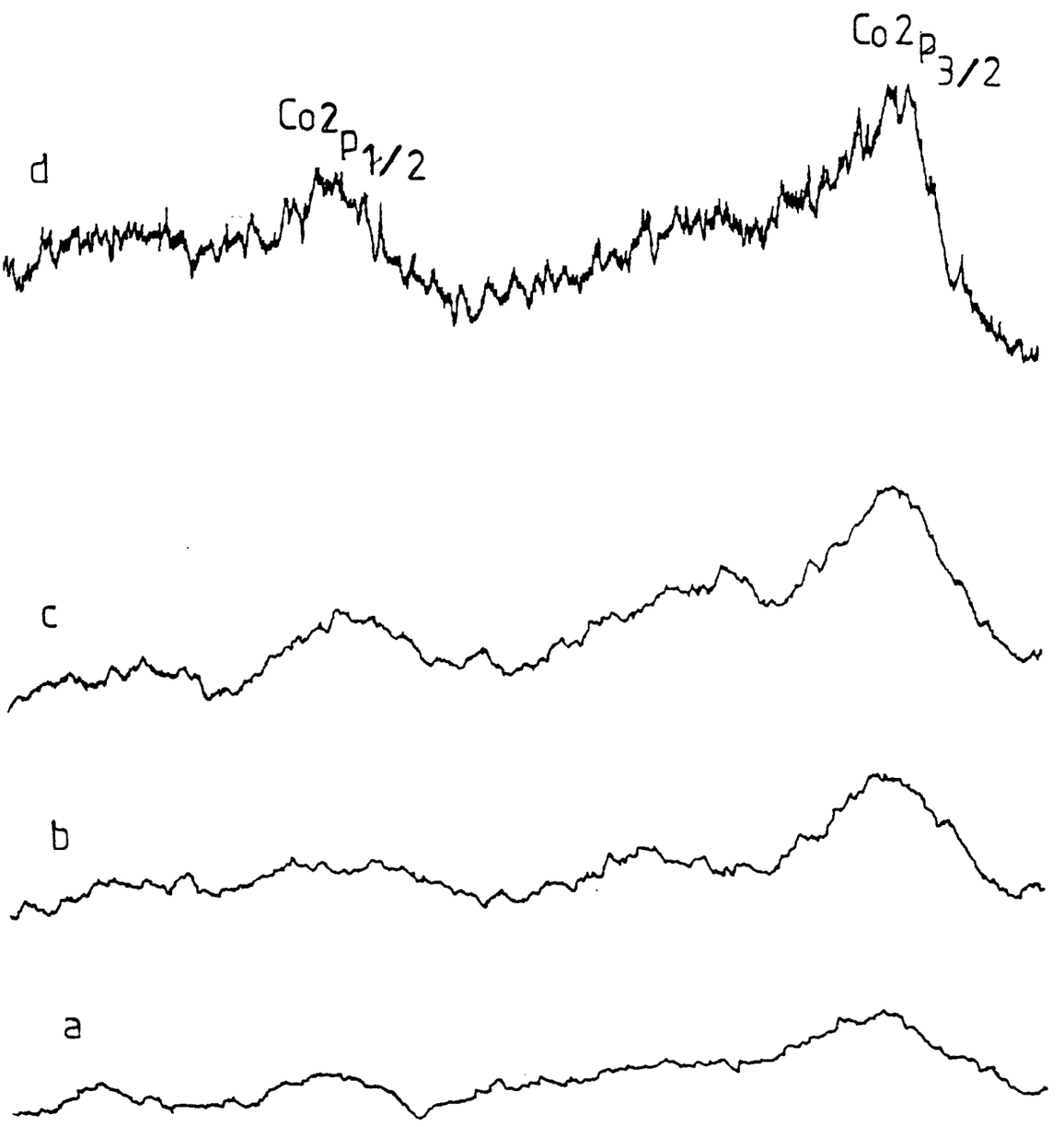

Fig. 4.38 XPS spectra of Co 2p where (a) CMT 7 catalyst, (b) MCT 7 catalyst, (c) CMTg 7 catalyst and (d) $CoMoO_4$.

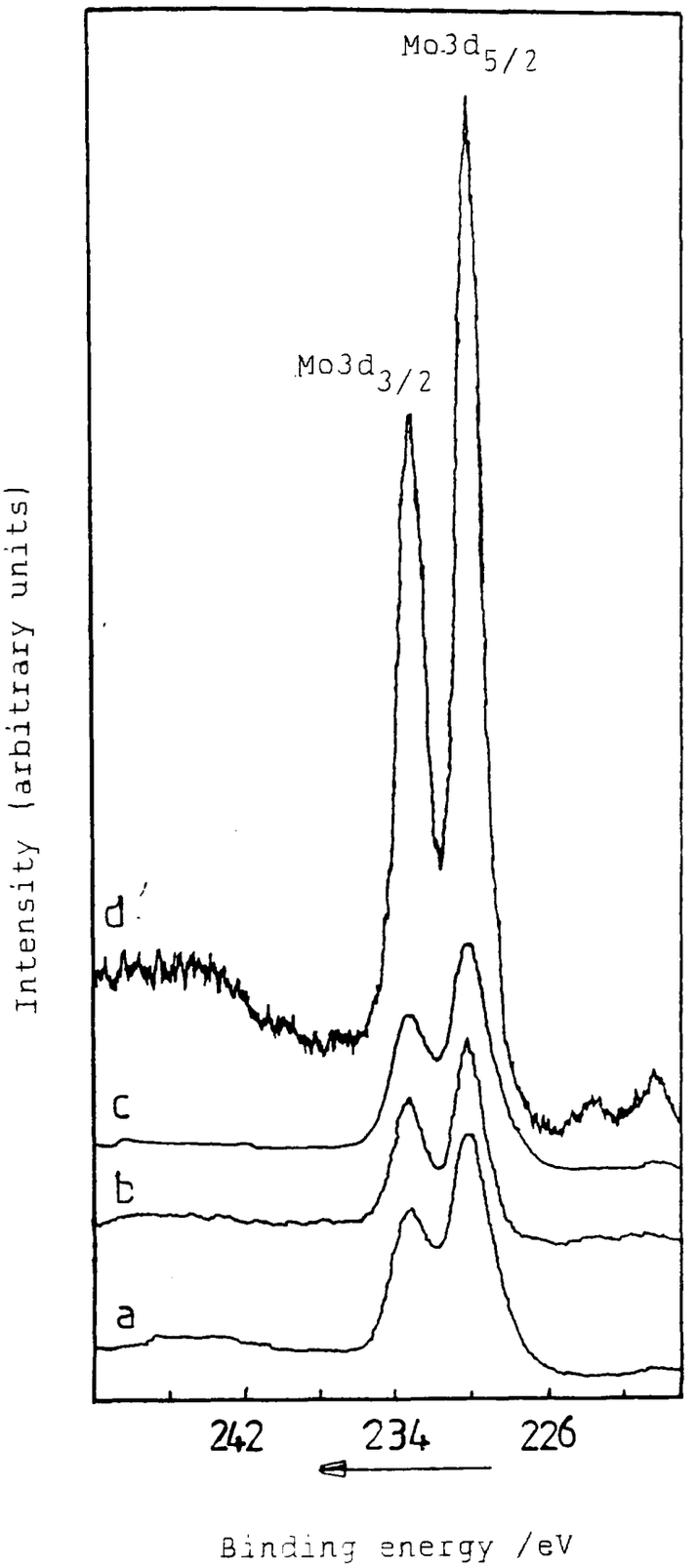

Fig. 4.39 XPS spectra of the Mo 3d where (a) CMT 7 catalyst, (b) MCT 7 catalyst, (c) CMTg catalyst, and (d) $CoMoO_4$.

Table 4.19

Binding energy values in eV for $CoO-MoO_3/TiO_2$ catalysts prepared by impregnation (CoO impregnated first then MoO_3, i.e. CMT series)

Sample	sample condition	loading		total $CoO+MoO_3$	$Ti2p_{1/2}$	$Co2p_{1/2}$	$Co2p^{+2}_{3/2}$	$Co2p^{3+}_{3/2}$	$Mo3d_{3/2}$ ( )x	$Mo3d_{5/2}$ ( )x
		CoO%	MoO_3%							
CMT1	calcined	0.30	0.60	0.90	464.5	797.1	782.9	781.2	235.8(2.4)	232.9(2.4
CMT2	"	0.60	1.20	1.80	464.3	796.9	782.8	780.9	235.6(2.3)	232.7 (2.3)
CMT3	"	1.20	2.40	3.60	464.1	796.7	782.7	780.6	235.4(2.2)	232.5(2.2)
CMT4	"	1.80	3.70	5.50	464.1	796.5	782.5	780.4	235.4(2.2)	232.4(2.2)
CMT5	"	2.30	4.90	7.20	463.9	796.2	782.3	780.3	235.2(2.1)	232.3(2.1)
CMT6	"	3.10	6.40	9.50	463.7	795.8	782.1	780.2	235.0(2.0)	232.1(2.8)
CMT7	"	4.70	9.20	13.9	463.5	795.5	782.0	780.1	235.1(1.9)	232.2(1.9)
CoO						795.4	780.3			
MoO_3									235.1(1.8)	232.2(1.8)
$CoTiO_3$						796.2	780.6			
$CoMoO_4$							781		236	232.5

x( ) = Full width at half maximum (FWHM) in eV

Table 4.20

Binding energy values in eV for $CoO-MoO_3/TiO_2$ catalysts prepared by impregnation (MoO_3 impregnated first, then CoO, i.e. MCT series)

sample	sample condition	loading		total $CoO+NoO_3$	$Ti2p_{1/2}$	$Co2p_{3/2}$	$Co2p^{2+}_{3/2}$	$Co2p^{3+}_{3/2}$	$Mo3d_{3/2}$ ( )[x]	$Mo3d_{5/2}$ ( )[x]
		CoO%	MoO_3%							
MCT1	calcined	0.30	0.60	0.90	464.4	797.1	780.7	780.1	235.8(2.4)	231.9(2.3)
MCT2	"	0.70	1.20	1.90	464.4	796.7	780.5	779.9	235.9(2.3)	232.7(2.2)
MCT3	"	1.40	2.40	3.80	464.4	796.5	780.5	779.7	235.7(2.2)	232.5(2.1)
MCT4	"	2.30	3.70	6.00	464.0	796.3	780.4	779.5	235.5(2.2)	232.3(2.1)
MCT5	"	2.80	5.00	7.80	464.4	796.3	780.3	779.5	235.1(2.1)	232.1(2.0)
MCT6	"	4.10	7.00	11.1	464.0	796.2	780.2	779.3	235.1(2.0)	232.0(1.9)
MCT7	"	5.00	8.90	13.9	464.4	796.1	780.1	779.1	234.9(1.9)	231.9(1.8)
CoO						795.4	780.3			
MoO_3									235.1(1.8)	232.2(1.8)
$CoTiO_3$						796.5	780.6			
$CoMoO_4$							781		236	232.5

[x] ( ) = Full width at half maximum (FWHM) in eV

Table 4.21

Binding energy values in eV for $CoO-MoO_3/TiO_2$ catalysts prepared by impregnation (CoO and MoO_3 impregnated together, i.e. CMTg series)

Sample	sample condition	loading		total $CoO+MoO_3$	$Ti2p_{3/2}$	$Co2p_{1/2}$	$Co2p^{2+}_{3/2}$	$Co2p^{3+}_{3/2}$	$Mo3d_{3/2}$ ( )x	$Mo3d_{5/2}$ ( )x
		CoO%	MoO_3%							
CMTg1	calcined	0.30	0.70	1.00	464.2	796.9	781.9	780.8	235.9(2.3)	231.8(2.2)
CMTg2	"	0.60	1.20	1,80	464.2	796.7	781.7	780.6	235.7(2.2)	231.5(2.1)
CMTg3	"	1.10	2.30	3.40	464.1	786.5	781.4	780.3	235.5(2.2)	231.4(2.1)
CMTg4	"	1.70	3.50	5.20	464.1	796.3	781.1	779.6	235.2(2.1)	231.2(2.0)
CMTg5	"	2.10	4.80	6.90	464.1	796.1	780.8	779.5	235.1(2.0)	231.1(1.9)
CMTg6	"	4.80	7.80	12.6	464.2	795.7	780.5	779.3	235.1(2.0)	231.1(1.9)
CMTg7	"	6.00	10.2	16.2	464.2	795.5	780.3	779.2	235.1(1.8)	231.)(1.7)
CoO						795.4	780.3			
MoO_3	"								235.1(1.8)	232.2(1.8)
$CoTiO_3$	"					796.5	780.3			
$CoMoO_4$							781		236	232.5

x( ) = Full width at half maximum (FWHM) in eV

The variation of the Co $2p_{3/2}/Ti2p_{3/2}$ and $Mo3d_{5/2}/Ti2p_{3/2}$ ratios for the CMT, MCT and CMTg series with CoO and MoO_3 content is shown in Figs. 4.40, 4.41, and 4.42, respectively. The shape of the curves in the CMT and MCT series are quite similar, but the CMTg series curves differ in shape. The results indicate different surface characteristics for each mode of impregnation.

4.1.4 Transmission electron microscopy (TEM)

4.1.4.1 MoO_3/TiO_2 catalysts

In order to obtain structural information about small metal particles, transmission electron microscopy (TEM) has been used for two series, i.e. MT/C and MOT/C. The TEM micrographs of 2wt.% MoO_3 and 4wt.% MoO_3 catalysts supported on TiO_2 anatase (CLD 867) of MT/C series are shown in Fig. 4.43 (a) and (b), respectively. The catalysts were reduced under TPR conditions (from room temperature to 1000°C). The average particle size of the Mo metal was 2-3nm, whereas the average particle size for the same loading but using molybdenum oxalate as precursor was 22-23nm as shown in Fig. 4.44.

4.1.4.2 CoO_x/TiO_2 catalysts

For the CoO_x/TiO_2 system, it is found that the metal particle size of $\overset{o}{Co}/TiO_2$ catalysts strongly depends on the method of preparation. For example, the average particle size for the $\overset{o}{Co}/TiO_2$ catalyst in CT/C series is about 8-9 nm as shown in Figs 4.45 and 4.46, whereas the average

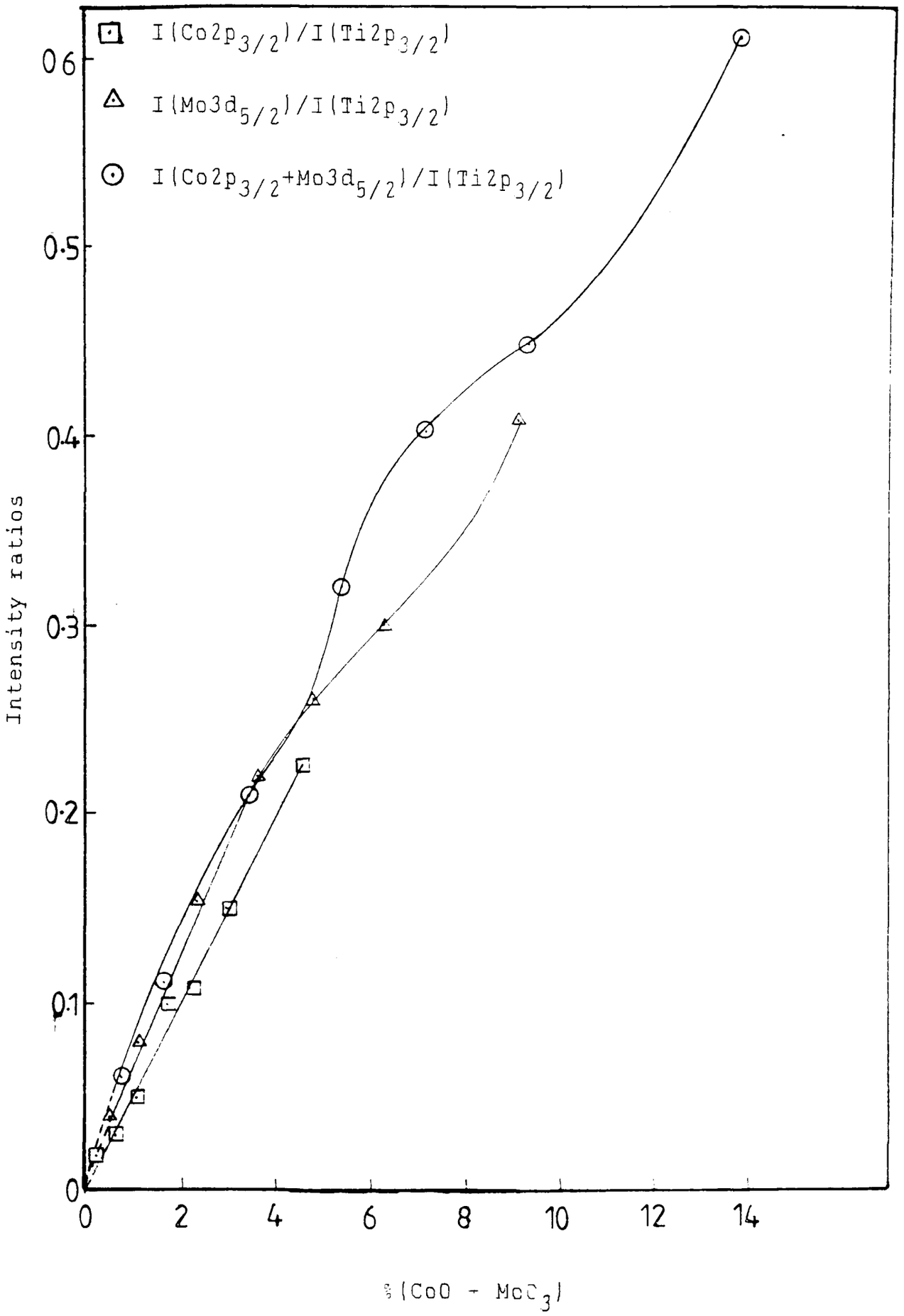

Fig. 4.40 Variation of intensity ratios with CoO and MoO_3 content for the CMT series.

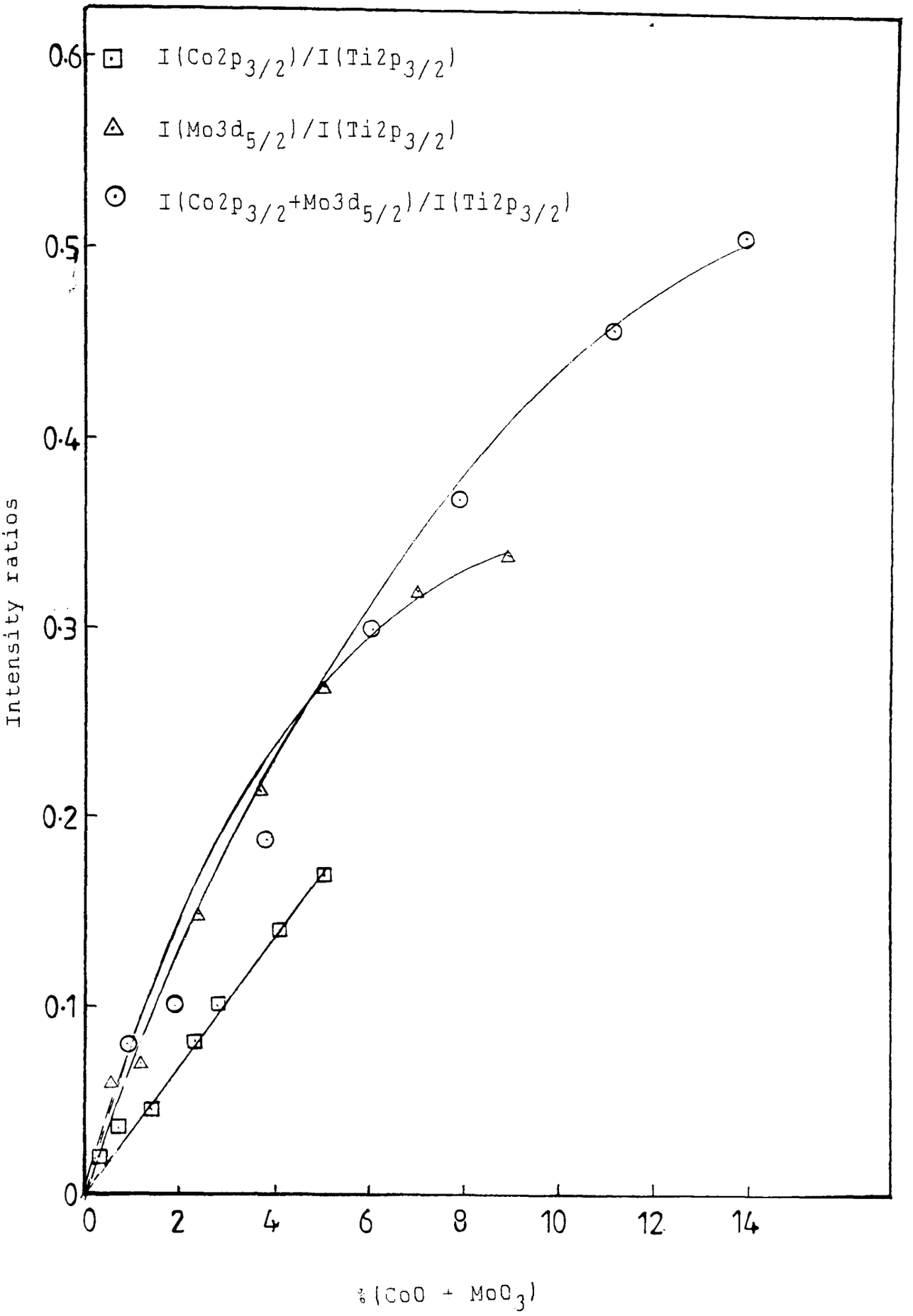

Fig. 4.41 Variation of intensity ratios with CoO and MoO_3 content for the MCT series

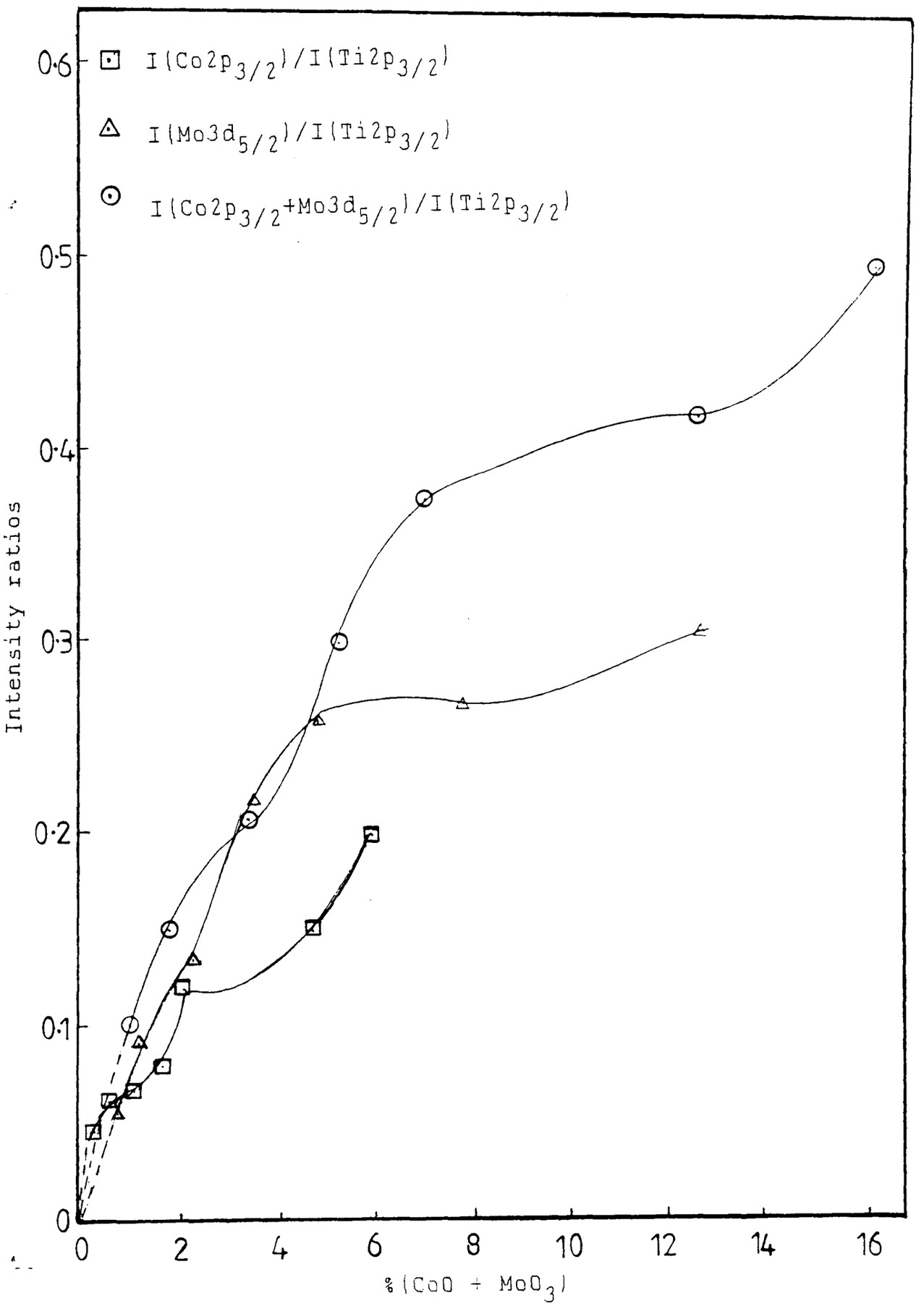

Fig. 4.42 Variation of intensity ratios with CoO and MoO_3 content for the CMTg series.

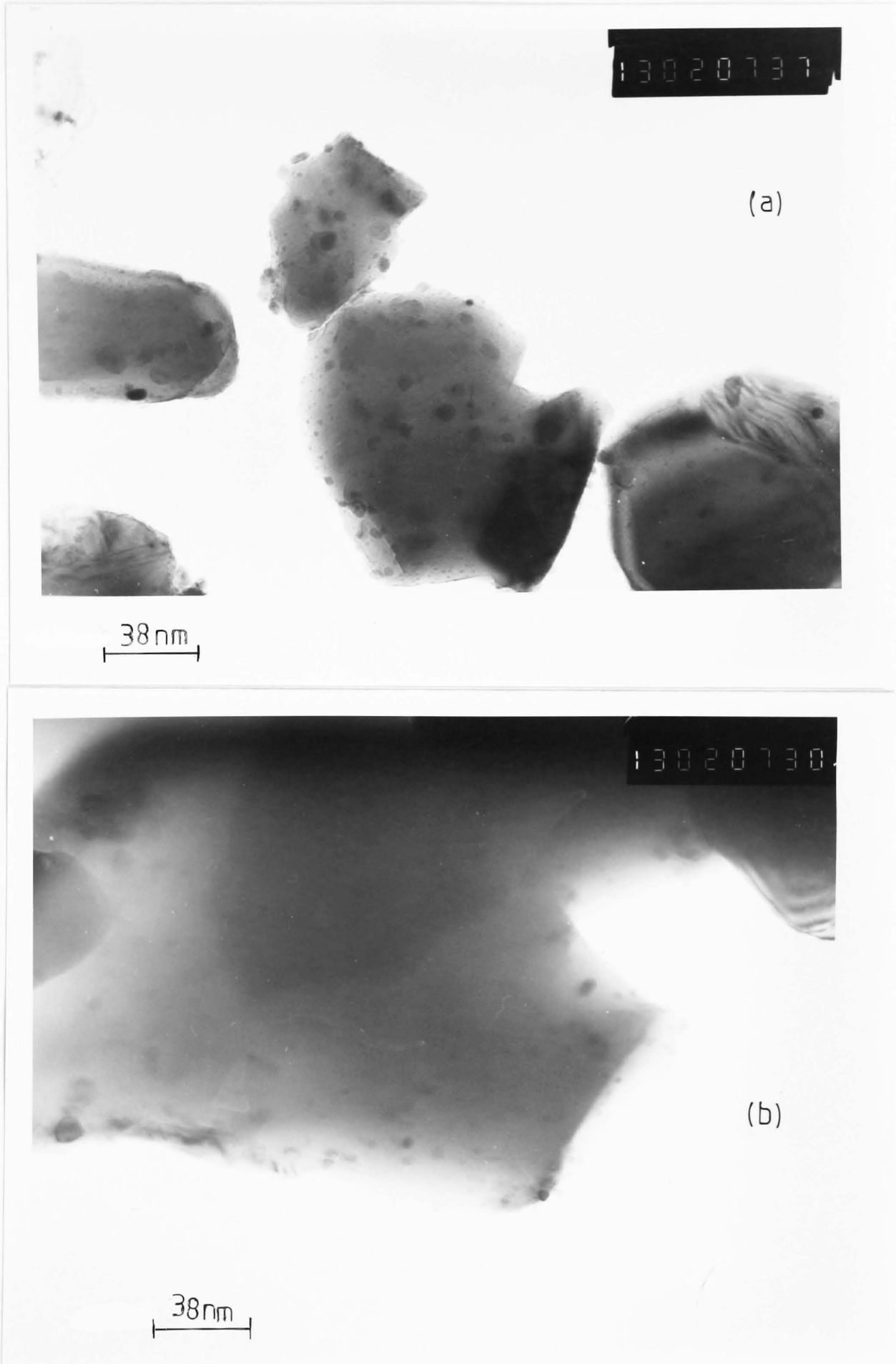

Fig. 4.43 Transmission electron micrographs of (a) 2% Mo/TiO_2 and (b) 4% Mo/TiO_2 catalysts prepared by impregnation using ammonium heptamolybdate and reduced at 1000°C.

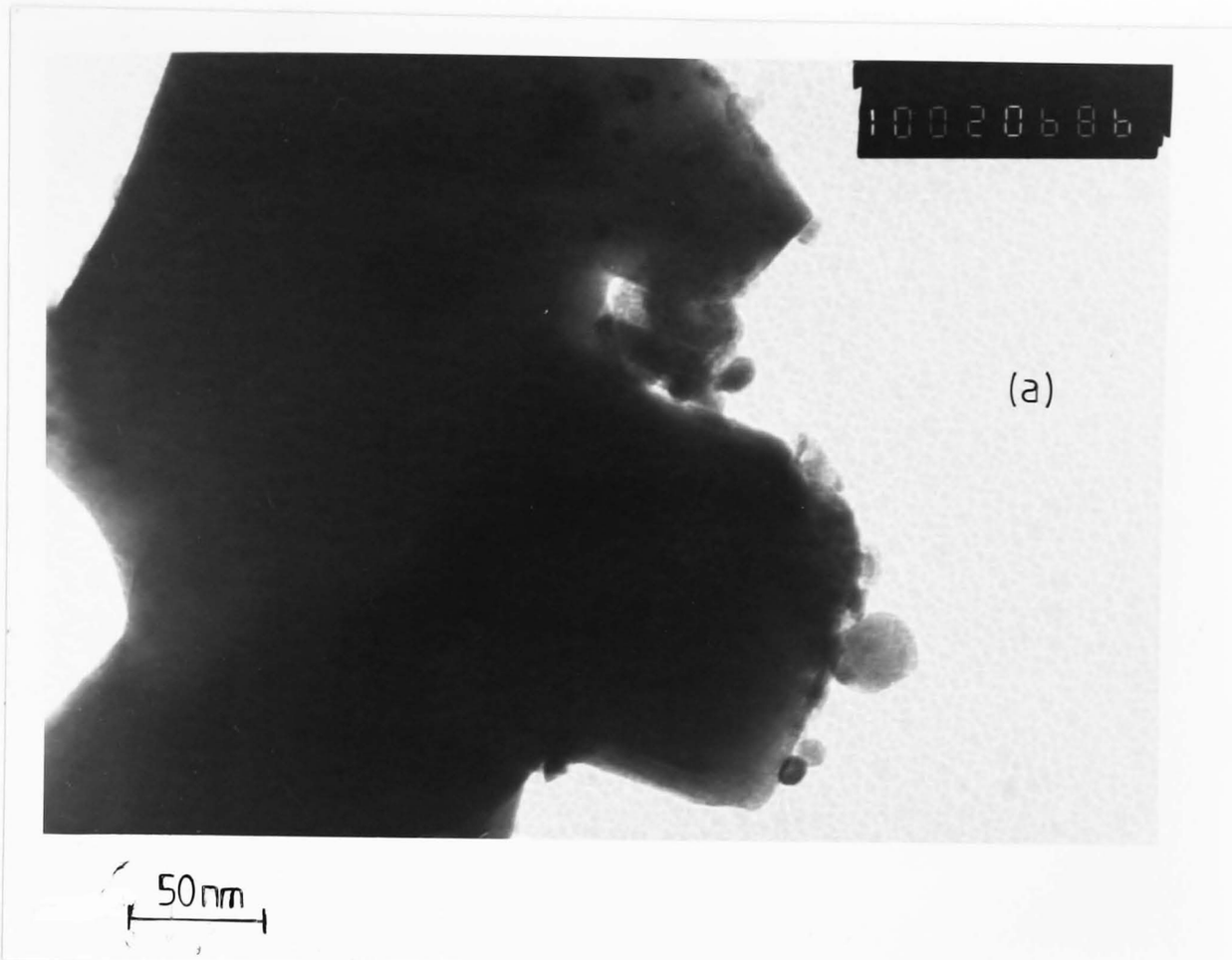

Fig. 4.44 Transmission electron micrographs of (a) 2% Mo/TiO_2 and (b) 4% Mo/TiO_2 catalysts prepared by impregnation using molybdenum oxalate and reduced at 1000°C.

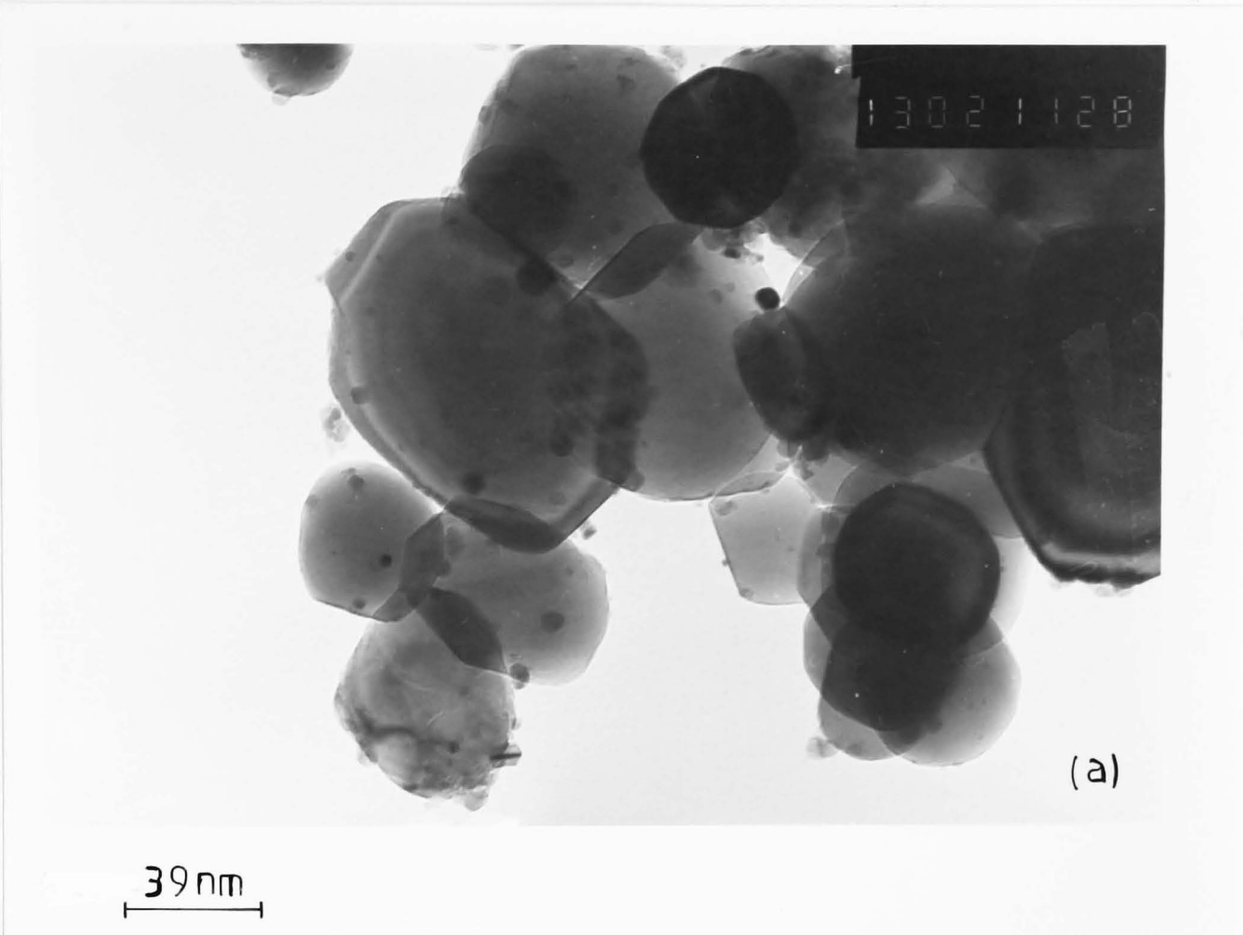

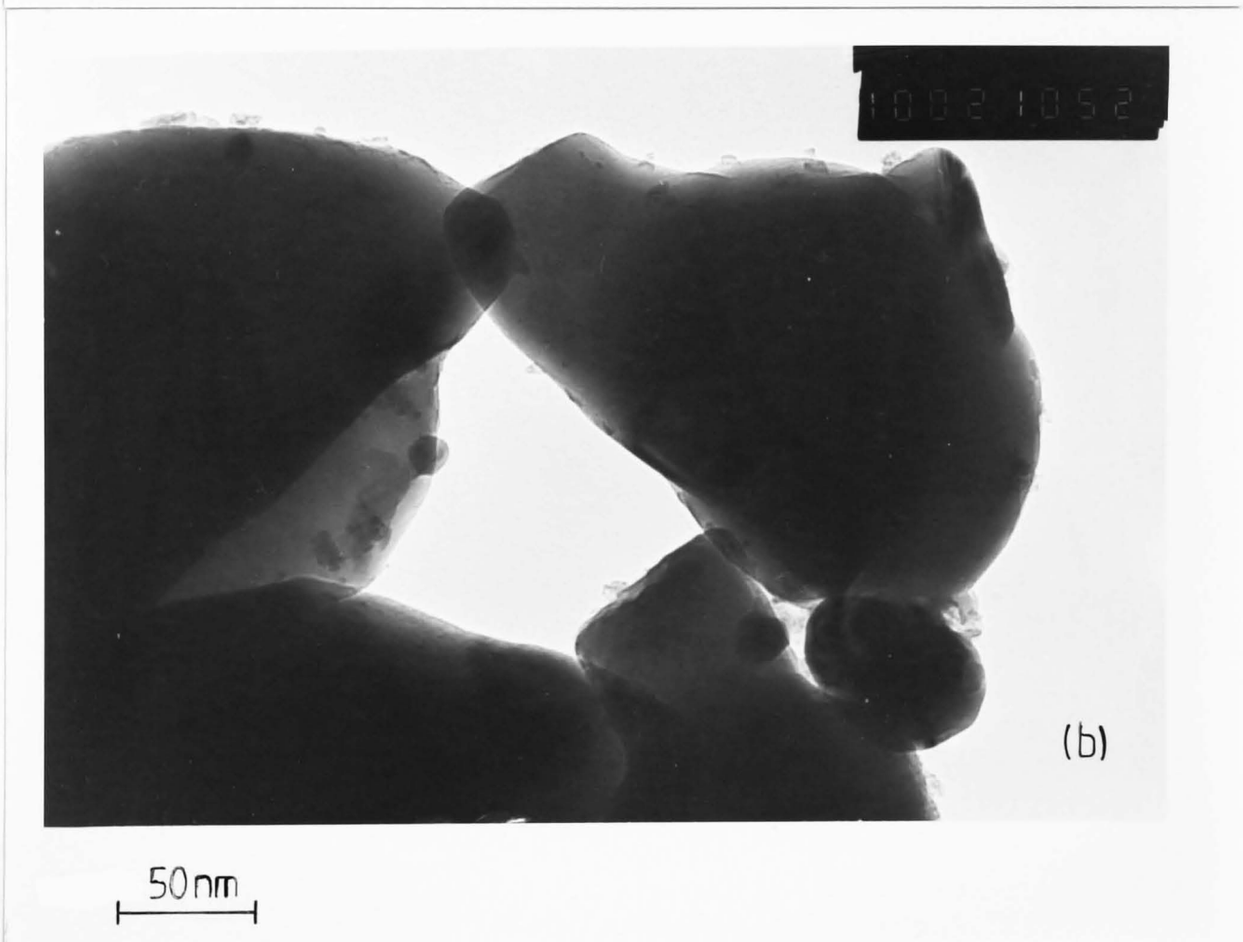

Fig. 4.45 Transmission electron micrographs of (a) 1.2% Co/TiO_2 and (b) 7.2% Co/TiO_2 catalysts prepared by impregnation using cobalt nitrate and reduced at 1000°C.

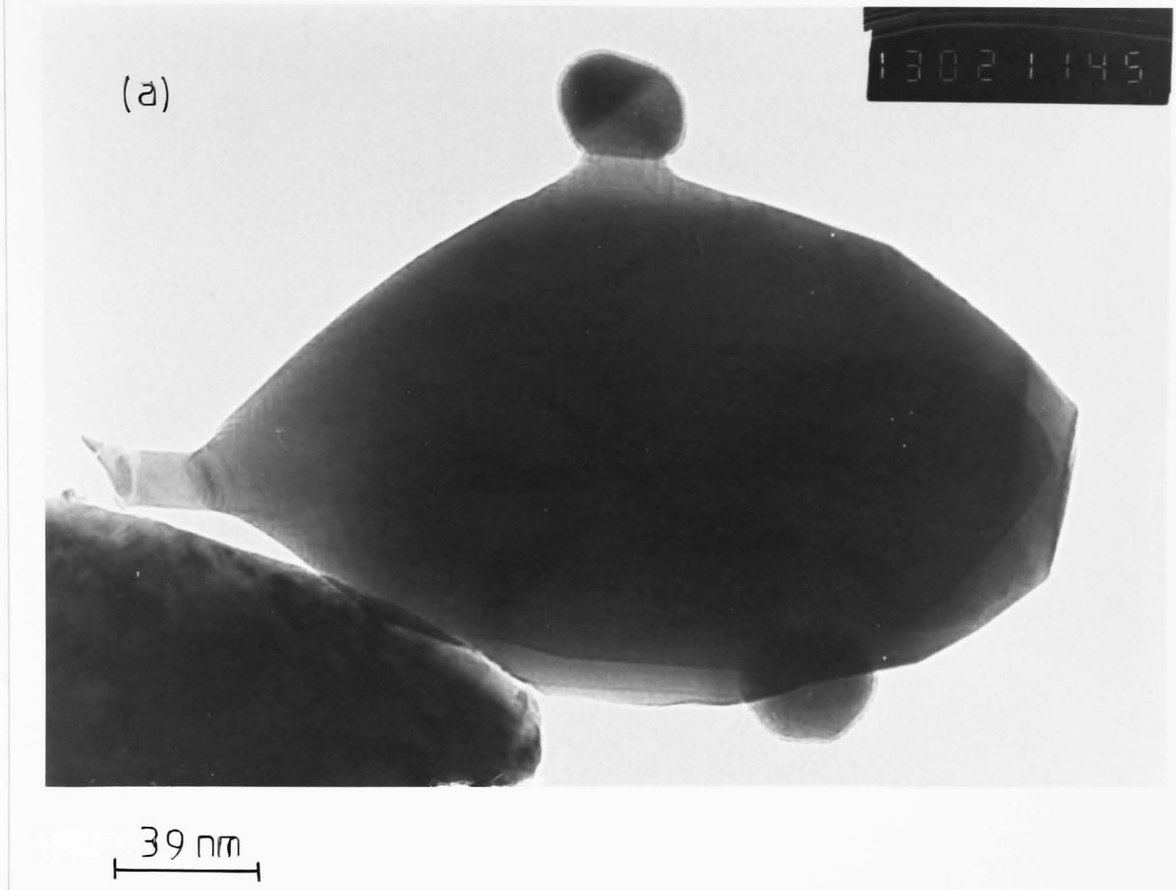

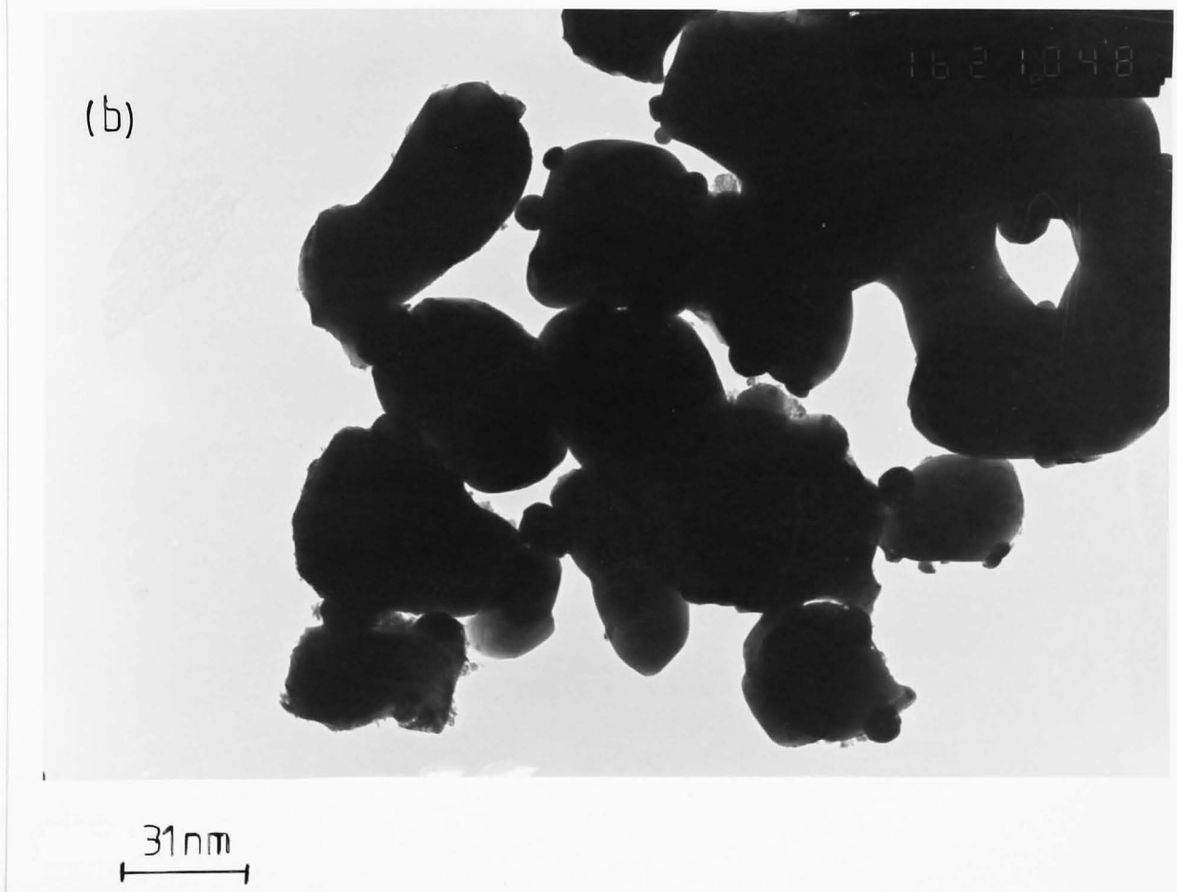

Fig. 4.46 Transmission electron micrographs of (a) 1.2% Co/TiO_2 and (b) 7.2% Co/TiO_2 catalysts prepared by impregnation using cobalt nitrate and reduced at 1000°C.

particle size of the $\overset{o}{Co}/TiO_2$ catalyst prepared by homogeneous precipitation is 2-3 nm as shown in Fig. 4.47, which makes it possible to distribute Co atoms more uniformly among the support, resulting in uniform distribution of small CoO clusters on the support when calcined. On the other hand, the impregnation method yields fairly large CoO clusters by the calcination. Finally, the average particle size of the $\overset{o}{Co}/TiO_2$ catalysts prepared by impregnation using cobalt acetate as precursor is 2-3 nm as shown in Fig. 4.48. One can say that not only the method of preparation but the type of precursor plays a significant role in determining the average particle size and the way the metal is dispersed on the support.

4.1.5 Catalytic decomposition of 2-propanol.

Decomposition of 2-propanol has been applied as a model reaction for studying the acidic properties of the following systems: (i) MoO_3/TiO_2 catalysts, (ii) CoO/TiO_2 catalysts, and (iii) $CoO\text{-}MoO_3/TiO_2$ catalysts.

4.1.5.1 MoO_3/TiO_2 catalysts

2-propanol decomposition was studied over two series of MoO_3/TiO_2 catalysts, prepared by impregnation using ammonium heptamolybdate (AHM), and molybdenum oxalate. MT/C stands for catalysts containing MoO_3/TiO_2, made using (AHM) as precursor, in the calcined state. MOT/C stands for catalysts containing MoO_3/TiO_2, made using molybdenum oxalate as precursor, in the calcined state.

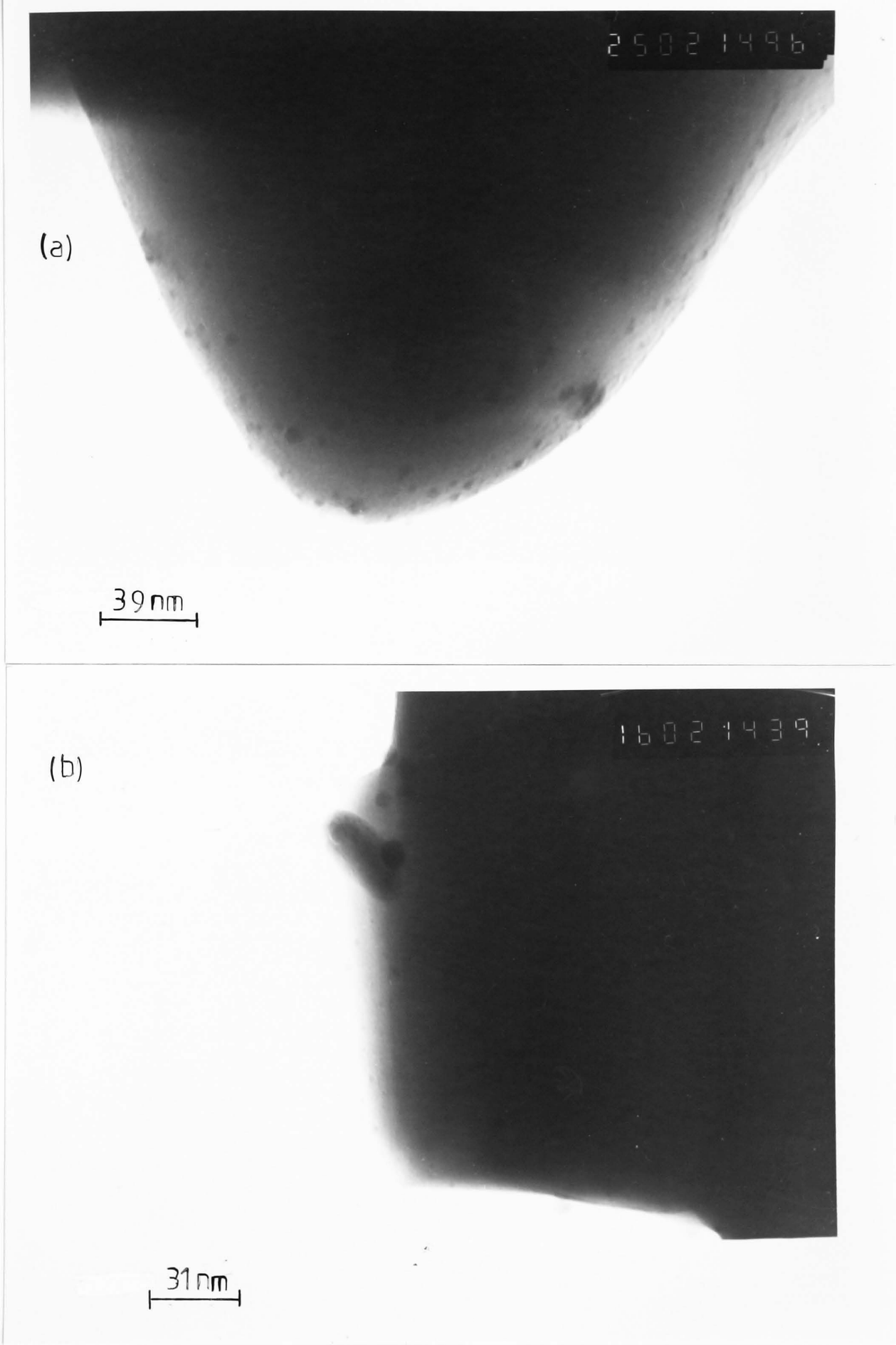

Fig. 4.47 Transmission electron micrographs of (a) 1.2 % Co/TiO_2 and (b) 7.2 Co/TiO_2 catalysts prepared by homogeneous precipitation using cobalt nitrate and reduced at 1000°C.

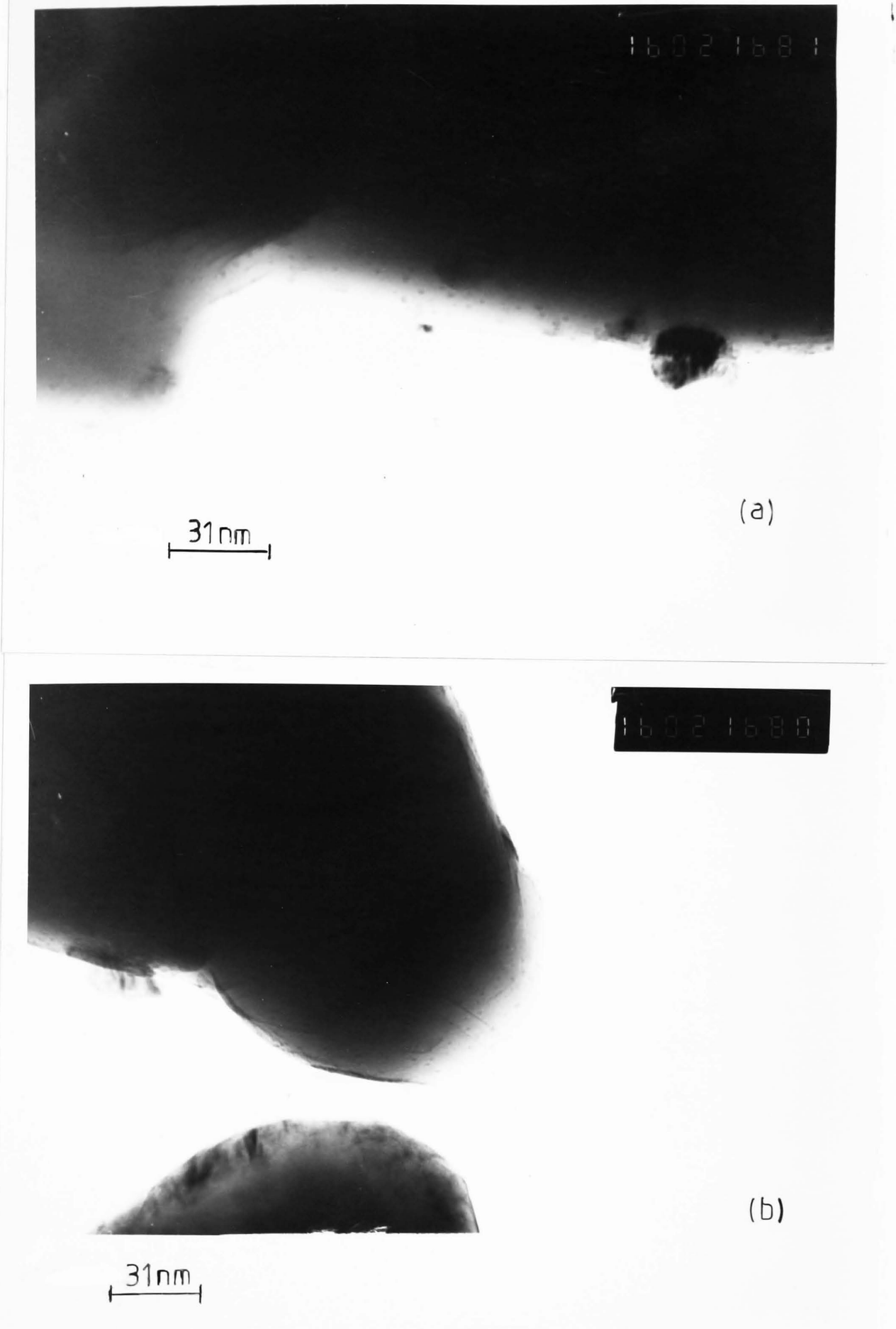

Fig. 4.48 Transmission electron micrographs of (a) 0.75% Co/TiO_2 and (b) 1.50%Co/TiO_2 catalysts prepared by impregnation using cobalt acetate and reduced at 1000°C.

The temperature dependence of the rate of a reaction, involving the rate constant k may be represented by:

$$k = A \exp(-E_a/RT) \qquad (1)$$

where E_a is the apparent activation energy and A the pre-exponential factor. Due to poor data for reaction rate of acetone, r_{Ac}, in both MT/C and MOT/C series, and to overcome the problem with measuring the activation energy for acetone formation, E_{Ac}, the following equations were proposed:

$$\frac{r_{Ac}}{r_P} = \frac{rS_A}{rS_P} \quad ; \quad \ln r_{Ac} = \ln r + \ln S_{Ac}$$

$$\ln r_{Ac} - \ln r_P = \ln S_{Ac} - \ln S_P$$

$$= \ln A_{Ac} - \frac{E_A}{RT} - \ln A_P + \frac{E_P}{RT}$$

$$= (\ln A_{Ac} - \ln A_P) - \left(\frac{E_A - E_P}{RT} \right)$$

Thus plotting $\ln (S_{Ac}/S_P)$ vs $1/T$ gives $(E_{Ac} - E_P)$.

Table 4.22 gives the kinetic parameters for the decomposition of 2-propanol over MT/C and MOT/C catalysts and for unsupported MoO_3 and TiO_2. Activation energies for acetone formation were determined according to the previous explanation. The reaction rates for 2-propanol removal and propene and acetone formation, i.e. r_{IPA}, r_P and r_{Ac}, were expressed in mmol. $h^{-1}.g^{-1}_{cat}$.

Table 4.22 Kinetic parameters for decomposition of 2-propanol over MT/C and MOT/C catalysts.

Catalyst	% conv.[1]	r_{IPA}[2]	r_P[3]	r_{Ac}[4]	S_P[5]	S_{Ac}[6]	E_{IPA}[7]	E_P[8]	E_{Ac}[9]
MoO_3	18.3	4.90	4.90	-	100	-	101.7	101.7	-
5%MT/C	2.10	0.56	0.56	-	100	-	97.7	97.7	-
1%MT/C	6.10	1.63	1.45	0.18	81.4	18.6	117.5	57.2	35.1
2%MT/C	11.1	2.97	2.74	0.23	92.4	7.6	80.5	80.1	36.1
3%MT/C	14.5	3.88	3.64	0.24	93.9	6.1	63.1	69.9	30.3
4%MT/C	8.86	2.37	2.18	0.19	91.8	8.2	73.8	85.9	42.9
.5%MOT/C	1.22	0.33	0.20	0.13	61.9	38.1	96.3	104.7	32.4
1%MOT/C	2.8	0.75	0.61	0.14	81.7	18.3	105.4	116.6	42.6
2%MOT/C	6.14	1.64	1.28	0.36	77.9	22.1	93.1	111.8	36.4
3%MOT/C	9.87	2.64	2.43	0.21	92.2	7.80	92.8	101.1	42.8
4%MOT/C	14.8	3.79	0.18	0.18	95.5	4.50	57.6	66.6	18.6
TiO_2 (CLD 867)	1.33	0.18	0.12	0.06	70.1	29.9	125.5	122.9	74.8

1 = % conversion

2 = rate of 2-propanol removal in mmol.h^{-1}.g_{cat}^{-1} at 453K.

3 = rate of propene formation in mmol.h^{-1}.g_{cat}^{-1} at 453K.

4 = rate of acetone formation in mmol.h^{-1}.g_{cat}^{-1} at 453K.

5 = propene % selectivity at 453K

6 = acetone % selectivity at 453K

7 = activation energy for 2-propanol in kJ mol^{-1}

8 = activation energy for propene in kJ mol^{-1}

9 = activation energy for acetone in kJ mol^{-1}

The variation in activation energy for the reactant removal and the product's formation, i.e. E_{IPA}, E_p and E_{Ac}, with MoO_3 content for both series are shown in Figs. 4.49 and 4.50, respectively.

A comparison of the change in selectivity with temperature for 4MT/C and 4MOT/C catalysts is shown in Figs. 4.51 and 4.52. Arrhenius plots for 2-propanol decomposition over 4MT/C and 4MOT/C catalysts are shown in Figs. 4.53 and 4.54. The activation energy was calculated at low conversion (between 1-10%) in the temperature range 413-453K for the 4MT/C catalyst, and 393K-463K for the 4MOT/C catalyst. The change in percentage conversion and selectivity for propene and acetone, i.e. S_p and S_{Ac} at that particular temperature (453K) is shown in Fig. 4.55(a). The reaction rates, i.e. r_{IPA}, r_p. and r_{Ac} with MoO_3 content for MT/C series at 453K, are shown in Fig. 4.55(b). The activity reaches a maximum at the 1% MT/C catalyst which is equivalent to about one monolayer and drops to a minimum at the 4% MT/C catalyst. From Fig. 4.55(a), it is obvious that selectivity for propene formation is higher than for acetone formation and is independent of MoO_3 content. MoO_3 being an acidic oxide favours the dehydration product (propene) rather than the dehydrogenation product (acetone).

For the MOT/C series, Fig. 4.56(a) shows the variation in percentage conversion and selectivity at 453K for propene and acetone with MoO_3 content. Here again, propene formation is greater than acetone formation. In other words, the selectivity for the dehydration product (propene)

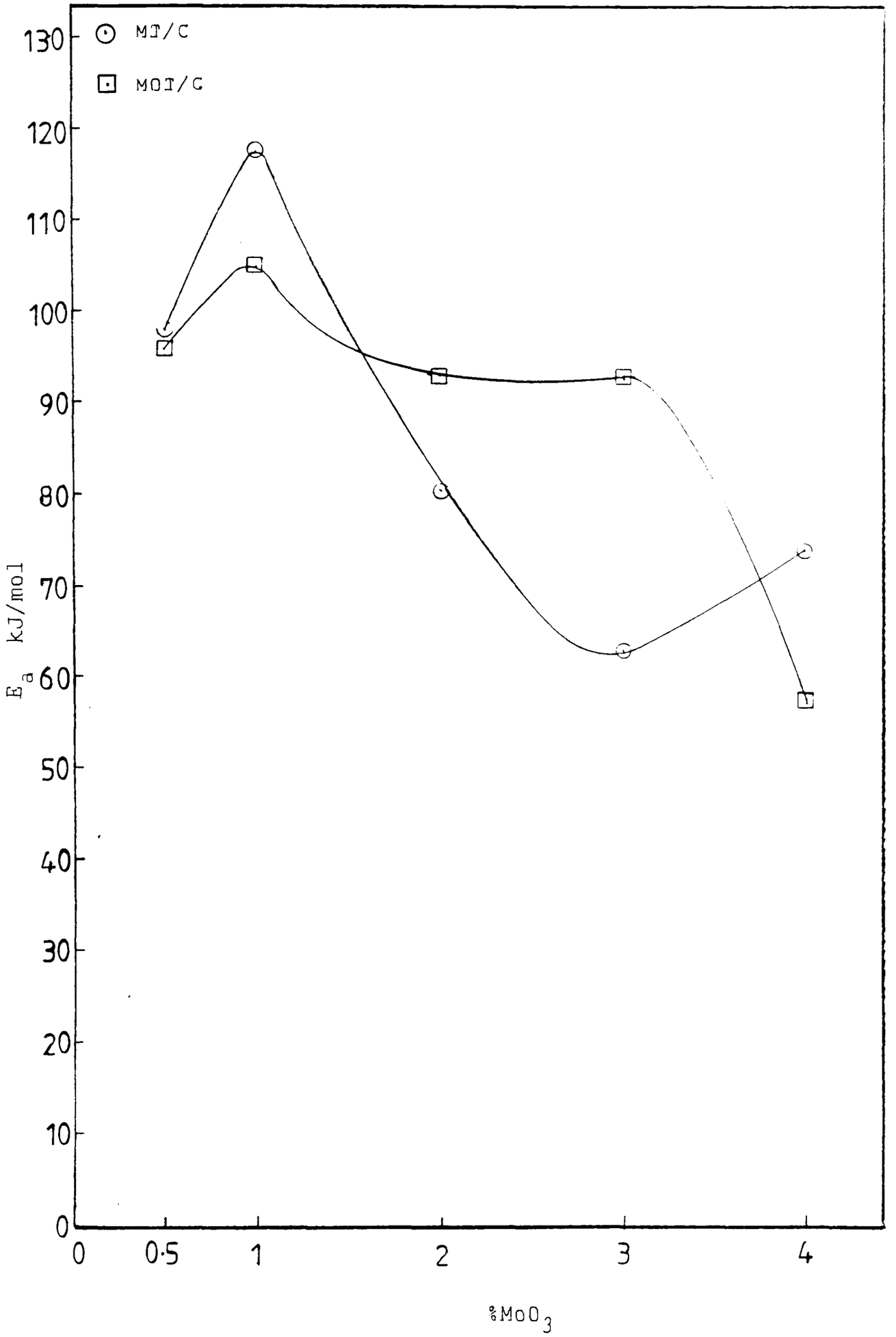

Fig. 4.49 Variation of E_{IPA} with MoO_3 content for MT/C and MOT/C series.

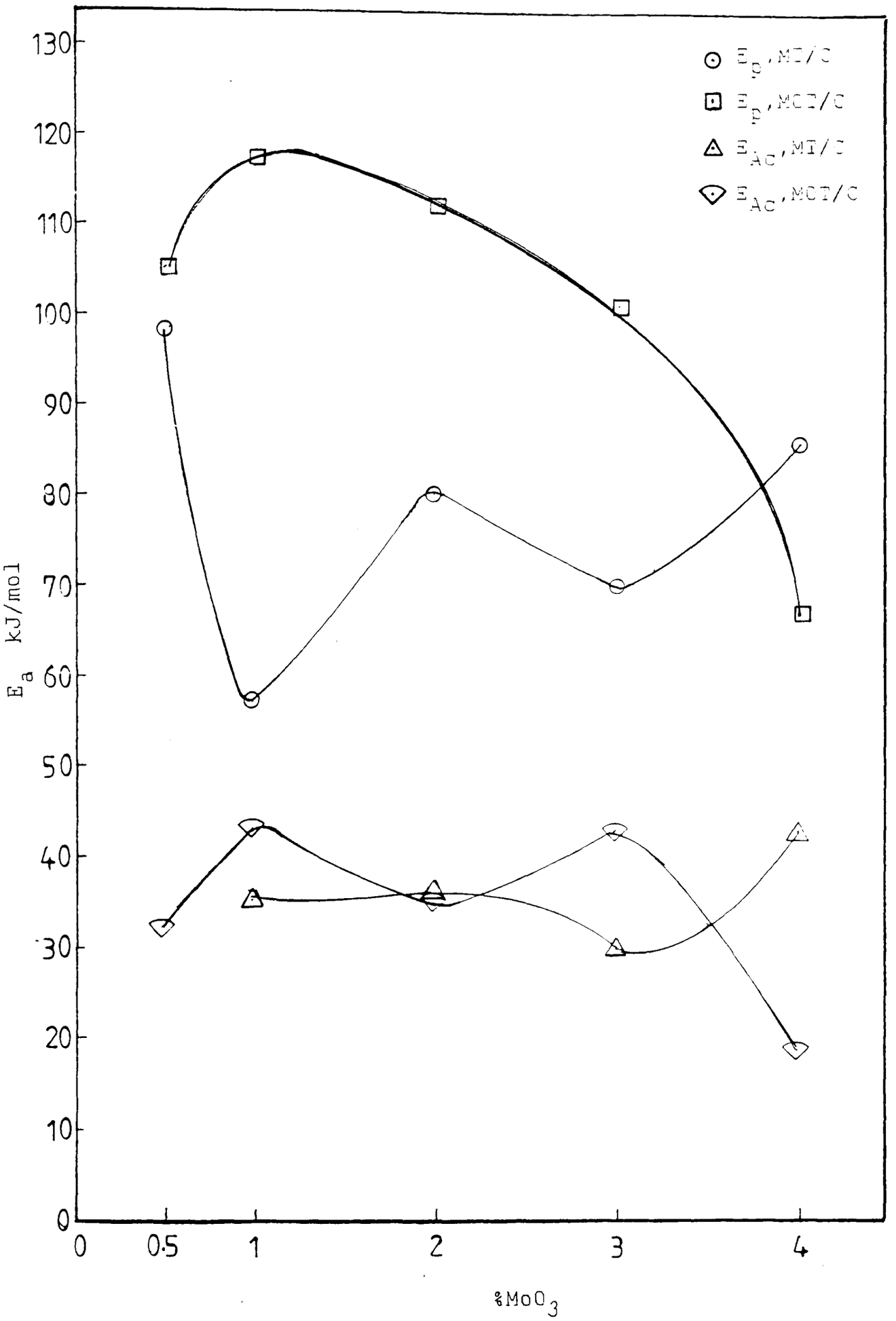

Fig. 4.50 Variation of E_p and E_A vs. MoO_3 content for MT/C and MOT/C series.

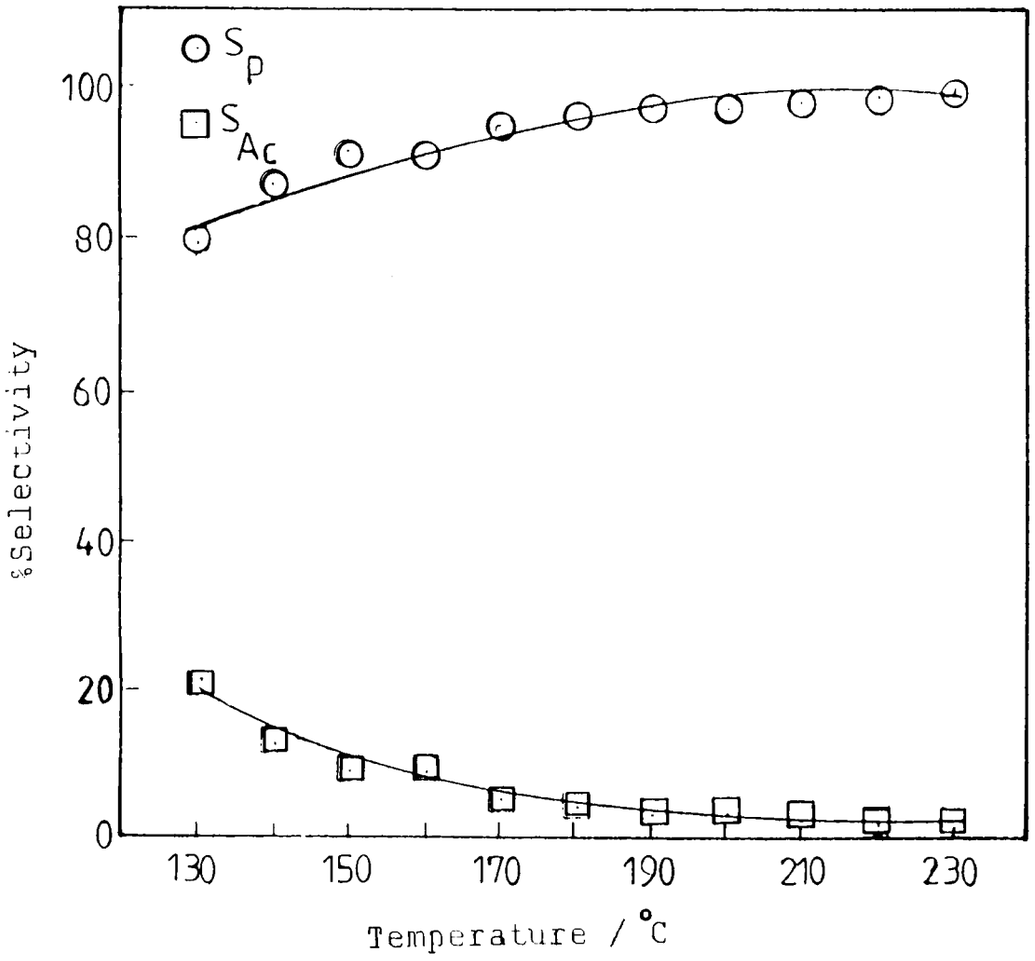

Fig. 4.51 Variation in selectivity to propene and acetone formation with temperature in 2-propanol decomposition over 4% MT/C catalyst.

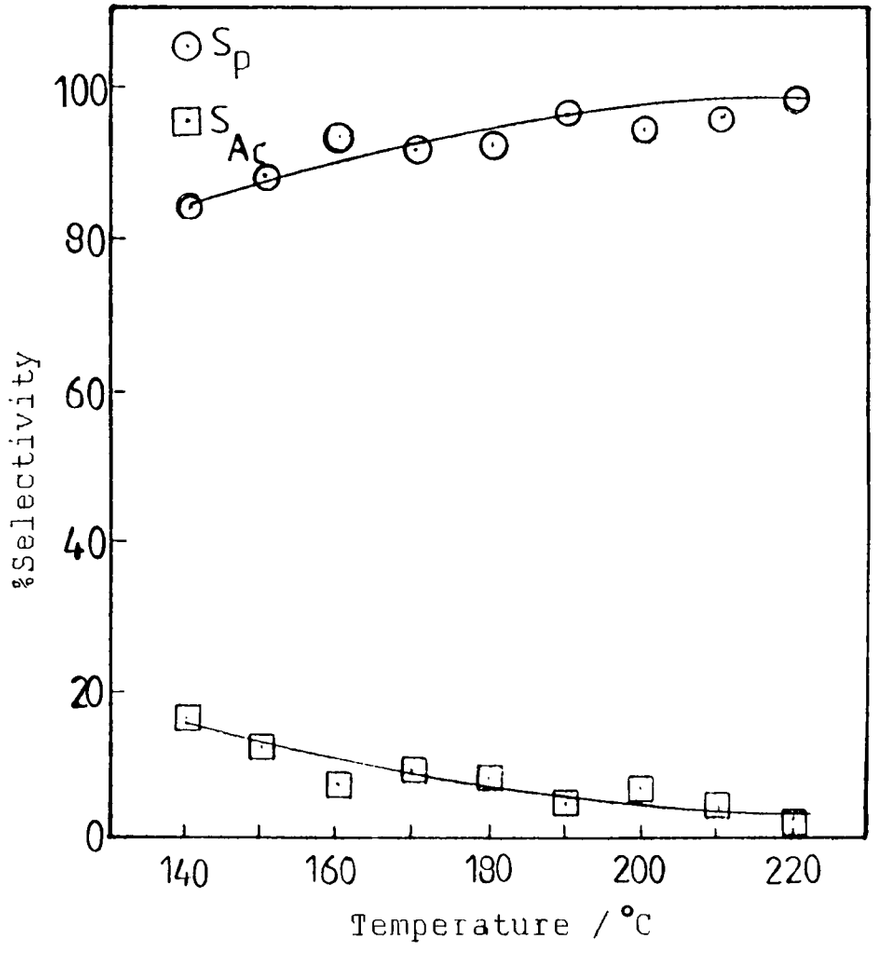

Fig. 4.52 Variation in selectivity to propene and acetone formation with temperature in 2-propanol decomposition over 4% MOT/C catalyst.

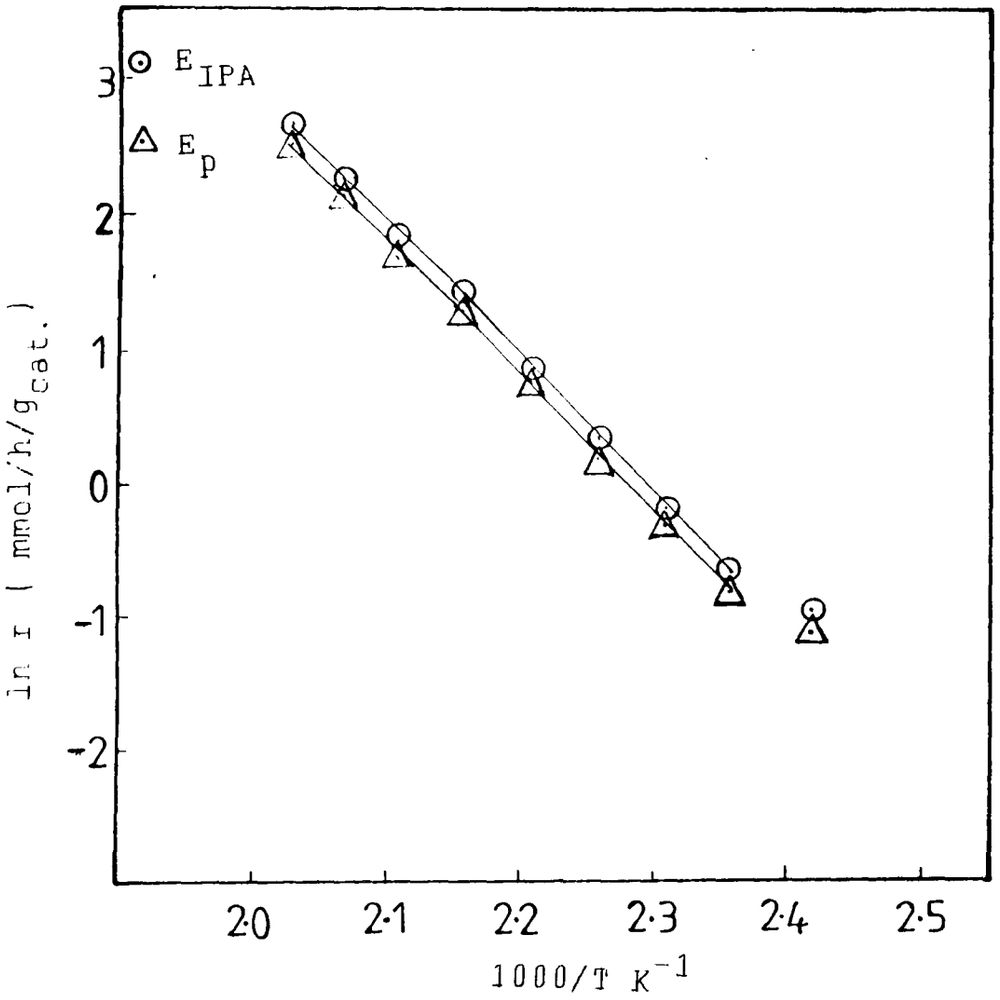

Fig. 4.53 Arrhenius plots for 2-propanol decomposition over 4% MT/C catalyst.

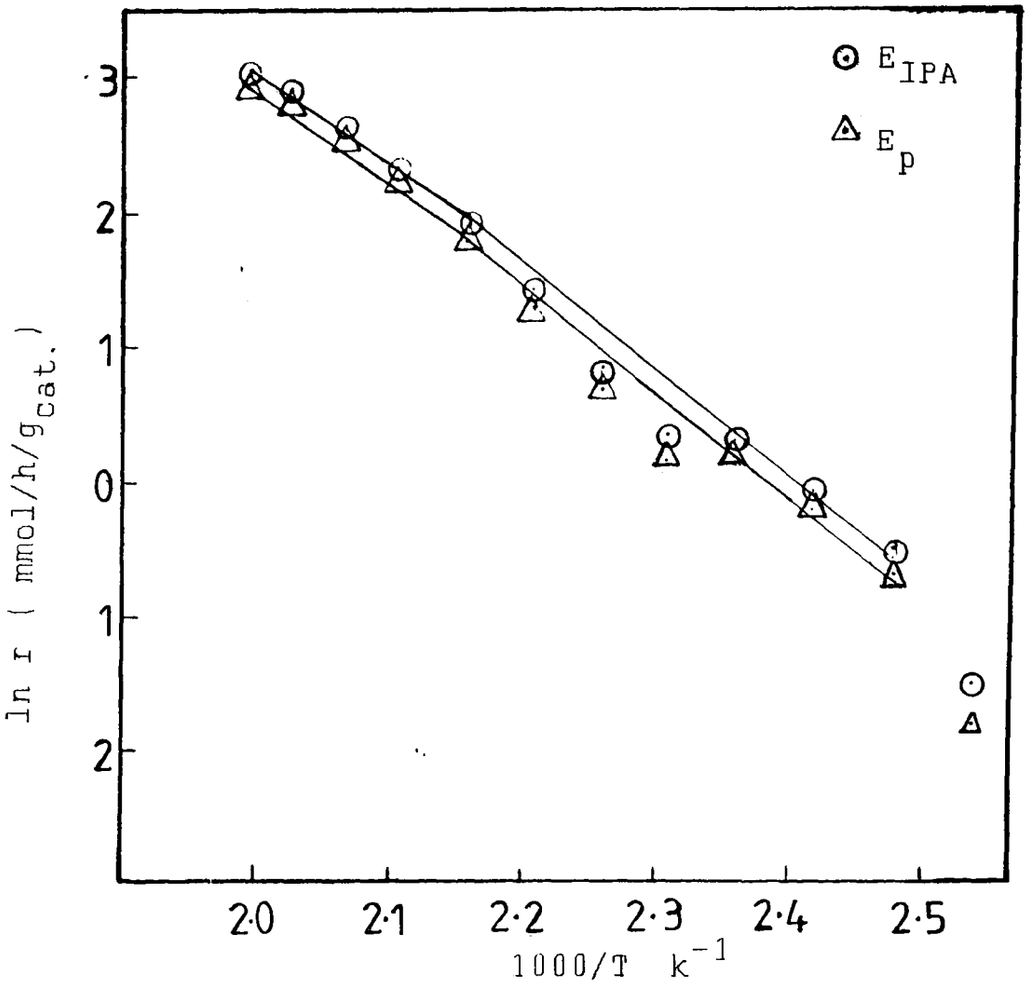

Fig. 4.54 Arrhenius plots of 2-propanol decomposition over 4% MOT/C catalyst.

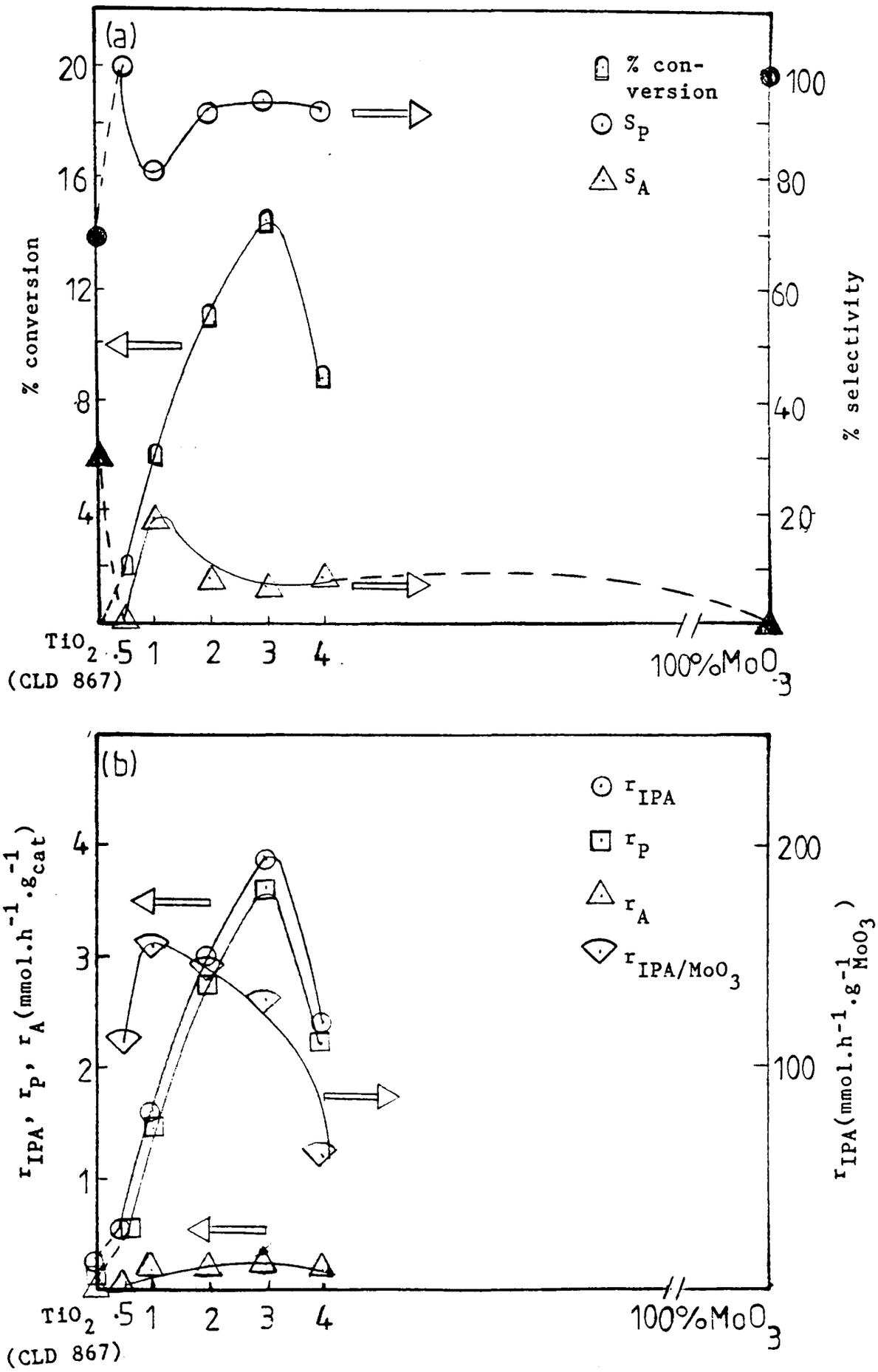

Fig. 4.55 (a) Variation of % conversion, S_P, and S_A with MoO_3 content
(b) Activity for MT/C catalysts as a function of MoO_3 at 453K.

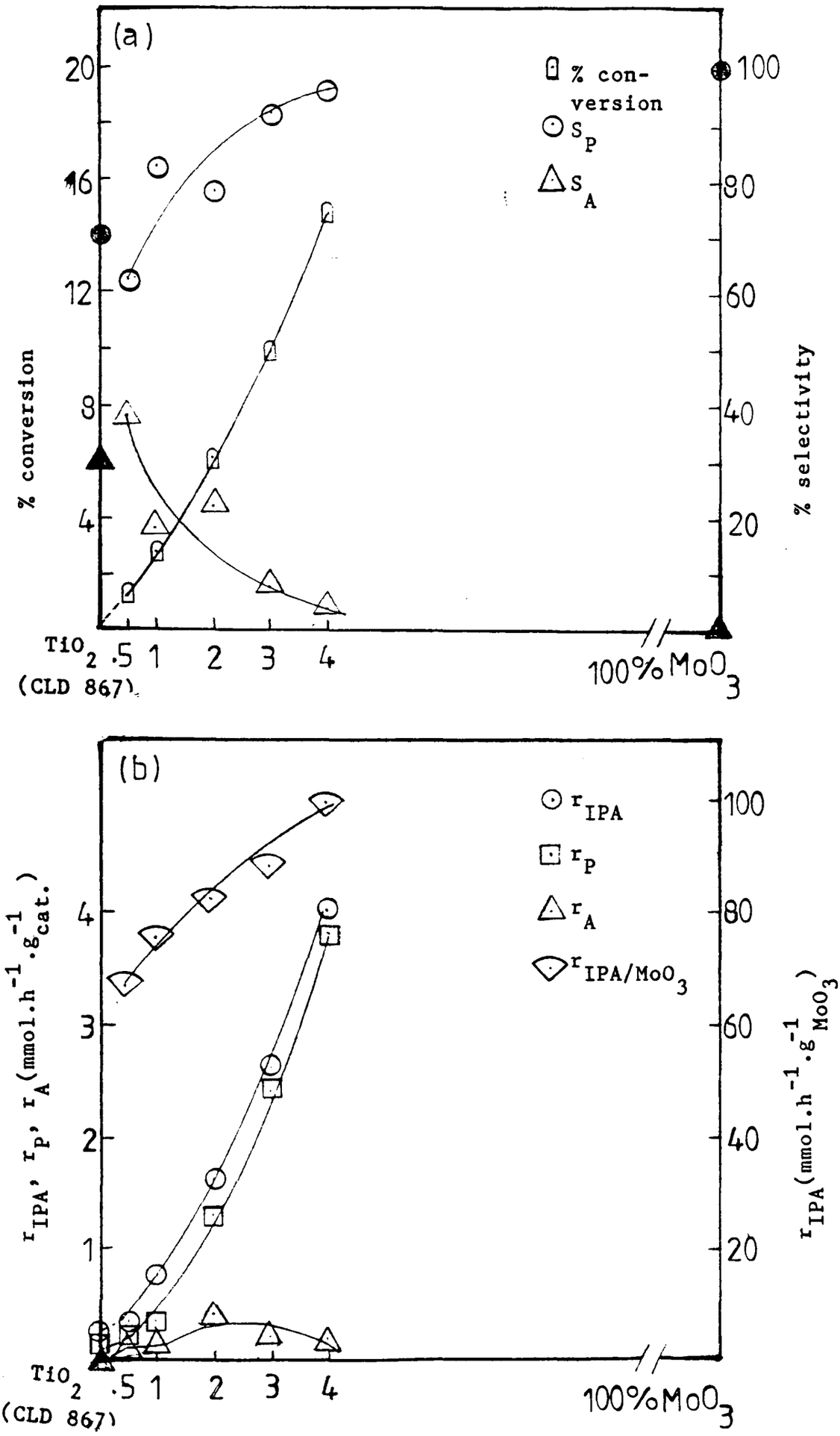

Fig. 4.56 (a) Variation of % conversion, S_P, and S_A with MoO_3 content
(b) Activity for MOT/C catalysts as a function of MoO_3 at 453K.

remains higher in both MT/C and MOT/C series than for the dehydrogenation product (acetone).

A linear correlation is often observed between the activation energy and the logarithm of the pre-exponential factor in catalysed reaction, although the root cause of this so-called compensation effect is still uncertain (8). For both MT/C and MOT/C catalysts, the compensation effect for 2-propanol decomposition is shown in Figs. 4.57 and 4.58, respectively. It is observed that for 2-propanol removal and propene formation (dehydration), the points lie on the same line, while the points for acetone formation (dehydrogenation) lie on different lines in both Figs. 4.57 and 4.58. This could indicate that active centres for the dehydration and dehydrogenation processes are not the same.

4.1.5.2 CoO/TiO_2 catalysts

Decomposition of 2-propanol over the CoO/TiO_2 catalysts, i.e. CT/C series, was studied. The experimental procedure is discussed in Section 3.3.3.

Table 4.23 gives the kinetic parameters for 2-propanol decomposition over CT/C series. The variation in activation energy for 2-propanol removal and for propene and acetone formation with CoO content is shown in Fig. 4.59. The activation energies for propene formation, E_P, in some of the catalysts are higher than those for acetone formation, E_A, so that the highest acetone selectivities are observed at the lowest temperatures (see Table 4.23).

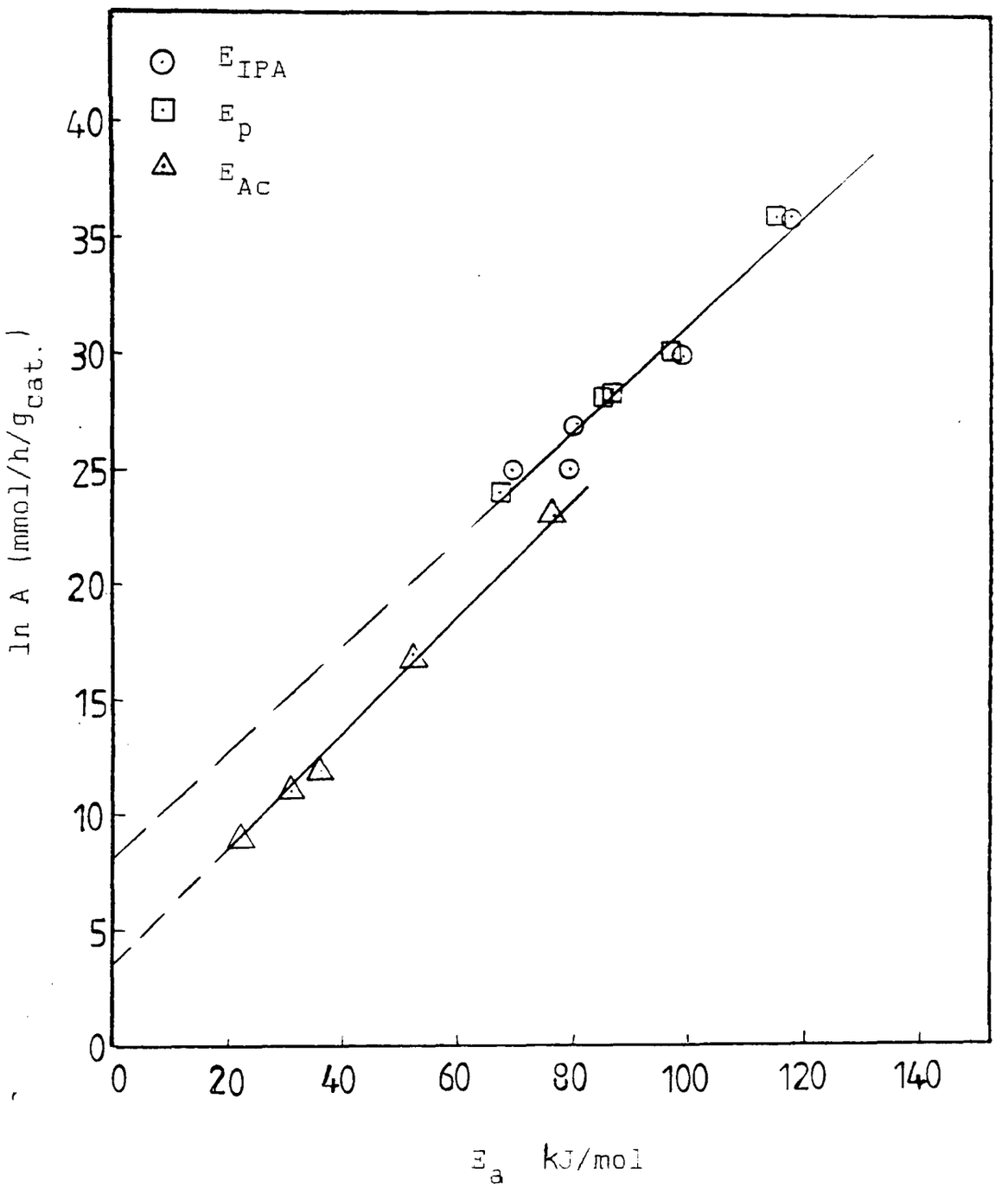

Fig. 4.57 Compensation effect for 2-propanol decomposition catalysed by MT/C series.

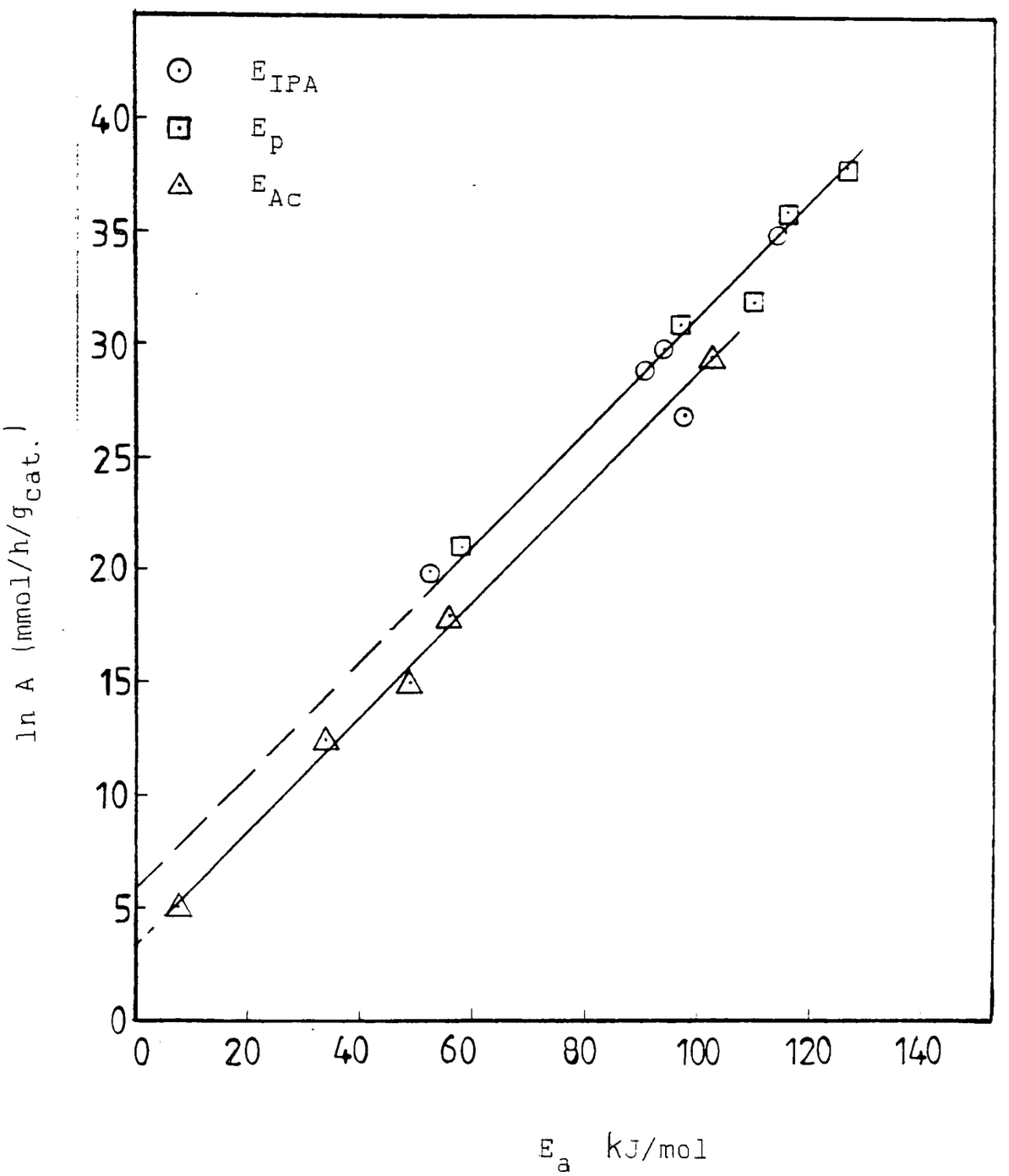

Fig. 4.58 Compensation effect for 2-propanol decomposition catalysed by MOT/C series.

Table 4.23 Kinetic parameters for decomposition of 2-propanol over CT/C series.

Catalyst	% conv.[1]	r_{IPA}[2]	r_P[3]	r_{Ac}[4]	S_P[5]	S_{Ac}[6]	E_{IPA}[7]	E_P[8]	E_{Ac}[9]
CoO	9.55	2.56	0.08	2.48	3.30	96.7	102	75.7	103.1
0.55%CT/C	2.66	0.71	0.43	0.28	60.5	39.5	108.4	120.1	94.9
1.11%CT/C	2.48	0.66	0.37	0.29	55.2	44.8	116.9	116	126.8
2.35%CT/C	2.05	0.55	0.34	0.21	62.4	37.6	105.4	123.6	65.5
4.65%CT/C	2.69	0.72	0.45	0.27	62.1	37.9	112.5	125.9	88.5
6.80%CT/C	2.83	0.76	0.40	0.36	53.2	46.8	108.4	121.8	96.1
8.7%CT/C	5.09	1.36	0.95	0.41	69.6	30.4	96.9	104.9	82.2
TiO_2 (CLD 867)	4.27	0.57	0.46	0.11	81.4	18.6	125.5	122.9	74.8

1 = % conversion

2 = rate of 2-propanol removal in mmol.h^{-1}.g_{cat}^{-1} at 513K.

3 = rate of propene formation in mmol.h^{-1}.g_{cat}^{-1} at 513K.

4 = rate of acetone formation in mmol.h^{-1}.g_{cat}^{-1} at 513K.

5 = propene % selectivity at 513K

6 = acetone % selectivity at 513K

7 = activation energy for 2-propanol in kJ mol^{-1}

8 = activation energy for propene in kJ mol^{-1}

9 = activation energy for acetone in kJ mol^{-1}

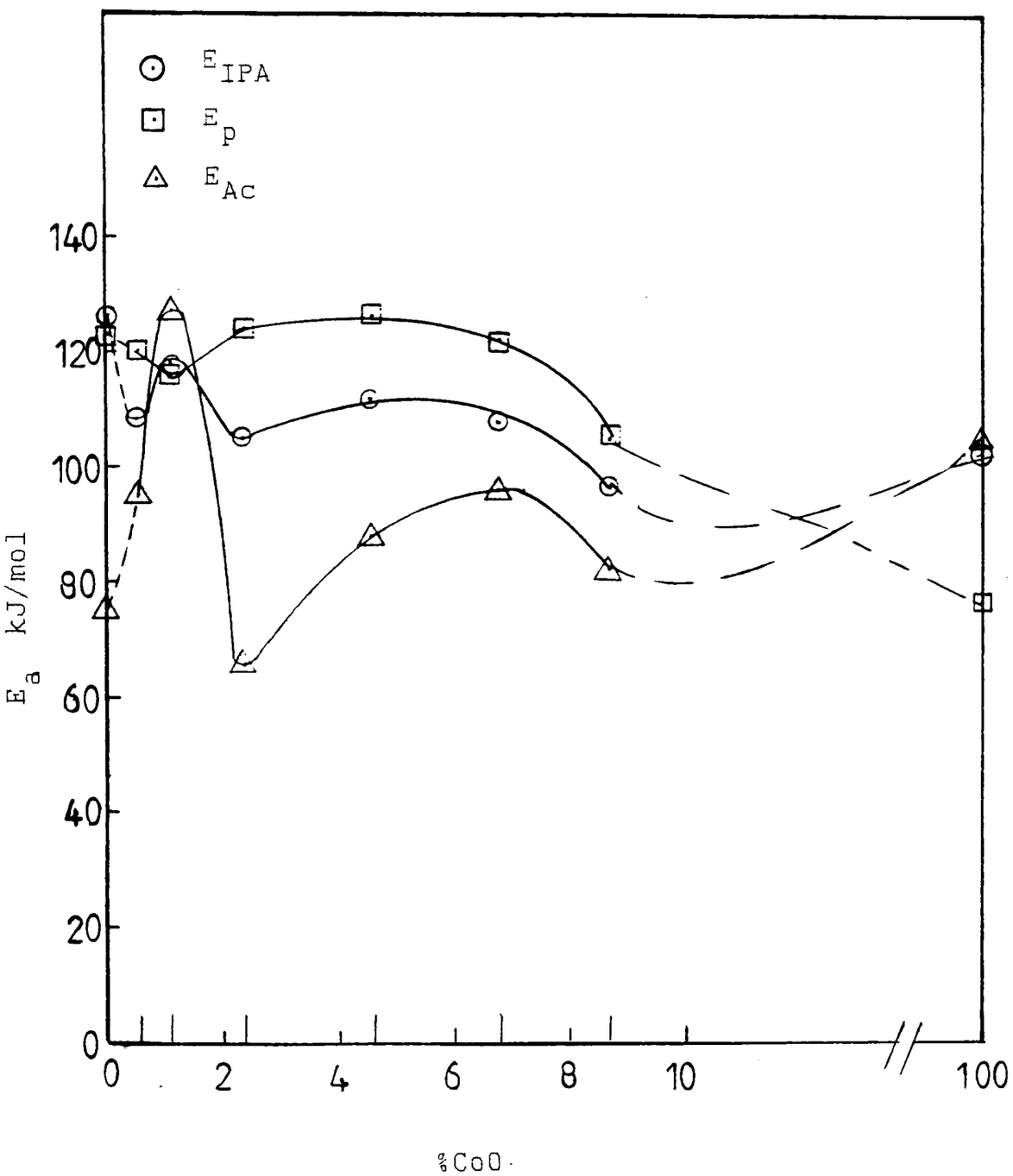

Fig. 4.59 Variation in E_{IPA}, E_p, and E_A as a function of Co content for the CT/C series, unsupported Co and TiO_2 are also illustrated.

Variation in selectivity with temperature for propene and acetone over 0.6%CT/C and 9.6%CT/C catalysts is shown in Figs. 4.60 and 4.61, respectively. With increasing temperature, selectivity increases for the dehydration product (propene) at a greater rate than for the dehydrogenation product (acetone) for both 0.6%CT/C and 9.6%CT/C catalysts.

Arrhenius plots for 0.6%CT/C and 9.6%CT/C catalysts are shown in Figs. 4.62 and 4.63, respectively. The variation in percentage conversion and selectivity with respect to propene and acetone formation at 513K are shown in Fig. 4.64(a). Conversion increases with increasing Co content, and selectivity for propene formation at 513K is higher than for acetone formation. The initial decrease in rates for 2-propanol removal and propene formation, i.e. r_{IPA} and r_P (Fig. 4.64b), is accompanied by a slight increase in the activation energies, which then show little change with increasing CoO content (Fig. 4.59). The variation in the rate per g CoO with CoO content is shown in Fig. 4.64 (b). The rate is decreasing with increasing CoO content accompanied by a slight decrease in activation energy for 2-propanol removal from 108 kJ mol^{-1} to 97 kJ mol^{-1}.

Fig. 4.65 shows the compensation effect plot for the Arrhenius parameters observed in the CT/C series relating to formation of products. Values of A are expressed as $mmol.h^{-1}.g_{cat}^{-1}$ to permit inclusion of the results for the

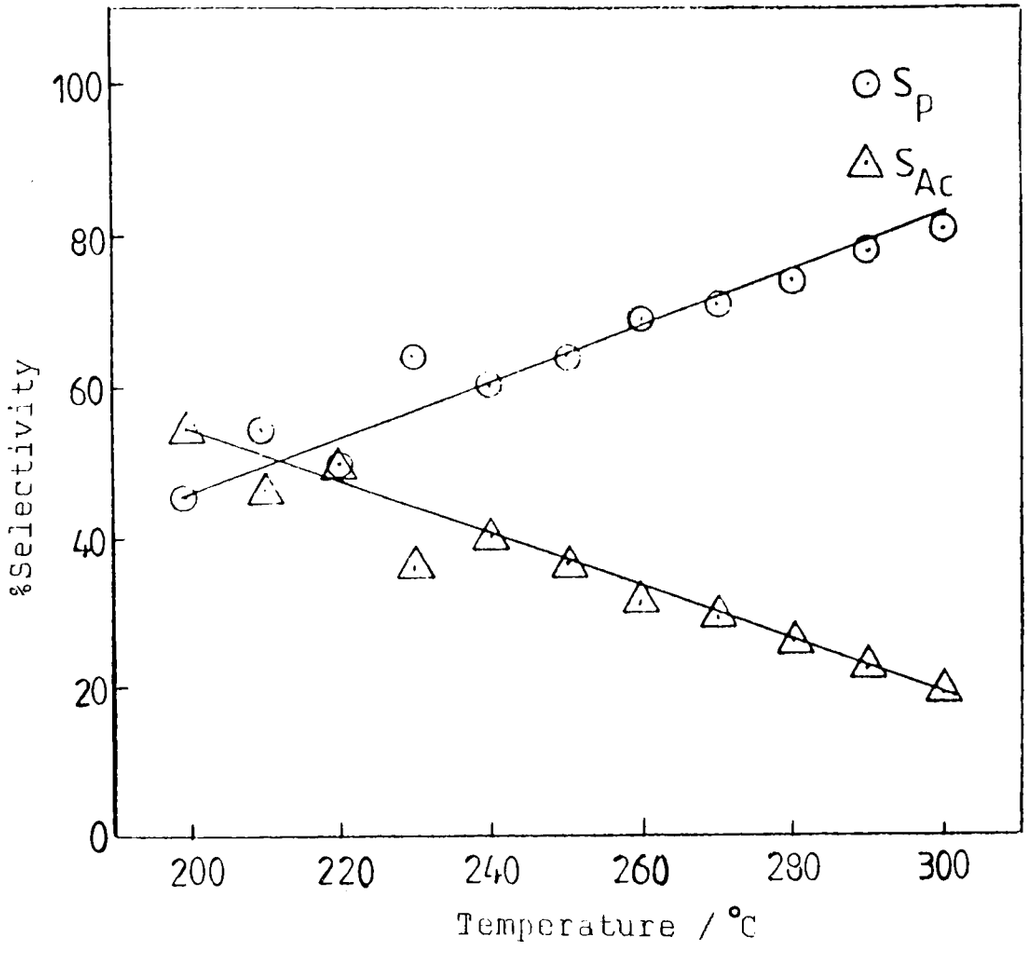

Fig. 4.60 Variation in selectivity to propene and acetone formation with temperature in 2-propanol decomposition over 0.6%CT/C catalyst.

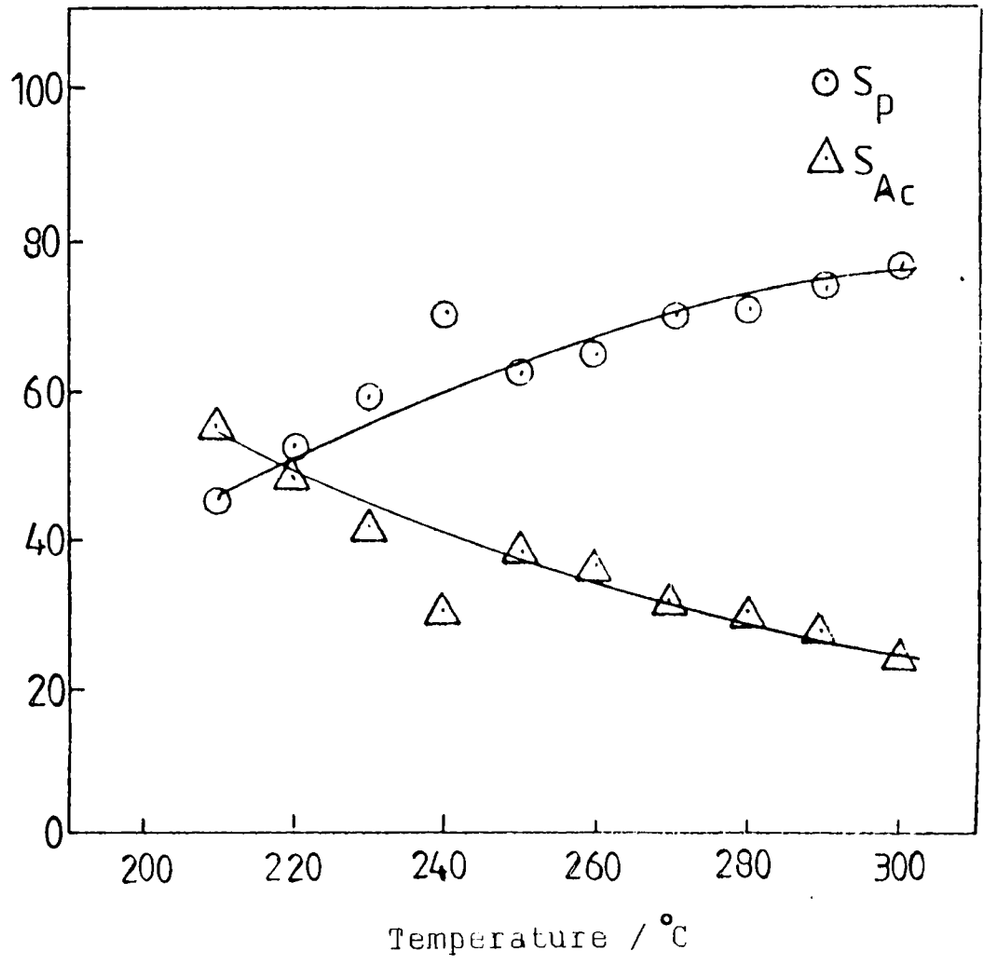

Fig. 4.61 Variation in selectivity to propene and acetone formation with temperature in 2-propanol decomposition over 9.6%CT/C catalyst.

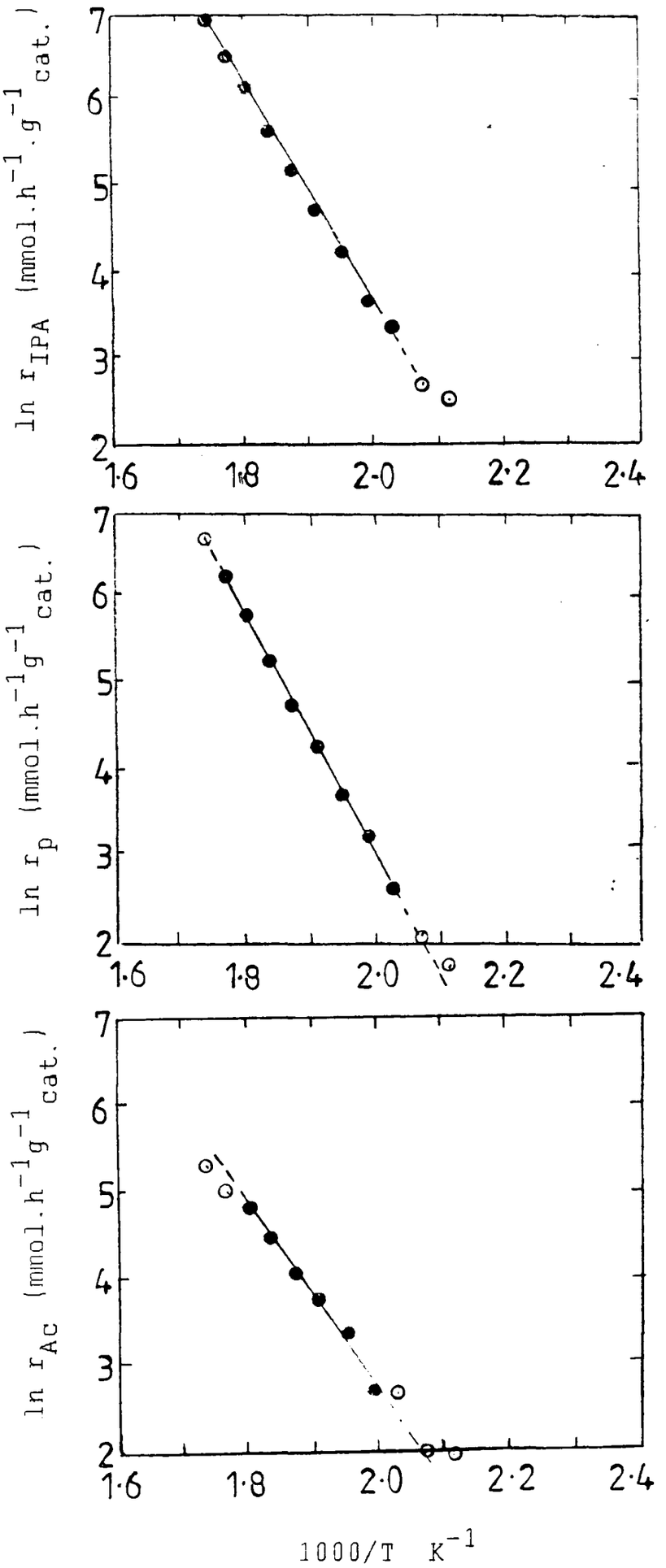

Fig. 4.62 Arrhenius plots for 2-propanol decomposition over 0.6% CT/C catalyst, (a) 2-propanol removal, (b) propene formation, and (c) acetone formation.

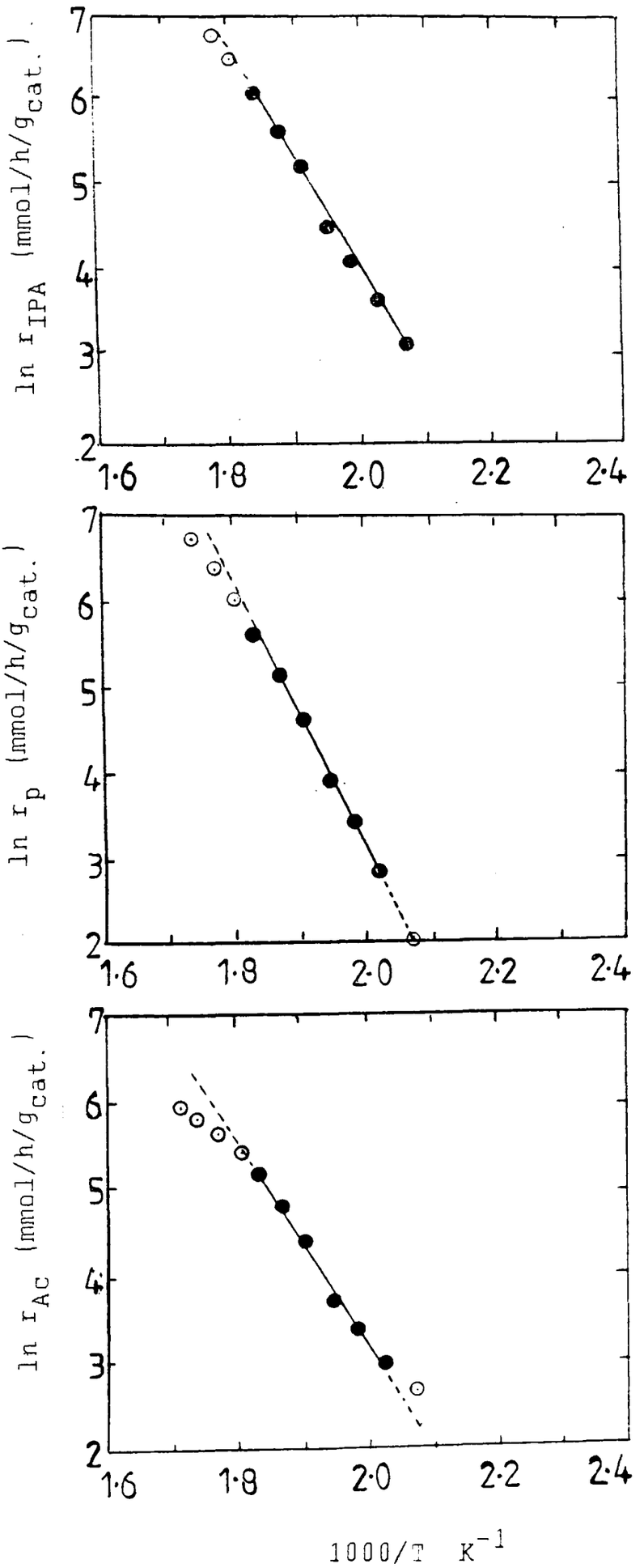

Fig. 4.63 Arrhenius plots for 2-propanol decomposition over 9.6% CT/C catalyst, (a) 2-propanol removal, (b) propene formation, and (c) acetone formation.

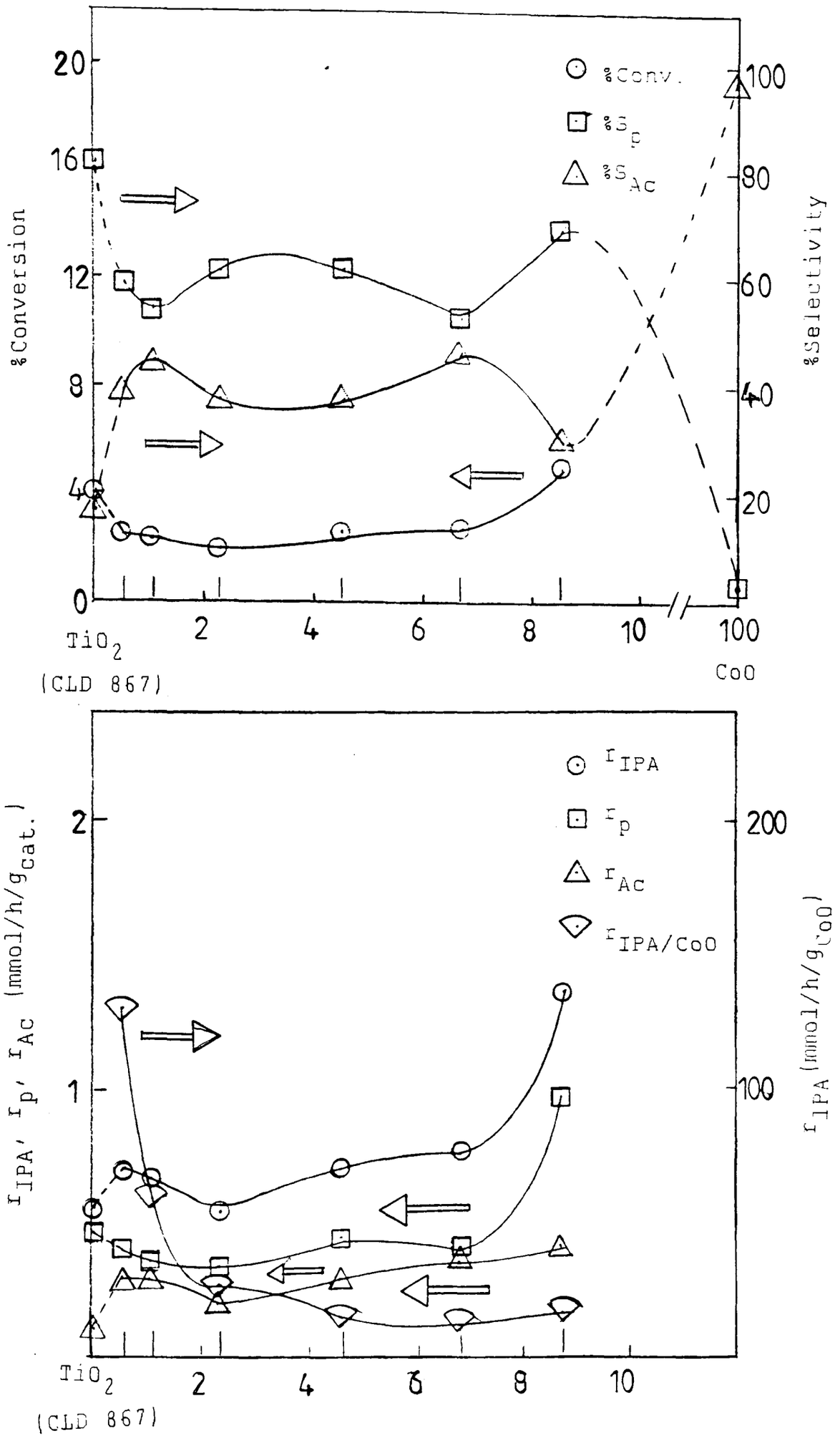

Fig. 4.64 (a) Variation in % conversion, S_p and S_A with CoO content
(b) Activity for CT/C catalysts as a function of CoO at 513K.

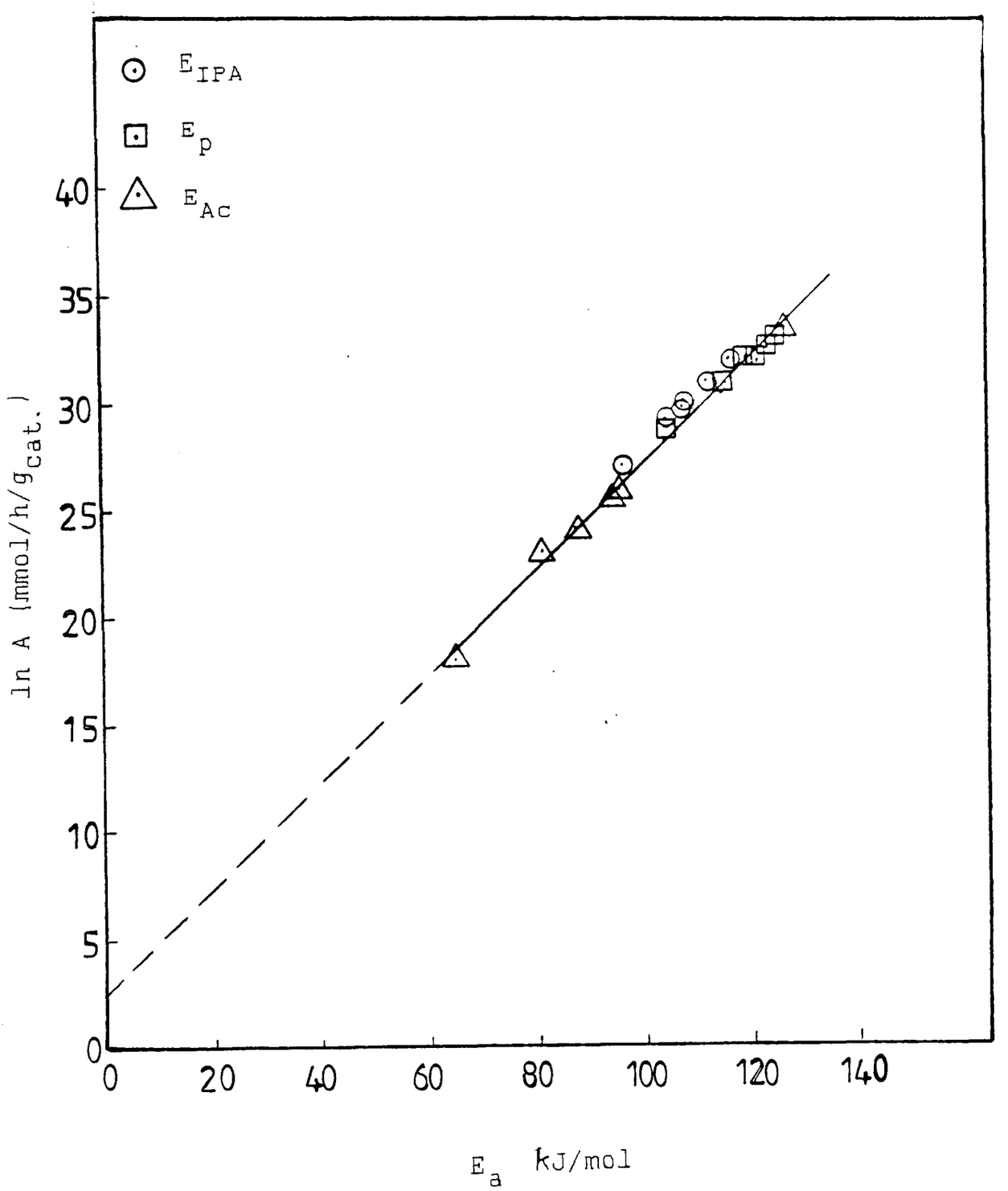

Fig. 4.65 Compensation effect for 2-propanol decomposition catalysed by the CT/C series.

TiO_2 support and also because it is more logical to use observed rates rather than those based on the total CoO content, only part in which is of high activity. Points for both reactions, i.e. dehydration and dehydrogenation, lie on about the same line, the slope of which corresponds to an isokinetic temperature of 527K. This suggests the identity of the active centres for the two reactions[8]. Recently, Bond and Flamerz[9] found very similar results for the V_2O_5/TiO_2 system with respect to 2-propanol decomposition.

4.1.5.3 $CoO-MoO_3/TiO_2$ catalysts

Three series of the $CoO-MoO/TiO_2$ system were studied for the decomposition of 2-propanol: (i) CoO impregnated first, then the MoO_3 (CMT series); (ii) MoO_3 impregnated first, then the CoO (MCT series); and (iii) the CoO and MoO_3 impregnated together (CMTg series).

The kinetic parameters for the 2-propanol decomposition over the CMT series are given in Table 4.24. The rate of 2-propanol removal, and propene and acetone formation, i.e. r_{IPA}, r_P, and r_{Ac}, increases with increasing the CoO and MoO_3 contents up to CMT4 catalysts, then it drops with CMT5 catalyst, and then increases again for CMT6 and CMT7 catalysts (Table 4.24). The variation of activation energies for 2-propanol removal and propene and acetone formation with total CoO and MoO_3 contents is shown in Fig. 4.66. It is clear that the activation energies for the

Table 4.24 Kinetic parameters for decomposition of 2-propanol over CMT series

Catalyst	% conv.[1]	r_{IPA}[2]	r_P[3]	r_{Ac}[4]	S_P[5]	S_{Ac}[6]	E_{IPA}[7]	E_P[8]	E_{Ac}[9]
$CoMoO_4$	2.53	0.68	0.68	-	100	-	64.7	63.3	-
CMT1	2.31	0.62	0.35	0.27	56.9	43.1	87.5	100.5	64.3
CMT2	4.20	1.12	0.82	0.30	67.0	33.0	80.0	87.0	69.9
CMT3	8.11	2.17	1.57	0.60	68.8	31.2	87.4	90.4	71.9
CMT4	11.6	3.10	2.29	0.81	73.9	26.1	95.3	107.4	58.3
CMT5	8.97	2.40	1.84	0.56	76.8	23.2	78.8	86.3	54.7
CMT6	16.4	4.39	3.84	0.55	87.4	12.6	70.5	78.8	42.5
CMT7	15.4	4.12	3.61	0.51	87.6	12.4	61.9	68.2	41.6
TiO_2 (P - 25)	2.22	0.59	0.59	-	100	-	61.8	61.0	-

1 = % conversion

2 = rate of 2-propanol removal in $mmol.h^{-1}.g_{cat}^{-1}$ at 453K.

3 = rate of propene formation in $mmol.h^{-1}.g_{cat}^{-1}$ at 453K.

4 = rate of acetone formation in $mmol.h^{-1}.g_{cat}^{-1}$ at 453K.

5 = propene % selectivity at 453K

6 = acetone % selectivity at 453K

7 = activation energy for 2-propanol in kJ mol^{-1}

8 = activation energy for propene in kJ mol^{-1}

9 = activation energy for acetone in kJ mol^{-1}

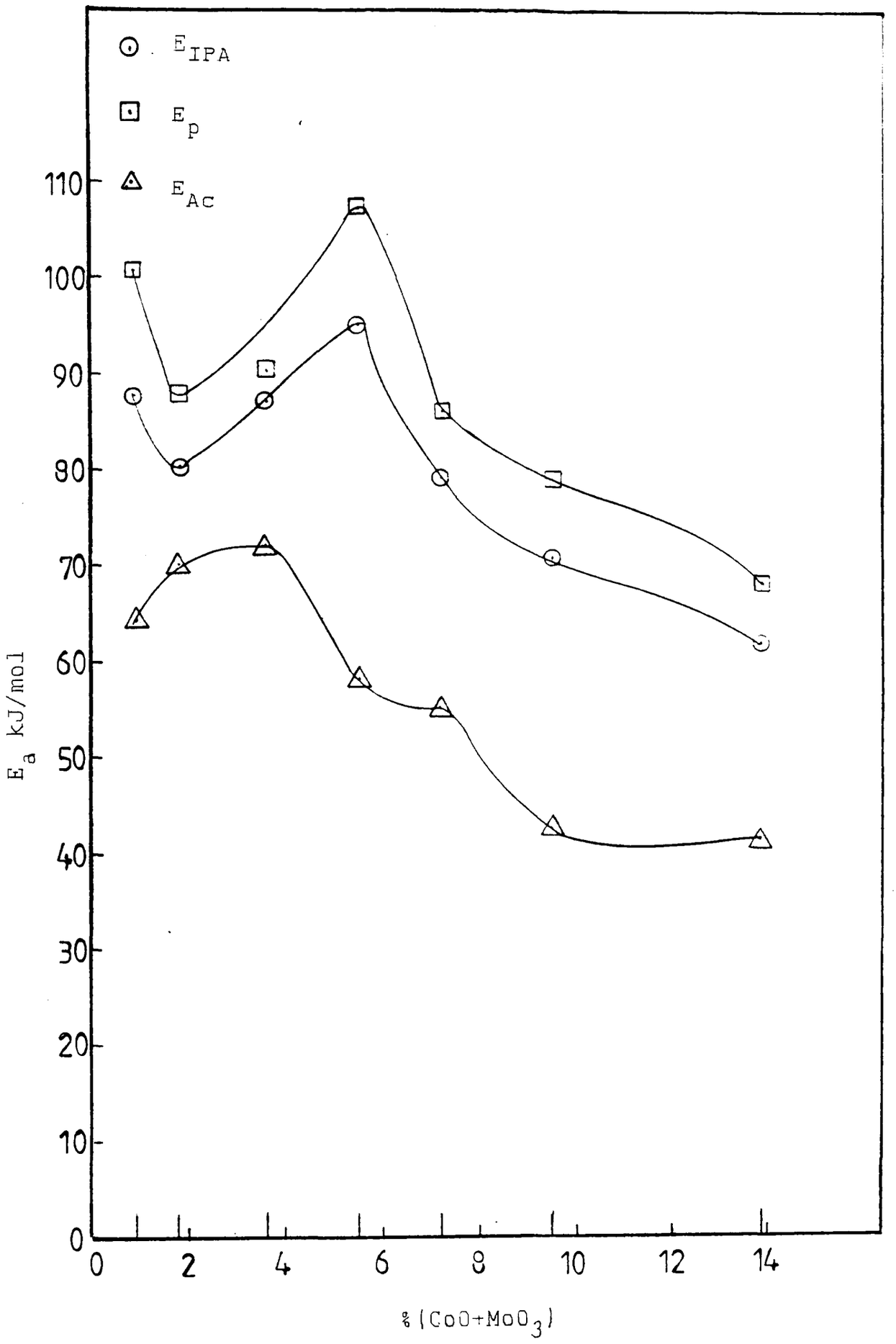

Fig. 4.66 Variation of activation energies E_{IPA}, E_p, and E_A as a function of ($CoO-MoO_3$) content for the CMT series.

dehydration process are higher than the dehydrogenation process for all the catalysts in the CMT series.

For simplicity, the CMT3 catalyst, i.e. 1.2wt.%CoO + 2.4wt% MoO_3 TiO_2 is chosen and the variation in selectivity with temperature for propene and acetone formation, i.e. S_P and S_{Ac} is shown in Fig. 4.67. It is clear that the selectivity for propene formation is higher than for acetone formation.

Arrhenius plots for 2-propanol decomposition over the CMT3 catalyst are shown in Fig. 4.68. Percentage conversion and selectivity as a function of CoO content are shown in Fig. 4.69(a). S_P increases with increasing CoO content from about 55% to 88% for all the catalysts, while S_{Ac} decreases from 44% to 10% for all the catalysts at 453K.

The reaction rate per g CoO decreases gradually with increasing CoO content until CMT4 catalyst composition. A sharp decrease is observed at CMT5 catalyst composition, and then increases to CMT6 catalyst composition, and then finally decreases again at CMT7 catalyst. There could be a phase transformation or poisoning effect above CMT4 catalyst, i.e. CMT5 catalyst, which contains 2.3 wt% CoO and 4.90 wt.% MoO_3, as shown in Fig. 4.69(b).

4.1.5.4 MCT series

The kinetic parameters such as percentage conversion, rates of reaction, selectivities and activation energies are given in Table 4.25 for the MCT series. The variation in activation energies for 2-propanol removal, propene and

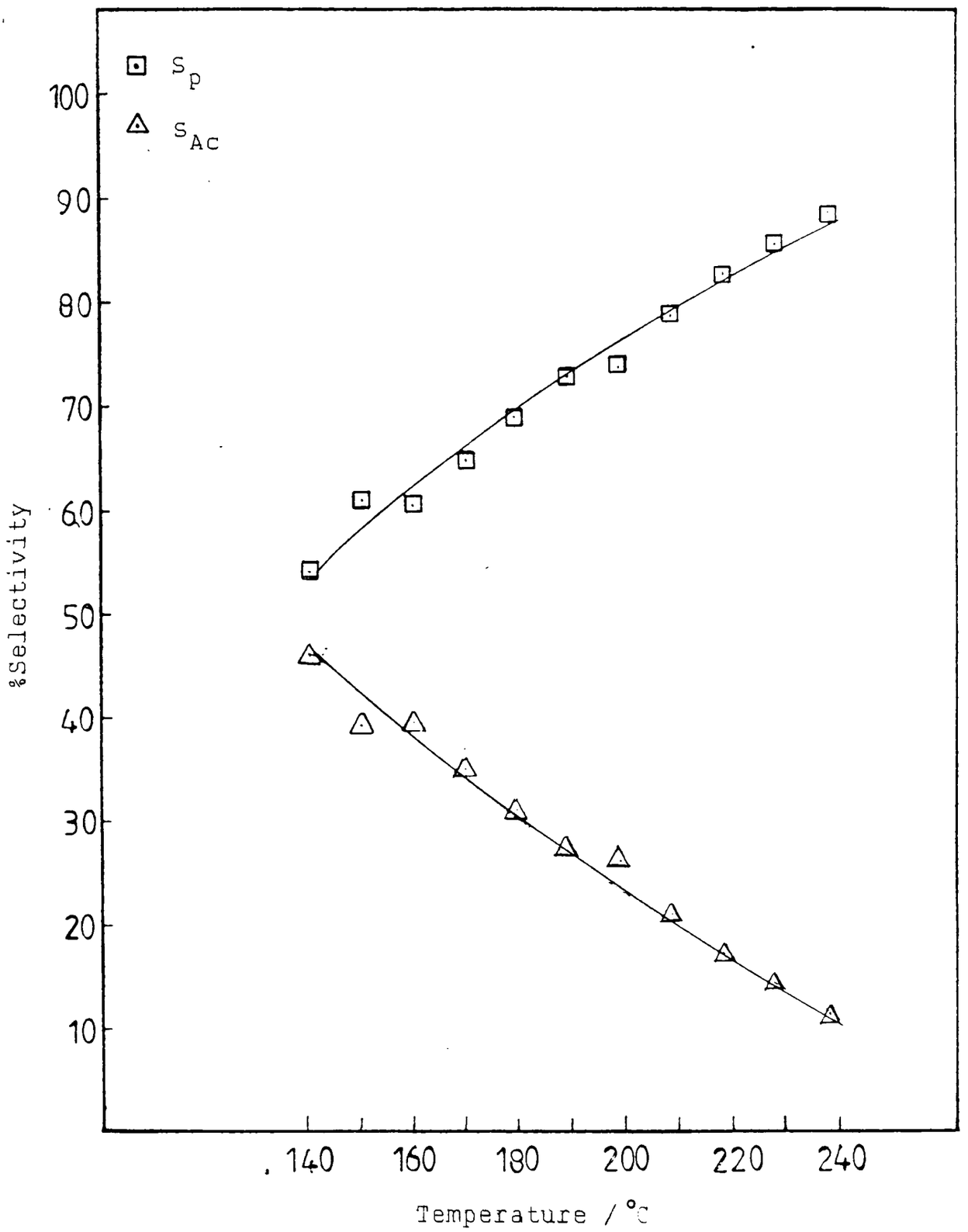

Fig. 4.67 Dependence of selectivity to propene and acetone formation with temperature in 2-propanol decomposition over the CMT3 catalyst.

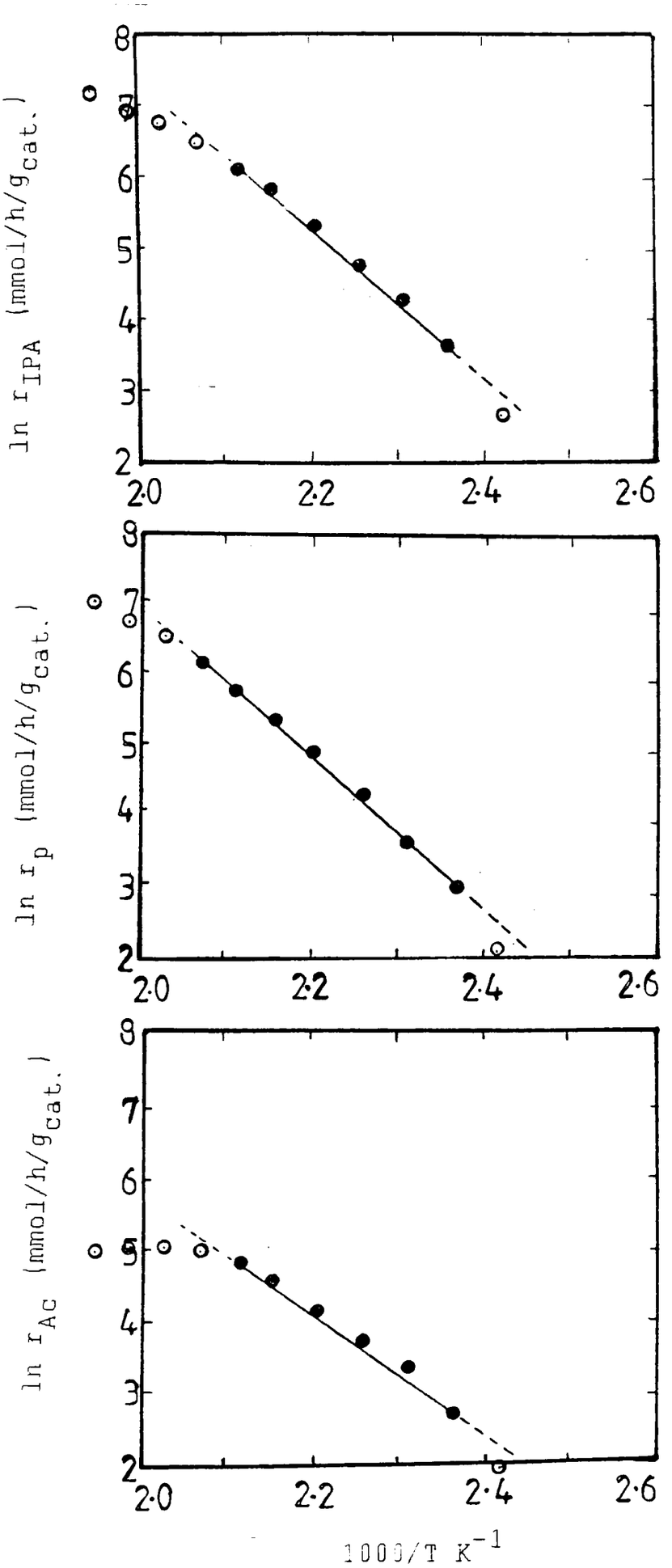

Fig. 4.68 Arrhenius plots for 2-propanol decomposition over CMT3 catalyst, (a) 2-propanol removal, (b) propene formation, and (c) acetone formation.

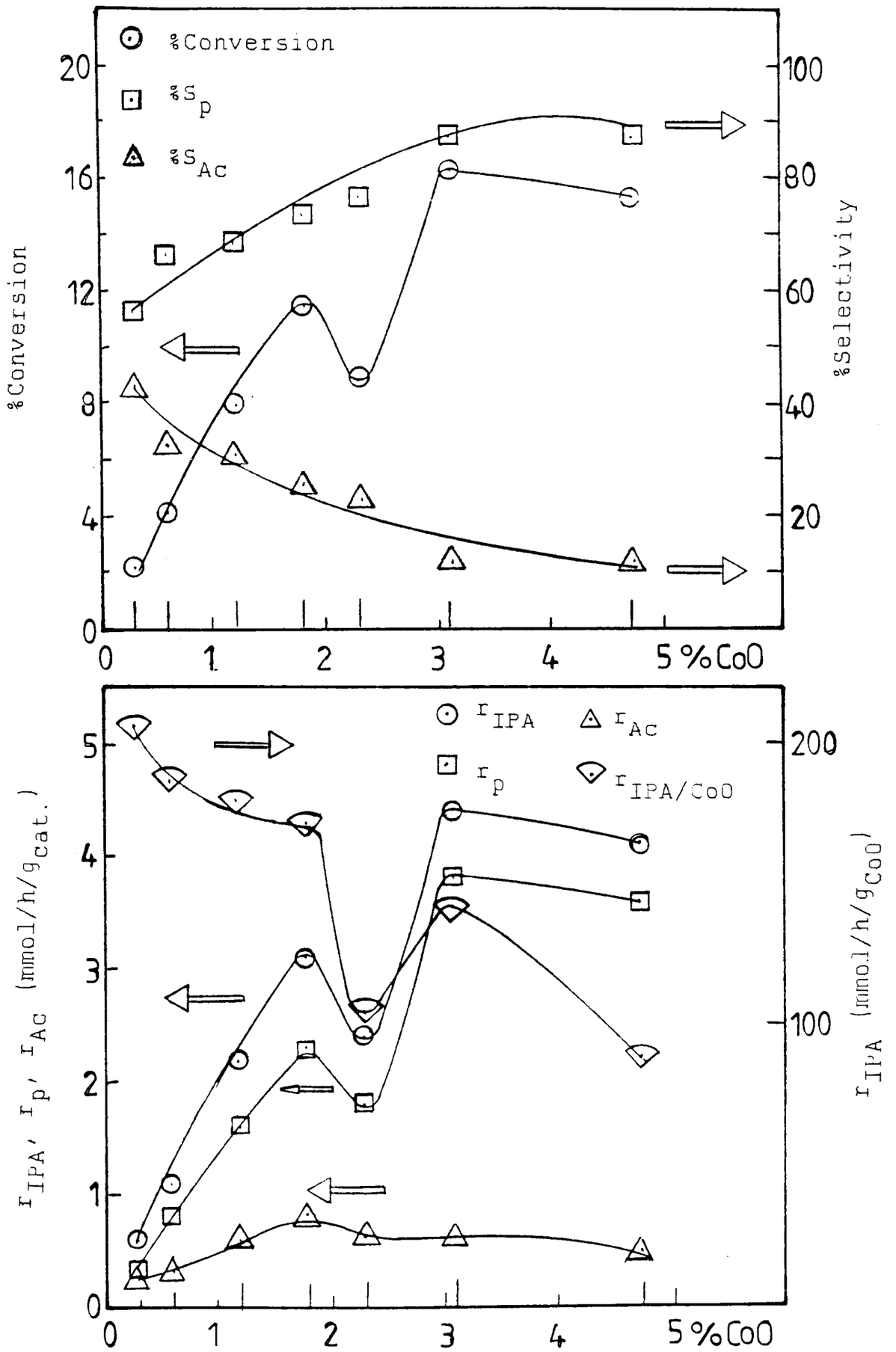

Fig. 4.69 (a) Variation in % conversion, S_p, and S_A with Co content for CMT series
(b) Activity for CMT catalysts as a function of CoO at 453K.

Table 4.25 Kinetic parameters for decomposition fo 2-propanol over MCT series

Catalyst	% conv.[1]	r_{IPA}[2]	r_P[3]	r_{Ac}[4]	S_P[5]	S_{Ac}[6]	E_{IPA}[7]	E_P[8]	E_{Ac}[9]
$CoMoO_4$	2.53	0.68	0.68	-	100	-	64.7	63.3	-
MCT1	4.01	1.07	0.63	0.44	59.1	40.9	81.1	94.7	59.8
MCT2	3.10	0.83	0.47	0.36	56.5	43.5	88.0	111.8	68.3
MCT3	4.91	1.31	0.88	0.43	67.0	33.0	84.3	94.7	66.05
MCT4	7.17	1.92	1.49	0.43	77.5	22.5	90.8	101.9	65.0
MCT5	7.32	1.96	1.47	0.49	75.1	24.9	81.2	94.5	61.8
MCT6	8,64	2.31	1.90	0.41	82.2	17.8	92.4	101.8	61.6
MCT7	11.5	3.09	2.52	0.57	81.7	18.3	77.5	83.6	70.6
TiO_2 (P - 25)	2.22	0.59	0.59	-	100	-	61.8	61.0	-

1 = % conversion

2 = rate of 2-propanol removal in mmol.h^{-1}.g_{cat}^{-1} at 453K.

3 = rate of propene formation in mmol.h^{-1}.g_{cat}^{-1} at 453K.

4 = rate of acetone formation in mmol.h^{-1}.g_{cat}^{-1} at 453K.

5 = propene % selectivity at 453K

6 = acetone % selectivity at 453K

7 = activation energy for 2-propanol in kJ mol^{-1}

8 = activation energy for propene in kJ mol^{-1}

9 = activation energy for acetone in kJ mol^{-1}

acetone formation, i.e. E_{IPA}, E_P, and E_{Ac}, with the total CoO and MoO_3 contents is shown in Fig. 4.70. The activation energies for the dehydration process remain higher than the dehydrogenation process as shown in Fig. 4.70.

The change in selectivity with temperature for propene and acetone formation, i.e. S_P and S_{Ac} for the MCT3 catalyst is shown in Fig. 4.71. Compared with the CMT3 catalyst, it is apparent that selectivity for propene formation is higher than selectivity for acetone formation.

Fig. 4.72 shows Arrhenius plots for 2-propanol decomposition over MCT3 catalyst. Fig. 4.73(a) shows the percentage conversion and S_P and S_A as a function of MoO_3 content for all the catalysts at 180°C. Conversion increases linearly with increasing MoO_3 loading, while S_P is higher than S_{Ac} for all the catalysts at 180°C. Fig. 4.73(b) shows the rates of reaction of 2-propanol removal, i.e. r_{IPA}, and for propene and acetone formation, i.e. r_P and r_{Ac}, as a function of MoO_3 content. The rate of 2-propanol removal per g MoO_3, i.e. r_{IPA}/MoO_3 is also shown in Fig. 4.73(b). There is a trend in the activity, it drops sharply from 178 $mmol.h^{-1}.g^{-1}_{MoO_3}$ for the MCT1 catalyst to 72 $mmol.h^{-1}.g^{-1}_{MoO_3}$ and keeps decreasing with an increasing MoO_3 content (see Fig. 4.73(b)).

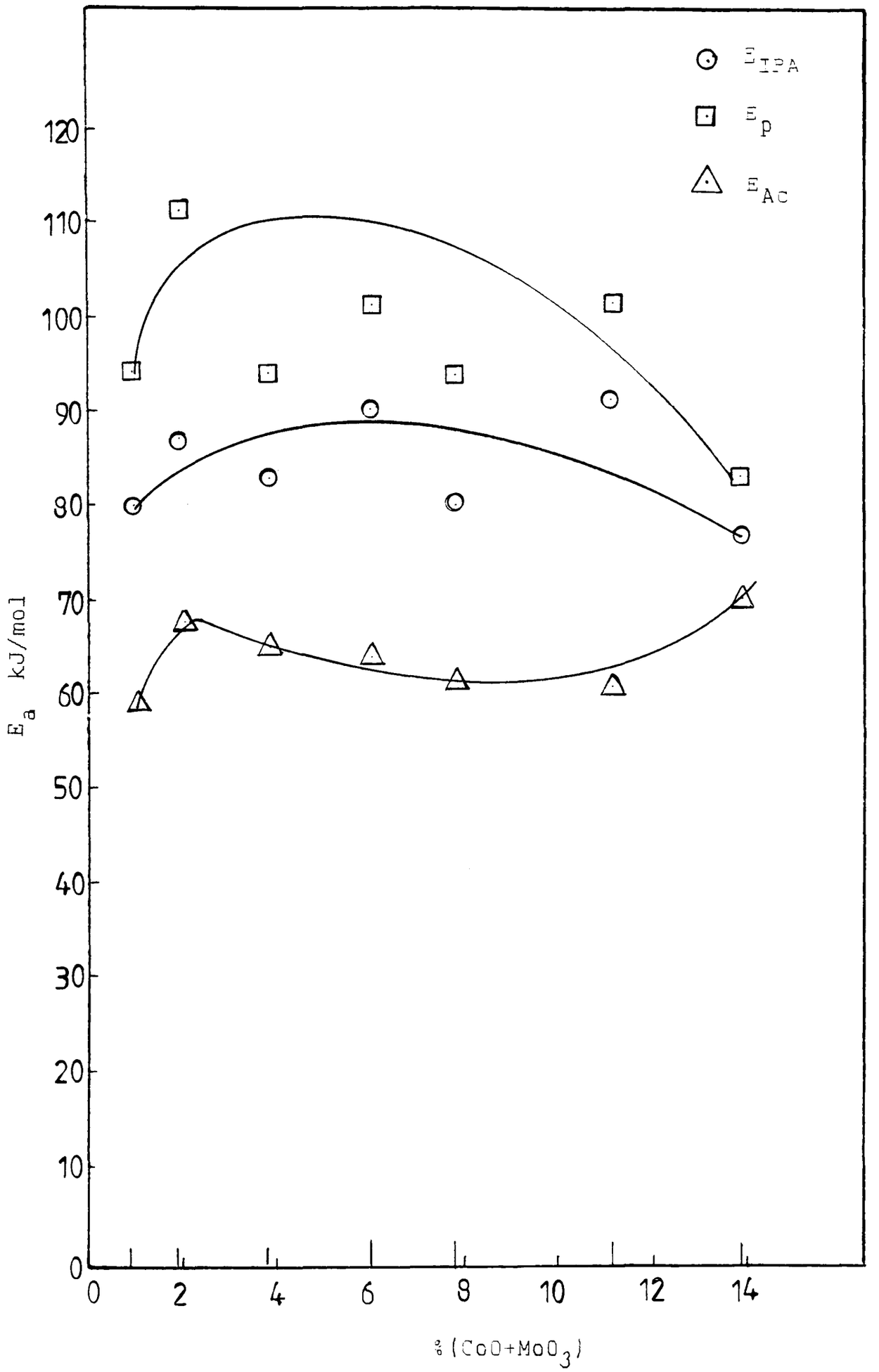

Fig. 4.70 Variation in activation energies E_{IPA}, Ep and E_A as a function of total CoO and MoO_3 content for the MCT series.

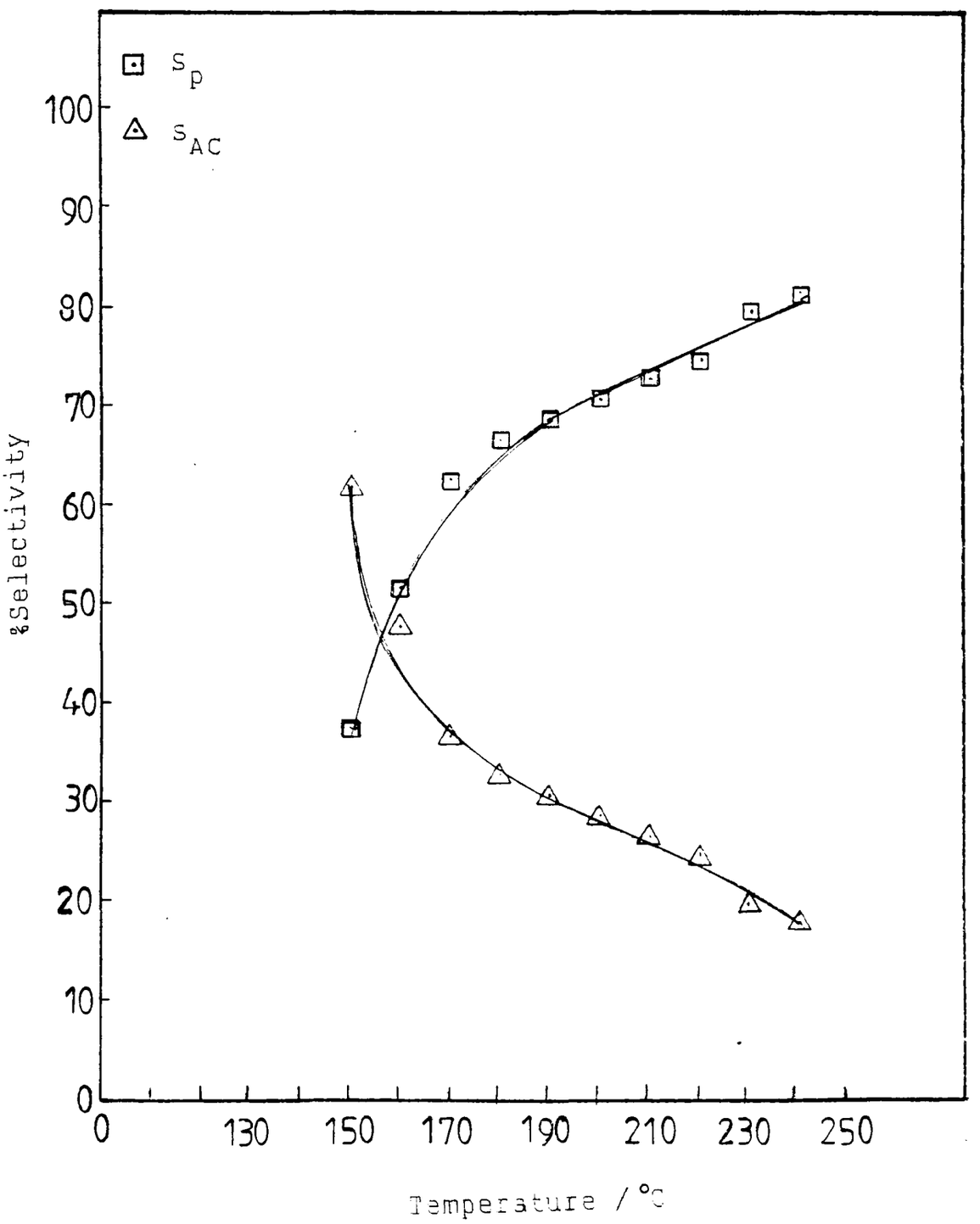

Fig. 4.71 Variation of selectivity to propene and acetone formation with temperature in 2-propanol decomposition over the MCT3 catalyst.

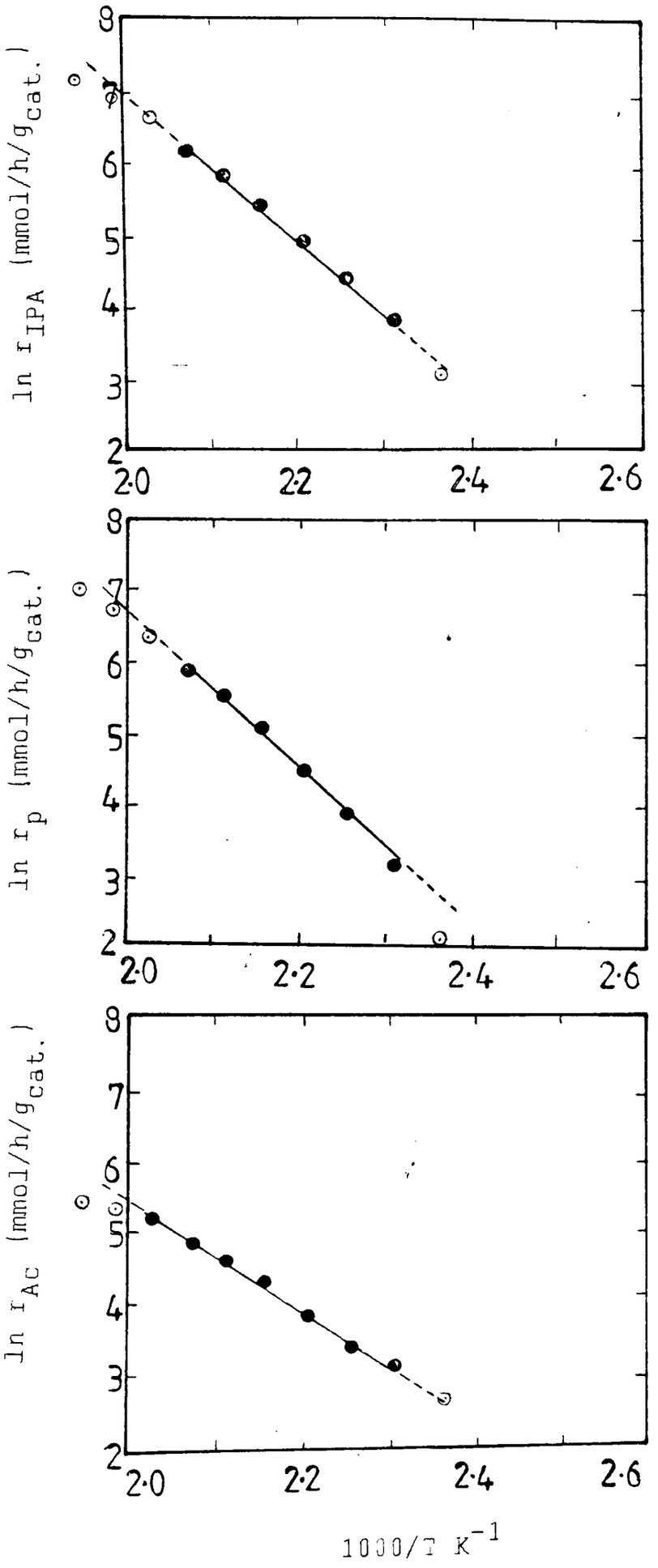

Fig. 4.72 Arrhenius plots for 2-propanol decomposition over MCT3 catalyst, (a) 2-propanol removal, (b) propene formation, and (c) acetone formation.

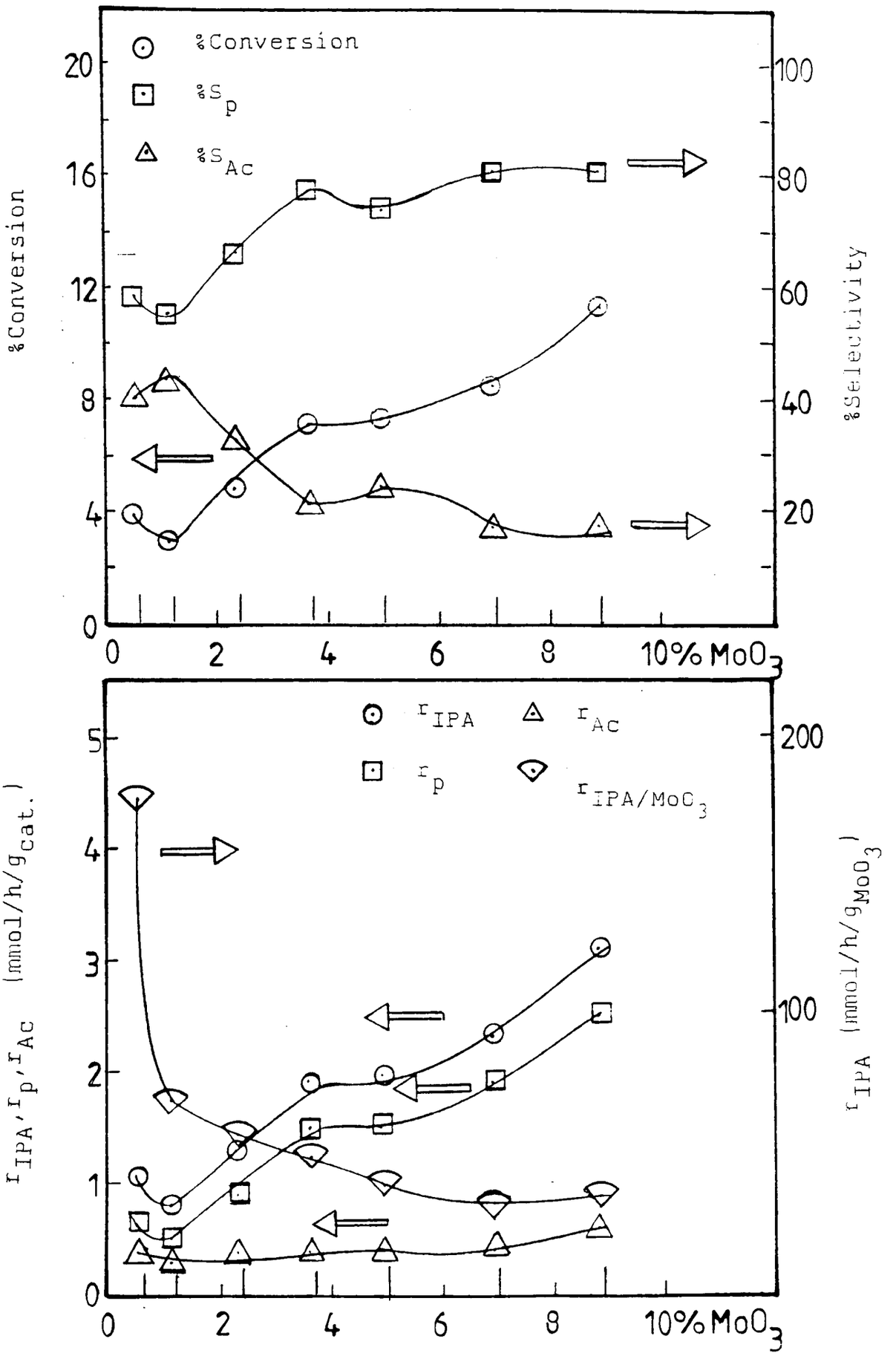

Fig. 4.73 (a) Variation in % conversions, S_p, and S_{Ac} with MoO_3 content for MCT series
(b) Activity for MCT catalysts as a function of MoO_3 at 453K.

4.1.5.5 CMTg series

Finally, the kinetic parameters for the decomposition of 2-propanol over the CMTg series are given in Table 4.26. The variation in E_{IPA}, E_p, and E_{Ac} with the total CoO and MoO_3 contents is shown in Fig. 4.74. E_p are higher than E_A, for all the catalysts, the same phenomenon as with the previous two series, i.e. CMT and MCT.

The variation in selectivities, i.e. S_p and S_{Ac} with temperature for the CMTg3 catalyst is shown in Fig. 4.75. With increasing temperature, S_p showed higher values than S_{Ac}. Arrhenius plots for 2-propanol decomposition over the CMTg3 catalyst are shown in Fig. 4.76.

Percentage conversion as a function of CoO content is shown in Fig. 4.77(a). It increases with increasing CoO content up to 2.1 wt.% and reaches a plateau at 4.8 wt.% CoO and then decreases at 6 wt.% CoO. S_p and S_{Ac} as a function of CoO content at 180°C for all the catalysts are shown in Fig. 4.77(a). S_p remains higher than S_{Ac} for all the catalysts as shown in Fig. 4.77(a). Fig. 4.77(b) shows the rates of reaction for 2-propanol removal and propene and acetone formation, i.e. r_{IPA}, r_p, and r_{Ac} as a function of CoO content. The rate of removal of 2-propanol per g CoO is also shown. The activity drops linearly as the CoO content increases for all the catalysts.

Fig. 4.78 shows the "compensation effect" plots for the Arrhenius parameters obtained in the CMT, MCT and CMTg series with respect to the products. Points for both reactions, i.e. dehydration and dehydrogenation, do not lie on the same line, the slopes of which correspond to an isokinetic temperature of 462K and 478K, respectively.

Table 4.26 Kinetic parameters for decomposition of 2-propanol over CMTg series

Catalyst	% conv.[1]	r_{IPA}[2]	r_P[3]	r_{Ac}[4]	S_P[5]	S_{Ac}[6]	E_{IPA}[7]	E_P[8]	E_{Ac}[9]
$CoMoO_4$	2.53	0.68	0.68	-	100	-	64.7	63.3	-
CMTg1	2.44	0.65	0.38	0.27	58.8	41.2	96.3	106.3	64.7
CMTg2	4.15	1.11	0.72	0.39	64.7	35.3	102.1	111.6	75.3
CMTg3	5.61	1.50	0.99	0.51	65.9	34.1	91.6	104.0	74.0
CMTg4	6.44	1.72	1.18	0.54	68.7	31.3	96.0	108	73.6
CMTg5	7.62	2.04	1.50	0.54	73.4	26.6	67.9	79.9	45.6
CMTg6	7.37	1.97	1.43	0.54	72.7	27.3	92.8	101.5	71.7
CMTg7	5.92	1.58	1.17	0.41	74.4	25.6	71.7	80.0	61.8
TiO_2 (P - 25)	2.22	0.59	0.59	-	100	-	61.8	61.0	-

1 = % conversion

2 = rate of 2-propanol removal in $mmol.h^{-1}.g_{cat}^{-1}$ at 453K.

3 = rate of propene formation in $mmol.h^{-1}.g_{cat}^{-1}$ at 453K.

4 = rate of acetone formation in $mmol.h^{-1}.g_{cat}^{-1}$ at 453K.

5 = propene % selectivity at 453K

6 = acetone % selectivity at 453K

7 = activation energy for 2-propanol in $kJ\ mol^{-1}$

8 = activation energy for propene in $kJ\ mol^{-1}$

9 = activation energy for acetone in $kJ\ mol^{-1}$

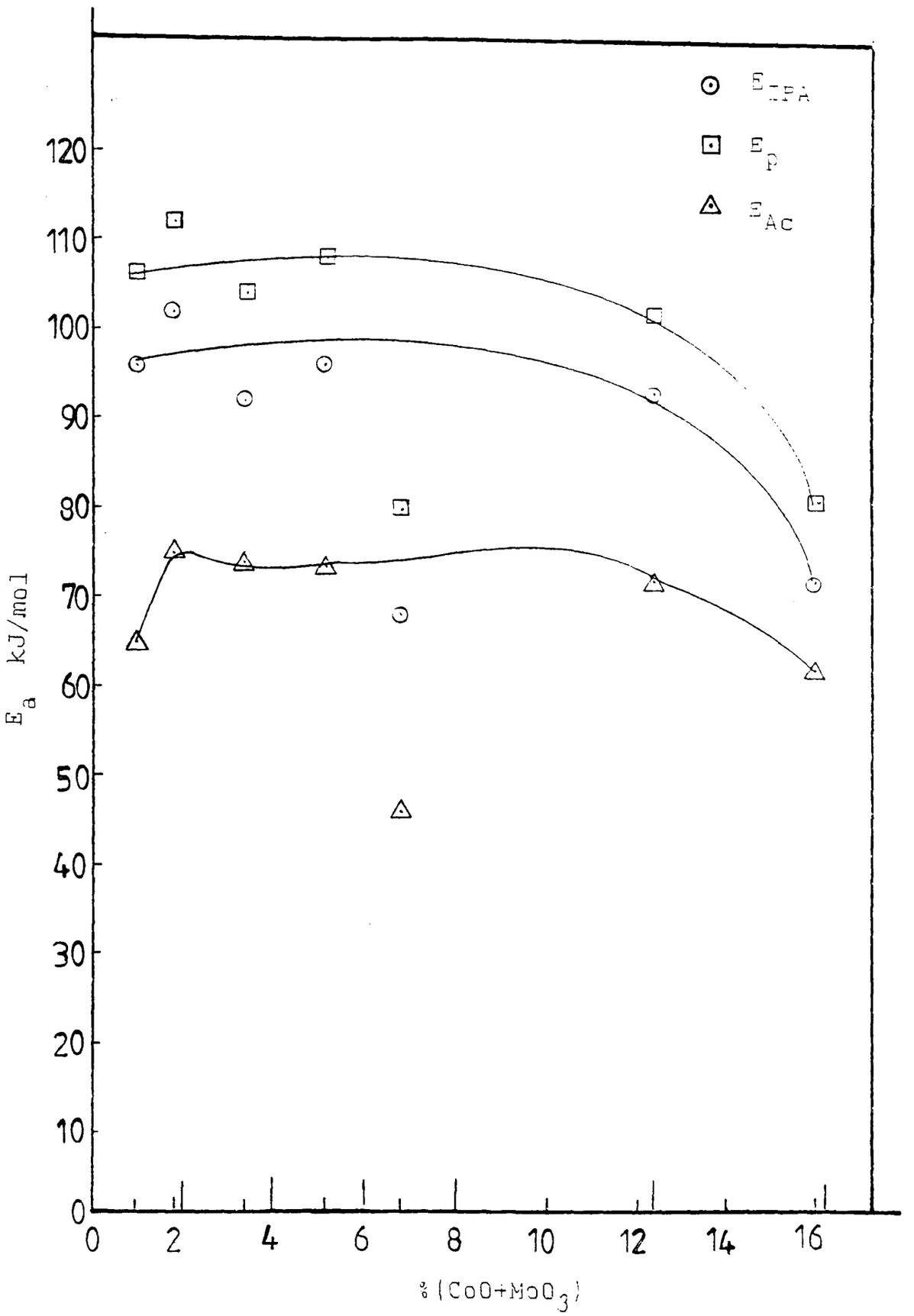

Fig. 4.74 Variation in activation energies E_{IPA}, E_P, and E_A as a function of total CoO and MoO_3 content for the CMTg series.

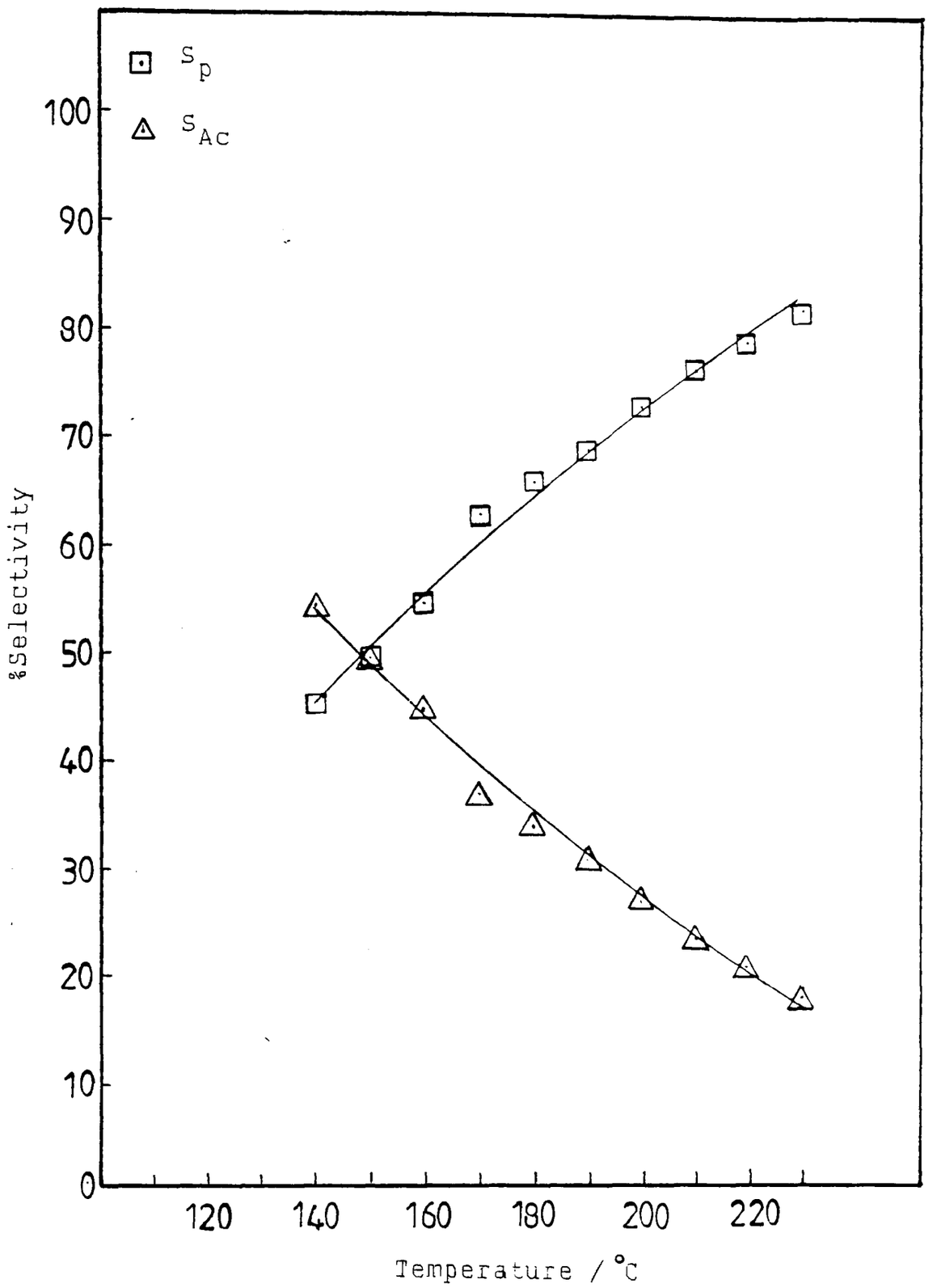

Fig. 4.75 Variation in selectivity to propene and acetone formation with temperature in 2-propanol decomposition over the CMTg3 catalyst.

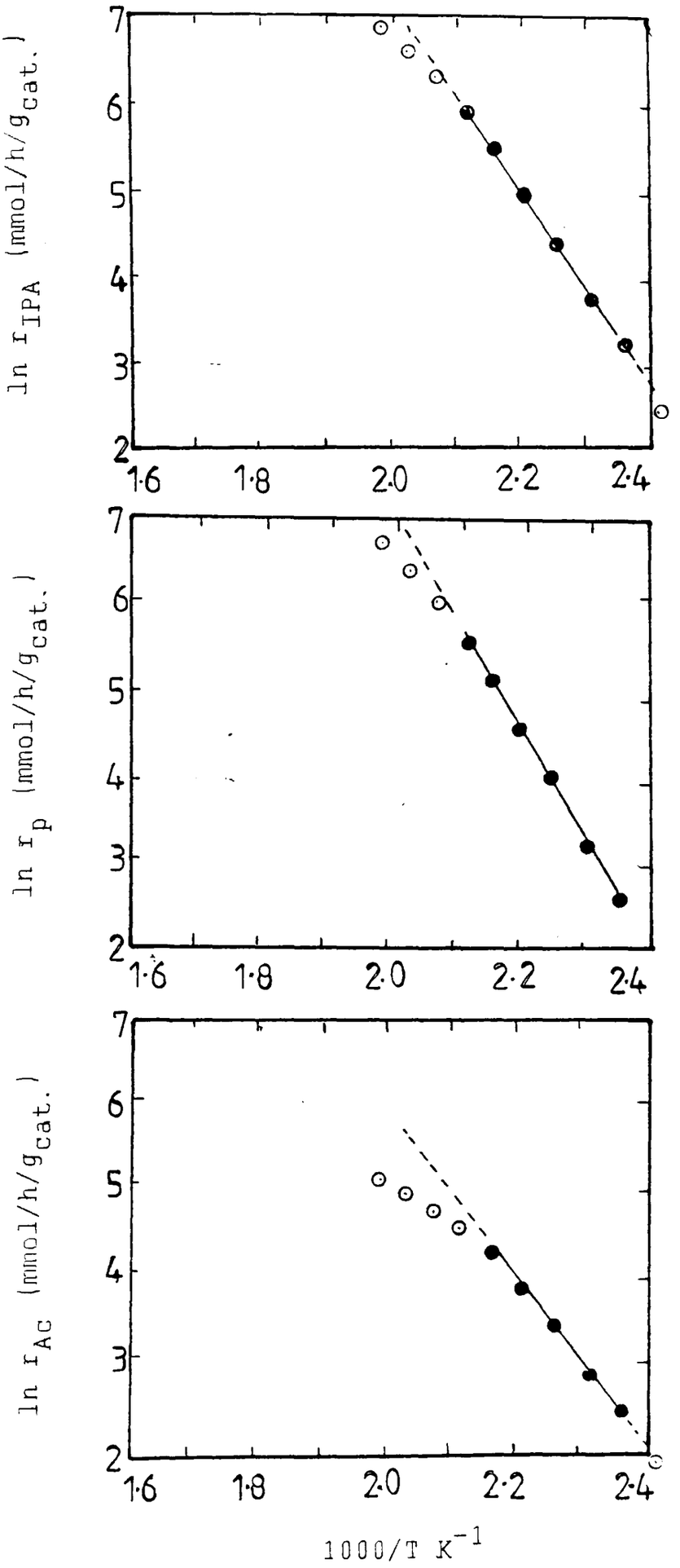

Fig. 4.76 Arrhenius plots for 2-propanol decomposition over CMTg3 catalyst, (a) 2-propanol removal, (b) propene formation, and (c) acetone formation.

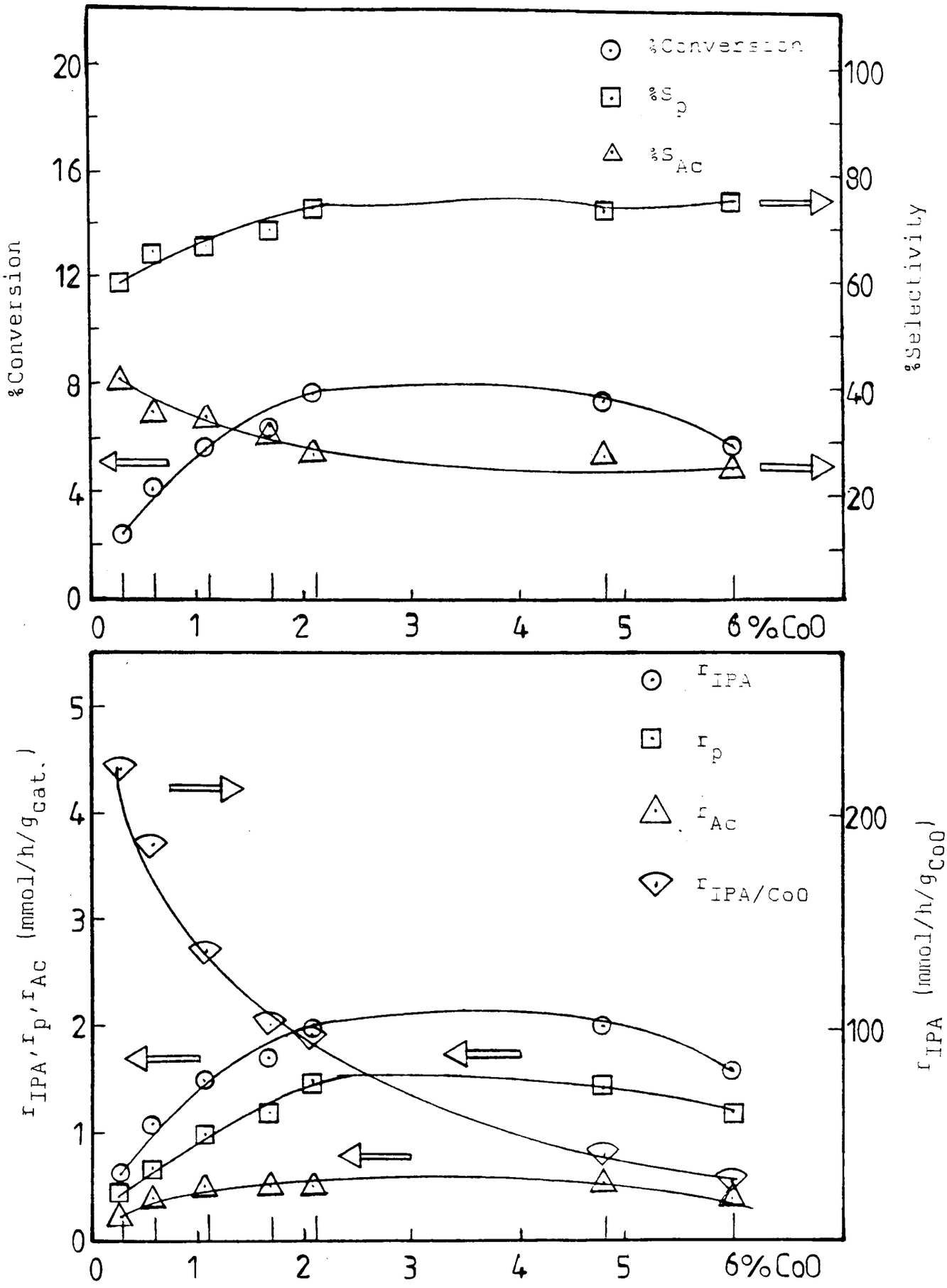

Fig. 4.77 (a) Variation in % conversion, S_p, and S_A with CoO content for CMTg series
(b) Activity of CMTg catalysts as a function of CoO at 453K

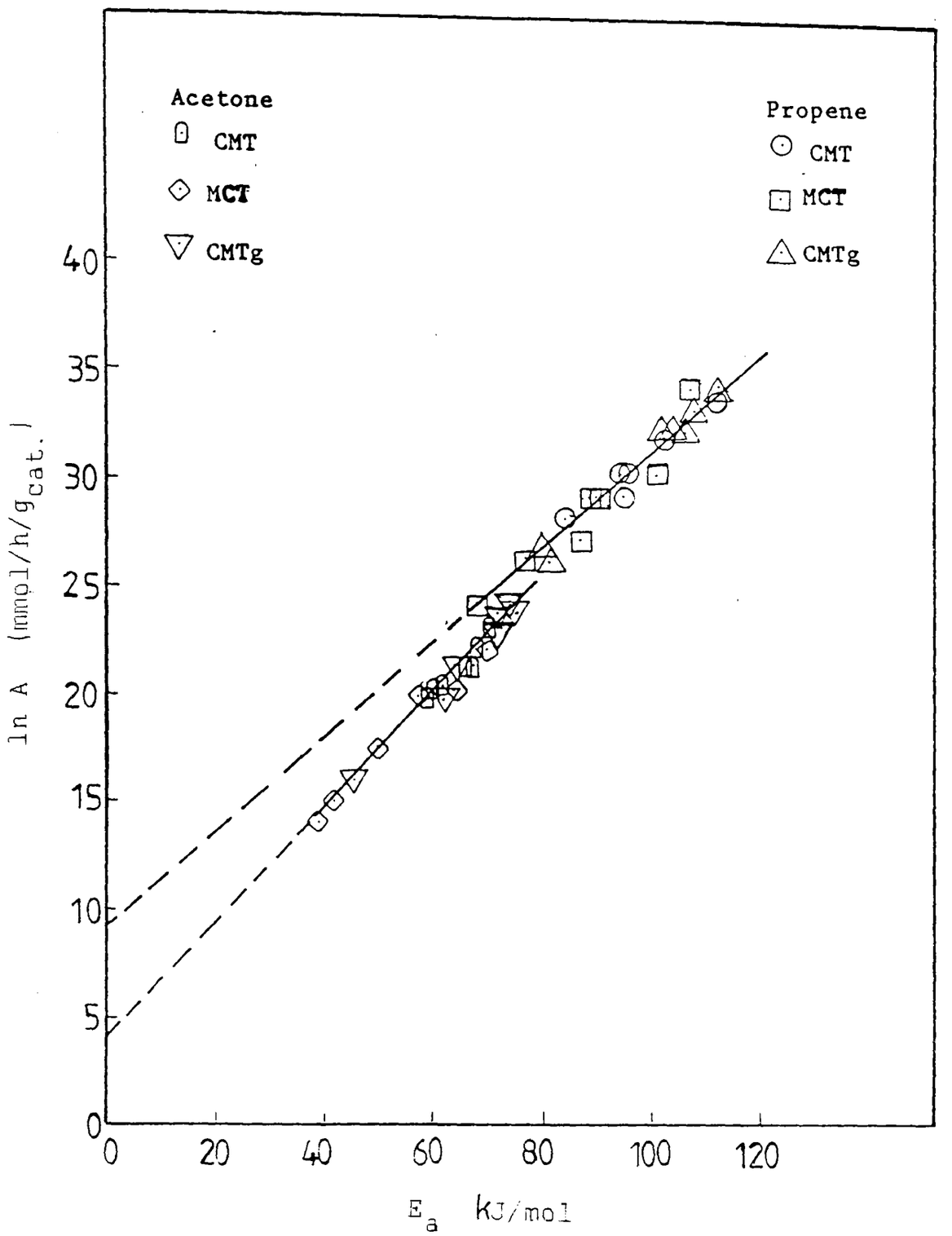

Fig. 4.78 Compensation effect for 2-propanol decomposition catalysed by $CoO-MoO_3/TiO_2$ catalysts.

4.2 References

1. J. R. Anderson and K. C. Pratt, in "Introduction to characterization and testing of catalysts" Academic Press, London and New York. (1985).

2. D. S. Zingg, L. E. Makovsky, R. E. Tischer, F. R. Brown and D. M. Hercules, J. Phys. Chem., 86, 360 (1980)

3. R. L. Chin and D. M. Hercules, J. Phys. Chem., 86, 360 (1980)

4. R. B. Greegor, F. A. Lytle, R. L. Chin, and D. M. Hercules, J. Phys. Chem., 86, 1232 (1981).

5. J. Grimblot and J. P. Bonnelle, J. Electron Spectr., 9, 449-457 (1976).

6. J. Haber and L. Ungier, J. Elec. Spec. Rel. Phen. 12, 305-312 (1977).

7. M. Oku and K. Hirokaw, J. Elec. Spec. Rel. Phen. 8, 475-481 (1976).

8. G. C. Bond, Z. Phys. Chem. Neue Folge, Bd. 144, S. 21-31 (1985).

9. G. C. Bond, and S. Flamerz, Appl. Catal. 33, 219 (1987).

CHAPTER 5 DISCUSSION

5.1 MoO_3/TiO_2 catalysts

5.1.1 Laser Raman spectroscopy (LRS)

Raman spectra for MoO_3/TiO_2 catalysts prepared by impregnation using ammonium heptamolybdate (AHM) and molybdenum oxalate, i.e. MT/C and MOT/C series, are given in Sec. 4.1.1.1.

TiO_2 as low surface area ($\sim 10 m^2 g^{-1}$) anatase shows relatively intense Raman bands at 640, 515 and 395 cm^{-1}, and with pure MoO_3 bands at 998, 821 and 668 cm^{-1} were readily detectable[1]. With the supported MoO_x however no significant bands were observed at MoO_3 contents of 1 wt.% or less for either the MT/C or the MOT/C series. At higher concentrations, bands at 980, and 972 (shoulder), 820 and 995 cm^{-1} appear, their intensities varying with MoO_3 content as shown in Figs. 4.1 and 4.2 (Sec. 4.1.1.1). The two former bands are clearly associated with some intermediate phase, as their intensities pass through maxima (2); the latter two are due to microcrystalline MoO_3.

The most prominent characteristic wave-number regions of vibrational modes of molybdate species are: 200-250, 300-350, 700-850, and 900-1000 cm^{-1}[2], which are to be assigned respectively to Mo-O-Mo deformation, Mo=O bending vibra-

tions, antisymmetric Mo-O-Mo stretching and symmetric and antisymmetric terminal Mo=O stretching vibrations [2,3].

Laser Raman spectroscopy was used to follow the morphology of surface and crystalline species as a function of metal loading, metal impregnation sequence and method of impregnation. In general, the spectra of MoO_3/Al_2O_3 catalysts reported by various research groups are comparable. The most marked band is that at 940-970 cm^{-1}. This band shifts to higher wave-numbers with increasing Mo content [3-7]; this can be attributed to the presence of a polymeric octahedrally co-ordinated surface species. The position and the intensity of this band can be modified by the presence of H_2O on the sample[8]. Recent Raman spectroscopic studies of a series of MoO_x/Al_2O_3 catalysts have shown that highly dispersed MoO_x readily interacts with H_2O and O_2, causing large shifts in the metal-oxygen stretching frequencies associated with surface oxide [9,10].

Thomas[11] found that the Raman spectra of Mo catalysts prepared by liquid phase adsorption (pH = 1 and 6) and by gas phase adsorption were essentially similar to the spectra of catalysts prepared by impregnation of Al_2O_3[11]. From the presence of weak bands at 295, 665, 820 and 998 cm^{-1}, he concluded that a small amount of MoO_3 was present in the catalyst prepared by liquid phase adsorption at pH = 1. Dufresne et al.[12] studied catalysts prepared via impregnation using high and low surface area Al_2O_3. Raman spectra show that MoO_4^{2-} ions were present in catalysts with low Mo

loading. For higher Mo concentrations, polymeric aggregates or two-dimensional polymolybdates were thought to be the major species, with Mo-O octahedra being the dominant species. For very high Mo contents, Raman bands were assigned to bulk MoO_3. Depending on the preparation conditions, the $Al_2(MoO_4)_3$ phase could also be detected[12]. They concluded that the dispersion of Mo species is very similar on the two Al_2O_3 supports. They also found that at low Mo loading, many more Mo species in the tetrahedral environment were detected on the low surface area Al_2O_3[12].

Wang and Hall[13] suggested that the band at 950 cm^{-1} corresponds to the Mo=O frequency of a tetrahedral molybdate group bonded to the surface. In addition, they interpreted the ratio of intensities at the 950 and 970 cm^{-1} band as a measure of the ratio of tetrahedral monomeric to octahedrally co-ordinated polymolybdate species. They found that this ratio decreased with increased loading[13]. Leyer et al.[14] prepared a MoO_x/Al_2O_3 monolayer catalyst by the incipient wetness method at pH = 6. The occurrence of low frequency bands in the Raman spectrum indicated the presence of a small percentage (_10%) of Mo as the tetrahedral monomeric species, while the other species were thought to be polymolybdates.

By Raman spectroscopy both bulk MoO_3 and Mo surface species have been detected for MoO_x/SiO_2 catalysts[15,16]. The nature of the surface phase can be considered in the same manner as has been described for MoO_x/Al_2O_3 catalysts, since it concerns the same Raman bands. Qualitatively, the

structure of MoO_x/SiO_2 catalysts thus resembles the structure of MoO_3/Al_2O_3 catalysts. From the presence of crystalline MoO_3 at surface coverages considerably lower than the theoretical monolayer coverage, it was concluded that the adsorption capacity of SiO_2 is lower than that of Al_2O_3[15,16]. The behaviour of SiO_2 is quite different from that of the other supports. In this case, adsorption of molybdate ions from acid solution is not effective for the formation of a complete MoO_x monolayer[17]. The SiO_2 surface is also incompletely covered with MoO_x via adsorption of $MoO_2(OH)_2$ from the gas phase[17]. MoO_x surface species/SiO_2 interactions will therefore be weak. As a consequence, the weakly held molybdate groups will largely decompose on SiO_2 during calcination to form crystalline MoO_3 even below monolayer coverage[3, 18]. Raman spectra of a series of MoO_3/SiO_2 catalysts prepared by impregnation showed a weak broad band appearing at 970 cm^{-1} at 2.8%MoO_3; in 6.7%MoO_3/SiO_2 this shifted to 956 cm^{-1} and an additional broad band at 884 cm^{-1} appeared. Following the band assignments as in MoO_3/Al_2O_3, these bands can be ascribed to a molybdena interaction species which must be considered as an analogue of a polyanion chemically interacting with support surface. The formation of crystalline MoO_3 was first detected in a sample having 6.7%MoO_3 as indicated by the occurrence of the two narrow bands at 996 and 821 cm^{-1}; these increase with increasing Mo loading of the sample[18]. The Raman spectrum for a MoO_x/SiO_2 catalyst (loading near the monolayer capacity) prepared by

the incipient wetness method at pH = 6 and calcined at 500°C showed that crystalline MoO_3 is the dominant species. A weak and broad band near 930 cm^{-1} was detected, which also indicates the formation of some surface molybdate[14]. Stencel et al.[19] studied $Mo^{VI}O_x/SiO_2$ catalysts by Raman spectroscopy and found that the surface of MoO_x/SiO_2 samples depended on the state of hydration/dehydration of the catalysts.

Two Mo species (i.e. Mo monolayer species and MoO_3) have been identified and quantified by Raman spectroscopy for both MT/C and MOT/C catalysts. The monolayer species was shown to increase with Mo loading up to 1 wt.% MoO_3 in both series, and to level off at higher Mo loadings[20]. MoO_3 was detected above 1 wt.% MoO_3 and shown to increase linearly with further Mo additions. The Mo speciation determined from Raman results was shown to correlate with XPS and X-ray diffraction measurements[20].

On the TiO_2 surface, Ti^{4+} ions are octahedrally co-ordinated and the OH groups are uniformly distributed, providing a homogeneous surface for adsorption of molybdate anions[21]. On the other hand, on Al_2O_3, Al^{3+} ions are octahedrally or tetrahedrally co-ordinated and OH groups are preferentially formed in parallel rows[21]. This requires extensive surface diffusion of Mo and rearrangement of the molybdate species deposited during the impregnation and has led to the significant differences between the Raman results of various investigators[21]. As a result, on TiO_2 we see MoO_3 formation only after exceeding the monolayer coverage,

whereas on Al_2O_3, MoO_3 is detected even at submonolayer loadings if the impregnation method of loading is used[21]. On SiO_2, however, at high surface coverages crystalline MoO_3 is formed also, due to weak interaction between MoO_3 and the support[22,23].

Raman results on TiO_2 indicate that, at low coverages, the majority of the surface monolayer molybdate species are in tetrahedral co-ordination[24]. As the coverage approaches one monolayer, polymerization occurs and octahedrally co-ordinated polymeric surface species are formed[24]. Loading beyond a monolayer results in a monolayer of polymeric surface species and bulk-like MoO_3 on top of the monolayer.

5.1.2 Temperature-programmed reduction (TPR)

TPR profiles for the MT/C and MOT/C catalysts are shown in Figs. 4.5 and 4.6, respectively. (See Section 4.1.2.1). Below the monolayer region, i.e. 0.5 wt.% MoO_3, four peaks are formed in both series. With increasing MoO_3 content, the number of peaks decreases from four to two well separated peaks, as shown in Figs. 4.5 and 4.6. T_{max} values are similar in both MT/C and MOT/C catalysts, as given in Tables 4.1 and 4.2 respectively (See Section 4.1.2.1).

Fransen et al.[25] studied the reduction of bulk MoO_3 and MoO_x/Al_2O_3 monolayer catalysts by measuring the valence state of Mo after 16h of reduction at control temperature. The TPR profile for bulk MoO_3 shows that MoO_3 is reduced to

Mo^{o} in two steps, passing through MoO_2 as an intermediate[26,27]. (It was observed that MoO_3 is reduced to MoO_2 at a temperature of 330°C but for MoO_x/Al_2O_3 this step occurs at 450°C. It was concluded that the higher valence state of Mo was stabilized by a strong interaction with the support. However, Yao[28] found that at 500°C the reducibility of a series of MoO_x/Al_2O_3 catalyst samples was higher than for bulk MoO_3. The reducibility for higher Mo loading was greater than for low Mo loading. Calcination at higher temperature for low Mo loading decreases the reducibility of MoO_x/Al_2O_3. He also found that complete reduction to Mo^{o} occurred rapidly at 900°C for pure MoO_3 while an additional hour at this temperature was required for complete reduction of the supported MoO_x samples.

Many reduction studies show that the average Mo valence after reduction at 500-600°C is +4, which is interpreted as being caused by the presence of mixtures of $Mo^{(VI)}$, $Mo^{(V)}$ and $Mo^{(IV)}$ ions[29, 30]. Thomas et al.[31, 32], and Arnoldy et al.[33], applied TPR to a series of MoO_x/Al_2O_3 catalysts. They found that the $Mo^{(VI)}$ monolayer species, which interacted strongly with the support, were reduced at higher temperatures (at 610-880°C) while the $Mo^{(VI)}$ bilayer/multilayer was reduced in one step to Mo^{o} at lower temperatures (between 380-460°C). Burch and Collins[34] observed that the TPR profiles for MoO_x/Al_2O_3 catalysts heated to 730°C show just one peak at 500-520°C which is due to reduction of $Mo^{(VI)}$ to $Mo^{(IV)}$. Caceres et al.[35] obtained TPR results for a series of MoO_3/Al_2O_3 prepared by equilibrium

adsorption and found that supported MoO_3 is reduced first to MoO_2 (at 415-590°C) and then to Mo^o (between 740-770°C). The authors concluded that strong interaction with the support at low Mo content may be due to high dispersion.

Fransen et al.[25] prepared $Mo^{VI}O_x/SiO_2$ catalysts by adsorption of molybdate ions from acid solution and by adsorption of $MoO_2(OH)_2$ from the gas phase; incomplete monolayers were formed. Valence measurements showed that the $Mo^{VI}O_x$ surface species was reduced to $Mo^{IV}O_x$ at 330°C as if it were pure MoO_3, while $Mo^{IV}O_x/Al_2O_3$ was reduced to $Mo^{IV}O_x$ only at 450°C. Thomas et al.[31] prepared two series of MoO_3/SiO_2 catalysts by wet and dry impregnation. They found that the major part of the molybdate species in the catalysts was reduced at lower temperature than pure MoO_3. At the lowest Mo contents, only one peak at about 480°C was observed. With increasing Mo content, the intensity of the peak at 630°C and the sharpness of 480°C peak both increased. The two reduction peaks pointed to the presence of two Mo phases, namely $Mo^{VI}O_x$ monolayer species and crystalline MoO_3. The $Mo^{VI}O_x$ monolayer species reduced completely to Mo^o in the low-temperature peak, whereas the crystalline MoO_3 reduced in two steps, viz. to MoO_2 and further to Mo^o in the low- and high-temperature peaks, respectively. Arnoldy et al.[33] prepared a series of MoO_x/SiO_2 catalysts by pore volume impregnation. Their TPR results were similar to those of Thomas et al.[31].

Reduction of MoO_3 to Mo^o is a two-step process[33], and there is no evidence for the occurrence of intermediates

which are not stable (Mo_9O_{26}, Mo_8O_{23}, Mo_4O_{11}) or not certain (Mo_2O);

$$MoO_3 + H_2 \longrightarrow MoO_2 + H_2O \quad \text{(TPR 1st peak)}$$
$$MoO_2 + 2H_2 \longrightarrow Mo + 2H_2O \quad \text{(TPR 2nd peak)}.$$

TPR results show that the reduction rate of MoO_3 to MoO_2 depends on experimental parameters, namely sample size, H_2O addition to the reducing mixture, particle size, heating rate and precalcination temperature[33]. The influence of H_2O pressure on MoO_2 reduction is explained by the thermodynamics of the equilibrium $MoO_2 + 2H_2 \rightleftharpoons Mo + 2H_2O$.

The thermal stability of TiO_2 (anatase) is lower than that of γ-Al_2O_3 since the transition to rutile occurs at about 600-700°C[36]. Of particular note is the reducibility of TiO_2, which results in the formation of various stoichimetric and non-stoichimetric lower oxides[36]. It is well known that TiO_2 with oxygen deficiency, expressed as TiO_{2-x}, shows n-type semiconductivity. Physico-chemical properties of TiO_2[36] are summarized in Table 5.1. The thermodynamic properties of Ti_4O_7 which are observed in strong metal-support interaction (SMSI) phenomena are uncertain.

The reduction of TiO_2 by H_2 is given by[37]:

$$3TiO_2 + H_2 \longrightarrow Ti_3O_5 + H_2O \quad \Delta H = +37.2 \text{ kJ mol}^{-1}$$

thus the reaction is only slightly endothermic. Thermodynamically, TiO_2 is easily reduced, compared with Al_2O_3 and SiO_2. It is frequently observed that the surface of TiO_2 changes its colour, from white to bluish gray, by reduction when it is treated with H_2 at elevated temperatures[36].

Table 5.1

Physico-chemical properties of TiO_2, Al_2O_3 and SiO_2

	TiO_2 (anatase)	Al_2O_3 (γ-alumina)	SiO_2 (silica gel)
Density/gcm^{-3}	3.90	3.66	2.2
Heat of formation /$kJmol^{-1}$	-911.2	-1191.3	-856.9
Thermal stability	600-700°C anatase-rutile	1100-1200°C	600-700°C sintering
Reducibility	possible existence of lower oxidation state	difficult	difficult
Surface area[(a)]/m^2g^{-1}	50-120	100-300	300-1000

(a) When hydrate is calcined at about 500°C

It is clear that the first reduction step for MoO_x species on the support occurs at a lower temperature than for pure MoO_3, although the second stage takes place at about the same temperature in both the MT/C and MOT/C series. (See Section 4.1.2.1). In the sub-monolayer region of both series, with increasing Mo content, the two stages of reduction continue to be well-defined, showing that MoO_2 is a stable intermediate in the sub-monolayer region. A

possible explanation is that peaks 1 & 2 are first stage and peaks 3 & 4 are second stage as follows:

peak 1 is monolayer tetrahedral
peak 2 is monolayer octahedral
} $Mo^{VI} \longrightarrow Mo^{IV}$

peak 3 is second stage of monolayer, $Mo^{IV} \longrightarrow Mo^{o}$

peak 4 is second stage of particulate, $Mo^{VI} \longrightarrow Mo^{o}$.

Peaks 1 and 2 are swamped by growing Mo octahedral forming particulate MoO_3 and appear to merge. Distinction between octahedral and tetrahedral may not be preserved into the second stage of reduction. T_{max} values for both stages increase in the one to four monolayer region, and then remain constant in spite of T_{max} for the first stage always remaining significantly lower than in pure MoO_3.

5.1.3 X-ray photoelectron spectroscopy (XPS)

The XPS spectra of the MT/C and MOT/C series prepared from AHM and molybdenum oxalate precursors are illustrated in Figs. 4.29 and 4.30, respectively. (See Section 4.1.3.1). The binding energies of the $Mo3d_{3/2}$ and $Mo3d_{5/2}$ levels in all samples are observed at 235.0 $\pm$ 0.2 and 231.8 $\pm$ 0.3 eV, respectively; these values are similar to the values of pure MoO_3 (235.1 and 232.2 eV) as given in Tables 4.14 and 4.15 for both series. Figs. 4.31 and 4.32 show the

intensity ratio of $Mo3d_{5/2}/Ti2p_{3/2}$ as a function of MoO_3 content for both series. The ratio initially increases in proportion to the MoO_3 content, but the curve deviates at about 1.0 wt.% MoO_3 in both the MT/C and the MOT/C series. This value is similar to the experimental monolayer capacity which was given by the $MoOCl_4$ method "grafting method"(1).

A large number of studies on MoO_3/Al_2O_3 catalysts have been made using XPS. Zingg et al. (38) studied MoO_3/Al_2O_3 catalysts by XPS and found the presence of only Mo^{VI} on the oxidic catalyst. They also studied the reduction of MoO_3/Al_2O_3 samples at 500°C and found that the Mo^{VI} intensity decreased rapidly with time, resulting in $Mo^{(V)}$ and $Mo^{(IV)}$. They explained that octahedral Mo^{VI} was reduced completely to Mo^{IV} after 12h of reduction at 500°C in H_2 while tetrahedral Mo^{VI} $[Al_2(MoO_3)_4]$ was reduced only to $Mo^{(V)}$. Thomas et al.(32) studied MoO_x/Al_2O_3 catalysts by XPS and found that the XPS intensity ratio (IMo3d/IAl2p) were in good agreement with the theoretical monolayer prediction. The authors concluded that the MoO_3 is highly dispersed and that a small deviation at the highest concentration was probably due to a non-uniform distribution of the MoO_3 phase over the catalysts. Dufresne et al.(12) studied MoO_3/Al_2O_3 catalysts prepared using both high and low surface area Al_2O_3 by XPS. The authors plotted the intensity ratio (IMo3d/IAl2p) as a function of Mo content expressed as the molar ratio Mo/Al and obtained two straight lines in the low Mo content range. This was explained by a monolayer coverage of Al_2O_3 by MoO_x species. They found

that deviations from a straight line began at Mo/Al ratios, of $4x10^{-2}$ and $9x10^{-2}$ - $10x10^{-2}$, which corresponded to completion of the monolayer for low- and high-surface area Al_2O_3 respectively. The dispersion of MoO_x species was similar between the two Al_2O_3 supports. Kasztelan et al.[39] applied XPS to MoO_3/Al_2O_3 catalysts prepared using an equilibrium adsorption method. They found that the increases in the XPS intensity ratio (IMo3d/IAl2p) after calcination were a consequence of a modification of dispersion, i.e. the migration of Mo from multilayer dispersion at the drying step to a monolayer dispersion at the calcination step. Leyrer et al.[14] heated a MoO_x/Al_2O_3 monolayer catalyst to 400°C in H_2 (2h) and the XPS results showed that the degree of reduction was low, but some Mo^{IV} and $Mo^{(V)}$ were formed.

Thomas et al.[31] studied MoO_3/SiO_2 catalysts by the XPS technique. The results showed that the intensity ratio (IMo3d/ISi2p) was lower compared to the theoretical monolayer prediction and the deviation of the experimental points from the monolayer line occurs at a lower Mo content than expected on the basis of the appearance of bulk MoO_3.

The variation in the XPS intensity ratio for both MT/C and MOT/C series (Figs. 4.31 and 4.32 in Section 4.1.3.1) strongly suggests a change in structure above the monolayer point. A simple theoretical model based on the structures in Fig. 5.1 was developed[40] in which the escape depths of the Ti2p and Mo3d electrons, and the fraction of surface covered by the "towers" are the only adjustable parameters.

Let the fraction of the surface covered by the "towers" be given by x=1/y and let m denote the number of monolayer equivalents to which the MoO_3 concentration corresponds. Then if all the "towers" are of uniform height, the number of layers n in each is given by

$$n = [(m-1)/x] + 1$$

Thus for example if x = 0.25 and the MoO_3 concentration corresponds to m = 2, the value of n is five, since the "tower" is formed above the monolayer (See Fig. 5.2). The

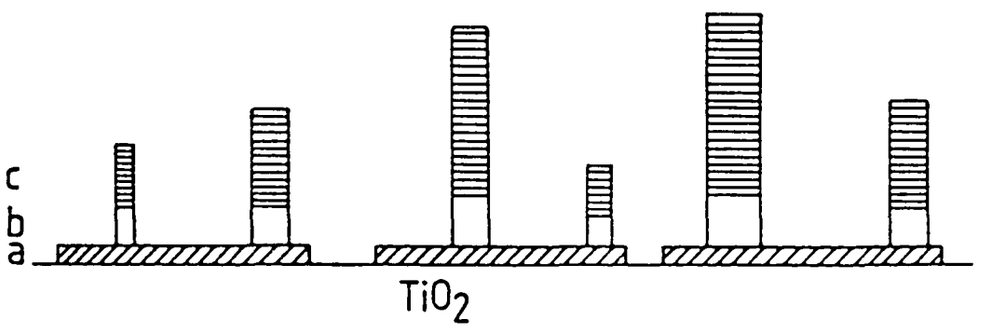

Fig. 5.1 Model of MoO_3 on TiO_2 showing the different phases which are formed as a function of MoO_3:
(a) up to one monolayer (surface MoO_x complexes);
(b) two-four monolayers (disordered MoO_x); and
(c) above four monolayers (particulate MoO_3).

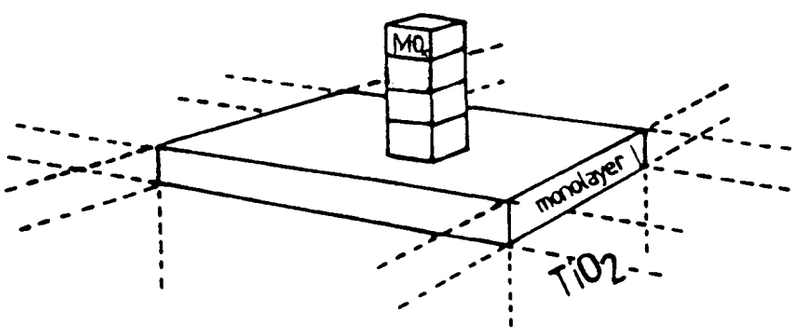

Fig. 5.2 Illustration of a "tower" on top of the monolayer.

fundamental expression for the dependence of signal intensity I upon the depth at which the electron originates is

$$I = Io \exp(-nd/\lambda)$$

for electrons emitted in a direction normal to the surface, λ being termed the escape depth[41] and d the thickness of a single layer of the oxide. Since we are only concerned with relative intensities, the value of Io is irrelevant, and so I(Ti) and I(Mo) are defined as the fractional intensities for each element, i.e I/Io. The expressions for the intensities of x, n and d/λ (denoted as f_1 for Ti and f_2 for Mo above the monolayer point are as follows:

$$I(Ti) = (1-x)[\exp(-f_1)] + x[\exp(-nf_1)];$$

$$I(Mo) = (1-x)[1-\exp(-f_2)] + x[1-\exp(-nf_2)].$$

The value of this intensity ratio may then easily be calculated as a function of the variable terms. Initially we assume the values of escape depths for electrons in TiO_2 and in MoO_3 as 1.5 and 2.7 nm, respectively, and the values of d equal (0.5 nm): thus $f_1 = f_2 = 0.3$. The effect of altering these assumptions is explored subsequently. The above expressions suppose that only those electrons reach the detector which are emitted through the monolayer or the top of the "towers". This is likely to be approximately true if the "towers" are not too high and for that part of the sample exposed to the incident X-rays and hence sensed by the measurements.

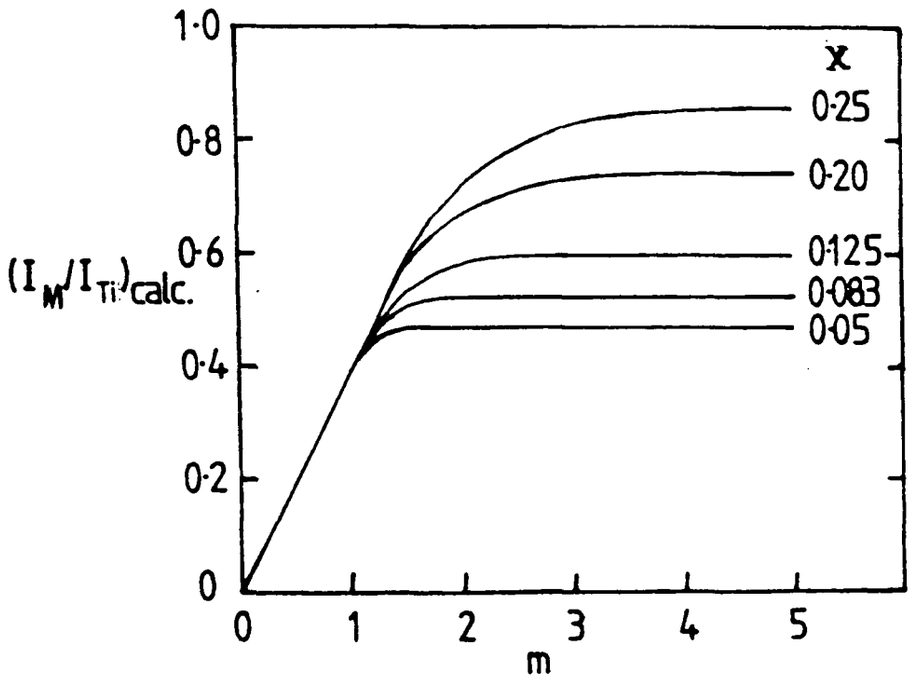

Fig. 5.3 Dependence of the calculated intensity ratio on number of monolayer equivalents for $f_1 = f_2 = 0.3$ and various values of x as shown.

Fig. 5.3 shows how the calculated Mo/Ti intensity ratio varies with the number of monolayer equivalents as x is varied, taking f_1 and f_2 as both equal 0.3. Clearly as x tends towards unity, the slope of the curve above the monolayer point increases until ultimately when x is exactly unity, we would have a uniform second and subsequent layers. As x tends to zero, the slope of the curve becomes less. It is a feature of the calculations that even for quite low values of x the intensity ratio continues to rise above the monolayer point, to an extent depending upon the value of x, before reaching a limiting value. The extent to which the calculated intensity ratio increases between the one monolayer point and the limiting value is a useful parameter to assist with fitting the calculated curves to the experimental points.

Although the value for the f parameter was selected on the basis of reasonable estimates for d and λ as described earlier, we have examined the sensitivity of the calculated curves to the values of f_1 and f_2 used. Changing $f_{1,2}$ from 0.27 to 0.39 only alters the ratio of I_∞/I_M (i.e. the factor by which the intensity ratio increases from its value of one monolayer to the limiting value) from 1.60 to 1.44; it is 1.50 when $f_{1,2}$ is 0.3. This change corresponds to decreasing the escape depth λ from 1.85 to 1.28 nm. Similarly, altering f_1 and f_2 independently between 0.27 and 0.39 affords values of I_∞/I_M in the same range. The calculated curves are not therefore highly responsive to the values of f_1 and f_2 employed.

Two of the other assumptions have also been looked at. It is improbable that all the "towers" will have the same height. We have calculated the intensity ratio for m = 2 (x = 0.1, $f_{1,2}$ = 0.3) assuming equal numbers of "towers" whose heights are in the ratio 1:2:3; the value obtained (0.538) is very close to that found (0.545) when all "towers" were taken as of equal height. Finally the projected dimensions of the "towers" are unlikely to be uniform. A trial calculation assuming one-half the surface has "large towers" (x = 0.2) and the other half has "small towers" (x = 0.1), the heights of which are such that the masses of MoO_3 in the two parts are the same, produced a curve of intermediate shape. However the introduction of too many disposable parameters having no experimental justification into such a simply-conceived calculation is

unprofitable. The quality of the fits obtained with the experimental results suggests that the "towers" are of fairly similar cross-sectional area.

The quantitative fitting of $I(Mo3d_{5/2})/I(Ti2p_{3/2})$ ratios is shown in Fig. 5.4. The curve is calculated for a surface coverage by "towers" of 10%. This fits the experimental points well up to about the ten monolayer point, but deviation is observed at higher MoO_3 contents, probably because more of the surface is covered by MoO_3 microcrystals in this region.

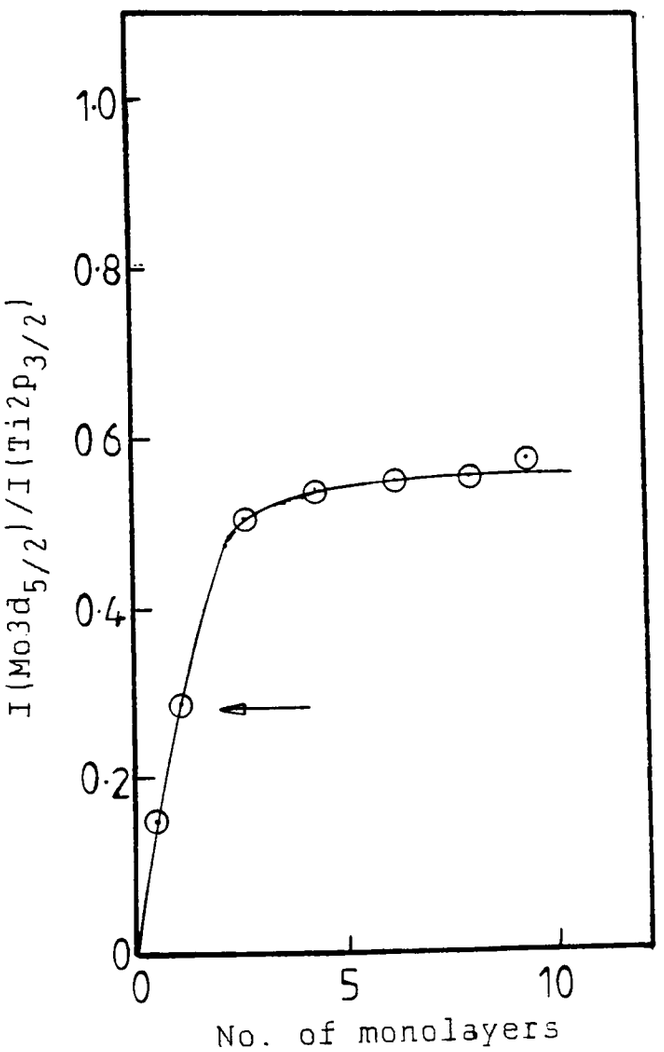

Fig. 5.4 XPS intensity ratios as a function of the number of monolayers for MoO_x/TiO_2 catalysts prepared by impregnation using AHM and molybdenum oxalate as precursors.

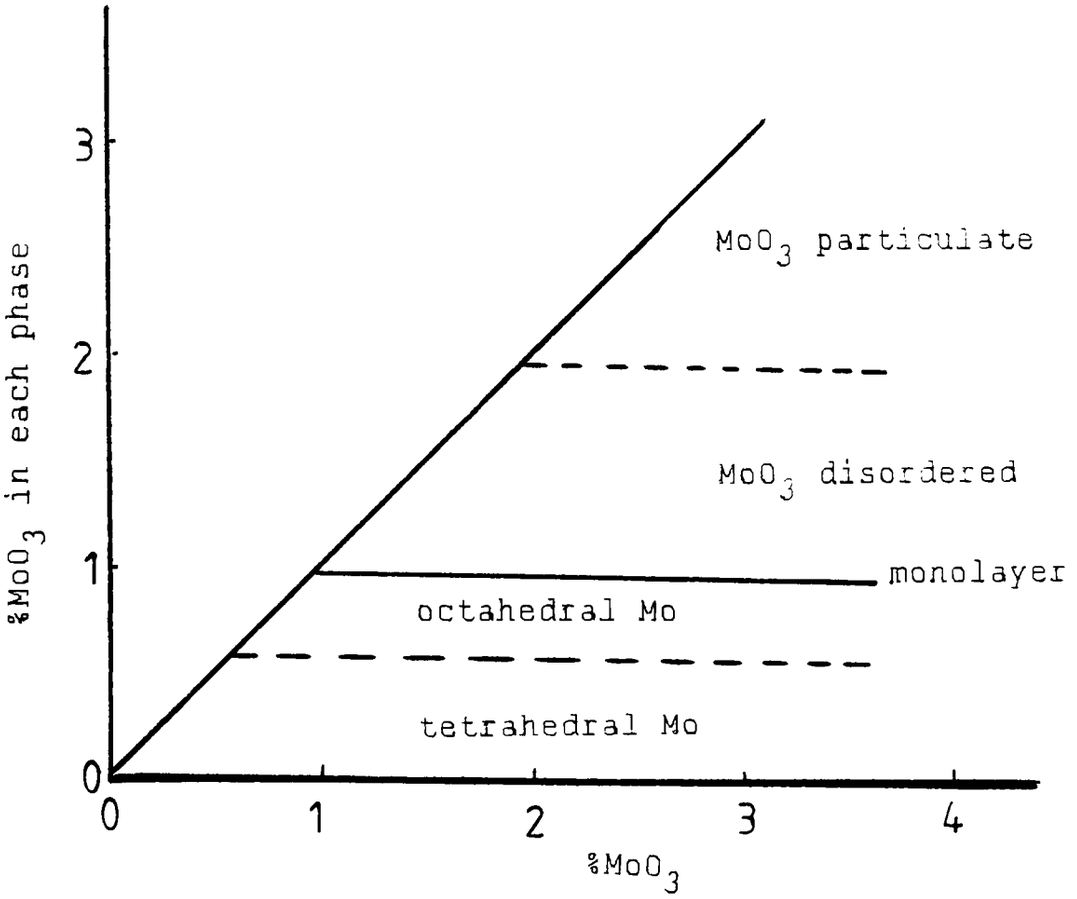

Fig. 5.5 Mo speciations as a function of MoO_3 content for both MT/C and MOT/C catalysts.

By combining the LRS, TPR and XPS results, four distinct species have been observed in both MT/C and MOT/C series. Below monolayer coverage two species are formed: both tetrahedral and octahedral Mo in the lattice of TiO_2. The tetrahedral species is formed preferentially at low loadings. Above monolayer coverage, both "disordered MoO_3" and MoO_3 have been identified.

Fig. 5.5 summarizes the phases observed on a MoO_x/TiO_2 surface and the approximate concentration ranges over which they occur. Monolayer coverage is about 1 wt.% MoO_3. Below the monolayer region, tetrahedral and octahedral Mo species are dominant. Above the monolayer coverage, both particulate or "disordered MoO_3" and MoO_3 appear. The position

of the horizontal lines is not accurately known, so that the phase-diagram is only semi-quantitative.

5.1.4 Transmission Electron Microscopy (TEM)

TEM micrographs of MT/C and MOT/C catalysts reduced under TPR conditions, i.e. from RT to 1000°C are shown in Figs. 4.43 and 4.44, respectively (see Section 4.1.4.1). The average particle size for MT/C catalysts was 2-3 nm, whereas the average particle size for MOT/C was 22-33 nm. The differences in particle size could be attributed to different types of crystal habit formed on decomposing the precursor in the calcined state.

5.1.5 Catalytic decomposition of 2-propanol

Many factors have been brought forward in the literature as exerting important influences upon the selectivity of metal oxide surfaces for catalytic dehydrogenation, ($-H_2$), or dehydration, ($-H_2O$), of aliphatic alcohols[47]. Two particular facets of the properties of oxide monolayers are relevant to their catalytic behaviour[48]: (i) their ease of reduction, and (ii) their acidic character.

A number of studies have been reported recently, bearing on the acidic character of supported transition metal oxides [49-55]. Many such systems show good activity for hydrocracking[56], but the well-established techniques of NH_3 desorption and spectral observation of adsorbed pyridine provide further detail[50-52]. Lewis acidity associated with co-ordinatively unsaturated sites is

sometimes detected[57] but Brønsted-type acidity is more frequently seen[49, 53]. First-principles quantum mechanical calculations[58] show that the latter depends on the number of doubly-bonded O atoms and is enhanced by delocalisation of charge into the support.

In our laboratory, 2-propanol decomposition was examined on VO_x/TiO_2[59] and MoO_x/TiO_2 systems[48], the latter being prepared by aqueous impregnation using solutions of either $(NH_4)_6Mo_7O_{24}.4H_2O$ or $H_2[MoO_3(C_2O_4)].H_2O$, followed by drying and calcination. Both low-area anatase and Degussa P-25 TiO_2 have been used as supports; these have only low activity at the temperatures used ($\sim 220^oC$ for VO_x/TiO_2; 180^oC for MoO_x/TiO_2) and tend to give propene as the chief product. For VO_x/TiO_2, rates expressed per g V_2O_5 are much higher for low loadings of V_2O_5 than for the unsupported oxide, and decrease with increasing loading, suggesting that the activity of the monolayer species is superior to that of the condensed phases formed when the monolayer capacity is exceeded. The selectivity to propene is much lower (30-40%) than for TiO_2 and is almost independent of V_2O_5 content, and activation energies are also notably lower[59].

2-propanol dehydration was used as a measure of catalyst acidity[60]. For SnO_2/V_2O_5, TiO_2/MoO_3 and TiO_2/V_2O_5 systems there was a good correlation between catalyst acidity and activity. For a study of a large number of oxides of the type V_2O_5-X_nO_m, Ai also used 2-propanol

dehydration-dehydrogenation as a measure of the acid-base nature of the catalyst system. It was assumed that:

(i) acidity $\propto$ dehydration rate,

(ii) basicity $\propto$ dehydrogenation rate/dehydration rate, and

(iii) dehydrogenation rate $\propto$ (acidity)(basicity).

For MoO_3-P_2O_5 catalysts, a maximum in 2-propanol activity and presumably for surface acidity was found when P/Mo = 0.1. Some of the behaviour could be accounted for by surface area variation with composition, but P_2O_5 alone is of low acidity and some enhancement must be caused by interaction of P_2O_5 and MoO_3 to give a new kind of acid site. The evidence would certainly support activity residing in Brønsted and/or Lewis-acid sites. However, subtle variation in activity can occur, affected by the strength of associated basic sites in dehydration catalysts.

Research into alcohol dehydration mechanisms has proved to be a very fertile area of investigation and the possible mechanistic pathways have been outlined by Vinek et al[61]. The following criteria can be used to define the mechanistic pathway:

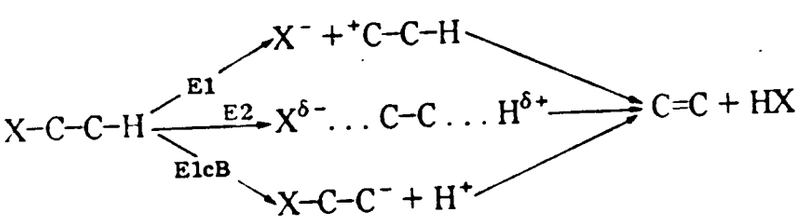

(a) E_1. C-OH bond rupture occurs with carbonium ion formation, the latter being capable of positional and geometrical isomerization, all possible alkenes being formed.

(b) E_2. Reaction is concerted, single step, with no intermediate formed. Saytzev alkene orientation occurs from 2-ols,i.e. there are more alk-2-enes than alk-1-enes.

(c) E_1cB. C-H bond rupture occurs via the most acidic proton. Hofmann orientation of alkenes occurs, i.e. alk-1-enes are formed preferentially from 2-ols and there is a tendency for dehydrogenation to occur.

The above categories are rarely clear cut and quite often an intermediate situation can occur, particularly with E_1 and E_2 pathways. The nature of the alcohol is of importance and the order of ease of dehydration is tertiary > secondary > primary[61] and tertiary alcohols tend to react via an E_1 mechanism because of the relative stability of the tertiary carbonium ion.

As to the activity of MT/C and MOT/C catalysts, the rate of 2-propanol removal per g of MoO_3 kept increasing as the MoO_3 increases for MOT/C, whereas the rate of 2-propanol removal per g MoO_3 increases up to 3wt.% MoO_3, and decreases again. This could be attributed to the striking fact that apart from the well-known equilibrium about aqueous AHM:

$$Mo_7O_{24}^{6-} + 4H_2O \rightleftharpoons 7MoO_4^{2-} + 8H^+$$

another process (or processes) must be involved. Tsigdinos et al.[62] suggested that the effect is caused by impurities; however, more important would seem to be an equilibrium which we may write as :

$$Mo_7O_{24}^{6-} + MoO_4^{2-} + 2H^+ \rightleftharpoons [H_2Mo_8O_{28}]^{6-}$$

This octamolybdate species tends to polymerize and eventually a precipitate is formed[63]. Another factor is that the crystal habit in the MoO_3 formed on calcination from molybdenum oxalate precursor is not the same as that from AHM precursor, which may lead the higher surface area for MoO_3 in the case of the MOT/C catalyst and lower surface area of MoO_3 in the MT/C catalyst[64].

5.2 CoO_x/TiO_2 catalysts

5.2.1 Temperature-programmed reduction (TPR)

Three series of the CoO_x/TiO_2 catalysts were prepared by aqueous impregnation using cobalt nitrate and cobalt acetate as precursors, i.e. CT/C and CAT/C, respectively; and by homogeneous precipitation, i.e. CT/HP (see Section 4.1.2.2). TPR profiles for CT/C, CT/HP, and CAT/C series, are shown in Figs. 4.11, 4.14, and 4.17, respectively (see Section 4.1.2.2). T_{max} values as a function of Co content for all the three series are also illustrated in Section 4.1.2.2. In the case of the CT/C series, two peaks and a shoulder are observed for all Co concentrations, whereas with CT/HP series, two main peaks are formed up to 4.8wt.% CoO_x. Above 4.8wt.% CoO_x, two more peaks are formed up to

9.6wt.% CoO_x. Finally, the CAT/C series showed four groups of TPR peaks. The reduction process of the supported CoO_x catalysts in all the three series starts at a temperature lower than that at which unsupported CoO and Co_3O_4 start to reduce.

Paryjczak et al.[65] have studied the TPR of 1-10wt.% Co_3O_4 on Al_2O_3 and SiO_2. For 10 wt.% Co_3O_4/SiO_2 the reduction peak is at 693K and reduction is complete by 873K. For the 1wt.% sample reduction is still incomplete at 873K. This reduction behaviour compares with that for bulk Co_3O_4, which reduces in a double peak with maxima at 593 and 663K, respectively. Clearly the increased difficulty of reduction in the unsupported samples reflects an interaction between the Co species and the SiO_2 support. For γ-Al_2O_3-supported samples reduction was much more difficult[66]. In the case of 10 wt.%Co_3O_4, reduction was still incomplete at 923K. This is yet another example of the much stronger interaction that tends to occur between Al_2O_3 supports and metal species.

A more recent study of 4 wt.% Co on Al_2O_3, 4 wt.% Co on SiO_2, and 2 wt.% Co on TiO_2 was carried out by Van't Blik[66]. Reduction of oxidized Co on Al_2O_3 was difficult, starting at 473K and still not complete at 773K. The TPR profile was characterized by two peaks, one at 573K and the other at 673K. Comparison with the profile for bulk Co_3O_4 showed that for the supported catalyst the reduction was also a sequential process[66]. In order to reduce the catalyst completely, the temperature had to be raised to

1373K and H_2 was consumed between 1073 and 1373K, probably arising from the reduction of a surface Co-Al spinel. In a study of reduced catalysts that had been passivated in air, the TPR results clearly indicated that during passivation corrosive chemisorption of O_2 had taken place. A similar observation was made regarding passivation of TiO_2-supported catalysts[67]. The oxidized Co/TiO_2 catalyst reduced in two peaks, at 588K and 686K, that were ascribed to reduction of a fraction of Co_3O_4 (588K) to CoO and reduction of CoO (686K) to Co^o. This explanation was confirmed as being correct by stopping the TPR at 646K (the minimum between the two peaks), cooling to 223K, then running a second TPR when only the 686K peak was observed.

Arnoldy and Moulijn[68] reported on Co/Al_2O_3 catalysts and their conclusions were broadly similar to those of Van't Blik. They suggested that four phases existed in such catalysts: Phase I reducing around 600K was ascribed to Co_3O_4 crystallites; phase II at about 750K consists of Co^{3+} in crystallites of stoichiometry Co_3AlO_6 or in a well-disposed surface species; phase III reducing at about 900K arises from surface Co^{2+} ions; and phase IV reducing around 1150K from either Co^{2+} in a diluted Co-Al spinel or in $CoAl_2O_4$.

In the TPR of oxidized Co/SiO_2 catalysts the reduction starts at 473K and is complete at 973K. The higher temperatures needed for reduction of the supported catalyst compared with bulk Co_3O_4 is in accordance with a metal-

support interaction - a similar conclusion to that of Paryjczak et al.[65].

For CT/C catalysts, as the increase in the Co content leads to a change in the nature of the Co-combining species (well dispersed Co^{2+} ions), the Co_3O_4 aggregates increase. However, in CT/HP catalysts the two main peaks are well separated in a way that suggests Co^{3+} to Co^{2+} reduction taking place, and then Co^{2+} which is formed by a surface species from $CoTiO_3$ to Co^{o}. A shift in T_{max} values to a lower temperature compared with unsupported $CoTiO_3$ could be due to a particle size effect. With CAT/C catalysts, the four main peaks can be attributed to the following: Co^{2+} tetrahedral, Co^{3+} tetrahedral, and Co^{3+} octahedral or Co-Ti surface species[69-71].

5.2.2 X-ray photoelectron spectroscopy (XPS)

All the three series, i.e. CT/C, CT/HP, and CAT/C were studied by XPS and gave different curve shapes when the intensity ratio (ICo2p/ITi2p) was plotted as a function of Co content, which suggests that each series has a different structure or phases from the other as shown in Fig. 5.6.

The change in the slope of curve I in Fig. 5.6 indicates that there is a difference in structure below and above the monolayer region. At low Co loadings, CoO is in tetrahedral lattice site and small quantities of Co^{2+}-Ti^{4+} ions probably octahedrally at low concentrations as low as 2 wt.% CoO. Using XPS results alone, it is not possible to distinguish between Co-tetrahedral and Co-octahedral. Above

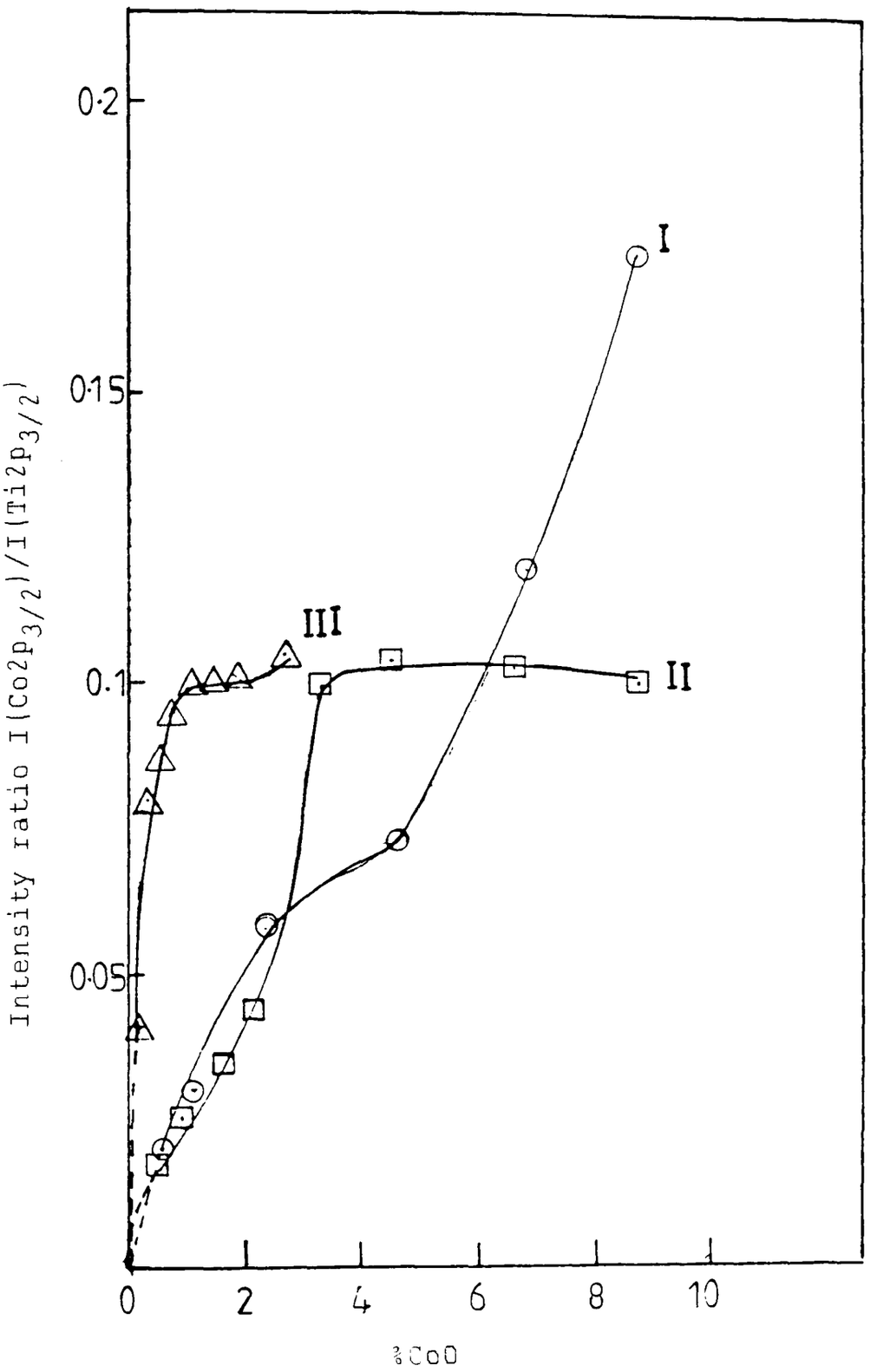

Fig. 5.6 Variation of intensity ratios of $I(Co2p_{3/2})/I(Ti2p_{3/2})$ with CoO contents for: (I) CT/C series; (II) CT/HP series; and (III) CAT/C series.

the monolayer capacity, i.e. 0.75 wt.% CoO, the intensity ratio of $ICo2p_{3/2}/ITi2p_{3/2}$ increased with increasing the Co loading, which could arise from the following: (i) the surface is not fully covered with CoO, and (ii) CoO is not well dispersed on the surface of TiO_2 because of the method of preparation. During impregnation steps, i.e. drying, calcination, perhaps, aggregates of CoO as well as Co_3O_4 were formed non-uniformly on the surface which leads us to say CoO_x is not well dispersed. Similar behaviour was observed by using the same method of preparation but on different supports such as Al_2O_3, and SiO_2[72-79]. In the case of curve II, the catalysts were prepared by the homogeneous precipitation method. At low concentrations Co is assumed to be in tetrahedral or octahedral lattice sites. Above the monolayer capacity,i.e. 0.75 wt.% CoO, the intensity ratio remained almost unchanged, which could be interpreted by the fact that the precipitation method has an advantage over the impregnation method in the way that more uniform surface patches of the oxide are formed, which lead to higher dispersion and better coverage of the support[75]. The sub-surface species that we think was formed in the CT/C series we expect to form above the monolayer coverage in this series, although there is no direct evidence for this speculation, as well as particulate "patches" of CoO. Finally, the CAT/C series intensity ratio variation as a function to the CoO loading almost as a combination of the previous two series. Although the catalysts were prepared by impregnation as in the case of CT/C series (curve I), but

using a different precursor, i.e. cobalt acetate, the shape of the curve indicates that at low loadings, Co is occupying either tetrahedral or octahedral sites below the monolayer region, and above the monolayer point, a plateau is formed up to 2.10 wt.% CoO, and then increases again up to 2.70 wt.% CoO. From TPR patterns, it is speculated that the Co^{2}-Ti^{4+} species is formed as well as a surface species of $CoTiO_3$, compared with T_{max} values of the unsupported $CoTiO_3$. Generally all the three series gave different shaped curves, from which we can conclude that different CoO_x species are formed due to different methods of preparation and different precursors were used. Based on the results of TPR and XPS, one can draw a phase diagram for each series. The diagrams in Fig. 5.7 could account in a semi-quantitative way for the types of species formed below and above the monolayer region.

A series of supported Co catalysts (Co/Al_2O_3, $Co/K\text{-}Al_2O_3$, Co/SiO_2, and Co/TiO_2) have been examined by XPS and microreactor studies[76]. At least three different types of Co species were present on the calcined samples. These included large particles of Co_3O_4, various Co^{2+} species, and $CoAl_2O_4$[76]. The Co_3O_4 particles were more readily reduced to metallic Co in H_2 than the Co^{2+} species were. Talipova et al. [71] used the methods of electronic diffuse-reflection spectroscopy (EDRS) and X-ray phase analogies for studying formation of surface and bulk compounds at various stages of preparation of the CoO TiO_2 system with variation of the calcination temperature from 90

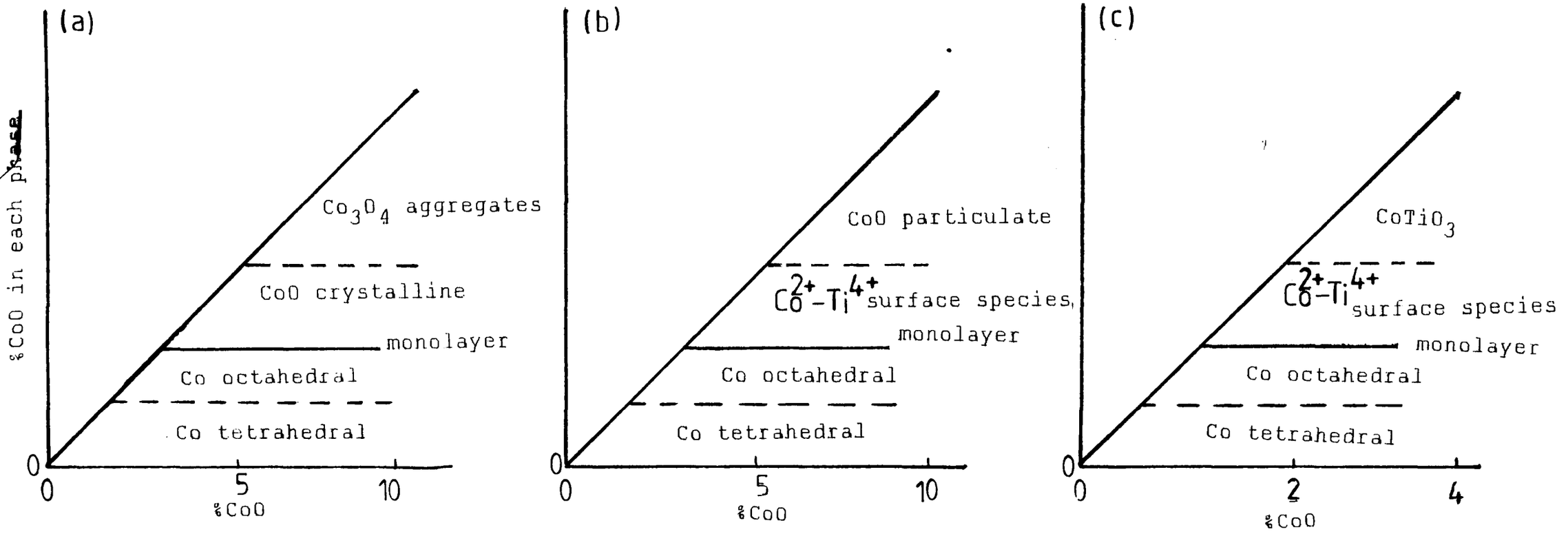

Fig. 5.7 Phase diagrams for Co surface speciations formed on , (a) CT/C series, (b) CT/HP series series, and CAT/C series.

to 1200°C and of the CoO content from 0.3 to 25 mass%. Surface compounds with tetrahedrally co-ordinated Co^{2+} ions were formed in amounts up to 5 mass%[71]. At higher Co-ion concentrations, the excess Co forms aggregates of $Co(NO_3)_2.6H_2O$ on the $TiO_2.xH_2O$ surface.

5.2.3 TEM

The micrographs of the reduced catalysts for the CT/C, CT/HP, and CAT/C series are illustrated in Section 4.1.4.2. The samples were reduced under TPR conditions, and each series gave different average particle sizes; for example, the CT/C catalyst gave 8-9 nm, where the CT/HP catalyst gave a smaller size, within 2-3 nm, the same as the CAT/C catalyst. It has been reported in the literature that impregnation methods usually give broad particle sizes, whereas alkoxide and precipitation methods usually give quite small particle sizes[42, 75]. When the size of the precipitated particles is small, the surface energy of the solid can appreciably affect the change in free energy on formation of a solid particle[75]. At relatively elevated concentrations the drop in free energy per unit volume is sufficiently large to cause the free energy to decrease even with very small particles, though less rapidly with smaller than with larger particles. When the concentration is not much beyond that of the solubility curve, the surface energy brings about that the difference in free energy passes through a (positive) maximum as the size of the solid particle increases[71]. The rate of reduction of solid

particles from a supersaturated solution strongly depends on the sign of the difference in free energy at very small particle sizes. When the difference in free energy drops at increasing particle size, the rate of nucleation is much higher than when this difference initially arises.

5.2.4 Catalytic decomposition of 2-propanol over CoO_x/TiO_2

2-propanol decomposition over the CT/C series was studied and the kinetic parameters are given in Table 4.23, Section 4.1.5.2. For unsupported CoO, selectivity towards the dehydrogenation product (acetone) was at its maximum (96.7%), compared with dehydration product (propene) (3.3%). TiO_2 (anatase) showed the opposite behaviour; 81.4% selectivity for propene, i.e. dehydration. TiO_2-supported CoO_x samples were 50-60% selective for dehydration, in other words less selective compared with MoO_x/TiO_2 results[48].

No literature has been published yet on 2-propanol decomposition over CoO supported catalysts. However, in our study, it has been found that the rate of 2-propanol decomposition per g of CoO decreases with increasing CoO content, as shown in Fig. 4.6.4 (b), Section 4.1.5.2. The most active sample was 0.6% CT/C catalyst, which suggests that Co has a poisoning effect on the surface of TiO_2 as the Co concentration increases, a phenomenon observed with Co on other reactions like hydrogenolysis reactions[77,78].

5.3 $CoO-MoO_3/TiO_2$ catalysts

5.3.1 Temperature-programmed reduction TPR

TPR profiles for unsupported CoO, Co_3O_4, MoO_3, $CoMoO_4$, and supported $CoO-MoO_3/TiO_2$ catalysts are shown in Figs. 4.20, 4.23 and 4.26, (Section 4.1.2.3). In each of the CMT, MCT, and CMTg series, four groups of peaks are formed. For the CMT series, group A consists of the reduction region 603-698K; group B, 643-743K; group C, 773-873K, and finally group D, 973-1003K. Nearly the same four groups apply to the MCT and CMTg catalysts. Hence by comparing TPR profiles of all the three series, it is difficult to say what the differences in reducibility are. In other words, T_{max} is almost identical to the extent that one cannot say whether one series is more easily reducible than the other.

The rate of temperature increase of a $CoMo/Al_2O_3$ hydrorefining catalyst during its activation with an $H_2S-H_2-N_2$ mixture affected its reducibility and activity[79]. The reducibility has been evaluated by a TPR method and the activity by hydrogenation of ethylene. The rapid temperature increase caused a decrease in the amount of H_2S evolved during TPR, an increase in the initial temperature of H_2S evolution and a decrease in the ethylene hydrogenation activity[70]. The activities of a series of ten industrial catalysts have been measured for the desulphurization of thiophene at atmospheric pressure[80]. The reducibility of the catalysts has been determined using static and temperature-programming techniques. It was found that there is a reasonable correlation between the

reducibility of the catalysts ($NiMo/Al_2O_3$ and $CoMo/Al_2O_3$) and their activity in the desulphurization of gas oil at high pressures[80]. However, the correlation between the reducibility and the activity for the desulphurization of thiophene at atmospheric pressure is less good. It was found that the method used to determine the H_2 consumption is unimportant providing precautions are taken to obtain reproducible results. Finally, it is concluded that the activity of a catalyst in the thiophene reaction is not a good indicator of activity under industrial operating conditions[80].

TPR was used to investigate the behaviour of $CoMo/Al_2O_3$ catalysts[81]. From the point of view of catalytic performances, the best value of the Co/Mo atomic ratio is about 0.35. All samples with this atomic ratio were characterized by a simple peak due to MoO_3 interacting with Al_2O_3[72]. This species is present in the fresh catalyst, but a large amount of it can be detected only after sulphurization. It is progressively destroyed during the industrial run or when the catalyst is submitted to high temperature[82]. Signals pointing to a Co/Al_2O_3 interaction became evident only when the Co/Mo ratio exceeds the above best value[81].

It is shown that TPR gives new information on the reducibility of $CoO-MoO_3/Al_2O_3$ catalysts[83]. The reduction of Mo^{6+} surface species (monolayer and bilayer species) is not significantly affected by the presence of Co, whereas the reduction of Co^{2+} ions is strongly influenced by the presence of Mo[82]. There appears to be a strong Co-Mo

interaction at moderate Co contents; the reduction maximum for dispersed Co^{2+} ions decreases from 1200K, found for CoO/Al_2O_3, to 800-850K for $Co\text{-}MoO_3/Al_2O_3$. At high Co contents, Co_3O_4 crystallites and Co^{3+} ions in surface positions or in a crystalline Co^{3+}-Al^{3+}-oxide of proposed stoichiometry Co_3AlO_6 have been found in addition to the Co-Mo interaction phase[82]. Solid-state diffusion of Co^{2+} ions starts already around 800K, resulting in destruction of the Co-Mo interaction phase and in formation of subsurface Co^{2+} ions of low reducibility. By calcination at 1125K, a significant loss of Mo takes, place, while some $CoMoO_4$ microcrystallites are formed. Also some α-Al_2O_3 is formed, probably initiated by the presence of $CoMoO_4$.

5.3.2 X-ray photoelectron spectroscopy (XPS)

The nature of the species present on the surface of $CoO\text{-}MoO_3/TiO_2$ catalyst is controlled by many variables, particularly the method of preparation. This factor more than any other is probably responsible for the contradictory interpretations in the literature. XPS analysis indicates that different surface characteristics appear for each of the CMT, MCT, and CMTg series. However, intensity ratios variation as a function of metal content for both the CMT and the MCT series showed similar behaviour, while for the CMTg series, the diagram is quite different (Section 4.1.3.3.).

Laser Raman spectroscopy, X-ray photoelectron spectroscopy, low-energy ion-scattering spectroscopy and X-ray

diffraction have been used to characterize a series of Co-Mo/Al_2O_3 catalysts[72], in their oxide, reduced, and sulphided forms. The results showed that the catalyst surface contains $CoMoO_4$ and irreducible Co^{2+} ions of tetrahedral symmetry when the CoO concentration is 0 to 6%. With 7 to 8% CoO, additional surface species includes Co_3O_4 crystallites on the γ-Al_2O_3 surface[72]. Formation of Co_3O_4 coincides with an increased Mo reducibility and a decreased BET surface area. These results are compared to previously published results on Co-Mo/Al_2O_3 and suggest that the state of dehydration-dehydroxylation of the Al_2O_3 surface before impregnation of Co and Mo affects their subsequent speciation[72]. Autoclave studies investigating the hydrodesulphurization (HDS) and hydroconversion of coal using these catalysts are also reported[72].

The influence of the temperature on the surface state of an industrial CoMo/γ-Al_2O_3 catalyst has been studied by XPS[73]. At room temperature Mo is present on the surface as $Mo^{(VI)}$. When increasing the temperature, $Mo^{(VI)}$ is reduced to $Mo^{(V)}$. The reduction is, however, never complete[73]. Co at room temperature is in the form of Co_3O_4 and the Co^{3+} ions are reduced to Co^{2+} ions to form $CoAl_2O_4$, and $CoMoO_4$ when the temperature increases[73].

The structural characteristics of Co-Mo/Al_2O_3 hydrodesulphurization catalysts have been investigated with a variety of surface spectroscopic techniques: XPS, ISS, and photoacoustic spectroscopy (PAS)[74]. All catalysts were prepared by sequential impregnation of Mo and Co into

γ-Al_2O_3 with the Mo concentration held constant at 15% MoO_3 by weight as the Co concentration was varied from 1 to 9% CoO. In all catalysts interaction between Co and the support was observed, which rendered a portion of the Co inert toward H_2 reduction and H_2S sulphidation[74]. This interaction species (Co-t) is dominant for catalysts of low Co loading (i.e. 1% CoO). As the Co concentration is increased a new phase was formed, characterized by interactions between Co and Mo[74]. This species (Co^o) is produced up to a concentration of 7% CoO. Above this level, Co_3O_4 is formed. From ISS it was determined that the Co ions were situated beneath the Mo ions as Co-t and the Co-Mo interaction species. The presence of Co was found to have no effect on the reduction or sulphidation of Mo[74].

A series of CoMo/γ-Al_2O_3 oxide catalysts containing 15.0 $\pm$ 0.6 wt.% of Co and Mo oxides (considered as Co_3O_4 and MoO_3) and r = Co/(Co + Mo) atomic composition ranging from 0.00 to 1.00 were studied by XPS and DRS[83]. These techniques and previously reported results on electron microscopy show that Mo occurs on γ-Al_2O_3 as tetrahedral oxidic $Mo^{(VI)}$ according to the $Mo^{(VI)}$ monolayer model, and also as $Mo^{(VI)}$ in multilayers having a bulk like MoO_3 or paramolybdate surrounding[83]. Co is poorly dispersed when alone (15%) on a γ-Al_2O_3 surface: in that case, the formation of Co_3O_4 clusters is extensive and very little $CoAl_2O_4$ is formed. In the r = 0.25 - 0.75 composition range, a strong interaction takes place between Mo of the monolayer and Co, which brings about a high dispersion on

Co and seems, in turn, to increase the dispersion of Mo[84]. As a consequence of the dispersion of Co, much $CoAl_2O_4$ is formed. The results, as well as the properties of the catalysts in the middle range of composition, were interpreted in terms of a model of the catalyst surface in which a bilayer of Co-Mo is formed on the $CoAl_2O_4$[83].

The surface compositions of Co-Mo binary oxide catalysts have been studied by XPS techniques for the calcined catalysts and for the catalysts exposed to various reactive gases relating to the hydrodesulphurization of thiophene[84]. In the cases of the Co-Mo catalysts prepared by calcining the mixtures of Co nitrate and ammonium paramolybdate, a surface segregation of Mo was observed over a wide range of the bulk composition of the catalyst, while a Co enrichment was observed in the catalyst with a small Co content (<6 at.%)[84]. However, the catalysts prepared by calcination of the mixed composite oxides, CoO and MoO_3, showed no enrichment of Co or Mo in the catalyst surface, except for the catalyst containing a small amount of CoO[84]. It was found that the surface composition of the catalyst was changed considerably by treatment at 400°C with 10 Torr of various reactive gases. H_2 reduction caused a surface enrichment of Mo, accompanied by the reduction of the oxides to MoO_2 and Co metal[84]. A similar behaviour was observed for a Zn-Mo binary oxide catalyst. It is concluded that the surface compositions of the Co-Mo catalysts depend strongly on the preparation procedures and on the kinds of gases in contact with the catalysts[84].

The surface chemical composition has been monitored by XPS for a series of hydrodesulphurization catalysts ($Co-Mo/Al_2O_3$) as a function of bulk Co concentration and fixed Mo concentration, with respect to sulphiding with a mixture of $H_2S:H_2$ at elevated temperatures[85]. The chemical species present on the surface of the Al_2O_3-based catalysts were compared with those present on C-based Co-Mo catalysts[85]. It was concluded that in addition to a sulphided Mo species, the catalyst surface was rich in a reduced, but not sulphided, Co species. For Al_2O_3 supports, the fraction of surface Co available for reduction was found to be tied directly to the method of catalyst fabrication[85].

Hydrodesulphurization (HDS) and hydrodenitrification (HDN) catalysts comprising Co+Mo and Ni+Mo have been extensively studied in many laboratories. Using XPS, particular emphasis has been placed on quantitative analysis for determining the dispersion of the Co, Mo or Ni oxides or mixed oxides on a SiO_2 or Al_2O_3 support. When MoO_3 is deposited on SiO_2, it was observed[86] that the Mo3d and O1s peaks had their binding energy values increased, with the amount of Mo. When Co was also present, the above peaks kept the same binding energies. The relative intensities I_{Mo}/I_{Si} remained constant up to 12% of supported phase and then drastically increased for higher amounts. These results indicate that a relatively strong interaction has occurred between Mo and SiO_2[86]. This interaction was weaker when Co was added to MoO_3/SiO_2 with the formation of

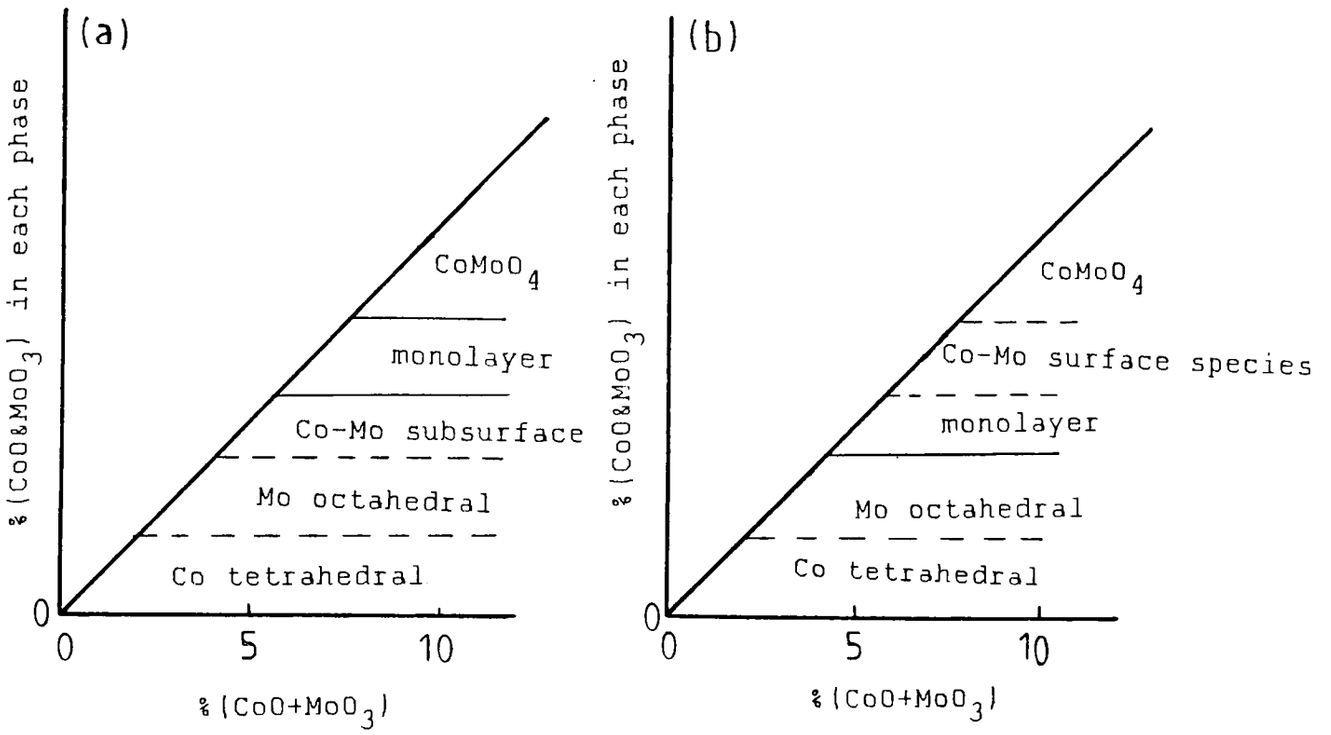

Fig. 5.8 Phase diagrams for $CoMo/TiO_2$ catalysts
(a) CMT and MCT series
(b) CMTg series.

$CoMoO_4$ at the expense of Mo/SiO_2 interaction. When the solids were reduced by H_2, the weak interaction between Mo and SiO_2 in the presence of Co (interaction weaker than that for Al_2O_3 support) resulted in the formation of $CoMoO_4$[87] rather than in the formation of CoMo "bilayer" precursor of the active phase in HDS. The Co or Mo in excess of the $CoMoO_4$ stoichiometry forms mainly Co_3O_4 or MoO_3 respectively covering the $CoMoO_4$ crystals[87]. When γ-Al_2O_3 was used as a support, a stronger interaction between Co and Mo oxides and the support exists. This leads to the formation of Co-Mo "bilayer" attached to the surface[88] and therefore to a better HDS catalyst.

Our TPR and XPS results showed that when CoO or MoO_3 were impregnated first, no big difference was observed

from TPR profiles or XPS intensity ratio, while for CMTg series, i.e. CoO and MoO_3 impregnated together, the shape of intensity ratio curve and the profiles of TPR indicated that there are surface species formed different from the previous two series. Phase diagrams for the CMT and the MCT series are illustrated in Fig. 5.8(a), while Fig. 5.8(b) shows the possible phases that are formed for the CMTg series. Chung and Massoth[89] found that the structure of $CoMo/Al_2O_3$ depended on the method of impregnation. However, some workers have indicated that methods when molybdenum impregnated first and molybdenum and cobalt together contain an interaction species between Co and Mo believed to be $CoMoO_4$[90,91]. Workers have observed bulk $CoMoO_4$ on catalysts prepared by Mo impregnated first by LRS and X-ray diffraction[90]. In contradiction to these findings, Cimino and De Angelis have excluded the possibility $CoMoO_4$ interaction species because the reducibility of the $CoMo/Al_2O_3$ catalysts was less than bulk $CoMoO_4$. Both α-$CoMoO_4$ and β-$CoMoO_4$ compounds were reduced at 400°C in hydrogen, then analysed by XPS. Both $CoMoO_4$ species reduced to metal Mo and some Co metal. However, the Mo did not reduce past Mo^{4+}, and only a small amount of Co reduction was observed on the catalyst[92].

5.3.3 Catalytic decomposition of 2-propanol

Three sets of results were chosen to interpret the decomposition of 2-propanol over $CoMo-MoO_3/TiO_2$ catalysts. First kinetic parameters of sub-monolayer catalysts for

MoO_3/TiO_2, CoO/TiO_2, and $CoO\text{-}MoO_3/TiO_3$ catalysts are given in Table 5.2. There is no big difference in activity for dehydration (propene formation) or dehydrogenation (acetone formation) when the mode of impregnation is varied; only when CoO was impregnated first did activity increase from 0.35 $mmol.h^{-1}.g^{-1}_{cat}$ to 0.63 $mmol.h^{-1}.g^{-1}_{cat}$, but selectivity remained nearly constant. The situation in the sub-monolayer region remains ambiguous, as the activity and selectivity of simple and binary supported TiO_2 catalysts are compared.

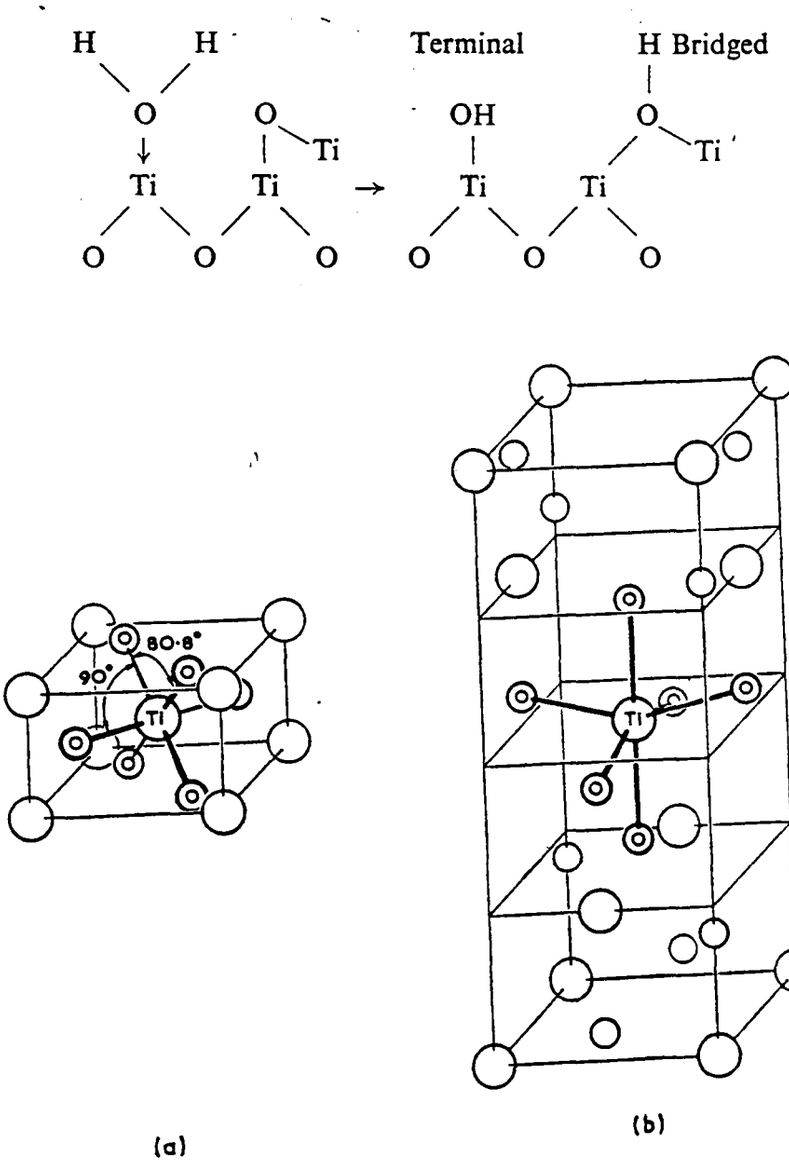

Fig. 5.9 Structure of (a) rutile and (b) anatase (94).

Table 5.2 Kinetic parameters for 2-propanol decomposition over sub-monolayer catalysts.

Sample	E_{IPA}(1)	E_P	E_{Ac}	r_P(2)	r_{Ac}	S_P
CoO	102	75.7	103.1	0.08	2.48	3.30
MoO_3	101.7	101.7	-	4.90	-	100
TiO_2 (CLD 867)	125.5	122.9	74.8	0.46	0.11	81.4
TiO_2 (P-25)	61.8	61.0	-	0.59	-	100
MT/C	97.7	97.7	-	112	-	100
CT/C	108.4	120.1	94.9	78.2	50.9	60.5
CMT1	87.5	100.5	64.3	117	90	56.9
MCT1	81.1	94.7	59.8	210	147	59.1
CMTg1	96.3	106.3	64.7	127	90	58.8
$CoMoO_4$	64.7	63.3	-	0.68	-	100

(1) All activation energies are expressed in $kJmol^{-1}$

(2) All rates are expressed in $mmol.h^{-1}.g^{-1}_{metal\ oxide}$

Secondly, the kinetic parameters for the monolayer catalysts are given in Table 5.3. There is an interesting difference in the activity and selectivity towards propene and acetone formation for unsupported TiO_2. Low surface area anatase(CLD 867) showed activity and selectivity to both dehydration and dehydrogenation while TiO_2 (P-25) was selective only for dehydration. This phenomenon could be due to the following: (i) in CLD 867 there is more anatase than rutile (90% anatase to 76.1% anatase in P-25) as shown in Fig. 5.9, and (ii) different types of OH groups[93] on the surface of TiO_2 could account for different activity behaviour. As illustrated in Table 5.3, monolayer MoO_3/TiO_2 catalyst exhibited activity towards propene formation almost three times higher than the unsupported TiO_2, whereas selectivity towards both dehydration and dehydrogenation remained unchanged. CoO_x/TiO_2 catalyst showed a little higher activity towards propene and less activity towards acetone, while selectivity for propene dropped from 81% to 55% and for acetone and increased from $\sim$18% for unsupported TiO_2 to $\sim$ 45% for TiO_2 supported CoO_x. With $CoO\text{-}MoO_3/TiO_2$ monolayer catalysts, in spite of varying the sequence of impregnation, activity towards propene formation decreased, while selectivity remained almost constant, and activity towards acetone formation was less than that of propene formation, and selectivity here again remained unchanged. Unsupported $CoMoO_4$ showed less activity to propene formation compared with the supported

Table 5.3 Kinetic parameters for 2-propanol decomposition over monolayer catalysts.

Sample	E_{IPA}(1)	E_p	E_{Ac}	r_p(2)	r_{Ac}	S_p
CoO	102	75.7	103.1	0.08	2.48	3.30
MoO_3	101.7	101.7	-	4.90	-	100
TiO_2 (CLD 867)	125.5	122.9	74.8	0.46	0.11	81.4
TiO_2 (P-25)	61.8	61.0	-	0.59	-	100
MT/C	117.5	57.2	35.1	145	18	81.4
CT/C	116.9	116	126.8	33.3	26.1	55.2
CMT	95.3	107.4	58.3	127	45	73.9
MCT	90.8	101.9	65.0	64.8	18.7	77.5
CMTg	96.0	108	73.6	69.4	31.8	68.7
$CoMoO_4$	64.7	63.3	-	0.68	-	100

(1) All activation energies are expressed in $kJmol^{-1}$

(2) All rates are expressed in $mmol.h^{-1}.g^{-1}_{metal\ oxide}$

$CoO-MoO_3/TiO_2$ catalysts and no activity towards acetone formation.

Finally, kinetic parameters for 2-propanol decomposition over what is equivalent to four-monolayer catalysts are given in Table 5.4. Compared with the previous submonolayer, and monolayer catalysts, the activity towards dehydration (propene formation) increased, while activity for dehydrogenation (acetone formation) remained almost constant. Selectivity increased for propene and decreased for acetone.

In spite of the importance of these catalysts in hydroprocessing, little is understood regarding the general fundamental basis for and origin of their catalytic activity. Chianelli[96] studied the fundamental properties of transition metal sulphide catalysts. When information is not available on oxides, the catalysts may be treated as analogous to sulphides. The properties which govern the ability of the transition metal sulphides to catalyse a given reaction are divided into four classes: electronic (effect of a particular transition metal in a sulphur environment), geometric (effect of structure for a given transition metal sulphide), chemical (effect of local active site configuration), and promotional effect.

5.3.3.1 The "Electronic Effect"

The general periodic variation of the ability of the transition metal sulphides to catalyse the HDS of sulphur bearing molecules was recently reported[95]. This ability

Table 5.4 Kinetic parameter for 2-propanol decomposition over four-monolayer catalysts.

Sample	E_{IPA}(1)	E_P	E_{Ac}	r_P(2)	r_{Ac}	S_P
CoO	102	75.7	103.1	0.08	2.48	3.3
MoO_3	101.7	101.7	-	4.90	-	100
TiO_2 (CLD 867)	125.5	122.9	74.8	0.46	0.11	81.4
TiO_2 (P-25)	61.8	61.0	-	0.59	-	100
MT/C	73.8	86.9	42.9	54.5	4.75	91.8
CT/C	96.9	104.9	82.2	10.9	4.71	69.6
CMT7	61.9	68.2	41.6	76.8	10.8	87.6
MCT7	77.5	83.6	70.6	50.4	11.4	81.7
CMTg7	71.7	80.8	61.8	19.5	6.83	74.4
$CoMoO_4$	64.7	63.3	-	0.68	-	100

(1) All activation energies are expressed in $kJmol^{-1}$

(2) All rates are expressed in $mmol.h^{-1}.g^{-1}_{metal\ oxide}$

varies smoothly over three orders of magnitude of catalytic activity from Group IV B to Group VII B yielding "volcano" curves for the second and third row elements with maxima occurring for the Group VIII B with the remainder of the first row elements being relatively inactive. Such curves have not been previously reported for transition metal sulphides, although Wakabajaski et al.[95] discussed the HDS of thiophene over Al_2O_3 supported metals, but found no smooth variation of activity probably because of superimposed effects of the Al_2O_3 support.

Additionally, Pauling percentage d-character for the transition metals correlates very well to HDS activity although we do not understand why this should do so[95]. The most that can be stated regarding these correlations is that the strength of the metal d-sulphur bond at the surface of the catalyst is important in determining HDS activity as well as the presence of 4d and 5d electrons in the catalyst.

5.3.3.2 The "Geometric Effect"

The crystal structure is of secondary importance in determining the activity of a transition metal sulphide (TMS) catalyst. However, structure becomes quite important when considering the activity optimization of a particular TMS. We define this secondary effect in TMS catalysts on the "geometric effect". The geometric effect is clearly manifested by the heat treating of a particular TMS catalyst under different conditions (changing properties such as surface area, pore size, and crystalline size) and observing

the effect on the catalytic activity. It is suggested that in any catalyst, there is an ideal set of heat treatment conditions for which the HDS activity is at a maximum. This effect has been studied for MoS_2, where due to its highly anisotropic layered structure, HDS activity does not correlate well with BET surface area[95].

5.3.3.3 The "Chemical Effect"

What is the structural nature of this site (MoS_2) and what is the concentration of these sites on the edge plane? Such questions are lumped in the term "chemical effect" in TMS catalysts. ESR is a tool of great potential utility in catalyst studies. It is a highly sensitive probe of defect sites in a material. Unpaired electrons and "dangling bonds" which are likely to be associated with active sites are easily detected even at the part per million level.

5.3.3.4 The "Promotional Effect"

It is well known that the presence of a second metal can in some cases lead to catalysts which have activities greater than the simple sum of the activities of catalysts based on binary oxides[96]. Such "promotion" of MoS_2 or WS_2 by Co and Ni occurs in either supported or unsupported catalysts. Although the subject of promotion has been well studied, no consensus exists as to the origin of this effect. It has been suggested that a relation exists between the activity of the well-known Co- and Ni-promoted MoS_2 and WS_2 catalysts and the period trends for the binary

sulphides[97]. Studies of promotion have led to the idea of "contact synergy" for sulphided catalysts containing Co or Ni together with Mo or W[98]. Even though this specific idea appears to be incorrect, Ni/Mo, Co/Mo, Co/W, and Ni/W can be said to behave as "synergic pairs" which retains the idea that the members of these pairs "work together or co-operate". The work by Topsøe et al.[99] has shown the presence in both supported and unsupported CoMo catalysts of a unique form for sulphided Co (the "CoMoS" phase) which correlates with activity.

5.3.3.5 The "Compensation Effect"

Fig. 5.10 illustrates two main phenomena. (i) There are different types of active centres responsible for the dehydration and dehydrogenation products, since all the points are not on the same line as shown in Fig. 5.10. (ii) The types of active sites are independent of the mode of impregnation with respect to both propene or acetone formation.

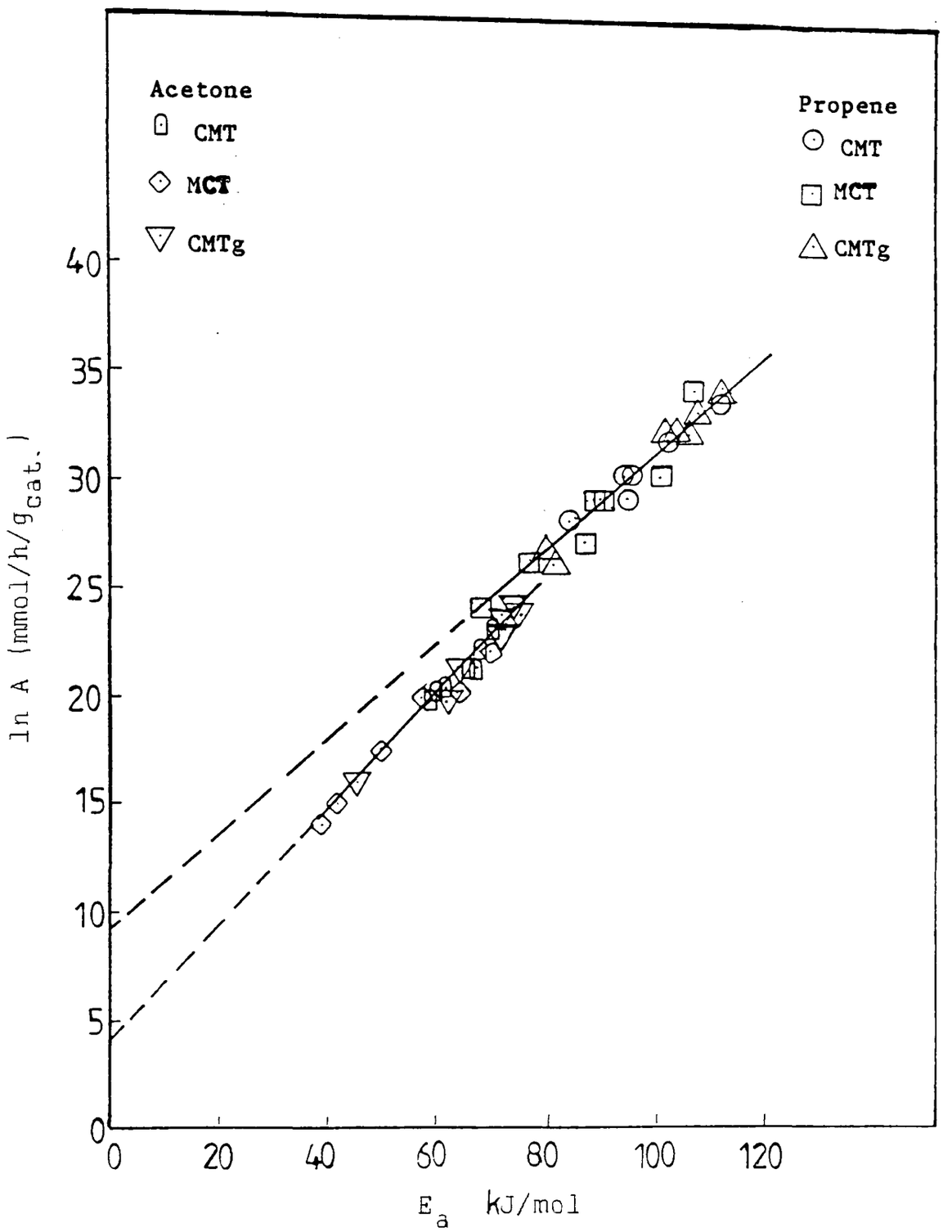

Fig. 5.10 Compensation effect for 2-propanol decomposition catalysed by $CoO-MoO_3/TiO_2$

5.4 References

1. G. C. Bond, S. Flamerz and L. Van Wijk, Catal. Today, 1, 229 (1987).

2. H. Jeziorowski, and H. Knözinger, H. J. Phys. Chem., vol. 83, No. 9, 1166-1173 (1979).

3. R. Thomas, M. C. Mittelmeijer-Hazeleger, F. P. M. J. Kerkhof, J. A. Moulijn, and V. H. J. de Beer "Proc. Third Int. Conf. on the Chem. and Uses of Molybdenum" Ann Arbor, USA, (Eds. H. F. Barry and P. C. H. Mitchell), 85 (1979).

4. L. Wang and W. K. Hall, J. Catal., 66, 251 (1980).

5. J. Medema, C. van Stam, V. H. J. de Beer, A. J. A. Konings and D. C. Koningsberger, J. Catal., 53, 386 (1978).

6. B. Sombert, P. Dhamelincourt, F. Wallart, A. C. Muller, M. Bouquet and T. Grosmangin, J. Raman Spectrosc. 9, 291 (1980).

7. M. Houalla, C. L. Kibby, L. Petrakis and D. M. Hercules, J. Catal., 83, 50 (1983).

8. Y. C. Liu, G. L. Griffin, S. S. Chan and J. E. Wachs, J. Catal., 94, 108 (1985).

9. E. Payen, S. Kasztelan, J. Grimblot and J. P. Bonnelle, J. Raman Spectrosc., 17, 233, (1986).

10. J. M. Stencel, L. E. Makovsky, T. A. Sarkus, J. de Vries, R. Thomas and J. A. Moulijn, J. Catal. 90, 314 (1984).

11. R. Thomas, PhD Thesis, University of Amsterdam, The Netherlands (1981).

12. P. Dufresne, E. Payen, J. Grimblot and J. P. Bonnelle, J. Phys. Chem. 85, 2344 (1981).

13. L. Wang and W. K. Hall, J. Catal. 83, 242 (1983).

14. J. Leyrer, B. Vielhaber, M. I. Zaki, Z. Shuxian, J. Weitkamp and H. Knözinger, Materials Chem. and Phys. 13, 301, (1985).

15. C. P. Cheng and G. L. Schrader, J. Catal. 60, 276 (1979).

16. P. Gajardo, D. Pirotte, P. Grange and B. Delmon, J. Phys. Chem. 83, 1780 (1979).

17. T. Fransen, P. C. van Berge and p. Mars, in "Preparation of Catalysts I" Eds. B. Delmon, P. A. Jacobs and G. Poncelet. Elsevier, Amsterdam, 405 (1976).

18. H. Jeziorowski, H. Knözinger, P. Grange and P. Gajardo, J. Phys. Chem. 84, 1825 (1980).

19. J. M. Stencel, J. R. Diehl, J. R. D'Este, L. E. Makovsky, L. Rodrigo, K. Marcinkowska, A. dnot, P. C. Roberge, and S. Kaliaguine, J. Phys. Chem. 90, 4739 (1986).

20. R. B. Quincy, M. Houalla, and D. M. Hercule, J. Catal. 106, 85-92 (1987).

21. H. Knözinger and P. Ratnasamy, Catal. Rev. Sci. Eng. 17, 31 (1978).

22. A. Castellan, J. C. J. Bart, A. Vaghi, and N. Giordano, J. Catal. 42, 162 (1976).

23. H. Jeziorowski, H. Knözinger, P. Grange, and P. Gajardo, J. Phys. Chem. 83, 1780 (1979).

24. K. Y. S. Ng and E. Gulari, J. Catal. 92 340 (1985).

25. T. Fransen, P. C. van Berge and P. Mars, React. Kinet. Catal. Lett. 5, 445 (1976).

26. A. J. van Hengstum, PhD Thesis, Twente University of Technology, Enschede, The Netherlands (1984).

27. P. Arnoldy, J. C. M. de jonge and J. A. Moulijn, J. Phys. Chem. 89, 4517 (1985).

28. H. C. Yao, J. Catal. 70, 440 (1981).

29. W. K. Hall and F. E. Massoth, J. Catal. 34, 41 (1974).

30. T. Fransen, O. van der Meer and P. Mars, J. Phys. Chem. 80, 2103 (1978).

31. R. Thomas, E. M. van Oers, V. H. J. de Beer, and J. A. Moulijn, J. Catal. 84, 275 (1983).

32. R. Thomas, V. H. J. de Beer and J. A. Moulijn, Bull Soc. Chim. Belg. 90, 1349 (1981).

33. P. Arnoldy, PhD Thesis, University of Amsterdam, The Netherlands (1985).

34. R. Burch and A. Collins, Appl. Catal. 18, 389 (1985).

35. C. V. Caceres, J. L. G. Fierro, A. L. Agudo, M. N. Blanco and H. J. Thomas, J. Catal. 95, 501 (1985).

36. S. Matsuda and A. Kato, Appl. Catal. 8, 149-165 (1983).

37. A. F. Wells, "Structural Inorganic Chemistry", Clarendon Press, Oxford (1962).

38. D. S. Zingg, L. E. Makovsky, R. E. Tischer, F. R. Brown and D. M. Hercules, J. Phys. Chem. 84, 2898 (1980).

39. S. Kasztelan, J. Grimblot, J. P. Bonnelle, E. Payen, H. Toulhoat and Y. Jacquin, Appl. Catal. 7, 91, (1983).

40. G. C. Bond, J. Perez Zurita and S. Flamerz, Appl. Catal. 27, 353 (1986).

41. J. C. Védrine, in "Surface Properties and Catalysis by Non-Metals" (Ed. J. P. Bonnelle, B, Delmon and E. Derouane), Reidel, Dordrecht, (1983) p. 159.

42. G. C. Bond, Surf. Sci. 156, 966-981 (1985).

43. J. W. E. Coenen and P. B. Wells, "Preparation of Catalysts III" (Eds. G. Poncelet, P. Grange and P. A. Jacobs), Elsevier, Amsterdam, 801 (1983).

44. G. C. Bond and R. Burch, in "Specialist Periodical Reports, Catalysis Vol. 6" (Eds. G. C. Bond and G. Webb) (Royal Society of Chemistry, London) (1982)

45. G.-M. Schwab, Adv. Catal. 27, 1 (1978).

46. F. Solymosi, Catal. Rev. 1, 233, (1967)

47. J. Cunningham, B. K. Hodnett, M. Ilyas, J. Tobin, E. L. Leahy and J. L. G. Fierro, Faraday Disc. Chem. Soc. 72, 283-302, (1982).

48. G. C. Bond, S. Flamerz and R. Shukri, Faraday Disc. Chem. Soc. 87, to be published (1989).

49. G. Busca, Mat. Chem. Phys., 19, 157 (1988).

50. H. Miyata, T. Mukai, T. Ono and Y. Kubokawa, J. Chem. Soc. Faraday Trans. 1, 84, 4137 (1988).

51. H. Miyata, K. Fujii and T. Ono, ibid., 84, 3121 (1988).

52. T. Kataoka and J. A. Dumesic, J. Catal.,112, 66 (1988).

53. M. Inomata, K. Mori, A. Miyamoto, T. Ui and Y. Murakami, J. Phys. Chem. 87, 754 (1983).

54. K. Arata, and H. Mino, in "Proc. 9th Internat. Congr. Catal.", (ed. M. J. Phillips and M. Ternan) (Chem. Inst. Canada, Ottawa, 1988) Vol. 4, p. 1727.

55. F. A. Ivanovskaya and D. Kh. Senbaev, Russ. J. Phys. Chem., 61, 253 (1987).

56. L. L. Murrell, D. C. Grenoble, C. J. Kin and N. C. Dispenziere, J. Catal. 107, 434 (1987).

57. H. M. Ismail, C. R. Theocharis, D. N. Waters, M. I. Zaki and R. B. Fahim, J. Chem. Soc. Faraday Trans. 1, 82, 1601, (1987).

58. J. Bernholc, J. A. Horsley, L. L. Murell, L. G. Sherman and S. Soled, J. Phys. Chem. 81, 1526 (1987).

59. G. C. Bond and S. Flamerz, Appl. Catal. 33, 219 (1987).

60. J. M. Winterbottom, in "Catalysis Specialist Periodical Reports" Vol. 4 ed. by C.Kemball and D. A. Dowden, Ch. 6 (1981).

61. H. Vinek, H. Noller,M. Ebal, and K. Schwarz, J. Chem. Soc., Faraday Trans. 1, 73, 734, (1977).

62. G. A. Tsigdinos, H. Y. Chen and B.J. Streusand, Ind. Chem. Prod. Res. Rev. 20, 619 (1981).

63. J. A. R. van Veen, H. De. Wit, C. A. Emeis and P. A. J. M. Hendriks, J. Catal. 107, 579-582 (1987).

64. J. Haber and E. Serwicka, Polyhedron vol. 5, No. 1/2, 107-109 (1986).

65. T. Paryjczak, J. Rynkowski, and S. Karski, J. Chromatog. 188, 254 (1980).

66. H. F. J. Van't Blik, PhD Thesis, Eindhoven, The Netherlands (1984).

67. J. H. A. Martens, H.F. J.van't Blik, and R. Prins, J. Catal. 97, 200-209 (1985).

68. P. Arnoldy and J. A. Moulijn, J. Catal. 93, 38 (1985).

69. J. J. Criado, B. Macias, C. Martin and V. Kives, J. Mat. Sci. 20, 1427-1433, (1985).

70. J. Rynkowski, Zesz. Nauk.-Politech Lodz., Chem. 41, 120 (1987).

71. Sh. A. Talipova, V.N. Vorobev, and M. G. Sattarov, Zh. Prikl, Khim (Leningrad) 60 (6), 1328 (1987).

72. L. E. Makovsky, J.M. Stencel, F. R. Brown, R. E. Tischer, and S.S. Pollack, J. Catal. 89, 334-347, (1984).

73. C. M. Demanet and M. Steinberg, Appl. Surf. Sci. 14, 271-280 (1982-83).

74. R. L. Chin and D. M. Hercules, J. Phys. Chem. 86, 3079-3089 (1982).

75. J. W. Geus, in "Preparation of Catalysts III" Eds. G. Poncelet, P. Grange and P. A Jacobs, Elsevier, Amsterdam, p.1 (1983).

76. D. G. Castner and D. S. Santilli, in "Catalytic Materials Relationship between Structure and Reactivity" Ed. by T. E. Whyte, Jr., R. A. Dalla Betta, E. G. Dervuane, and R. T. K. Baker, ACS Symp. Ser. 248, Washington D. C. 39-56 (1984).

77. L. D. Schmidt and C.-P. Lee, in "Catalyst Deactivation" Chemical Industries Vol. 30, ed. by E. E. Petersen and A. T. Bell, 297 (1987).

78. A. Arleaga, J. L. G. Fierro, P. Grange and B. Delmon, in "Stud. Surf. Sci. Catal. 34" ed. by B. Delmon and G. F. Froment, 59 (1987).

79. V. Stuchly and K. Klusaceh, Appl. Catal. 34, 263-273 (1988).

80. S. Betteridge and R. Burch, Appl. Catal. 23, 413-424 (1986).

81. G. Leofanti, F. Genoni, and P. Padovan, Calorim. Anal. Therm. 16, 379-384 (1985).

82. P. Arnoldy, M. C. Franken, B. Scheffer, and J. A. Moulijn, J. Catal. 96, 381-395 (1985).

83. P. Gajardo, P. Grange and B. Delmon, J. Catal. 63, 201-216 (1980).

84. Y. Okamoto, T. Shimokawa, T. Imanda, and S. Teranishi, J. Catal. 57, 153-166 (1979).

85. J. S. Brinen and W. D. Armstrong, J. Catal. 54, 57-65 (1978).

86. P. Gajardo, D. Pirotta, C. Defosse, P. Grange and B. Delmon, J. Electron. Spectrosc. 17, 121 (1979).

87. P. Gajardo, P. Grange, and B. Delmon, J. Phys. Chem. 83, 1771 (1979).

88. P. Gajardo, D. Pirotta, P. Grange and B. Delmon, ibid. 83, 1780 (1979).

89. K. S. Chung and F. E. Massoth, J. Catal. 64, 320 (1980).

90. D. M. Hercules and J.C. Klein, in "Applied Electron Spectroscopy for Chemical Analysis", Ed. by H. Windawi and F. F.-L. Ho, J. Wiley and Sons, Ch. 8 (1982).

91. P. Grange, Cat. Rev. Sci. Eng. 21, 135 (1980).

92. A Cimino and B. A. De Angelis, J. Catal. 36, 11 (1975).

93. T. J. Wiseman, in "Characterization of Powder Surfaces" Ed. by G. D. Parfitt and K. S. W. Sing, Ch. 4 (1976).

94. R. J. H. Clark, in "The Chemistry of Titanium and Vanadium", Ch. 9, Elsevier, (1968).

95. R. R. Chianelli, in Ref. 41, p. 361.

96. R. R. Chianelli, in "Catalysis and Surface Science", ed. by H. Heinemann and G. A. Somorjai, Chemical Industries vol. 21 p. 61 (1985).

97. T. A. Pecoraro and R. R. Chianelli, J. Catal. 67, 430-445 (1981).

98. B. Delmon, in "Proceedings of the Third International Conference on the Chemistry and Uses of Molybdenum" Ann Arbor, Michigan, August 19-23, pp. 73-85 (1979).

99. H. Topsøe, B. S. Clausen, R. Candia, C. Wivel, and S. Morey, J. Catal. 68(2) 433 (1981).

CHAPTER 6 CONCLUSIONS

Some of the questions raised in Chapter 1 can be answered on the basis of the results presented in this thesis. Others remain fully or partly unsolved, calling for further research.

It has been shown that it is possible to deposit complete or nearly complete monolayers of MoO_3 and CoO on TiO_2.

Monolayer formation is dependent on the interaction between MoO_3 and the support. Not completely elucidated was the exact mechanism according to which molybdate-polyanions depolymerize prior to adsorption (Chapter 2). Neither was it possible to establish the exact mutual co-ordination of the molybdate polyhedra on the support. More research is needed to establish the configuration in which Mo-anions primarily adsorb on TiO_2 and the structure in which these primarily adsorbed species are transformed on drying and calcination. As this research requires a technique suitable for analyzing structures in solid phases, Laser Raman spectroscopy (LRS) seems very promising.

Not many techniques can be applied in establishing the existence and structure of a monolayer and in discriminating between monolayer and crystalline MoO_3 and CoO. Among the various techniques Laser Raman spectroscopy (LRS) and temperature-programmed reduction (TPR) are the most adequate. The techniques are complementary: LRS can only be

used qualitatively whereas TPR provides a quantitative analysis of the different surface species.

XPS is also a surface sensitive technique as the inelastic mean free path (escape depth) of the photo-electrons is between $\sim$ 1 nm and 3 nm in the kinetic energy range usually recorded. Hence we get quantitative or at least semi-quantitative information from the measurements of the peak areas of the characteristic lines of the elements in the catalyst. In particular several models have been developed recently to estimate the monolayer coverage of supported or adsorbed species by using XPS. However, the great disadvantage of XPS is the need for using ultra high vacuum conditions which are far from the catalytic conditions.

The importance of transmission electron microscopy (TEM) and related techniques for the characterization of practical catalysts is justified by the fact that analytical electron microscopy (AEM) is involved in the investigation of many different features: nature of the phases, size and shape of particles, dispersion, and repartition of the supported species.

Whereas some catalysts exhibit stability towards thermal treatment and/or reduction, others do not, and undergo structural changes due to the dissolution of MoO_3 and CoO into the support. Structural changes are well reflected by changes in catalytic behaviour (Chapters 4 and 5).

Not fully resolved was the nature of the driving force for the various structural changes. However, it is believed that the degree of fit of crystallographic planes at the interface of different MoO_3 and CoO and the support plays an important role.

The solution of the problem of predicting the catalytic activity is a major problem of the theory of catalysis and requires a deep understanding of the nature of catalysis, which can be obtained on the basis of the study of features of the kinetics and mechanism of individual classes of reactions[1]. The creation of a single theory of catalysis, generalizing all varieties of catalytic processes, is impracticable at the current level of our knowledge. The search for a theoretical substantiation of regularities in individual classes and types of catalytic processes is most advisable.

An important step in the classification of catalytic processes was the division proposed by Roginskii[2] of reactions, and the catalysts, into two major groups: oxidation-reduction and acid-base.

The search for regularities for a broad class of oxidation-reduction catalytic processes led to significant success in the selection of active and selective catalysts and to their theoretical substantiation[3-6]. Clear regularities, associating the catalytic activity of samples with their physico-chemical properties and nature of active centres, have as yet not been observed for catalytic processes of the acid-base type[1]. Numerous attempts to

reveal a correlation between catalytic activity and surface acidity have led to certain positive results[7], but there is no clear answer to this question. Today we still cannot predict what acidity a catalyst should possess for the occurrence of a certain process. The issue is not as to what type of acidic centres certain reactions occur at. The presence, or on the other hand, the absence of correlations between the catalytic activity and catalyst acidity can already give very valuable information on the mechanism of catalytic processes and will help reveal regularities of the selection of active and selective acid-base catalysts.

To determine the general regularities of selection of catalysts of the acid-base type, it is necessary to study the mechanism of the investigated reactions, which cannot be understood without answering the question about the nature of active centres and the character of their interaction with the reactant[1]. Unfortunately, our knowledge in this field is as yet limited. The intimate reaction mechanism can change as a function of the reaction and conditions and the nature of active centres.

From the experimental results, one can conclude that the activity of the catalysts for the decomposition of 2-propanol to yield propene (dehydration product) is as follows:

$V_2O_5 > MoO_3 > MoO_3/TiO_2 > CoO\text{-}MoO_3/TiO_2 >$

$V_2O_5/TiO_2 > CoO/TiO_2 > TiO_2$,

and for the decomposition of 2-propanol to yield acetone (dehydrogenation product) is as follows:

CoO/TiO_2 > $CoO\text{-}MoO_3/TiO_2$ > MoO_3/TiO_2 > V_2O_5/TiO_2 > V_2O_5 > MoO_3 > TiO_2.

Because of the complexity it is impossible to come to a general theory for the relationship between catalytic activity for 2-propanol decomposition and the structural properties.

_____ // _____

6.1 References

1. V.V. Goncharuk, Ukr. Khim. Zh. Vol. 48 (11),p. 8-13 (1982).

2. S. Z. Roginskii, "Fundamentals of Theory of Catalysis", Probl. Kinetiki i Kataliza, no. 6, pp. 9-53, (1949).

3. G. K. Boreskov, Catalysis in Sulfuric Acid Production [in Russian]. Goskhimizdat, Moscow, (1954).

4. V. A. Roiter, Selected Papers [in Russian], Nauk. Dumka, (1976).

5. O.V. Krylov,"Catalysis by Nonmetals", Academic Press, New York and London (1970).

6. G. I. Golodets,"Heterogeneous-Catalytic Reactions Involving Molecular Oxygen", Stud. Surf. Sci. Catal. 15, Elsevier, (1983)

7. T. Tanabe, "Solid Acids and Bases" Kodansha, Japan, Academic Press, London and New York (1970).

Appendix I

Theoretical wt.% MoO_3 for a monolayer

a. Estimate based on the concentration of Ti-OH groups

Data: surface area of TiO_2 = 9.6 m^2g^{-1}

molecular weight of MoO_3 = 143.94 $g.mol^{-1}$

maximum number of OH^- groups* = 4.5/nm^2

density of MoO_3 = 4.692 gcm^{-3}

Wt. % of MoO_3 =

$$\frac{9.6\ m^2g^{-1} \times 4.5 \times 10^{18}\ OH's\ m^{-2}}{6.02 \times 10^{23}\ mol} \times 143.94\ g.mol^{-1} \times 100\%$$

$$= 1.0329\%$$

$$\simeq 1.03\%$$

Thickness of a monolayer

$\rho = m/V \quad \Rightarrow \quad V = m/\rho$

$$V = \frac{143.94 g.mol^{-1}}{4.692 g.cm^{-3}} \times \frac{1\ mol}{6.02 \times 10^{23}\ mol} \times \frac{1 m^3}{10^6\ cm^3}$$

$= 5.096 \times 10^{-29}\ m^3/mole.$

Volume = $(side)^3 \quad \Rightarrow \quad = side = (volume)^{1/3}$

side $\Rightarrow$ thickness = $3.71 \times 10^{-10} m$

Area = $1.37 \times 10^{-19} m^2$

---

* J. R. Anderson, in "Structure of Metallic Catalysts" Academic Press, 1975.

b. Density of Ti^{4+} ions method

Estimate based on the surface concentration of Ti^{4+} ions.

Data: surface area of TiO_2 = 9.6 $m^2.g^{-1}$

molecular weight of MoO_3 = 143.94 $g.mol^{-1}$

number of Ti_s (surface Ti atom)* = 6.25 Ti/nm^2

Wt. % of MoO_3 =

$$\frac{9.6 m^2 g^{-1} \times 6.25 \times 10^{18} m^{-2}}{6.02 \times 10^{23} \text{ mol}} \times 143.94 g.mol^{-1} \times 100\% = 1.4346\%$$

$$\simeq 1.43\%$$

c. Estimate based on the density of MoO_3

from method (a)

Area = 1.37×10^{-19} m^2

Number of molecules of MoO_3 required to cover TiO_2 surface =

$$9.6 m^2 g^{-1} \times \frac{\text{moles}}{1.37 \times 10^{-19} m^2} = 6.97 \times 10^{19} \text{ moles.}$$

$$\text{No. of moles} = 6.97 \times 10^{19} \times \frac{1 \text{ mole}}{6.02 \times 10^{23}}$$

$$= 1.16 \times 10^{-4} \text{ moles}$$

Wt. of MoO_3 = $1.16 \times 10^{-4} \times 143.94 = 1.66 \times 10^{-2}$

Wt. of MoO_3 for monolayer:

$$\text{Wt.\%} = \frac{1.66 \times 10^{-2}}{1 + 1.66 \times 10^{-2}} = 1.6403 \times 10^{-2}$$

$$= 1.64\%$$

---

* G. C. Bond, S. Flamerz and L. van Wijk, Catal. Today 1(1987) 229.

Appendix II

a. Theoretical wt.% Co_3O_4 for a monolayer

Estimate based on the surface concentration of Ti^{4+} ions

Data: surface area of TiO_2 = $9.6\ m^2g^{-1}$

molecular weight of Co_3O_4 = $240.80 gmol^{-1}$

number of Ti_s (surface Ti atoms) = $6.25\ Ti/nm^2$

density of Co_3O_4 = $6.07\ g.cm^{-3}$

Wt. % of Co_3O_4 =

$$\frac{9.6 m^2g^{-1} \times 6.25 \times 10^{18}\ m^{-2}}{6.02 \times 10^{23}\ \text{moles}} \times 240.80\ gmol^{-1} \times 100\% = 2.4\%$$

Thickness of a monolayer

$\rho = m/V \Rightarrow V = m/\rho$

$$V = \frac{240.80 g.mol^{-1}}{6.07 g.cm^{-3}} \times \frac{1\ \text{mole}}{6.02 \times 10^{23}\ \text{mol}} \times \frac{1 m^3}{10^6\ cm^3}$$

$= 6.59 \times 10^{-29}\ m^3/\text{moles}.$

Volume = $(\text{side})^3 \Rightarrow$ side = $(\text{volume})^{1/2}$

side $\Rightarrow$ thickness $\Rightarrow$ = 4.04×10^{-10} m

Area = $1.63 \times 10^{-19}\ m^2$

b. Estimate based on the density of Co_3O_4

From method (a): Area of Co_3O_4 molecule = 1.63×10^{-19} m^2.

Number of molecules of Co_3O_4 required to cover TiO_2 surface

$$9.6\ m^2 \times \frac{\text{moles}}{1.63 \times 10^{-19}\ m^2} = 5.88 \times 10^{19} \text{ moles}$$

$$\text{No. of moles} = 5.88 \times 10^{19} \times \frac{1 \text{ mole}}{6.02 \times 10^{23}}$$

$$= 9.77 \times 10^{-5} \text{ moles.}$$

$$\text{Wt. of } Co_3O_4 = 9.77 \times 10^{-5} \times 240.80 = 2.35 \times 10^{-2} g$$

Wt.% of Co_3O_4 for monolayer:

$$\text{Wt\%} = \frac{2.35 \times 10^{-2}}{1 + 2.35 \times 10^{-2}} = 2.298 \times 10^{-2}$$

$$\simeq 2.30\%.$$

c. Estimate based on the concentration of Ti - OH groups

Data: surface area of TiO_2 = 9.6 m^2g^{-1}

molecular weight of Co_3O_4 = 240.8 $g.mol^{-1}$

maximum number of OH^- groups = 4.5×10^{18} m^{-2}

Wt. % of Co_3O_4 =

$$\frac{9.6 m^2 g^{-1} \times 4.5 \times 10^{18} m^{-2}}{6.02 \times 10^{23} \text{ mol}} \times 240.80 \text{ gmol}^{-1} \times 100\% = 1.728\%$$

$$\simeq 1.73\%$$

---

d. Theoretical wt.% CoO for a monolayer

Estimate based on the surface concentration of Ti^{4+} ions

Data: surface area of TiO_2 = 9.6 m^2g^{-1}

molecular weight of CoO = 74.93 $gmol^{-1}$

number of Ti_s (surface Ti atom) = $6.25 \times 10^{18} m^{-2}$

Wt.% of CoO =

$$\frac{9.6 m^2 g^{-1} \times 6.25 \times 10^{18} m^{-2}}{6.02 \times 10^{23} \text{ mol}} \times 74.93 \text{ gmol}^{-1} \times 100\% = 0.746\%$$

$$\simeq 0.75\%$$

e. Estimate based on the concentration of Ti-OH groups

Data: surface area of TiO_2 = $9.6\ m^2g^{-1}$

molecular weight of CoO = $74.93\ gmol^{-1}$

maximum number of OH^- groups = $4.5 \times 10^{18} m^{-2}$

Wt.% of CoO =

$$\frac{9.6\ m^2g^{-1} \times 4.5 \times 10^{18}\ m^{-2}}{6.02 \times 10^{23}\ mol} \times 74.93\ gmol^{-1} \times 100\% = 0.537\%$$

$$\simeq 0.54\%$$

Appendix III

Monolayer Capacity for $CoO-MoO_3/TiO_2$ Catalysts (OH groups method)

CoO/TiO_2	surface area of TiO_2(P-25)	54.8 m^2g^{-1}
	total no. of OH groups	4.9/nm^2
	M. wt. of CoO	74.93 $gmol^{-1}$

$$\frac{4.9 \times 54.8 \times 10^{18}}{6.023 \times 10^{23}} \times 74.93 \times 100 = 3.34\%$$

MoO_3/TiO_2

M. wt. of MoO_3 143.94

$$\frac{4.9 \times 54.8 \times 10^{18}}{6.023 \times 10^{23}} \times 143.94 \times 100 = 6.42\%$$

For one monolayer coverage of 50% CoO and 50% MoO_3 will be

$$\frac{3.34}{2} + \frac{6.42}{2} = 1.67\%CoO + 3.21\%MoO_3$$

1. 0.42%CoO - 0.8%MoO_3/TiO_2 (1/4CL + 1/4ML)*
2. 0.84%CoO - 1.6%MoO_3/TiO_2 (1/2CL + 1/2ML)
3. 1.67%CoO - 3.21%MoO_3/TiO_2 (1CL + 1/2ML)
4. 2.51%CoO - 4.81%MoO_3/TiO_2 (1 1/2CL +1 1/2ML)
5. 3.34%CoO - 6.42%MoO_3/TiO_2 (2CL + 2ML)
6. 5.01%CoO - 9.63%MoO_3/TiO_2 (3CL + 3ML)
7. 6.68%CoO - 12.84%MoO_3/TiO_2 (4CL + 4ML)

* CL = CoO Layer, ML = MoO_3 Layer

Appendix IV

An example for estimating theoretical H_2 uptake of $(0.4\%\ CoO\text{-}0.8\%\ MoO_3)/TiO_2$ catalyst

0.004 g CoO $\equiv$ 0.004/74.93 = 5.34×10^{-5} mol

Reduction $Co^{2+} \longrightarrow Co^{o}$ needs 1 H_2 $\therefore$ 5.34×10^{-5} mol H_2

0.008 g MoO_3 $\equiv$ 0.008/143.94 = 5.56×10^{-5} mol

Reduction $Mo^{6+} \longrightarrow Mo^{o}$ needs 3 H_2 $\therefore$ 1.668×10^{-4} mol H_2

Total = 2.202×10^{-4} mol H_2

If all Co present as Co^{3+}, reduction to Co^{o} need 1.5 H_2

$\therefore$ 8.01×10^{-5} mol H_2

Total = 2.469×10^{-4} mol H_2